Atmos. Chem. Phys., 12, 3527–3557, 2012
www.atmos-chem-phys.net/12/3527/2012/
doi:10.5194/acp-12-3527-2012
© Author(s) 2012. CC Attribution 3.0 License.

Atmospheric Chemistry and Physics

Observed and simulated time evolution of HCl, $ClONO_2$, and HF total column abundances

R. Kohlhepp[1], R. Ruhnke[1], M. P. Chipperfield[2], M. De Mazière[3], J. Notholt[4], S. Barthlott[1], R. L. Batchelor[5,6], R. D. Blatherwick[7], Th. Blumenstock[1], M. T. Coffey[6], P. Demoulin[8], H. Fast[9], W. Feng[2], A. Goldman[6], D. W. T. Griffith[10], K. Hamann[1], J. W. Hannigan[6], F. Hase[1], N. B. Jones[10], A. Kagawa[11,12], I. Kaiser[1], Y. Kasai[11], O. Kirner[13], W. Kouker[1], R. Lindenmaier[5], E. Mahieu[8], R. L. Mittermeier[9], B. Monge-Sanz[2], I. Morino[14], I. Murata[15], H. Nakajima[16], M. Palm[4], C. Paton-Walsh[10], U. Raffalski[17], Th. Reddmann[1], M. Rettinger[18], C. P. Rinsland[19,†], E. Rozanov[20,21], M. Schneider[1], C. Senten[3], C. Servais[8], B.-M. Sinnhuber[4,1], D. Smale[22], K. Strong[5], R. Sussmann[18], J. R. Taylor[5,23], G. Vanhaelewyn[3], T. Warneke[4], C. Whaley[5], M. Wiehle[1], and S. W. Wood[22]

[1]Karlsruhe Institute of Technology (KIT), Institute for Meteorology and Climate Research (IMK-ASF), Karlsruhe, Germany
[2]Institute for Climate and Atmospheric Science, School of Earth and Environment, University of Leeds, Leeds, UK
[3]Belgian Institute for Space Aeronomy (BIRA-IASB), Brussels, Belgium
[4]Institute of Environmental Physics, University of Bremen, Bremen, Germany
[5]Department of Physics, University of Toronto, Toronto, Ontario, Canada
[6]National Center for Atmospheric Research (NCAR), Boulder, CO, USA
[7]Department of Physics and Astronomy, University of Denver, Denver, CO, USA
[8]Institute of Astrophysics and Geophysics, University of Liège, Liège, Belgium
[9]Environment Canada, Toronto, Ontario, Canada
[10]Centre for Atmospheric Chemistry, University of Wollongong, Wollongong, Australia
[11]National Institute of Information and Communications Technology, Tokyo, Japan
[12]Fujitsu FIP Corporation, Tokyo, Japan
[13]Karlsruhe Institute of Technology (KIT), Steinbuch Centre for Computing, Karlsruhe, Germany
[14]Center for Global Environmental Research, National Institute for Environmental Studies (NIES), Japan
[15]Department of Environmental Studies, Graduate School of Environmental Studies, Tohoku University, Japan
[16]Atmospheric Environment Division, National Institute for Environmental Studies (NIES), Japan
[17]Swedish Institute of Space Physics (IRF), Kiruna, Sweden
[18]Karlsruhe Institute of Technology (KIT), Institute for Meteorology and Climate Research (IMK-IFU), Garmisch-Partenkirchen, Germany
[19]NASA Langley Research Center, Hampton, VA, USA
[20]ETH Zürich, Institute for Atmospheric and Climate Science (IACETH), Zürich, Switzerland
[21]Physical-Meteorological Observatory, World Radiation Center, Davos, Switzerland
[22]National Institute of Water and Atmospheric Research Ltd (NIWA), Lauder, New Zealand
[23]National Ecological Observatory Network (NEON), Boulder, CO, USA
[†]deceased

Correspondence to: R. Kohlhepp (regina.kohlhepp@kit.edu)

Received: 28 September 2011 – Published in Atmos. Chem. Phys. Discuss.: 7 December 2011
Revised: 15 March 2012 – Accepted: 2 April 2012 – Published: 12 April 2012

Abstract. Time series of total column abundances of hydrogen chloride (HCl), chlorine nitrate ($ClONO_2$), and hydrogen fluoride (HF) were determined from ground-based Fourier transform infrared (FTIR) spectra recorded at 17 sites belonging to the Network for the Detection of Atmospheric Composition Change (NDACC) and located between 80.05° N and 77.82° S. By providing such a near-global overview on ground-based measurements of the two major

stratospheric chlorine reservoir species, HCl and $ClONO_2$, the present study is able to confirm the decrease of the atmospheric inorganic chlorine abundance during the last few years. This decrease is expected following the 1987 Montreal Protocol and its amendments and adjustments, where restrictions and a subsequent phase-out of the prominent anthropogenic chlorine source gases (solvents, chlorofluorocarbons) were agreed upon to enable a stabilisation and recovery of the stratospheric ozone layer. The atmospheric fluorine content is expected to be influenced by the Montreal Protocol, too, because most of the banned anthropogenic gases also represent important fluorine sources. But many of the substitutes to the banned gases also contain fluorine so that the HF total column abundance is expected to have continued to increase during the last few years.

The measurements are compared with calculations from five different models: the two-dimensional Bremen model, the two chemistry-transport models KASIMA and SLIMCAT, and the two chemistry-climate models EMAC and SOCOL. Thereby, the ability of the models to reproduce the absolute total column amounts, the seasonal cycles, and the temporal evolution found in the FTIR measurements is investigated and inter-compared. This is especially interesting because the models have different architectures. The overall agreement between the measurements and models for the total column abundances and the seasonal cycles is good.

Linear trends of HCl, $ClONO_2$, and HF are calculated from both measurement and model time series data, with a focus on the time range 2000–2009. This period is chosen because from most of the measurement sites taking part in this study, data are available during these years. The precision of the trends is estimated with the bootstrap resampling method. The sensitivity of the trend results with respect to the fitting function, the time of year chosen and time series length is investigated, as well as a bias due to the irregular sampling of the measurements.

The measurements and model results investigated here agree qualitatively on a decrease of the chlorine species by around $1\,\%\,yr^{-1}$. The models simulate an increase of HF of around $1\,\%\,yr^{-1}$. This also agrees well with most of the measurements, but some of the FTIR series in the Northern Hemisphere show a stabilisation or even a decrease in the last few years. In general, for all three gases, the measured trends vary more strongly with latitude and hemisphere than the modelled trends. Relative to the FTIR measurements, the models tend to underestimate the decreasing chlorine trends and to overestimate the fluorine increase in the Northern Hemisphere.

At most sites, the models simulate a stronger decrease of $ClONO_2$ than of HCl. In the FTIR measurements, this difference between the trends of HCl and $ClONO_2$ depends strongly on latitude, especially in the Northern Hemisphere.

1 Introduction

Short-lived reactive inorganic chlorine (e.g. Cl and ClO) is released in the stratosphere via photo-dissociation of chlorinated source gases by UV radiation (e.g. chlorofluorocarbons (CFCs), hydrochlorofluorocarbons (HCFCs), carbon tetrachloride (CCl_4), methyl chloride (CH_3Cl), methyl chloroform (CH_3CCl_3), and halons). Reactive chlorine plays a crucial role in the thinning of the stratospheric ozone layer and particularly in polar ozone depletion as it is involved in ozone-destroying catalytic cycles (Molina and Rowland, 1974; Crutzen et al., 1978). In the 1970s and 1980s, the emission of anthropogenic halogenated source gases characterised by a strong ozone depletion potential (ODP) increased massively. So in order to stabilise the stratospheric ozone layer and enable its recovery, the Montreal Protocol and its amendments and adjustments have been progressively implemented to reduce or even stop the production and release of the important chlorinated source gases.

Figure 1 shows the time development of the mean global surface volume mixing ratios of total organic chlorine (CCl_y) and total organic fluorine (CF_y) according to the halocarbon scenarios that were used as boundary conditions for the model simulations, between 1992 and 2010. Additionally, their relative annual growth rates are shown. CCl_y is defined here as 3 CFC-11 + 2 CFC-12 + 3 CFC-113 + 2 CFC-114 + CFC-115 + 4 CCl_4 + 3 CH_3CCl_3 + HCFC-22 + 2 HCFC-141b + HCFC-142b + Halon-1211 + CH_3Cl and CF_y is represented by CFC-11 + 2 CFC-12 + 3 CFC-113 + 4 CFC-114 + 5 CFC-115 + 2 HCFC-22 + HCFC-141b + 2 HCFC-142b + 2 Halon-1211 + 3 Halon-1301 + 2 Halon-1202 + 4 Halon-2402. According to the A1 scenario from WMO (2007), CCl_y is assumed to have reached its tropospheric maximum in 1993, whereas CF_y is expected to have reached a plateau with a small positive growth rate of about 0.1 % per year in 2010 (Fig. 1). The older scenario Ab from WMO (2003) assumes CCl_y to have reached its maximum only in 1995. In contrast, CF_y peaks earlier than in the A1 scenario, already in 2005, so that the growth rate in the Ab scenario in 2010 is already negative. A small part of the difference between the two scenarios probably results from the fact that in the WMO (2003) Ab scenario, Halon-2402 and Halon-1202 are not considered.

Once released from chlorinated source gases (CCl_y), chlorine atoms undergo a number of reactions in the stratosphere forming different species which are summarised as the total inorganic chlorine budget (Cl_y = HCl + $ClONO_2$ + ClO + 2 Cl_2O_2 + OClO + 2 Cl_2 + Cl + HOCl + BrCl). The largest contribution to Cl_y comes from the reservoir species HCl and $ClONO_2$. However, it is the shorter-lived, highly reactive ClO_x species (i.e. Cl + ClO + 2 Cl_2O_2) that efficiently destroy ozone.

In addition to chlorine atoms, fluorine is released by the decomposition of CFCs and HCFCs. However, in contrast to chlorine, fluorine forms long-lived substances such as COF_2

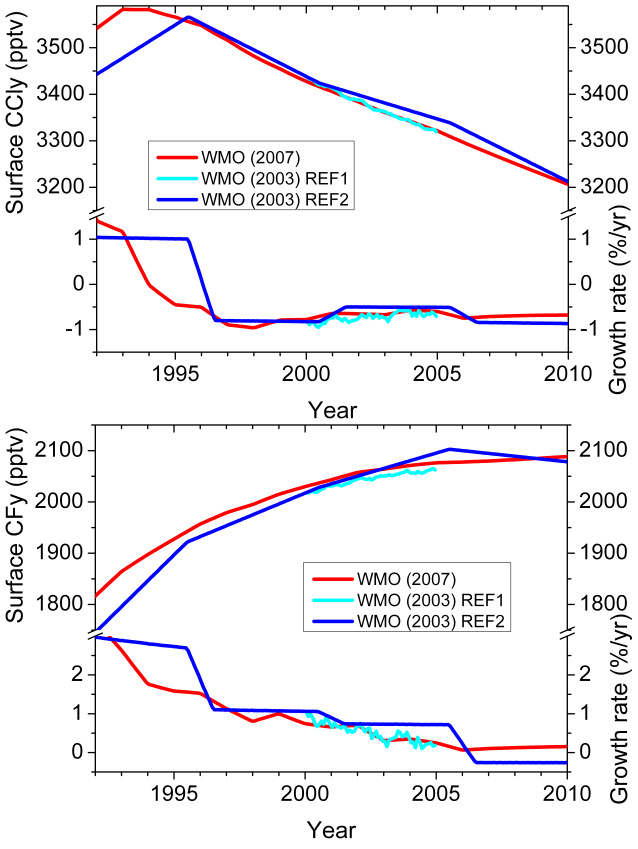

Fig. 1. Time series of monthly mean CCl_y (top) and CF_y (bottom) surface volume mixing ratios (in pptv) and growth rates (in % per year) from different halocarbon scenarios between 1992 and 2010. The one called "WMO (2003) REF2" corresponds to the scenario Ab in WMO (2003) and was used by KASIMA and the 2-D model. The "WMO (2003) REF1" time series of CCl_y and CF_y are based on that same scenario until the year 2000, but were corrected by additional measurements between 2000 and 2004. It was used by SOCOL. The "WMO (2007)" scenario is the one called A1 in WMO (2007) and was used by SLIMCAT and EMAC in this study.

and ultimately HF whose only known sink is transport to the troposphere followed by rainout. Due to its long stratospheric lifetime, fluorine, and in particular HF, is not involved in catalytic ozone destruction. It is often used as a tracer for stratospheric dynamics and transport, and hence as a reference for chemically more active trace gases like HCl (Chipperfield et al., 1997). Because fluorine is also contained in CFC substitutes, the HF total column abundance is expected to have continued increasing during the time range considered in the present study.

Thus, measurements of the time development of the reservoir species (HCl and $ClONO_2$ for the inorganic chlorine and HF for the inorganic fluorine) provide a means of verifying the effectiveness of the above-mentioned international regulations.

There have been several investigations of HCl trends from long-term ground-based measurements (Zander et al., 1987; Rinsland et al., 1991; Wallace and Livingston, 1991; Wallace et al., 1997). As they were performed before the Montreal Protocol and its amendments took effect, they report increasing HCl total column abundances. Later studies confirmed stratospheric HCl or total Cl_y to have reached a plateau at the end of the 1990s and to be decreasing since (e.g., Newchurch et al., 2003; Froidevaux et al., 2006; Lary et al., 2007).

In the investigation by Rinsland et al. (2003), time series of HCl and $ClONO_2$ from Fourier transform infrared (FTIR) total column measurements at 9 stations belonging to the Network for the Detection of Atmospheric Composition Change (NDACC) until 2001 were compared with HALOE data at 55 km and calculations from a 2-D model. The measurements agreed on a stabilisation of the stratospheric inorganic chlorine content so that Rinsland et al. (2003) were able to confirm the effectiveness of the Montreal Protocol and amendments. The FTIR measurements within NDACC have been continued until present, and more stations have joined the network. Therefore, the present study is able to continue and extend the investigations of Rinsland et al. (2003) by reporting measurements at 17 sites until the end of 2009. The primary question addressed is whether the expected decrease of the total global inorganic chlorine abundance can be confirmed now with the FTIR measurements. Furthermore, five atmospheric chemistry models were included in the study in order to investigate and inter-compare their ability to reproduce the HCl, $ClONO_2$, and HF total column amounts, their seasonal cycles and their temporal evolution, as measured by the FTIR instruments.

In the framework of the SPARC CCMVal (2010) initiative, a comparison between different chemistry-climate models (CCMs) was performed for HCl and $ClONO_2$. The two CCMs taking part in the present study, EMAC and SOCOL, were also involved in this activity. The CCM calculations were compared with FTIR measurements above the Jungfraujoch and with satellite data sets with respect to the mean annual cycle, mean profiles and total column abundances. So the present study extends the SPARC CCMVal (2010) comparison with respect to additional geolocations and compares the CCM results of EMAC and SOCOL with those of other kinds of models (a 2-D model and two chemistry-transport models, CTMs).

This paper does not aim at explaining in detail differences between models or between models and measurements. Such an analysis requires much more detailed investigations, which are beyond the scope of this study. Instead, it intends to show the global inorganic chlorine decrease seen in the FTIR measurements at 17 NDACC sites, the increase in HF, and to analyse the overall ability of different state-of-the-art atmospheric chemistry models to reproduce these measurements.

An overview of the measurements and models is given in Sect. 2 and 3, respectively. Section 4 compares the time

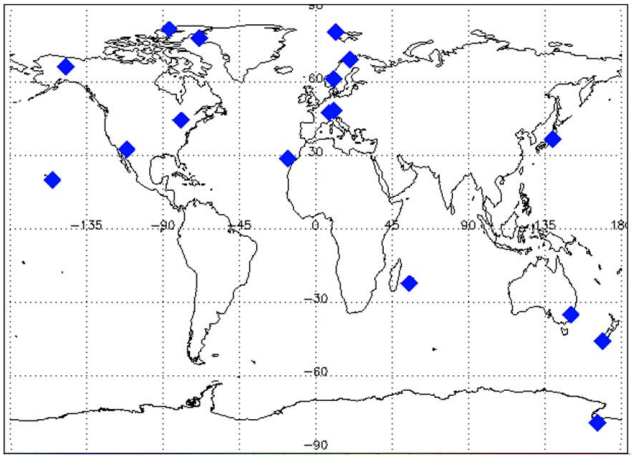

Fig. 2. Geographical distribution of the measurement sites.

series of measurements and models with respect to the mean differences between the data sets and also the mean seasonal cycle and its amplitude of the three gases. The trends of HCl, $ClONO_2$, and HF are presented in Sect. 6, but before, an investigation of the dependency of the trend results on some influencing factors is made (Sect. 5). The results are discussed in Sect. 7 and concluding remarks are given in Sect. 8.

2 Instrumentation

The observational data used in this paper were obtained from ground-based solar absorption measurements of high-spectral-resolution Fourier transform infrared (FTIR) spectrometers operated at 17 sites. They all belong to the Network for the Detection of Atmospheric Composition Change (NDACC; http://www.ndacc.org) and are located between 77.82° S and 80.05° N (see Table 1 and Fig. 2). For these measurements, the atmosphere must be free of clouds and the sun needs to be above the horizon. This implies that during polar night, no measurements are possible. Of course, this dependency on direct sunlight leads to an irregular sampling of the measurements, with considerable gaps especially during the winter at the polar sites.

The spectrometers cover the spectral range approximately 600 to 4300 cm^{-1}. In the network, it is common practice to record spectra within limited spectral bands, using a set of appropriate optical bandpass filters, in order to improve the signal-to-noise ratio. The spectral range is covered with two liquid-nitrogen-cooled detectors, namely an Indium-Antimonide (InSb) detector for the short wavelength part of the range and a Mercury-Cadmium-Telluride (MCT) detector for the long wavelength end of the range.

The high-resolution spectra include many distinct and overlapping absorption lines of a large number of atmospheric constituents. The area under the absorption lines provides information about the total abundance of the absorber gas along the line-of-sight. The spectral line shape gives additional information about the vertical distribution of the absorber in the atmosphere, based on the pressure-broadening characteristics of the line. The vertical distribution can be retrieved with limited resolution only. The so-called inversion of the spectra, to derive the vertical distribution or total column abundance of the target absorber gas from the spectra, generally uses one or a few selected spectral micro-windows. The purpose is to optimise the information content regarding the target gas and to minimise the impact of interfering species. The retrievals are based on a non-linear least squares line-by-line fit of the spectra. The more recent retrieval algorithms use a semi-empirical implementation of the optimal estimation method developed by Rodgers (2000). Only a few different retrieval codes are used within the NDACC infrared community, namely SFIT1 and SFIT2, PROFFIT and GFIT. SFIT1 and SFIT2 were developed jointly at the NASA Langley Research Center, Hampton, VA, United States, the National Center for Atmospheric Research (NCAR) at Boulder, CO, United States, and the National Institute of Water and Atmospheric Research (NIWA) at Lauder, New Zealand (Rinsland et al., 1998). SFIT1 is the older version, which does not retrieve any vertical profile information: it only performs a scaling of the a priori vertical profile. PROFFIT was developed at the Institute for Meteorology and Climate Research of the Karlsruhe Institute of Technology (KIT), and it was demonstrated that the results are equivalent to those derived with SFIT2 (Hase et al., 2004; Duchatelet et al., 2010). GFIT was developed by G. Toon at the Jet Propulsion Laboratory and performs a profile scaling similar to SFIT1 (Washenfelder et al., 2006).

The data analysis needs corresponding pressure/temperature profiles: These are taken from the National Center for Environmental Prediction (NCEP) (Lait et al., 2005) or from local or nearby radiosonde data (see supplement to the present publication). The spectroscopic parameters of the absorption lines are usually taken from the HITRAN database (Rothman et al., 1992, 1998, 2003, 2005), or from the ATMOS line list (Brown et al., 1996).

Since the retrieval of vertical profile information is based on the absorption line shapes, it is fundamental to know the instrumental line shape function (ILS) precisely. Therefore, absorption spectra of HBr in a cell at low pressure are regularly recorded. These spectra can also be used as a proxy for comparison since the HBr cells have identical origins (Coffey et al., 1998). The analysis of the resulting HBr absorption line shape, usually done with the program LINEFIT (Hase et al., 1999), yields precise knowledge of the instrument's alignment and the associated instrumental line shape function.

Different kinds of FTIR instruments have been used for the measurements analysed in this study (please see the description of the sites below), called Bruker 120M, 120HR, and 125HR, and Bomem DA8. The instrumental differences between the Bruker spectrometers are small, especially

Table 1. Overview of the geographical coordinates of the 17 sites and the time ranges covered by the HCl, $ClONO_2$, and HF measurements.

Measurement site	Latitude	Longitude	Altitude a.s.l. (m)	HCl meas. since	$ClONO_2$ meas. since	HF meas. since	Meas. used until
Eureka, Canada	80.05° N	86.42° W	610	1997	1997	1997	2009
Ny Ålesund, Svalbard, Norway	78.92° N	11.93° E	15	1992	1992	1992	2009
Thule, Greenland, Denmark	76.53° N	68.74° W	225	1999	1999	1999	2009
Kiruna, Sweden	67.84° N	20.41° E	419	1996	1996	1996	2009
Poker Flat, Alaska, USA	65.12° N	147.43° W	610	1999		1999	2004
Harestua, Norway	60.20° N	10.8° E	596	1994	1994	1994	2009
Zugspitze, Germany	47.42° N	10.98° E	2964	1995	1996	1995	2009
Jungfraujoch, Switzerland	46.55° N	7.98° E	3580	1984	1986	1984	2009
Toronto, Canada	43.66° N	79.4° W	174	2002		2002	2009
Tsukuba, Japan	36.05° N	140.12° E	31	1998		1998	2009
Kitt Peak, Arizona, USA	31.90° N	111.6° W	2090	1981	1980	1980	2009
Izaña, Tenerife, Spain	28.30° N	16.48° W	2367	1999	1999	1999	2009
Mauna Loa, Hawaii, USA	19.54° N	155.58° W	3397	1991		1995	2009
Réunion Island, France	21.80° S	55.5° E	50	2004		2004	2009
Wollongong, Australia	34.45° S	150.88° E	30	1996	1996	1996	2009
Lauder, New Zealand	45.04° S	169.68° E	370	1990	1990	1992	2009
Arrival Heights, Antarctica	77.82° S	166.65° E	250	1992	1997	1997	2009

between 120HR and 125HR. The latter is the newer version with improved electronics which in the end helps to reduce the noise in the spectra. The 120M instrument is the mobile version which is therefore smaller and more compact than the 120HR. In general, it is more difficult to adjust the 120M than the 120HR spectrometer, which may lead to a slightly worse ILS of the 120M. However, this would affect mostly the profile retrievals, not the total column abundances dealt with in this study. So there are no significant discrepancies expected between the different Bruker instruments. Furthermore, when a new instrument was installed at one site, if possible, an intercomparison was performed with the old one so that the here presented data sets can be assumed to show self-consistent time series. The discrepancies between a Bruker 125HR and a Bomem DA8 instrument were investigated in detail for the total column abundances of the three gases analysed here by e.g. Batchelor et al. (2010) and were found to amount to less than 3.5 %.

Concerning the vertical averaging kernels, the corresponding height-dependent sensitivity of the retrieval, the degrees of freedom for signal, and the overall errors associated with the measurements, no detailed information is given here. It can be found in the references given for every site, or other publications, for example in Kohlhepp et al. (2011) for Kiruna. In addition, a paper comprising the retrieval settings and errors for many gases, including HCl, $ClONO_2$, and HF, at all NDACC IRWG sites is in preparation at the moment.

Hereafter, some characteristics of the various observation sites are given from north to south. Table 1 lists their coordinates and measurement time periods used in this study. In the Supplement to this publication, the most significant settings for the retrieval of HCl, $ClONO_2$, and HF at each site are described.

2.1 Eureka (80.05° N)

Environment Canada operated a Bomem DA8 FTS at the Eureka NDACC observatory every spring and nearly every fall from 1993 until 2008. Details of this instrument, observations and retrieval methods are given in Fast et al. (2011). In July 2006, the Canadian Network for the Detection of Atmospheric Change (CANDAC) installed a Bruker 125HR FTS in the observatory, now known as the Polar Environment Atmospheric Research Laboratory (PEARL). This instrument makes measurements at $0.0035\,cm^{-1}$ resolution throughout the sunlit parts of the year (mid-February to mid-October). It was run simultaneously with the Bomem DA8 during three campaigns in 2007 and 2008 before the removal of the DA8 in February 2009. Full details of the instrument and retrieval parameters are given in Batchelor et al. (2009). Measurements shown for Eureka in this work include daily average total column densities from the Environment Canada Bomem DA8 between February 1997 and March 2006, and from the CANDAC Bruker 125HR from July 2006 onwards. The biases between the use of the HITRAN 1992 spectral database (for analysis of the DA8 data) and HITRAN 2004 (for analysis of the 125HR data) have been quantified by Fast et al. (2011) based on retrievals from DA8 spectra recorded for one day and for the microwindows indicated for the DA8 in the Tables 1 to 3 of the supplement to the present publication. They are −0.4 % for HCl, +15.6 % for $ClONO_2$, and 0.0 % for HF.

2.2 Ny Ålesund (78.92° N)

At the AWIPEV research base in Ny Ålesund on the Svalbard archipelago, FTIR measurements have been performed since 1990. In the period 1990 to 1995 a Bruker 120M was used. This spectrometer was replaced by a 120HR in 1995. The instruments are operated by the AWI Potsdam and the University of Bremen. Measurements in solar absorption geometry are performed from the end of March until the end of September each year. During polar night, measurements in lunar absorption geometry are performed, which are not used here. The observation range is 600 to 8000 cm^{-1}, depending on the instrument setup, which is changed for the different experiments.

2.3 Thule (76.53° N)

The NDACC FTS stationed at Thule, Greenland, is operated by the National Center for Atmospheric Research (NCAR). The instrument and observing system are described in Hannigan et al. (2009). The instrument is a Bruker 120M FTS that has been blind compared (Goldman et al., 1999) prior to installation at Thule in 1999. The system operates autonomously to record solar absorption spectra in the mid-IR on approx. 30 % of the days between 20 February and 20 October. Observations are taken up to five times per day depending upon weather conditions.

2.4 Kiruna (67.84° N)

Since March 1996, a Bruker IFS 120HR FTIR spectrometer has been operated continuously by the Institute for Meteorology and Climate Research (IMK-ASF) of the Karlsruhe Institute of Technology (KIT, formerly Research Center Karlsruhe) at the Swedish Institute of Space Physics (IRF) in Kiruna, northern Sweden, in collaboration with the IRF Kiruna and the University of Nagoya (Japan). A side-by-side comparison was performed in 1998 with the travelling NDACC standard spectrometer (Meier et al., 2005). The instrument is remotely controlled since July 2004. It was upgraded to a 125HR spectrometer in July 2007. Experimental details have been published elsewhere (e.g. Blumenstock et al., 2006). On average, measurements are taken on about 80 days per year.

2.5 Poker Flat (65.12° N)

The FTS spectrometer, a Bruker 120HR, is located at the Poker Flat Research Range (PFRR) of the Geophysical Institute at the University of Alaska Fairbanks (GI/UAF) under the responsibility of Japan's National Institute of Information and Communications Technology (NICT). The solar absorption spectra used here have been recorded between 1999 and 2004. The FTS automatically records spectra typically on about 100 days per year between February and October. The error analysis for HCl and HF was reported by Kagawa et al. (2007). $ClONO_2$ is not measured operationally at the Poker Flat site and hence no results are reported in this paper.

2.6 Harestua (60.20° N)

Chalmers University of technology has conducted continuous solar FTIR measurements at the Harestua site within NDACC since the end of 1994, with 50–70 measurements per year. The measurement site is a former solar observatory, situated on a hill at 600 m altitude, 50 km north of Oslo. The instrument used is a Bruker 120M spectrometer connected to a solar tracker. Between 1994 and 2004 the original solar tracker of the site was used (coeliostat) but it was later replaced by a custom-built solar tracker allowing remote control of the measurements. The site is frequently located underneath the edge of the polar vortex and the columns measured therefore show a large variability during spring time.

2.7 Zugspitze (47.42° N)

A high-resolution solar absorption infrared sounding system has been operated continuously on the Zugspitze since March 1995 as part of NDACC under the responsibility of the Institute for Meteorology and Climate Research (IMK-IFU) of the Karlsruhe Institute of Technology (KIT). The measurements are performed with a Bruker IFS 125HR interferometer on typically 120–140 days per year. Details have been described by Sussmann and Schäfer (1997).

2.8 Jungfraujoch (46.55° N)

The Jungfraujoch spectra of relevance to the present study have been obtained under the responsibility of the University of Liège, with two FTIR spectrometers, namely a homemade instrument which began routine observations in 1984 and a commercial 120HR model from Bruker, operated since 1990. The measurement density has increased from a yearly average of 50 days between 1985 and 1990 to 114 days from 1991 onwards. The spectral resolution varies between 0.003 and 0.006 cm^{-1}, depending on the species and on the geometry of observation. More details on the instrumentation can be found in Zander et al. (2008). The Jungfraujoch time series used here for HCl and $ClONO_2$ are completely consistent with those of the Rinsland et al. (2003) study; hence the description of the strategies and algorithms used to produce the Jungfraujoch data set given in Appendix A2 of that paper still applies.

2.9 Toronto (43.66° N)

The Toronto Atmospheric Observatory (TAO) was established in 2001 with the installation of a Bomem DA8 FTS. Spectra have been recorded routinely since May 2002. A description of the operations and data analysis can be found in Wiacek et al. (2007). Side-by-side comparisons with two

lower-resolution FTSs were performed in 2005 and are described in Wunch et al. (2007) and Taylor et al. (2008). At present, $ClONO_2$ has not been retrieved at Toronto.

2.10 Tsukuba (36.05° N)

The solar absorption spectra at Tsukuba, Japan were obtained with a Bruker 120M FTS from March 1998 to October 2006 and with a Bruker 120HR FTS since May 2001. The organisations responsible for the analysis of HCl and HF are Tohoku University and the National Institute for Environmental Studies (NIES) in Japan. The spectral fitting algorithm to derive the vertical column densities is based on SFIT1.09e, and is improved with a vertical shift procedure of the initial profile to minimise the residual of the spectral fitting (Murata et al., 2005). In this paper, the data have been derived from the spectra recorded with the Bruker 120M from March 1998 to December 2005 and with the Bruker 120HR from January 2006 to December 2009. Measurement density is 80 days per year on average. $ClONO_2$ has not been retrieved at Tsukuba.

2.11 Kitt Peak (31.90° N)

Measurements of HCl, $ClONO_2$, and HF from Kitt Peak are recorded with the 1-m OPD (optical path difference) FTS (Brault, 1978) in the US National Solar Observatory (NSO) facility in southern Arizona, USA, under the responsibility of NASA Langley Research Center. A five-year gap in observations has occurred, limiting the analysis of the database for the trend in chlorine loading. Limited measurements have restarted in 2009 and have been combined with the previous measurements to produce the total column time series of daily average measurements shown in this paper, with additional measurements anticipated in the near future.

2.12 Izaña (28.30° N)

Since the beginning of 1999, a Bruker IFS 120M FTIR spectrometer has been operated continuously at the Izaña Observatory on Tenerife Island (Schneider et al., 2005). Since 2005, a Bruker 125HR instrument has been used, which was run side-by-side with the 120M spectrometer in April and May 2005. The responsibility for the FTIR experiment lies with IMK-ASF of the Karlsruhe Institute for Technology (KIT). Measurements are taken on about 100 days per year.

2.13 Mauna Loa (19.54° N)

The Mauna Loa Observatory is located on the big island of Hawaii at an altitude of 3.40 km. The observatory is maintained by NOAA's ESRL (Earth Systems Research Laboratory, formerly CMDL, Climate Monitoring and Diagnostics Laboratory). From 1991 to 1995, a Bomem DA8 was located at the site and was replaced by a Bruker 120HR in 1995. FTS data from this site were used in the 1995 Mauna Loa stratospheric ozone inter-comparison (McPeters et al., 1999). The instruments were operated by the University of Denver from 1991 to 2007, and have been operated by NCAR since then (Hannigan et al., 2009). $ClONO_2$ is not retrieved at Mauna Loa due to its low abundance at low latitude.

2.14 La Réunion (21.80° S)

The observing system of the Belgian Institute for Space Aeronomy (BIRA-IASB) at St Denis on Ile de La Réunion is a Bruker IFS 120M spectrometer. Until 2008, this system was deployed at St Denis on a campaign basis; in May 2009, the system was installed for quasi-permanent operation. The data included in the present work come from two measurement campaigns, one in 2004 (August to October) and a second one in 2007 (May to October), and from continuous measurements since May 2009. The instrument and operation characteristics during the 2004 campaign have been described in Senten et al. (2008). In 2007 and 2009, the same instrument was operated in an almost identical way, apart from the fact that the instrument is no longer located in a container on the roof of a university building but in a dedicated laboratory inside the same building. The observations are taken at different spectral resolutions, depending on the solar zenith angle. $ClONO_2$ retrievals have been unsuccessful so far, due to the high humidity at the site and the low $ClONO_2$ abundances at this low latitude.

2.15 Wollongong (34.45° S)

The NDACC site at Wollongong is operated by the local University. It used a Bomem DA8 FTS from 1996 to 2007 (Griffith et al., 1998; Paton-Walsh et al., 2004, 2005). During 2007 the instrument was replaced with a Bruker 125HR FTS. In August 1999, the optical band pass filter that was used to record spectra on the MCT detector was changed from one that transmitted in the 700–1350 cm^{-1} range to two separate filters transmitting in the 700–1050 cm^{-1} and 1000–1350 cm^{-1} ranges.

2.16 Lauder (45.04° S) and Arrival Heights (77.82° S)

The instrument at Arrival Heights was a Bomem from 1991 to 1996 and is since then a Bruker 120M Fourier Transform Spectrometer (FTS), jointly operated by NIWA and the University of Denver, with support from the New Zealand Antarctic Institute. For Lauder, the instrument was an ABB Bomem MB104 in 1986, 1987, and 1989, a Bomem DA2 between 1990 and 1992, a Bruker 120M Fourier Transform Spectrometer until 2001 and a Bruker 120HR from then. Retrievals performed on Lauder data taken between 1986 and 1991 have been analysed with a column scaling algorithm (SFIT1). Fits of the broad absorption of $ClONO_2$ use the technique of pre-fitting interfering gases in a region around the absorption at the 780 cm^{-1} window and then fitting $ClONO_2$ in a smaller microwindow there (Reisinger et al., 1995). HBr cell and ILS measurements (LINEFIT) are

Table 2. Overview of the models. Please note that the vertical domains are pressure altitudes as most models operate on a pressure grid.

Model	Model type	Horizontal resolution	Vertical domain (approx.)	Strat. vertical resolution	Init. year	Bound. cond. (GHG/CFC scenario)	Chemical kinetics
Bremen 2-D model	2-D model	9.5°	0–100 km	∼3.5 km	1958	IPCC (2001) A1B/WMO (2003) Ab	Sander et al. (2006)
KASIMA	CTM	5.6°×5.6° (T21)	7–120 km	∼0.75–3 km	1972	IPCC (2001) A1B/WMO (2003) Ab	Sander et al. (2002)
SLIMCAT	CTM	5.6°×5.6°	0–60 km	∼2 km	1977	IPCC (2001) A1B/WMO (2007) A1	Sander et al. (2002)
EMAC	CCM	2.8°×2.8° (T42)	0–80 km	∼2 km	1958	IPCC (2001) A1B/WMO (2007) A1	Sander et al. (2002)
SOCOL	CCM	3.6°×3.6° (T30)	0–80 km	∼1–5 km	1960	IPCC (2001) A1B/WMO (2003) Ab	Sander et al. (2002, 2006), Atkinson et al. (2004, 2006)

done on a monthly basis at both instrument sites. At Arrival Heights, solar measurements are made from August to March.

3 Models

In addition to the FTIR measurements, results from five different atmospheric models are used in this study, comprising a two-dimensional (2-D) altitude-latitude model similar to the one used in Rinsland et al. (2003), called the Bremen 2-D model, two three-dimensional (3-D) chemistry transport models (CTMs), KASIMA and SLIMCAT, and two 3-D chemistry climate models (CCMs), EMAC and SOCOL (see Table 2). Thereby, the influence of the differing architecture of the models on the trend estimation can be investigated. On the other hand, the two CTMs KASIMA and SLIMCAT can help to estimate the influence of the irregular sampling of the measurements on the trend results (Sect. 5.4). This is possible because those two models use reanalyses calculated from actual measurements so that the state of the atmosphere simulated by the models can be assumed to be as close as possible to reality (please see the specific descriptions below). In contrast, the 2-D model uses only one repeating annual cycle. The two CCMs calculate their own independent and consistent meteorology and dynamics which is not necessarily or rather probably not corresponding to the real meteorological situation.

For the trend calculation and comparison with the FTIR measurements, results from the Bremen 2-D model are used between 2000 and 2008, from EMAC, KASIMA and SLIMCAT between 2000 and 2009, and from SOCOL between 2000 and 2004.

For all five models, the time evolution of the greenhouse gases and ozone-depleting substances was prescribed as a boundary condition at the lower model boundary. The emission scenario for the most important anthropogenic greenhouse gases, i.e. CO_2, CH_4, and N_2O, was the IPCC scenario A1B for all simulations considered here (see also Table 2). It assumes very rapid economic growth, low population growth, and the rapid introduction of new and more efficient technologies (Nakicenovic et al., 2000). The time evolution of the global surface volume mixing ratios of the ozone-depleting substances (ODS) was prescribed according to different so-called baseline scenarios. This means the scenarios represented the best guess for both past and future source gas emissions at the time of their publication. A comparison between them is shown in Fig. 1. KASIMA and the 2-D model applied the Ab scenario from WMO (2003), called REF2 in Fig. 1, while SOCOL used the REF1 modification where updates from newer observations for some source gases were made between 2000 and 2004. The ODS in SLIMCAT and EMAC follow the scenario A1 of WMO (2007). All the ODS data were provided in the framework of the SPARC (Stratospheric Processes And their Role in Climate Change) CCMVal (Chemistry-Climate Model Validation activity) initiative (Eyring et al., 2006, 2007) and were recommended for use as lower boundary conditions in the simulations for the 2006 and 2010 WMO Ozone Assessments.

For the comparison with the FTIR measurements, the model data were interpolated to the locations of the instruments from the adjacent grid points.

3.1 Bremen 2-D model

The 2-D model used in this study is the Leeds-Bremen interactive transport, chemistry and radiation model most recently described by Chipperfield and Feng (2003) and Sinnhuber et al. (2009). It uses the dynamical core of the so-called "two-and-a-half-dimensional" THINAIR model (Kinnersley, 1996) together with the chemistry scheme from the SLIMCAT model (Chipperfield, 1999). The stratospheric dynamics are forced by the amplitudes of waves 1 to 3 of the Montgomery potential at the 380 K isentrope (essentially the same as the amplitudes of the 100 hPa geopotential waves). Here we use the daily Montgomery potential from meteorological analyses with a repeating annual cycle for the period of May 1980 to April 1981. There is no quasi-biennial oscillation (QBO) in the model, i.e. the modelled tropical stratospheric wind is always in a weak easterly state. As we have used no inter-annual variability in the dynamical forcing here, all inter-annual variability comes from changes in

the source gases and aerosol surface area. In this simulation, the following halogen-containing gases are treated explicitly: CFC-11, CFC-12, CFC-113, CCl_4, CH_3CCl_3, Halon-1301, Halon-1211, HCFC-22, and CH_3Cl. In contrast, HCFC-141b is not treated explicitly, but proportionately added to CH_3Cl_3 so that the additional chlorine atoms are accounted for. Analogously, the CFC-114, CFC-115, and HCFC-142b surface mixing ratios are considered in the HCFC-22 value. This model run is the same as used in the 2006 WMO Ozone Assessment (WMO, 2007). Data are available every fifth day until the end of 2008 only.

3.2 KASIMA

The 3-D chemistry transport model KASIMA (Karlsruhe Simulation Model of the Middle Atmosphere) used in this study is a global circulation model including stratospheric chemistry for the simulation of the behaviour of physical and chemical processes in the middle atmosphere (Kouker et al., 1999; Reddmann et al., 2001; Ruhnke et al., 1999). The meteorological component is based on a spectral architecture with the pressure altitude $z = -H\ln(p/p_0)$ as the vertical coordinate, where $H = 7$ km is a constant atmospheric scale height, p is the pressure, and $p_0 = 1013.25$ hPa is a constant reference pressure.

For the present study, the KASIMA version as described in Reddmann et al. (2001) which yields realistic stratospheric age-of-air values (Stiller et al., 2008) was used. The necessary meteorological data of temperature, vorticity and divergence are taken from the European Centre for Medium-Range Weather Forecasts (ECMWF), using ERA-40 data until 2002 and operational ECMWF analyses from 2003 on. In this version, the KASIMA model is relaxed (nudged) toward the ECMWF data between 18 and 48 km pressure altitude using forcing terms with a timescale of 4 h. Below 18 km, the meteorology is based on ECMWF analyses without nudging, and above 48 km pressure altitude, the prognostic model integrating the primitive equations without additional forcing from ECMWF data is used. The model consists of 63 vertical layers between 7 and 120 km and has a horizontal resolution of approximately $5.6° \times 5.6°$(T21).

The photolysis rates are calculated online in KASIMA using the Fast-J2 model of Bian and Prather (2002).

3.3 SLIMCAT

SLIMCAT is an off-line 3-D CTM which has been widely used for the study of stratospheric chemistry (e.g. Feng et al., 2007). The model uses a hybrid $\sigma - \theta$ coordinate (Chipperfield, 2006) and in the stratosphere (θ-level domain), vertical motion is calculated from diagnosed heating rates. This approach gives a reasonable description of the stratospheric circulation and age-of-air (see Monge-Sanz et al., 2007). The model has a detailed description of stratospheric chemistry (see Chipperfield, 1999).

For this study the model was integrated (run 509) from 1977 to 2010 at a horizontal resolution of $5.6° \times 5.6°$ and with 32 levels from the surface to about 60 km. The model was forced using ECMWF reanalyses: ERA-40 from 1977–1988 and then ERA-Interim from 1989–2009. This run did not have an explicit treatment of tropospheric convection but the model assumed that long-lived tracers in the troposphere were well-mixed (see Hossaini et al., 2010).

3.4 EMAC

The chemistry climate model EMAC (ECHAM/MESSy Atmospheric Chemistry model) has been developed at the Max-Planck-Institute for Chemistry in Mainz (Jöckel et al., 2006). It is a combination of the general circulation model (GCM) ECHAM5 (Roeckner et al., 2006) with different submodels, for example the chemistry submodel MECCA (Module Efficiently Calculating the Chemistry of the Atmosphere) (Sander et al., 2005) linked by the Modular Earth Submodel System (MESSy) interface (Jöckel et al., 2005). The simulation performed here includes a comprehensive stratospheric chemistry. The volcanic stratospheric aerosols and the solar irradiance were constant, the QBO was not included and additional bromine with respect to the very short-lived substances (VSLS) was not added. Sea surface temperature (SST) and sea ice cover (SIC) datasets have been used from one of the IPCC-AR4 ECHAM5/MPI-OM coupled model A1B scenario runs performed for the IPCC Fourth Assessment Report (IPCC, 2007).

3.5 SOCOL

The SOCOL_v2.0 (SOlar Climate Ozone Links Version 2) CCM combines the MAECHAM4 GCM (Manzini et al., 1997) with the CTM Mezon (Egorova et al., 2003). SOCOL contains a comprehensive stratospheric chemistry scheme consisting of 41 chemical species, 118 gas-phase reactions, 33 photolysis reactions and 16 heterogeneous reactions (Egorova et al., 2005; Schraner et al., 2008). Inorganic fluorine species (e.g. HF) are not simulated. The Cl_y member species (HCl, $ClONO_2$, HOCl, OClO, Cl, ClO, Cl_2O_2) are individually transported, while the 14 organic-chlorine-containing species present in the model are grouped into two families (short- and long-lived) and these two families are then explicitly advected. After each transport step, the individual members of the two families are partitioned before the chemical computations. 13 photolytic, 14 $O(^1D)$ and 8 OH reactions are used to model the photochemical breakup of the 14 organic-chlorine-containing species. Implications of employing such a scheme are investigated in Struthers et al. (2009).

The model data used in this study originate from the NIWA-SOCOL REF-B1 simulation performed for the WMO SPARC CCMVal2 activity (Eyring et al., 2008). Boundary conditions and model parameters used in the REF-B1

Table 3. Mean differences between models and FTIR measurements in % (calculated as (model-meas)/meas) averaged over all sites, and their standard deviations, for HCl, $ClONO_2$, and HF. The differences for KASIMA and SLIMCAT were calculated from the daily values, while for EMAC, SOCOL, and the 2-D model, the monthly means were used.

gas	KASIMA	SLIMCAT	2-D model	EMAC	SOCOL
HCl	-11.90 ± 8.58	$+10.48 \pm 7.92$	$+8.32 \pm 15.93$	-24.84 ± 8.08	$+9.49 \pm 13.83$
$ClONO_2$	$+11.57 \pm 58.33$	$+90.00 \pm 146.78$	$+15.40 \pm 41.13$	$+30.10 \pm 90.59$	-17.31 ± 22.96
HF	$+1.79 \pm 10.44$	$+36.25 \pm 12.72$	-14.28 ± 12.63		

CCMVal2 simulations are described in Morgenstern et al. (2010). The data available here are monthly means until the end of 2004 only.

4 Time series

Before calculating and comparing the HCl, $ClONO_2$, and HF trends, the consistency of the total column abundances between the FTIR measurements and the different models is investigated (Figs. 3 to 5). Table 3 shows the mean relative differences between each model and the measurements, averaged over all sites. The differences for the CTMs KASIMA and SLIMCAT were calculated from the daily means of the FTIR measurements and the 12:00 UTC model output because these two models use meteorological analyses as boundary conditions so that every day's atmospheric state should be comparable. In contrast, for the CCMs EMAC and SOCOL and the 2-D model, the monthly means from models and measurements were used for the comparison because these models calculate their own dynamics and meteorology which do not necessarily correspond to the real situation on each day. The normalised mean monthly mean values determined for 2000 to 2009 (Figs. 6 to 8) allow us to investigate the characteristics of the seasonal cycle of each gas and its amplitude. These mean monthly means were calculated by dividing the monthly means by the corresponding annual mean and then averaging each month over the whole time period 2000–2009. In all three gases, a seasonal cycle is expected that is connected with the seasonal variation of the tropopause height. This variation results from the stratospheric general circulation transporting air from the summer to the winter hemisphere. The higher the tropopause, the smaller is the relative contribution of the stratosphere to the total column abundance. This again results in a lower total column abundance of HCl, $ClONO_2$, and HF in summer, because they are all mainly produced in the stratosphere. In the high latitude regions, HCl and $ClONO_2$ are in addition influenced by the absence of solar irradiation in winter. Chlorine activation on the surface of polar stratospheric clouds (PSCs) leads to a decrease in the total column abundances of the chlorine reservoir species and a strong peak at the end of the winter due to the deactivation of active chlorine. So the seasonal cycle is expected to exhibit its largest amplitude at the polar sites.

4.1 HCl

Measurements and models both indicate a steady increase of HCl until about the mid-1990s. Afterwards, a decrease of the HCl total column abundances is observed at all sites, with the Southern Hemisphere delayed by a few years with respect to the Northern Hemisphere (Fig. 3).

In comparison to the FTIR measurements, KASIMA underestimates the total column abundances of HCl (Fig. 3 and Table 3). Reasons for this are discussed in Kohlhepp et al. (2011, and references therein) and include the horizontal resolution, the data set used for nudging, and the parameterisation of tropospheric processes, for example. In contrast, the other CTM, SLIMCAT, tends to overestimate the total HCl content compared to the measurements. The average bias is smallest for the 2-D model (Table 3). EMAC underestimates the HCl total column even more than KASIMA, while SOCOL overestimates it.

In the FTIR data, the annual maximum of HCl occurs in spring, around April/May in the Northern Hemisphere and October/November in the Southern Hemisphere (Fig. 6). This seasonal cycle is qualitatively captured at most sites by all models except the 2-D one. At some sites, KASIMA and SOCOL simulate the annual maximum about one month too early.

4.2 $ClONO_2$

Because of its weak spectral signature, interference by water vapour, and the low column abundances especially at lower latitudes, $ClONO_2$ is not easy to measure with a ground-based FTIR spectrometer. For this reason there are no $ClONO_2$ time series from the FTIR sites Poker Flat, Toronto, Tsukuba, Mauna Loa, and La Réunion which are therefore not included in the comparisons in Figs. 4 and 7 and Table 3.

All measurement and model datasets show an increase of $ClONO_2$ until the late 1990s and a decrease afterwards (Fig. 4).

At the Northern Hemisphere high latitude sites Ny Ålesund, Thule, and Kiruna, the models tend to overestimate the total atmospheric $ClONO_2$ content, especially the annual minima (Fig. 4). At most sites, the SLIMCAT model shows the highest values, followed by EMAC and the 2-D model. On average, KASIMA, SOCOL, and the 2-D model agree best with the measurements (Table 3).

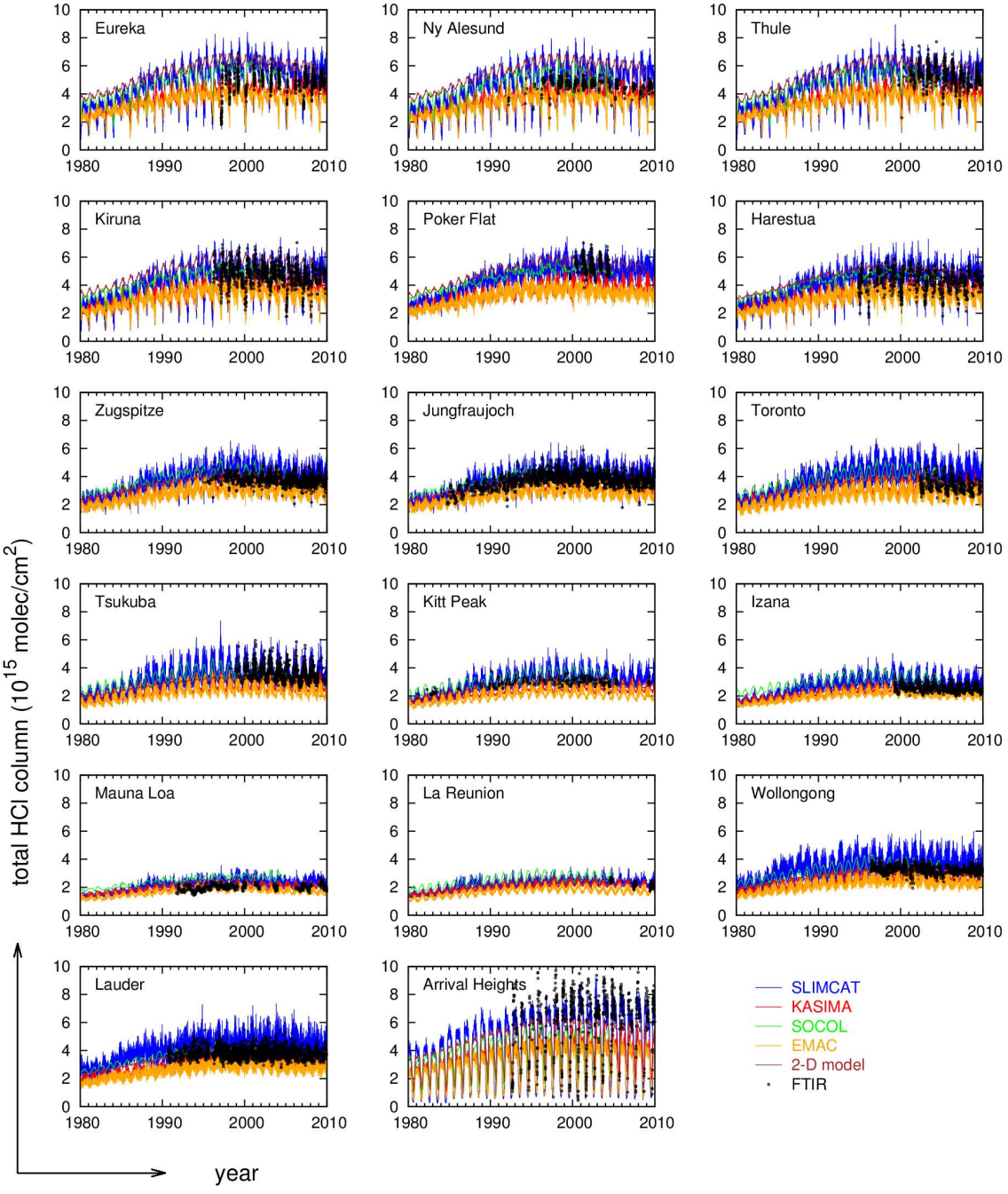

Fig. 3. Time series of HCl total column abundances in molecules per cm^2 at the different sites as measured by FTIR (black dots) and simulated by SLIMCAT (blue line), KASIMA (red line), SOCOL (green line), EMAC (orange line), and Bremen 2-D model (brown line).

SLIMCAT simulates a stronger relative seasonal variation than the other models at most Northern Hemisphere sites (Fig. 7). At midlatitudes, this means SLIMCAT overestimates the $ClONO_2$ amplitude, while closer to the poles, the other models tend to underestimate it. The annual $ClONO_2$ maximum occurring in February or March at most Northern Hemisphere sites is captured qualitatively by most models. Especially in the Northern Hemisphere midlatitudes, EMAC tends to simulate the maximum in April, which is about one month later than the other models which agree with the measurements. At the Southern Hemisphere sites Wollongong and Lauder, the maximum predicted by the models between August and October is not very pronounced in the measurements.

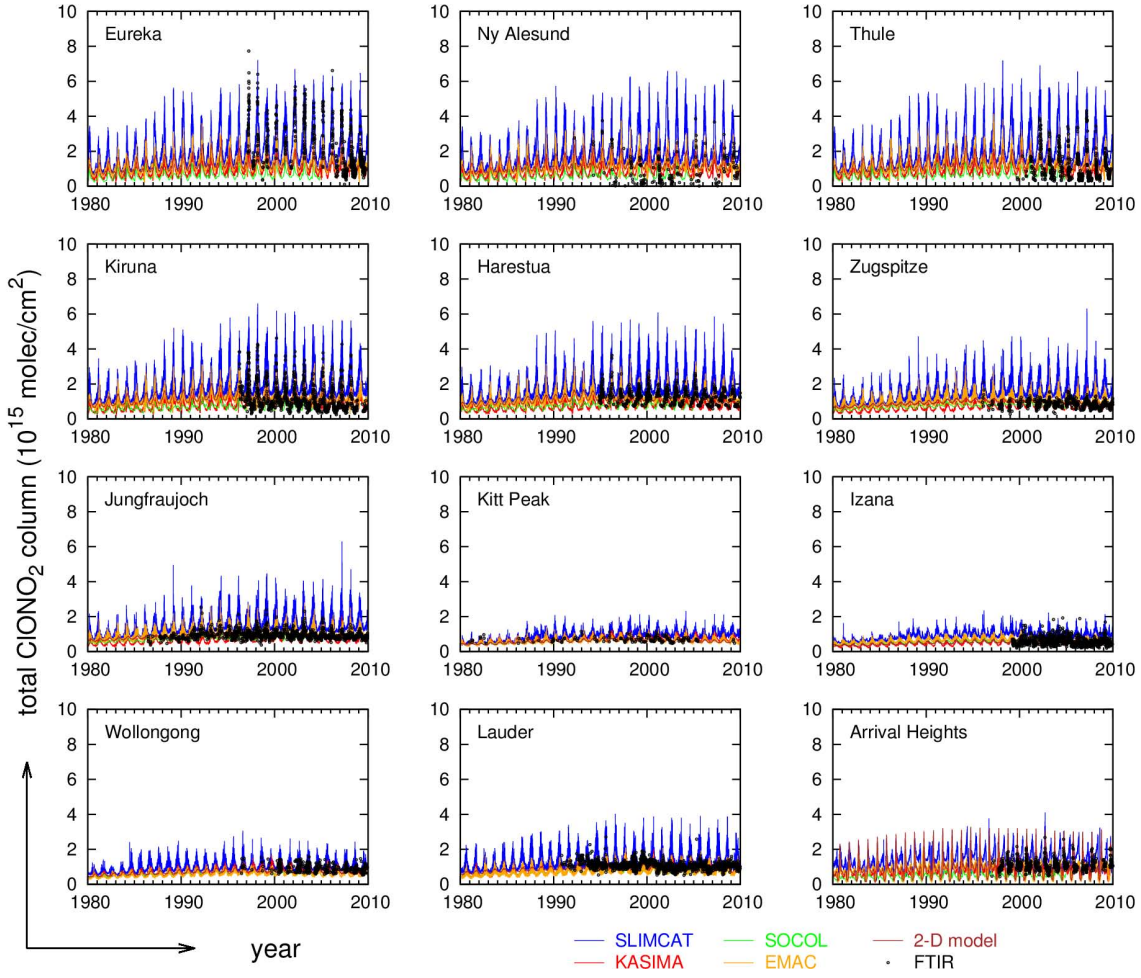

Fig. 4. Time series of $ClONO_2$ total column abundances in molecules per cm^2 at the different sites as measured by FTIR (black dots) and simulated by SLIMCAT (blue line), KASIMA (red line), SOCOL (green line), EMAC (orange line), and Bremen 2-D model (brown line).

4.3 HF

The two CCMs EMAC and SOCOL do not simulate the atmospheric HF content, therefore only the results from the CTMs KASIMA and SLIMCAT and from the 2-D model can be compared with the FTIR measurements at the 17 sites. They show an increase over the largest part of the time range that weakens in the last few years (Fig. 5).

The SLIMCAT model tends to overestimate the HF total column abundance, while KASIMA on average agrees better with the measurements. The 2-D model shows a behaviour very similar to KASIMA apart from some low and midlatitude sites (e.g. Toronto, Kitt Peak, Izaña, and La Réunion) where it tends to underestimate the increase especially in the 1990s (Fig. 5). This results in a mean underestimation of the measured total column abundances by the 2-D model (Table 3).

The amplitude of the seasonal HF cycle as simulated by the two CTMs KASIMA and SLIMCAT fits very well to the one measured by the FTIR spectrometer at most sites (Fig. 8). The annual maximum around March and April in the Northern Hemisphere and in October in the Southern Hemisphere is also represented in the two models. The seasonal cycle from the 2-D model is very similar to those from KASIMA and SLIMCAT in the northern polar latitudes, but its amplitude is mostly too weak, especially at the Northern Hemisphere midlatitude sites.

4.4 Summary of the time series comparison

In summary, there is good overall agreement between the FTIR measurements and the models considered here concerning the increase of the total column abundances of HCl and $ClONO_2$ until about the mid-1990s, a decrease afterwards, and on a HF increase that slowly reached a plateau in the last few years. Also the mean annual cycles derived from the different datasets are similar.

The SLIMCAT model tends to overestimate the atmospheric content of the three gases and, especially at midlatitudes, the amplitude of the seasonal cycle of $ClONO_2$.

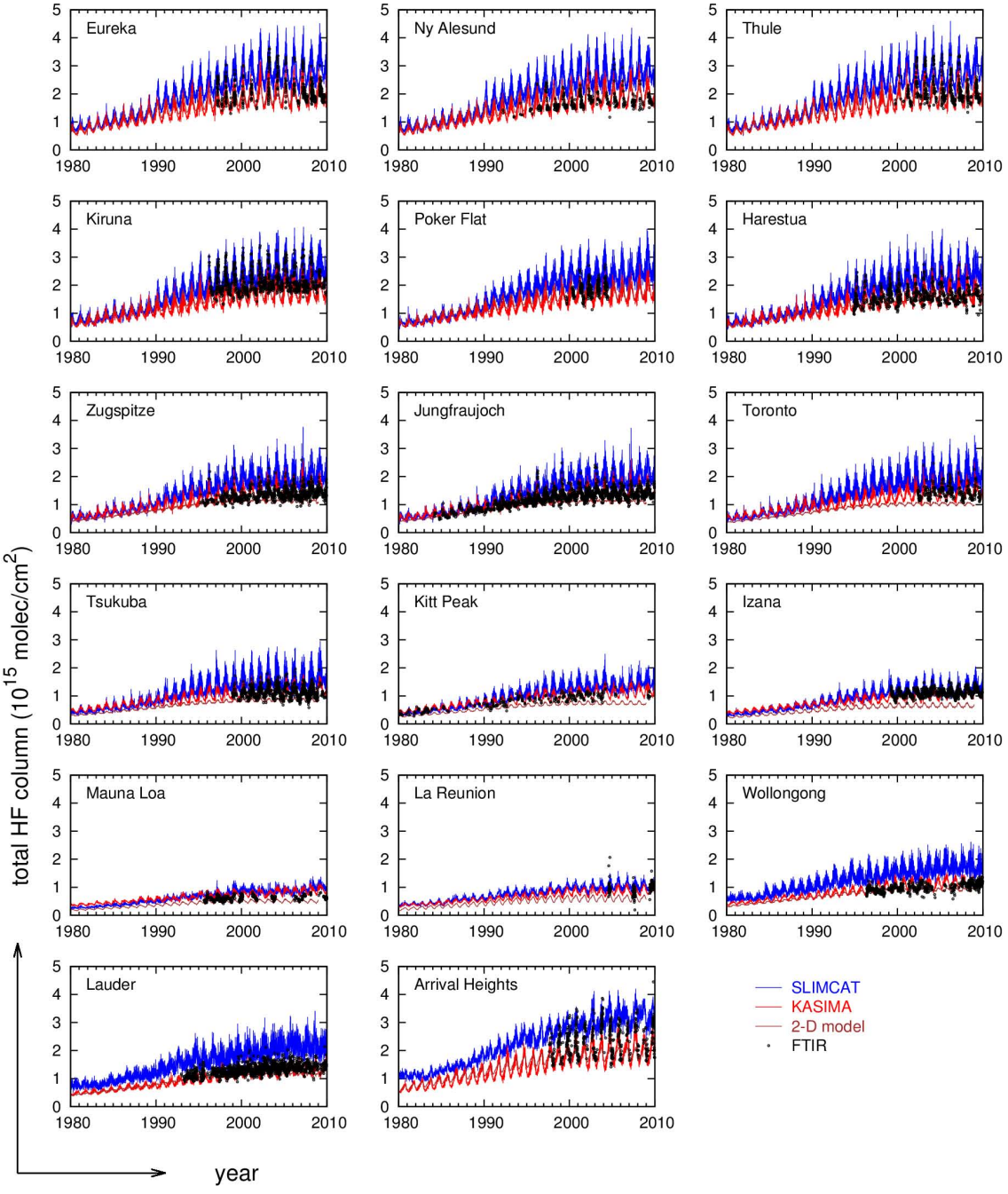

Fig. 5. Time series of HF total column abundances in molecules per cm^2 at the different sites as measured by FTIR (black dots) and simulated by SLIMCAT (blue line), KASIMA (red line), and Bremen 2-D model (brown line).

KASIMA and EMAC tend to underestimate the HCl total column abundance, while SOCOL and the Bremen 2-D model overestimate it, especially in the Northern Hemisphere. The 2-D model underestimates the HF increase at some low and midlatitude sites.

5 Trend method and sensitivity studies

In this section, a short description of the trend calculation method is given, especially also of the bootstrap method used to estimate the trend uncertainty. In addition, we investigate the dependence of the trend result on the type of fit function, the time period, and on sampling. The first two influencing factors are analysed using the FTIR measurements, while

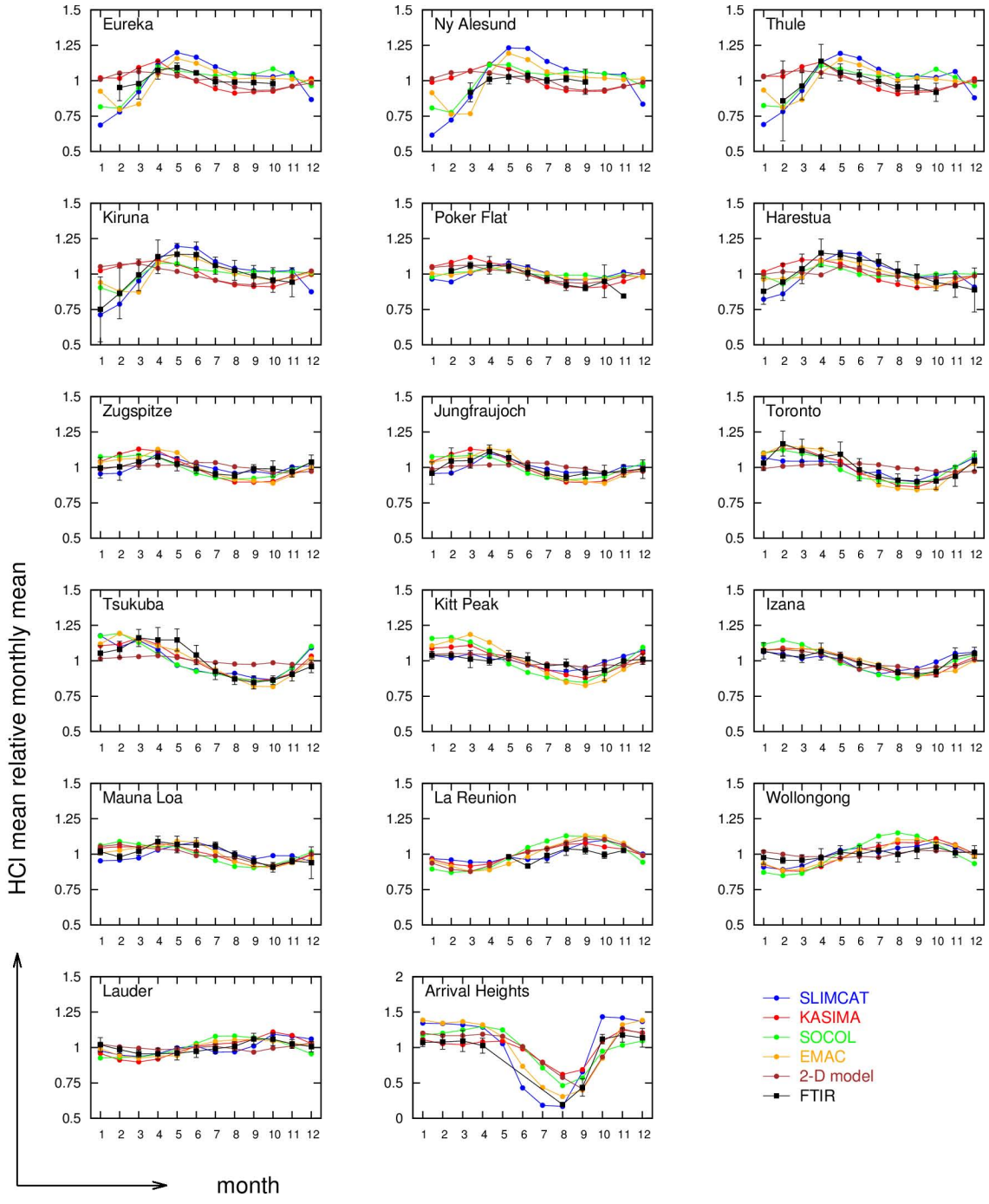

Fig. 6. Annual cycle of HCl at the different sites as determined from the FTIR instruments (black) and simulated by SLIMCAT (blue), KASIMA (red), SOCOL (green), EMAC (orange), and the Bremen 2-D model (brown). The mean relative monthly means were calculated by normalising the monthly means with the respective annual mean and then averaging over the period 2000–2009. The error bars of the FTIR measurements represent the standard deviation.

the sampling influence can be estimated with the help of the CTM data. The main time period chosen for the trend and its sensitivity investigations is 2000–2009. This was done because a continuous decrease is expected for the chlorine gases and an increase for HF during this time so that a linear trend fit can be assumed to sufficiently represent the temporal evolution of the total column abundances. Moreover, nearly all sites included in this study measured during this time (see Table 1).

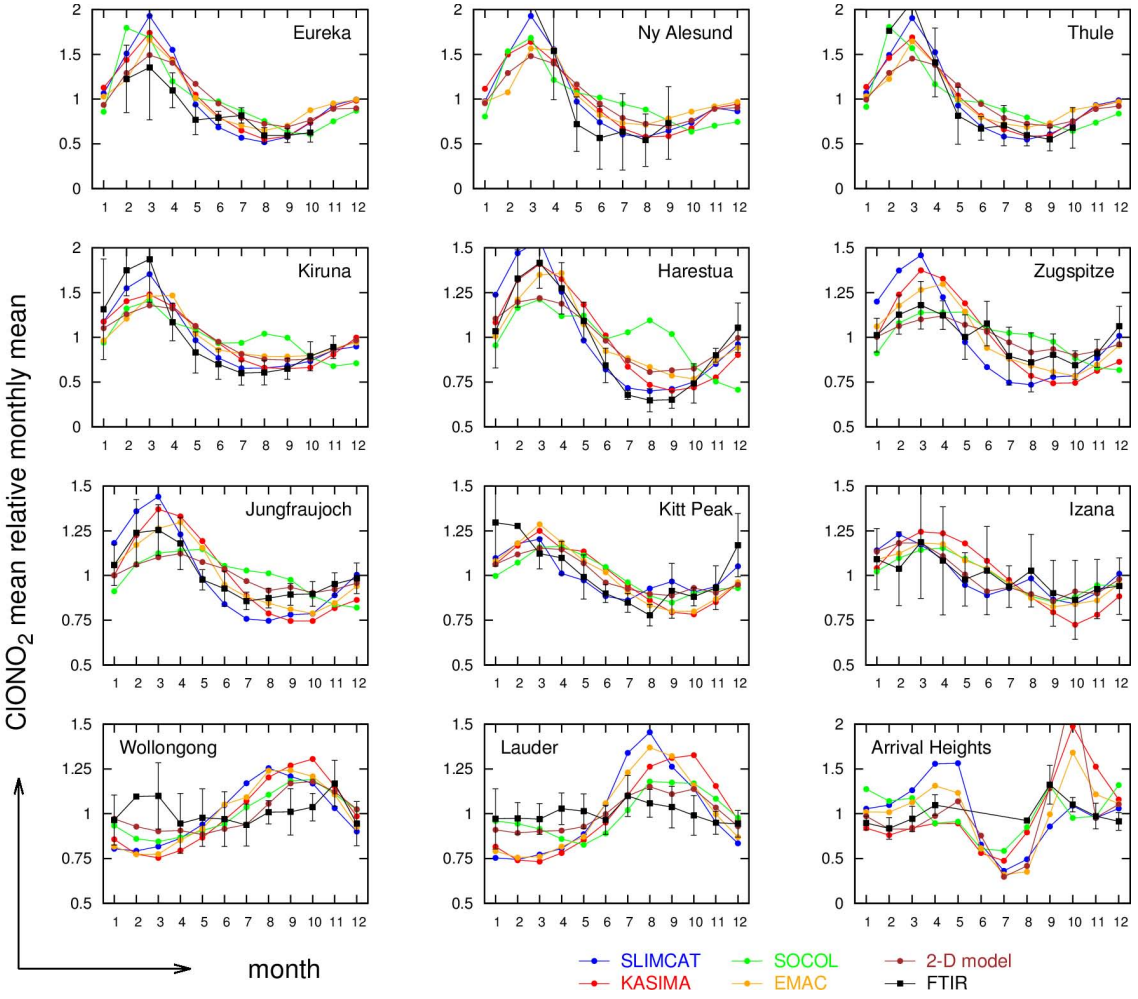

Fig. 7. Annual cycle of $ClONO_2$ at the different sites as determined from the FTIR instruments (black) and simulated by SLIMCAT (blue), KASIMA (red), SOCOL (green), EMAC (orange), and the Bremen 2-D model (brown). The mean relative monthly means were calculated by normalising the monthly means with the respective annual mean and then averaging over the period 2000–2009. The error bars of the FTIR measurements represent the standard deviation.

5.1 Trend determination method

A linear trend function, combined with a Fourier series accounting for the seasonal cycle, is fitted to the time series using a least squares method. The precision of the fit parameters and thus of the trend is determined with the bootstrap resampling method. This method is only described shortly here, however, more detailed information can be found for example in Gardiner et al. (2008, and references therein). It has been used in previous trend studies from FTIR measurements (e.g., Gardiner et al., 2008; Mikuteit, 2008; Vigouroux et al., 2008; Kohlhepp et al., 2011). From the main fit to the data, the differences between fit and data are calculated. These residuals are then added randomly (with replacement) to the fit result in order to create a new, artificial data set. Another fit using the same function as for the real data is performed on the artificial data set, giving an artificial value for every parameter, including the trend. This procedure is applied 5000 times in this study, following the example of Gardiner et al. (2008). From the 97.5 and 2.5 percentiles of the resulting 5001 trend values, the 95 % confidence interval characterising the trend uncertainty can be estimated. The reason for choosing this method to determine the trend uncertainty is that it does not assume that the residuals of the fit to the data are normally distributed. Instead, it only assumes that there are enough data points for the residuals to sufficiently represent their own distribution. The assumption of a normal (Gaussian) distribution of the residuals might not be valid because the fit is not always able to capture the complete annual cycle, e.g. the strong peak in $ClONO_2$ at the polar sites in spring. The main reason for this is that the peak does not always occur at exactly the same time of year.

At all sites between 70° S and 70° N except La Réunion, a third order Fourier series is used to account for the seasonal

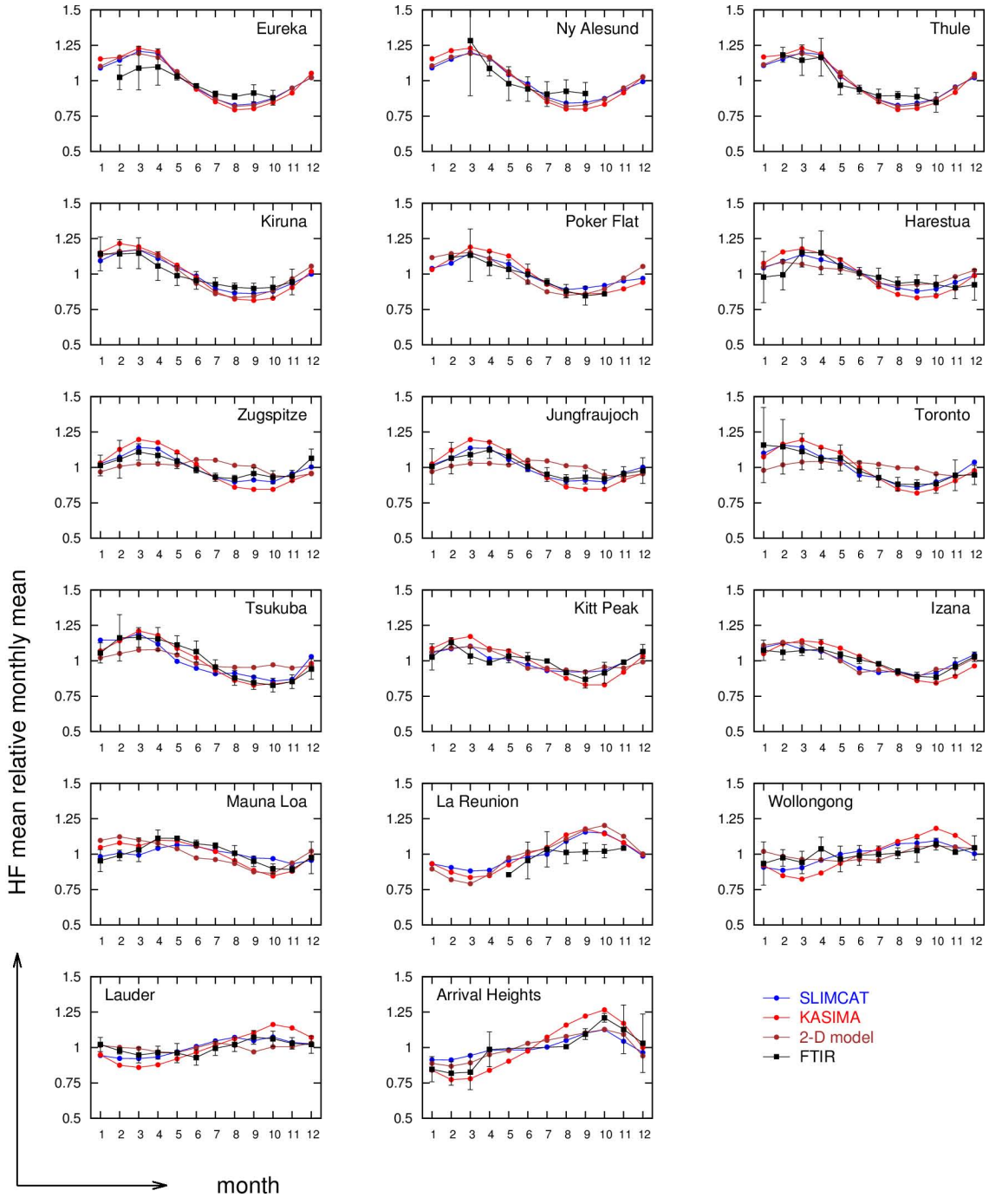

Fig. 8. Annual cycle of HF at the different sites as determined from the FTIR instruments (black) and simulated by SLIMCAT (blue), KASIMA (red), and the Bremen 2-D model (brown). The mean relative monthly means were calculated by normalising the monthly means with the respective annual mean and then averaging over the period 2000–2009. The error bars of the FTIR measurements represent the standard deviation.

cycle. As also found by Gardiner et al. (2008), this approach represents most time series very well and at the same time avoids over-fitting the data. But at the sites poleward of 70° N and S, the FTIR measurements are limited by polar night so that the comparably strong seasonal cycle is only partly represented in the time series. Similarly, a large part of the seasonal cycle is missing also in the La Réunion data where the measurements were performed on a campaign basis. This is why at these sites, for some of the gases, the bootstrap method together with the third order Fourier series fit did not

produce reliable results. So finally, only a first order Fourier series was fitted for all gases measured at these sites in order to account at least for some seasonal variation.

All trend values in this paper are given in % per year referring to the linear fit value computed for 1 January 2000, 12:00 UTC.

For HCl and HF, results for all 17 sites are presented, while for $ClONO_2$, only 12 time series are available (see Table 1). Please note that the measurements at Poker Flat ended in 2004.

5.2 Dependence on the trend calculation approach

In order to estimate the dependence on the type of fit function used, the trends between 2000 and 2009 were determined by fitting a linear function only (this approach is called "linear" from now on) and a linear function combined with a third or first (see above) order Fourier series (called "standard") to the FTIR measurements (Fig. 9). Trends were also calculated by considering the summer and autumn data separately (June to November and December to May in the Northern and Southern Hemisphere, respectively), which are assumed to show less variability, using a simple linear fit function. This method is called "summer/autumn" or "s/a" from now on.

At Toronto and La Réunion, the measurements were started after the year 2000, in 2002 and 2004, respectively. For Toronto, the dependence on the trend calculation approach was determined for the time range 2002–2009, while La Réunion was not considered in this section. There are no results for $ClONO_2$ at Ny Ålesund displayed in Fig. 9. For the summer/autumn series at this site, the bootstrap method did not produce reliable results, and both the linear and the standard procedures led to trend values (10.9 and 6.8 % yr^{-1}, respectively) much higher than at the other sites so that for clarity of the majority of the results, the y-range used here was adapted to them. Analogously, the trend for $ClONO_2$ at Eureka from the linear fit function cannot be displayed (-7.2 % yr^{-1}), and neither the linear HF trend at Poker Flat (3.1 % yr^{-1}).

The confidence interval determined with the bootstrap method is obviously larger for the linear trend alone and the summer/autumn data only than when a linear function combined with a Fourier series is fitted to all data (Fig. 9). This suggests that the linear function alone does not sufficiently represent the time series. Also, the time series restricted to the summer/autumn data naturally contain fewer measurements which is probably the reason for the large error bars noted in these cases.

The results for HCl from the different trend calculation approaches agree within their errors at all sites. For $ClONO_2$, the error bars are larger than those for HCl at most sites. This can be explained partly by the larger amplitude of the seasonal cycle of $ClONO_2$ which cannot be completely represented by the fitting function. In addition, $ClONO_2$ is

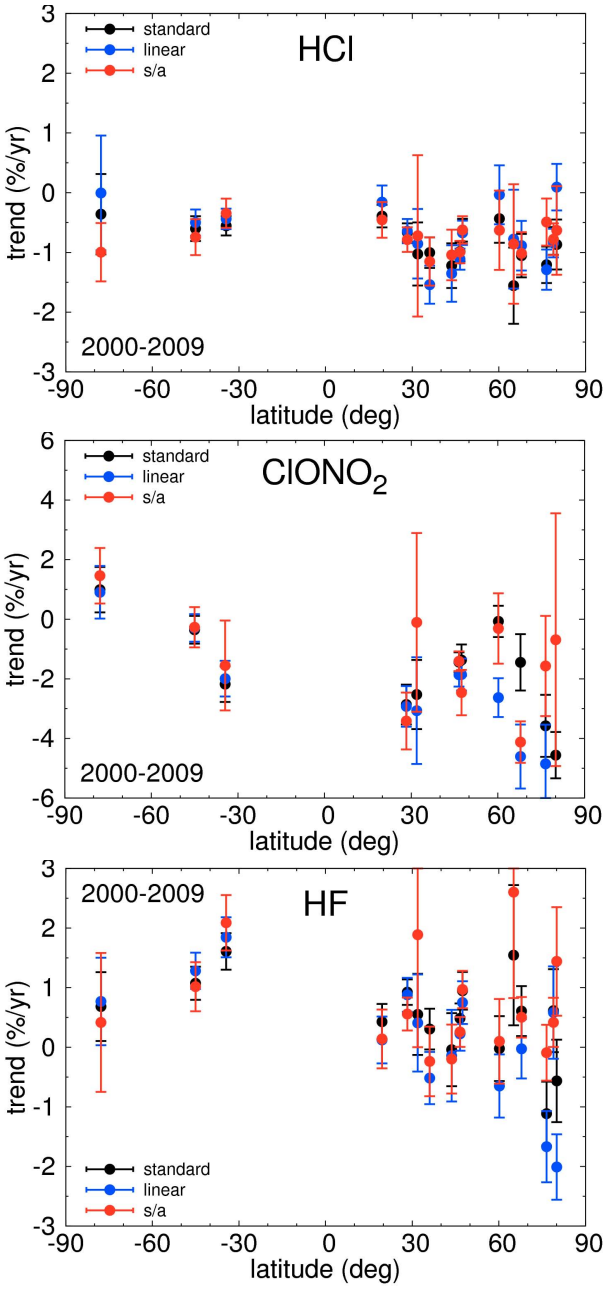

Fig. 9. Dependence of the resulting trend (in % per year) on the type of fitting function, determined from the FTIR measurements of HCl (top), $ClONO_2$ (mid), and HF (bottom) for the time range 2000–2009 (except at Toronto where it is 2002–2009, and at Poker Flat it is 2000–2004). Please note the different y-scales. The results of the "standard" procedure using a linear function with a third or first order Fourier series are shown in black, those of the "linear" trend calculation in blue and of the linear calculation with summer/autumn data only ("s/a") in red. The error bars were determined with the bootstrap method. Concerning the reasons for missing trend values please see text.

difficult to measure and therefore the scatter characterising the total column time series is larger, too. Apart from Eureka, Kiruna, and Harestua, the trend results for $ClONO_2$ from the different approaches agree within errors. The HF trends also agree within errors except at the polar sites Eureka, Thule, and Poker Flat.

There are a few possible reasons for the disagreement of the different trend determination methods at some of the high latitude sites. Due to the influence of the polar vortex, the amplitude of the seasonal cycle is very large and therefore especially the result from fitting the linear function alone very much depends on the start and end time of year. But also the Fourier series cannot capture the sometimes strong variations on a short timescale resulting from the movement of the polar vortex. In addition, the high-latitude seasonal cycles are not completely represented in the time series because solar FTIR measurements are not possible during polar night. Furthermore, at some sites, the time series contain very few data points for the summer/autumn months, for example the $ClONO_2$ series from Ny Ålesund and Wollongong, and all three series from Kitt Peak. At Eureka, the DA8 measurements were performed on a (spring and autumn) campaign basis so that until the installation of the 125HR spectrometer in 2006, there were years with no measurements during "summer/autumn" at all.

5.3 Dependence on the time period used

In order to investigate the influence of time series length and the time period chosen, the FTIR trends were calculated for the three periods 1996–2009, 2000–2009 and 2004–2009 (Fig. 10). The longest period was selected because not all, but more than half of the stations performed measurements during this time, while only a few did before. The longer the time series, the smaller the error bars and the better the trend estimate is expected to be. During the second period, all sites except La Réunion and Toronto performed measurements (see below). From earlier studies, e.g. the one by Rinsland et al. (2003), we expect the inorganic chlorine species total column abundances to have reached their plateau around 1996–1999 and not to strongly change during this time. So the decrease expected due to the Montreal Protocol may be weaker if these four additional years are included in the trend calculation. The latest and shortest period was included in this study in order to investigate whether there was a change in the rate of increase (of HF) or decrease (of HCl and $ClONO_2$) during the last few years.

The approach called "standard" here was used, which means the fitting function was the linear one with a third or first order Fourier series (see above) representing the seasonal cycle. The sites where the required time ranges were not available were not considered in this comparison, except for Toronto, where the trend with the 2000–2009 colour actually covers the time range between 2002 and 2009. There are no trend results for Poker Flat between 2004 and 2009

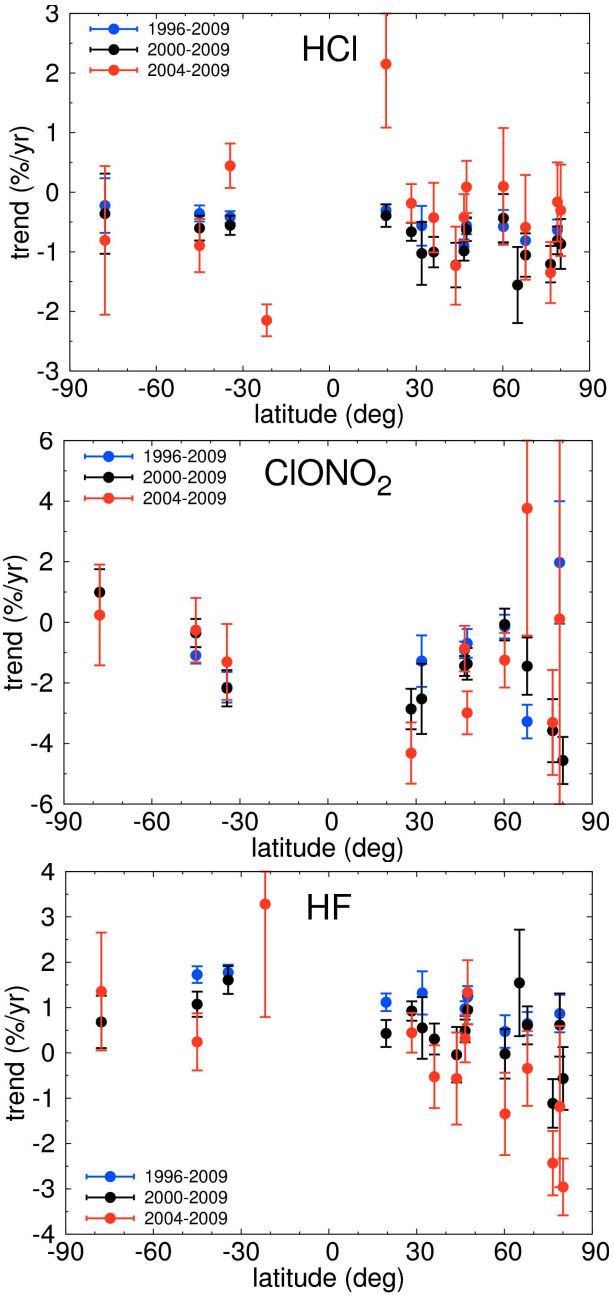

Fig. 10. Dependence of the resulting trend (in % per year) on the time period, determined for the FTIR measurements of HCl (top), $ClONO_2$ (mid), and HF (bottom). Please note the different y-scales. The fitting function is the linear one with seasonal cycle, which is called "standard" here. The results for 1996–2009 are shown in blue, those for 2000–2009 in black (at Toronto, this is 2002–2009, and at Poker Flat it is 2000–2004) and for the 2004–2009 period in red. The error bars were determined with the bootstrap method. Concerning the reasons for missing trend values please see text.

because the time series end in 2004 (see Table 1). In the Kitt Peak data, there is a large gap around 2006 to 2008 so that especially the determination of the seasonal cycle between 2004 and 2009 is not possible and the 2004–2009 trends at this site could not be included either. In the $ClONO_2$ picture of Fig. 10, the trends for Eureka between 2004 and 2009 and for Ny Ålesund between 2000 and 2009 are missing because they are larger than the y-scale (-6.2 and $6.8\,\%\,yr^{-1}$, respectively). The same is the case for the Wollongong and Mauna Loa HF trends between 2004 and 2009: they amount to 4.2 and $22.8\,\%\,yr^{-1}$, respectively.

The shorter the time series, the larger the error bar of the trend (Fig. 10).

In the Northern Hemisphere mid and low latitudes, the HCl trends tend to be less strongly negative for the period from 2004 to 2009 than for the two longer periods, but strongest for 2000 to 2009 at most sites. It must be considered that six years are not enough to reliably determine such small trends (see also Weatherhead et al., 1998). In the Southern Hemisphere, no clear signal is detectable.

For HCl and $ClONO_2$, the trends from 1996 to 2009 and 2000 to 2009 agree within errors at most sites. The expected tendency of a weaker decrease in the chlorine species during 1996–2009 that was discussed above can indeed be found in the presented results, especially for HCl. It is probably due to the stratospheric chlorine loading reaching a plateau at the end of the 1990s and only then slowly starting to decrease.

The reason for the HF trend differing for the three time periods at most sites is probably that the column abundances seem to have reached a plateau in the last few years (see also Fig. 5). The trend is strongest and mostly positive for the longest period, while for the later and shorter periods it weakens or even becomes negative, especially in the Northern Hemisphere.

5.4 Influence of sampling

Due to varying weather conditions at all sites, polar night and midnight sun, and instrumental failures, the sampling of the FTIR data points is not regular and some time series contain gaps. The sampling influence on the trend can be investigated with the chemistry transport models KASIMA and SLIMCAT. As they use meteorological analyses to calculate the atmospheric chemistry processes and transport, the meteorological conditions are assumed to be as close as possible to reality. Therefore, two different model trends for HCl, $ClONO_2$, and HF have been determined by fitting a linear function with a third or first order Fourier series to the CTM data: one from the complete CTM time series containing one value per day and the other one only from the days where FTIR measurements have been taken. The period chosen for this comparison is again 2000–2009. This means La Réunion is not included and the trend calculations for Toronto all start in 2002, while for Poker Flat, they end in 2004, like in Sect. 5.2.

In Fig. 11, the KASIMA (left column) and SLIMCAT (right column) trends from the complete time series are compared with those from the measurement days only and with the FTIR results. It is obvious that there are differences in the trends between the differently sampled time series for both models. At the same time, it is not easy to quantify this sampling influence. However, at most sites, the influence is not very strong so that the trends agree within their bootstrap error bars. The locations where this is not the case are mostly high latitude sites where due to polar night a large portion of the relatively strong annual cycle is missing in the measurement time series, or other sites with large measurement interruptions. At such sites, the error induced by sampling is obviously not negligible.

5.5 Summary of the FTIR trend dependencies

Especially at locations where the seasonal cycle of the gas investigated has a large amplitude, the trend results depend on whether the Fourier series is included in the fit function or not (Sect. 5.2). The linear function alone clearly cannot sufficiently represent the time series. Selecting only the summer/autumn data where the variability is expected to be small does not strongly diminish the confidence intervals. Probable reasons for this are that at some sites, there are not many data points left when removing those measured in winter and spring, and that there is still some variability left in the summer/autumn time series.

When calculating trends for different parts of the time series, the shorter the time series, the larger the error bars (Sect. 5.3). The results for the six-year period 2004 to 2009 should be treated cautiously. Still, there is a considerable tendency towards a decrease of the positive HF trend in the last few years at many Northern Hemisphere measurement sites.

Moreover, as shown in Sect. 5.4, a considerable bias may be induced in the trend results at sites with very irregular sampling or large gaps in the time series. This must be kept in mind when trends from FTIR data are compared with those from model calculations.

It can be concluded that, overall, the agreement between the different trend determination approaches and the different time ranges is good. This means the results are robust. For the trend determination from models and measurements in the following (Sect. 6), the so-called standard approach fitting a linear trend with a Fourier series is used because its error bars are the smallest. The best time period to determine the trends would of course be the longest one (1996–2009), but because many sites started measuring after 1996, in order to ease the comparison or rather to be able to consider more sites, the period chosen for the model-measurement comparison is 2000–2009.

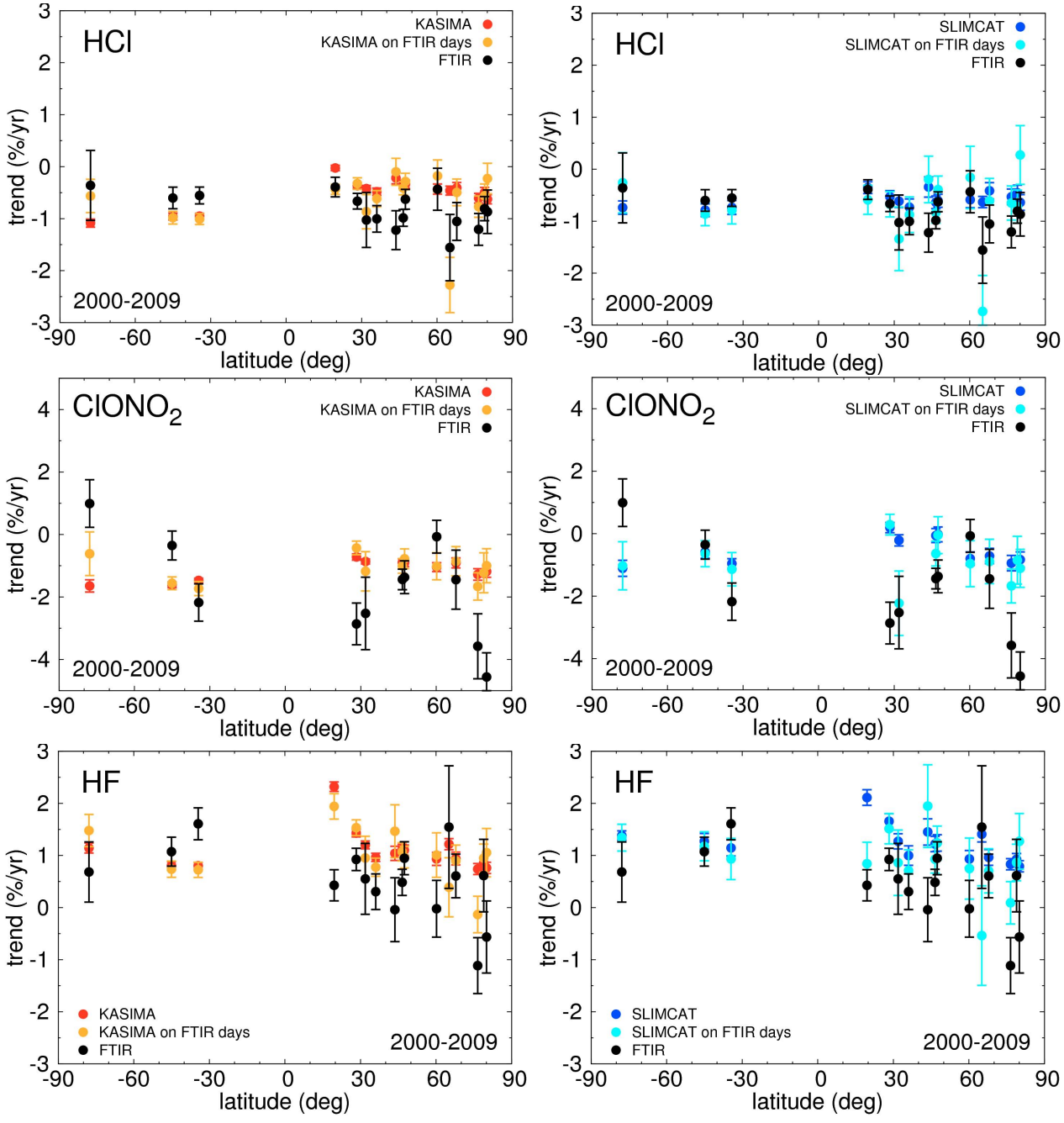

Fig. 11. The dependence of the resulting trend (in % per year) on sampling is investigated by comparing trends from the KASIMA data on all days (left column; red) with those calculated from the model time series on days with FTIR measurements only (orange) and with the FTIR trends themselves (black). The same comparison is shown for SLIMCAT (right column; blue) and SLIMCAT only on FTIR days (cyan). Please note the different y-scales. The error bars were determined with the bootstrap method.

6 Comparison of FTIR and model trends

In this section, the trends from the FTIR measurements are compared with the results from all five models SLIMCAT, KASIMA, SOCOL, EMAC and the 2-D model (see Fig. 12 and Tables 4 to 6). For all models, the trends were determined from all available data, which is one value per day for KASIMA, SLIMCAT, and EMAC, one every fifth day for the Bremen 2-D model, and monthly means for SOCOL. Still, the investigations of Sect. 5.4 have to be kept in mind, showing an influence of the FTIR sampling on the trend results. The period considered here is 2000 to 2009 and the

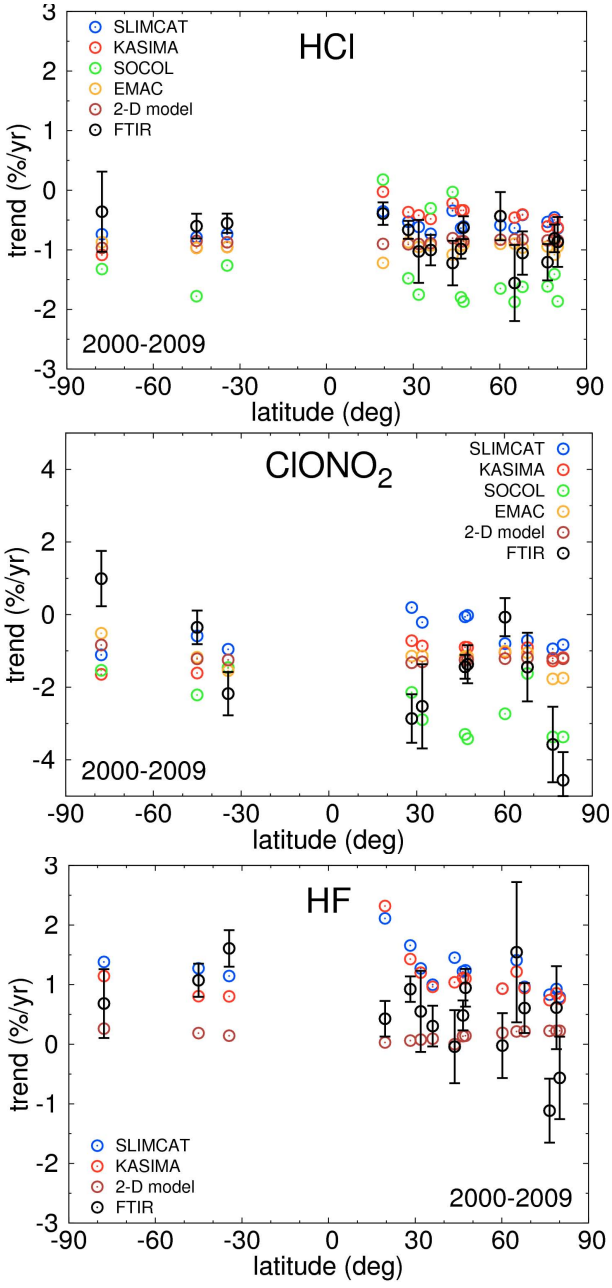

Fig. 12. Comparison of the trends from the FTIR measurements (black) between 2000 and 2009 (in % per year) with those modelled by SLIMCAT (blue), KASIMA (red), SOCOL (green), EMAC (orange), and the Bremen 2-D model (brown) for HCl, $ClONO_2$, and HF. In order not to overload the picture, the bootstrap error bars for the modelled trends are not shown, only those for the measurements. Concerning the reasons for missing trend values please see text.

fit function the linear one with seasonal cycle, following the conclusions of Sect. 5.5.

Concerning SOCOL, it must be remembered that the model time series end in 2004 so that the trends are only determined from a five-year period. Therefore, the trends should not be interpreted quantitatively, but they might qualitatively reproduce the measured signal.

6.1 HCl

In the Northern Hemisphere mid and high latitudes, all models except SOCOL underestimate the decrease of HCl, while in the Southern Hemisphere, they tend to overestimate it (Fig. 12, Table 4). This is mostly due to the FTIR trends indicating a stronger decrease in the Northern Hemisphere than in the Southern Hemisphere and most models not showing a difference between the hemispheres at all. The only model simulating slightly different trends is KASIMA, but its signal is opposite to the FTIR one with relatively stronger negative trends at the Southern Hemisphere sites. SOCOL overestimates the decreasing trend in the mid and high latitudes in both hemispheres but underestimates it at some sites in the Northern Hemisphere tropics. The tendency towards a relatively weaker decrease in the lower latitudes than everywhere else can also be found in KASIMA and SLIMCAT and corresponds to the results from the measurements. EMAC shows the opposite signal and the 2-D model none.

6.2 $ClONO_2$

The $ClONO_2$ trends of models and measurements do not agree as well as the HCl results and also show stronger latitudinal dependencies (Fig. 12, Table 5). In the Northern Hemisphere, all models except SOCOL underestimate the relative decrease seen in the FTIR measurements, as for HCl. The FTIR trends are stronger in polar and low latitudes than in the midlatitudes. An increasingly negative trend towards the north pole can also be seen in all models apart from the 2-D model. One should keep in mind that the measured Eureka $ClONO_2$ trends might be influenced by the bias between the two different line lists used, which is described in Sect. 2.1. In the Southern Hemisphere, for Wollongong the models underestimate the decrease seen in the measurements, while above Lauder, the FTIR trend is weaker than the models simulate. The measured $ClONO_2$ trend is positive above Arrival Heights and becomes increasingly negative towards lower latitudes. The EMAC results behave qualitatively similar there, while the other models show no clear signal.

6.3 HF

Of the three models which actually simulate HF, the 2-D model shows the weakest increase, which does not vary strongly with latitude (Fig. 12, Table 6). KASIMA and SLIMCAT agree well on a positive trend at all sites, with the highest values in the Northern Hemisphere low latitudes, at Mauna Loa and Izaña. In the Southern Hemisphere, none of the models shows a distinct latitudinal dependency, while the FTIR results suggest that the increase weakens towards

Table 4. HCl trend in % per year between 2000 and 2009, calculated by fitting a linear function combined with a first (sites poleward of 70°) or third order Fourier series to the data. The error bars were determined with the bootstrap method.

Measurement site	FTIR	KASIMA	SLIMCAT	2-D model	EMAC	SOCOL
Eureka	-0.87 ± 0.42	-0.63 ± 0.09	-0.64 ± 0.15	-0.84 ± 0.03	-0.95 ± 0.12	-1.86 ± 0.82
Ny Ålesund	-0.81 ± 0.23	-0.50 ± 0.10	-0.46 ± 0.15	-0.84 ± 0.03	-1.08 ± 0.12	-1.41 ± 0.96
Thule	-1.21 ± 0.31	-0.61 ± 0.09	-0.53 ± 0.15	-0.84 ± 0.03	-0.94 ± 0.12	-1.61 ± 0.85
Kiruna	-1.05 ± 0.36	-0.41 ± 0.10	-0.42 ± 0.16	-0.83 ± 0.02	-0.96 ± 0.12	-1.62 ± 0.86
Poker Flat	-1.56 ± 0.64	-0.46 ± 0.09	-0.63 ± 0.11	-0.83 ± 0.02	-0.90 ± 0.09	-1.87 ± 0.60
Harestua	-0.44 ± 0.40	-0.43 ± 0.10	-0.59 ± 0.15	-0.83 ± 0.03	-0.90 ± 0.10	-1.65 ± 0.73
Zugspitze	-0.63 ± 0.19	-0.34 ± 0.08	-0.61 ± 0.13	-0.85 ± 0.02	-0.91 ± 0.09	-1.87 ± 0.56
Jungfraujoch	-0.98 ± 0.16	-0.34 ± 0.07	-0.64 ± 0.12	-0.86 ± 0.02	-0.93 ± 0.09	-1.80 ± 0.56
Toronto	-1.22 ± 0.37	-0.22 ± 0.11	-0.34 ± 0.19	-0.80 ± 0.02	-1.08 ± 0.15	-0.03 ± 1.44
Tsukuba	-1.00 ± 0.25	-0.48 ± 0.07	-0.73 ± 0.16	-0.89 ± 0.02	-0.93 ± 0.10	-0.30 ± 0.56
Kitt Peak	-1.03 ± 0.53	-0.42 ± 0.06	-0.62 ± 0.12	-0.90 ± 0.03	-0.95 ± 0.09	-1.75 ± 0.38
Izaña	-0.66 ± 0.15	-0.37 ± 0.06	-0.53 ± 0.12	-0.91 ± 0.04	-0.87 ± 0.08	-1.48 ± 0.39
Mauna Loa	-0.39 ± 0.19	-0.03 ± 0.05	-0.35 ± 0.11	-0.90 ± 0.03	-1.22 ± 0.06	0.18 ± 0.72
Wollongong	-0.55 ± 0.16	-0.95 ± 0.05	-0.74 ± 0.13	-0.87 ± 0.02	-0.96 ± 0.09	-1.26 ± 0.50
Lauder	-0.60 ± 0.21	-0.96 ± 0.07	-0.79 ± 0.12	-0.85 ± 0.02	-0.97 ± 0.09	-1.78 ± 0.67
Arrival Heights	-0.36 ± 0.67	-1.09 ± 0.08	-0.74 ± 0.13	-0.97 ± 0.15	-0.87 ± 0.09	-1.32 ± 1.26

Table 5. $ClONO_2$ trend in % per year between 2000 and 2009, calculated by fitting a linear function combined with a first (sites poleward of 70°) or third order Fourier series to the data. The error bars were determined with the bootstrap method.

Measurement site	FTIR	KASIMA	SLIMCAT	2-D model	EMAC	SOCOL
Eureka	-4.56 ± 0.78	-1.18 ± 0.19	-0.83 ± 0.25	-1.21 ± 0.10	-1.75 ± 0.16	-3.37 ± 2.87
Ny Ålesund	6.79 ± 5.01	-1.03 ± 0.20	-0.62 ± 0.26	-1.20 ± 0.08	-1.59 ± 0.17	-1.84 ± 3.07
Thule	-3.58 ± 1.04	-1.28 ± 0.18	-0.94 ± 0.25	-1.20 ± 0.07	-1.77 ± 0.16	-3.37 ± 2.46
Kiruna	-1.45 ± 0.95	-0.91 ± 0.16	-0.71 ± 0.24	-1.19 ± 0.04	-1.05 ± 0.17	-1.62 ± 2.36
Harestua	-0.07 ± 0.52	-1.05 ± 0.14	-0.80 ± 0.21	-1.21 ± 0.03	-1.01 ± 0.16	-2.73 ± 1.58
Zugspitze	-1.37 ± 0.52	-0.90 ± 0.12	-0.02 ± 0.24	-1.24 ± 0.05	-1.16 ± 0.15	-3.42 ± 0.62
Jungfraujoch	-1.44 ± 0.33	-0.90 ± 0.12	-0.06 ± 0.22	-1.25 ± 0.05	-1.16 ± 0.15	-3.30 ± 0.61
Kitt Peak	-2.53 ± 1.16	-0.86 ± 0.08	-0.21 ± 0.18	-1.31 ± 0.05	-1.14 ± 0.12	-2.89 ± 0.67
Izaña	-2.86 ± 0.67	-0.72 ± 0.10	0.19 ± 0.16	-1.33 ± 0.08	-1.14 ± 0.10	-2.14 ± 0.66
Wollongong	-2.18 ± 0.60	-1.47 ± 0.07	-0.96 ± 0.16	-1.25 ± 0.04	-1.54 ± 0.11	-1.46 ± 0.92
Lauder	-0.35 ± 0.46	-1.61 ± 0.09	-0.59 ± 0.20	-1.22 ± 0.05	-1.18 ± 0.16	-2.21 ± 0.74
Arrival Heights	0.99 ± 0.76	-1.65 ± 0.20	-1.11 ± 0.26	-0.84 ± 0.82	-0.52 ± 0.23	-1.54 ± 3.71

the pole. At the Northern Hemisphere sites, the measurements show a much weaker increase of HF than KASIMA and SLIMCAT, at some sites even a decrease.

7 Discussion

Total column abundances of HCl, $ClONO_2$, and HF were determined from FTIR measurements at 17 sites between 80.05° N and 77.82° S and compared to the calculations of five different models with focus on the time period 2000–2009. Different aspects should be considered and discussed before the trends calculated from the FTIR measurements and model data for this study are interpreted and compared.

The offset in the absolute values between models and measurements seen in Sect. 4 is assumed to be constant in time and sufficiently small so that it does not strongly influence the trend result.

In contrast, the FTIR trends depend on whether or not a Fourier series is incorporated in the fitting function to account for the seasonal cycle, although the different results mostly agree within their errors (Sect. 5.2). Because the seasonal cycle of the investigated gases is very pronounced, especially in polar regions, and the time series considered are not very long, the trends calculated without including the Fourier series depend on the start and end time of year.

When the FTIR data are restricted to a period with less variability, in this case summer and autumn (corresponding to June to November in the Northern and December to May in the Southern Hemisphere), the error bars are quite large so that an agreement with the trends from the complete time series is found at most of the sites (Sect. 5.2). One reason

Table 6. HF trend in % per year between 2000 and 2009, calculated by fitting a linear function combined with a first (sites poleward of 70°) or third order Fourier series to the data. The error bars were determined with the bootstrap method.

Measurement site	FTIR	KASIMA	SLIMCAT	2-D model
Eureka	-0.56 ± 0.69	0.76 ± 0.11	0.79 ± 0.11	0.23 ± 0.03
Ny Ålesund	0.61 ± 0.70	0.85 ± 0.10	0.93 ± 0.11	0.23 ± 0.03
Thule	-1.11 ± 0.54	0.74 ± 0.11	0.83 ± 0.11	0.22 ± 0.03
Kiruna	0.61 ± 0.42	0.94 ± 0.12	0.96 ± 0.15	0.22 ± 0.04
Poker Flat	1.54 ± 1.18	1.22 ± 0.11	1.41 ± 0.15	0.21 ± 0.04
Harestua	-0.02 ± 0.54	0.93 ± 0.12	0.93 ± 0.16	0.19 ± 0.03
Zugspitze	0.95 ± 0.32	1.10 ± 0.10	1.24 ± 0.16	0.14 ± 0.05
Jungfraujoch	0.48 ± 0.25	1.11 ± 0.10	1.22 ± 0.15	0.14 ± 0.05
Toronto	-0.04 ± 0.61	1.04 ± 0.14	1.45 ± 0.25	0.00 ± 0.05
Tsukuba	0.31 ± 0.34	0.96 ± 0.08	1.00 ± 0.19	0.09 ± 0.04
Kitt Peak	0.55 ± 0.68	1.20 ± 0.07	1.27 ± 0.15	0.08 ± 0.04
Izaña	0.92 ± 0.21	1.43 ± 0.07	1.66 ± 0.15	0.06 ± 0.06
Mauna Loa	0.43 ± 0.30	2.32 ± 0.09	2.11 ± 0.15	0.03 ± 0.05
Wollongong	1.61 ± 0.31	0.80 ± 0.07	1.15 ± 0.15	0.14 ± 0.04
Lauder	1.07 ± 0.28	0.81 ± 0.08	1.27 ± 0.15	0.19 ± 0.04
Arrival Heights	0.68 ± 0.58	1.14 ± 0.10	1.38 ± 0.09	0.26 ± 0.04

for the large error bars is probably that there is still some variability left in the summer data. Furthermore, some of the time series contain only few data points during this time of year probably due to the weather conditions and because at some sites, the measurements have been performed on a campaign basis.

All FTIR sites taking part in this study except La Réunion and Toronto started operation before the year 2000. This is why for the more thorough investigation, the time period 2000 to 2009 was chosen so that nearly all measurement time series have the same length. Of course, the error bars for the longer period between 1996 and 2009 are usually smaller when compared for the sites where operation was started before or in 1996 (Sect. 5.3). The trends calculated for the six-year period 2004 to 2009 are probably not significant in terms of Weatherhead et al. (1998). As discussed by Weatherhead et al. (1998), the length of a time series necessary to determine a certain trend depends on the magnitude of the expected trend, the standard deviation, and the autocorrelation of the time series. The trends expected here are quite small and the standard deviations quite large, especially in polar regions, where the Fourier series does not fully capture the amplitude of the seasonal cycle, especially for $ClONO_2$. The autocorrelation is not easy to determine because the time series are not continuous.

Still, when comparing the trends from models and measurements, it must be considered that the time ranges do not always agree exactly, especially for Poker Flat whose measurement series ends in 2004, and for Toronto where the trends from 2002–2009 are compared with those for 2000–2009 from the other sites. Concerning the models, the time series from SOCOL ends in 2004, and the one from the 2-D model in 2008 for all species at all sites. Moreover, in contrast to the model output, the sampling of the FTIR data is not regular because the instrument needs clear sky conditions and the sun above the horizon so that it cannot measure in cloudy weather and during polar night.

The trends determined for HCl and $ClONO_2$ (roughly around -1 to $-2\,\%\,yr^{-1}$) agree very well with those presented by the WMO (2011) for the stratospheric inorganic halogen abundance (EESC = Equivalent Effective Stratospheric Chlorine) estimated from tropospheric measurements of ozone-depleting substances. This EESC was calculated from the chlorine- and bromine-containing source gases by accounting for the transport time to the stratosphere and considering the dependency of the fractional release values on the mean age-of-air (Newman et al., 2007). A decrease of midlatitude EESC of 11 % between the peak in 1997 and 2008 is reported by the WMO (2011) corresponding to a trend of about $-1\,\%\,yr^{-1}$. The peak in the Antarctic polar vortex occurred later, in 2002. Until 2008, the EESC abundance decreased by about 5 % there (WMO, 2011) which corresponds to a trend of about $-0.8\,\%\,yr^{-1}$. This slightly weaker decrease in the southern high latitudes cannot be seen clearly in the FTIR measurements analysed and presented here. Two models (EMAC and the 2-D model) show this tendency towards weaker $ClONO_2$ and EMAC also towards weaker HCl trends when approaching the south pole for the 2000–2009 trends (Sect. 6).

The present study is also able to confirm the results of many other preceding investigations on stratospheric inorganic chlorine and fluorine measurements. The stabilisation of the stratospheric HCl content at the end of the 1990s described in Sect. 4.1 was already seen for example by Considine et al. (1999), Rinsland et al. (2003), and Newchurch et al. (2003). Also the subsequent negative trend in the

stratospheric chlorine abundance was reported before by other studies. For example, Lary et al. (2007) found a decrease towards the end of their study in which they analysed a stratospheric Cl_y time series between 1991 and 2006 that was created from a combination of many different (mainly satellite) measurements. For HCl, a trend was estimated from measurements made by the MLS (Microwave Limb Sounder) instrument aboard the Aura satellite between 50 and 65 km height and 60° S and 60° N by Froidevaux et al. (2006). They reported a decrease in the volume mixing ratio of (-0.78±0.08)% yr^{-1} between August 2004 and January 2006. This value also agrees very well with those found in the present study. A similar result for HCl was published by Jones et al. (2011) who combined HALOE (Halogen Occultation Experiment) data with ACE-FTS (Atmospheric Chemistry Experiment Fourier Transform Spectrometer) results between 35 and 45 km to form a time series of HCl from 1993 to 2008. They found a significantly negative trend of about -5.1 % $decade^{-1}$ to -5.8 % $decade^{-1}$ for the time period 1997–2008, depending on latitude. Measurements with the McMath-Pierce solar telescope on Kitt Peak (Arizona, US) showed a slightly larger decrease of the HCl total column abundance of (-1.8 ± 0.4)% yr^{-1} between 1997 and 2007 (Wallace and Livingston, 2007). Concerning the HF total column abundance, a strong increase of (10.9 ± 1.1)% yr^{-1} above Kitt Peak between 1977 and 1990 was reported by Rinsland et al. (1991). It weakened during the 1990s so that the trend for the period 1977–2001 amounted to (4.30 ± 0.15)% yr^{-1} only (Rinsland et al., 2002). A leveling-off could be seen by Zander et al. (2008) above Jungfraujoch around 2003–2004. This agrees very well with the results of the present study at some of the northern hemisphere sites, where the HF trends are much weaker for the period 2004–2009 than for 2000–2009 and 1996–2009, or even negative (Sect. 5.3).

Part of the discrepancy between the modelled trends can be explained by the different halocarbon scenarios used in the simulations. Considering a time shift of a few years due to the transport of CCl_y and CF_y from the surface to the stratosphere, the weakest chlorine decrease in 2000–2009 would be expected from the WMO (2007) Ref 2 scenario used by KASIMA and the 2-D model (Fig. 1). KASIMA indeed at most sites shows the weakest decrease in HCl and $ClONO_2$, along with SLIMCAT (Fig. 12 and Tables 4 and 5). In contrast, the 2-D model shows a stronger decrease than expected from the scenario. Above most of the measurement sites, also EMAC and SOCOL show stronger HCl and $ClONO_2$ decreases than expected from the surface halocarbon scenarios they used. For HF, the 2-D model calculated much weaker increases than KASIMA and SLIMCAT did (Fig. 12 and Tab. 6). This cannot be explained by the different scenarios because as already mentioned, KASIMA and the 2-D model used the same one. A possible reason for a part of this discrepancy in the HF trends is the fact that the 2-D model does not treat all halogen-containing species explicitly (please see Sect. 3.1). Instead, the mixing ratios of some are added proportionately to those of others with similar lifetimes by considering the number of chlorine atoms. But this means that for some gases, the contained amount of fluorine is not represented correctly so that very roughly about 50 pptv are missing in the surface CF_y mixing ratio. As the missing amount of CF_y increases with time, the trend of the HF total column abundance is expected to be slightly too small in the 2-D model.

The trends of HCl, $ClONO_2$, and HF between 2000 and 2009 have been examined with respect to differences between the hemispheres (Sect. 6). The FTIR measurements suggest a stronger decrease of HCl and $ClONO_2$ in the Northern Hemisphere than in the Southern Hemisphere, while the models, except KASIMA, do not show a hemispheric dependency. However, the KASIMA signal is inverse to the FTIR one: the relative decrease is stronger in the Southern Hemisphere. According to the measurements, the HF total column abundances in the Southern Hemisphere still increase while the sites in the Northern Hemisphere show a more differentiated picture. There are some with positive trends as well, especially in the low latitudes, but also some without a significant trend. In the high latitudes, there are two sites showing a negative trend. This tendency towards a HF stabilisation or even decrease in the Northern Hemisphere in the last few years is also visible in other FTIR time series for the later and shorter period 2004–2009 (Sect. 5.3). In contrast, the models show a more or less strong increase of HF at all locations without a discernible difference between the hemispheres.

At some sites, the trends of HCl and $ClONO_2$ show significant discrepancies in magnitude (Sect. 6). This was already described by Kohlhepp et al. (2011) for Kiruna and in the SPARC CCMVal (2010) report for the Jungfraujoch. In Kiruna, the trends between 1996 and 2009 of these two gases differ by about a factor of four both for the FTIR measurements and the KASIMA model calculations (Kohlhepp et al., 2011). When extending this investigation for Kiruna by the other 16 sites and four models in the present study, a latitudinal dependency of the difference can be found in the FTIR measurements in the Northern Hemisphere. In the low and high latitudes, $ClONO_2$ decreases much faster than HCl, while in the midlatitudes, it decreases only slightly faster. Concerning the difference between high and midlatitudes, EMAC and SOCOL and to a certain degree also SLIMCAT show a similar signal, while the other models do not show a distinct latitudinal dependency but a slightly stronger decrease of $ClONO_2$ at all sites.

8 Conclusions

There is an overall agreement between the models and measurements in a decrease of HCl and $ClONO_2$ during the period 2000–2009, as is expected from the ban or restrictions

on the production of the anthropogenic chlorine source gases (e.g. CFCs and HCFCs) in the Montreal Protocol and its amendments and adjustments. Because fluorine emission is not explicitly restricted, the HF total column abundances are expected to be still increasing, which can be seen especially in the model simulations. The measurements also confirm this, but suggest a stabilisation of HF in the last few years, at least in the Northern Hemisphere.

The models tend to underestimate the decrease seen in the HCl and $ClONO_2$ measurements in the Northern Hemisphere and to overestimate it in the Southern Hemisphere. Analogously, they tend to overestimate the increase of HF in the Northern Hemisphere. The FTIR trend results depend both on hemisphere and on latitude, while the models do not show distinct differences between the hemispheres, but most of them simulate a dependency on latitude.

Supplementary material related to this article is available online at: http://www.atmos-chem-phys.net/12/3527/2012/acp-12-3527-2012-supplement.pdf.

Acknowledgements. We thank the NASA Goddard Space Flight Center for providing NCEP daily temperature and pressure profiles (via the automailer system) which were used for the calibration and inversion of the FTIR spectra at most of the measurement sites.

The PEARL Bruker 125HR measurements at Eureka were made by the Canadian Network for the Detection of Atmospheric Change (CANDAC) and in part by the Canadian Arctic ACE Validation Campaigns, and were supported by the Atlantic Innovation Fund/Nova Scotia Research Innovation Trust, Canada Foundation for Innovation, Canadian Foundation for Climate and Atmospheric Sciences, Canadian Space Agency, Environment Canada, Government of Canada International Polar Year funding, Natural Sciences and Engineering Research Council, Northern Scientific Training Program, Ontario Innovation Trust, Polar Continental Shelf Program, and Ontario Research Fund. For the DA8 measurements at Eureka we gratefully acknowledge the collaborative effort between the Japan Meteorological Agency (JMA) and Environment Canada, and the financial support provided by the Canadian Foundation for Climate and Atmospheric Science to the University of Toronto for our joint measurement program at Eureka in 2002–2003. The recording of DA8 atmospheric solar absorption spectra, from 2004 to 2008, was made possible through collaboration with the Atmospheric Chemistry Experiment (ACE) Arctic Validation Team. The authors wish to thank the staff at the Eureka weather station and CANDAC for the logistical and on-site support provided at Eureka.

The National Center for Atmospheric Research is supported by the National Science Foundation. The NCAR FTS observation program at Thule, GR is supported under contract by the National Aeronautics and Space Administration (NASA). This work is also supported by the NSF Office of Polar Programs (OPP). The Mauna Loa FTS program is supported by the National Aeronautics and Space Administration. We wish to thank the Danish Meteorological Institute for support at the Thule site.

The TAO Bomem DA8 measurements were supported by ABB Bomem, the Canada Foundation for Innovation, Canadian Foundation for Climate and Atmospheric Science, Canadian Space Agency, Environment Canada, Natural Science and Engineering Research Council, Ontario Research and Development Challenge Fund, Premier's Research Excellent Award, and University of Toronto.

The University of Liège contribution to the present work has primarily been supported by the SECPEA and A3C PRODEX projects funded by the Belgian Federal Science Policy Office (BELSPO, Brussels). The ULg team further acknowledges the International Foundation High Altitude Research Stations Jungfraujoch and Gornergrat (HFSJG, Bern) for supporting the facilities needed to perform the observations. E. Mahieu is Research Associate with the F.R.S.-FNRS (Fonds de la Recherche Scientifique, Brussels, Belgium).

We acknowledge the support of the European Commission through GEOmon (contract number FP6-2005-Global-4-036677) and HYMN (contract no. 037048 (GOCE)) projects under the 6th Framework Programme.

We further acknowledge support by Deutsche Forschungsgemeinschaft and Open Access Publishing Fund of Karlsruhe Institute of Technology.

Finally, we wish to thank the Editor J. B. Burkholder and two anonymous reviewers very much for their helpful and constructive comments regarding our manuscript.

Edited by: J. B. Burkholder

References

Atkinson, R., Baulch, D. L., Cox, R. A., Crowley, J. N., Hampson, R. F., Hynes, R. G., Jenkin, M. E., Rossi, M. J., and Troe, J.: Evaluated kinetic and photochemical data for atmospheric chemistry: Volume I – gas phase reactions of O_x, HO_x, NO_x and SO_x species, Atmos. Chem. Phys., 4, 1461–1738, doi:10.5194/acp-4-1461-2004, 2004.

Atkinson, R., Baulch, D. L., Cox, R. A., Crowley, J. N., Hampson, R. F., Hynes, R. G., Jenkin, M. E., Rossi, M. J., Troe, J., and IUPAC Subcommittee: Evaluated kinetic and photochemical data for atmospheric chemistry: Volume II – gas phase reactions of organic species, Atmos. Chem. Phys., 6, 3625–4055, doi:10.5194/acp-6-3625-2006, 2006.

Batchelor, R. L., Strong, K., Lindenmaier, R., Mittermeier, R. L., Fast, H., Drummond, J. R., and Fogal, P. F.: A new Bruker IFS 125HR FTIR spectrometer for the Polar Environment Atmospheric Research Laboratory at Eureka, Canada – measurements and comparison with the existing Bomem DA8 spectrometer, J. Atmos. Ocean. Tech., 26, 1328–1340, doi:10.1175/2009JTECHA1215.1, 2009.

Batchelor, R. L., Kolonjari, F., Lindenmaier, R., Mittermeier, R. L., Daffer, W., Fast, H., Manney, G., Strong, K., and Walker, K. A.: Four Fourier transform spectrometers and the Arctic polar vortex: instrument intercomparison and ACE-FTS validation at Eureka during the IPY springs of 2007 and 2008, Atmos. Meas. Tech., 3, 51–66, doi:10.5194/amt-3-51-2010, 2010.

Bian, H. and Prather, M. J.: Fast-J2: Accurate simulation of stratospheric photolysis in global chemical models, J. Atmos. Chem., 41, 281–296, 2002.

Blumenstock, T., Kopp, G., Hase, F., Hochschild, G., Mikuteit, S., Raffalski, U., and Ruhnke, R.: Observation of unusual chlorine activation by ground-based infrared and microwave spectroscopy in the late Arctic winter 2000/01, Atmos. Chem. Phys., 6, 897–905, doi:10.5194/acp-6-897-2006, 2006.

Brault, J. W.: Solar Fourier transform spectroscopy, in Proceedings of the JOSO Workshop, Future Solar Optical Observations, Needs and Constraints, edited by: Godoli, G., Noci, G., and Righin, A., 33–52, Florence, Italy, 1978.

Brown, L. R., Gunson, M. R., Toth, R. A., Irion, F. W., Rinsland, C. P., and Goldman, A.: Atmospheric Trace Molecule Spectroscopy (ATMOS) linelist, Appl. Optics, 35, 2828–2848, 1996.

Chipperfield, M. P., Burton, M., Bell, W., Paton Walsh, C., Blumenstock, Th., Coffey, M. T., Hannigan, J. W., Mankin, W. G., Galle, B., Mellqvist, J., Mahieu, E., Zander, R., Notholt, J., Sen, B., and Toon, G. C.: On the use of HF as a reference for the comparison of stratospheric observations and models, J. Geophys. Res., 102, 12901–12919, 1997.

Chipperfield, M. P.: Multiannual simulations with a three-dimensional chemical transport model, J. Geophys. Res., 104, 1781–1805, 1999.

Chipperfield, M. P. and Feng, W.: Comment on: Stratospheric Ozone Depletion at northern mid-latitudes in the 21st century: The importance of future concentrations of greenhouse gases nitrous oxide and methane, Geophys. Res. Lett., 30, 1389, doi:10.1029/2002GL016353, 2003.

Chipperfield, M. P.: New Version of the TOMCAT/SLIMCAT Off-Line Chemical Transport Model: Intercomparison of Stratospheric Tracer Experiments, Q. J. Roy. Meteorol. Soc., 132, 1179–1203, doi:10.1256/qj.05.51, 2006.

Coffey, M. T., Goldman, A., Hannigan, J. W., Mankin, W. G., Schoenfeld, W. G., Rinsland, C. P., Bernardo, C., and Griffith, D. W. T. : NOTE: Improved Vibration-Rotation (0-1) HBr Line Parameters for Validating High Resolution Infrared Atmospheric Spectra Measurements, J. Quant. Spectrosc. Ra., 60, 863–867, 1998

Considine, G. D., Deaver, L. E., Remsberg, E. E., and Russell, J. M. III: Analysis of near-global trends and variability in Halogen Occultation Experiment HF and HCl data in the middle atmosphere, J. Geophys. Res., 104, 24297–24308, 1999.

Crutzen, P. J., Isaksen, I. S. A., and McAfee, J. R.: The impact of the chlorocarbon industry on the ozone layer, J. Geophys. Res., 83, 345–363, 1978.

Duchatelet, P., Demoulin, P., Hase, F., Ruhnke, R., Feng, W., Chipperfield, M. P., Bernath, P. F., Boone, C. D., Walker, K. A., and Mahieu, E.: Hydrogen fluoride total and partial column time series above the Jungfraujoch from long-term FTIR measurements: Impact of the line-shape model, characterization of the error budget and seasonal cycle, and comparison with satellite and model data, J. Geophys. Res., 115, D22306, doi:10.1029/2010JD014677, 2010.

Egorova, T. A., Rozanov, E. V., Zubov, V. A., and Karol, I. L.: Model for investigating ozone trends (MEZON), Atmos. Ocean. Phys., 39, 277–292, 2003.

Egorova, T., Rozanov, E., Zubov, V., Manzini, E., Schmutz, W., and Peter, T.: Chemistry-climate model SOCOL: a validation of the present-day climatology, Atmos. Chem. Phys., 5, 1557–1576, doi:10.5194/acp-5-1557-2005, 2005.

Eyring, V., Butchart, N., Waugh, D. W., Akiyoshi, H., Austin, J., Bekki, S., Bodeker, G. E., Boville, B. A., Brühl, C., Chipperfield, M. P., Cordero, E., Dameris, M., Deushi, M., Fioletov, V. E., Frith, S. M., Garcia, R. R., Gettelman, A., Giorgetta, M. A., Grewe, V., Jourdain, L., Kinnison, D. E., Mancini, E., Manzini, E., Marchand, M., Marsh, D. R., Nagashima, T., Newman, P. A., Nielsen, J. E., Pawson, S., Pitari, G., Plummer, D. A., Rozanov, E., Schraner, M., Shepherd, T. G., Shibata, K., Stolarski, R. S., Struthers, H., Tian, W., and Yoshiki, M.: Assessment of temperature, trace species, and ozone in chemistry-climate model simulations of the recent past, J. Geophys. Res., 111, D22308, doi:22310.21029/22006JD007327, 2006.

Eyring, V., Waugh, D. W., Bodeker, G. E., Cordero, E., Akiyoshi, H., Austin, J., Beagley, S. R., Boville, B. A., Braesicke, P., Brühl, C., Butchart, N., Chipperfield, M. P., Dameris, M., Deckert, R., Deushi, M., Frith, S. M., Garcia, R. R., Gettelman, A., Giorgetta, M. A., Kinnison, D. E., Mancini, E., Manzini, E., Marsh, D. R., Matthes, S., Nagashima, T., Newman, P. A., Nielsen, J. E., Pawson, S., Pitari, G., Plummer, D. A., Rozanov, E., Schraner, M., Scinocca, J. F., Semeniuk, K., Shepherd, T. G., Shibata, K., Steil, B., Stolarski, R. S., Tian, W., and Yoshiki, M.: Multi-model projections of stratospheric ozone in the 21st century, J. Geophys. Res., 112, D16303, doi:16310.11029/12006JD008332, 2007.

Eyring, V., Chipperfield, M. P., Giorgetta, M. A., Kinnison, D. E., Manzini, E., Matthes, K., Newman, P. A., Pawson, S., Shepherd, T. G., and Waugh, D. W.: Overview of the New CCMVal Reference and Sensitivity Simulations in Support of Upcoming Ozone and Climate Assessments and the Planned SPARC CCMVal Report, SPARC Newsletter, 30, 20–26, 2008.

Fast, H., Mittermeier, R. L., and Makino, Y.: A ten-year record of Arctic trace gas total column measurements at Eureka, Canada, from 1997 to 2006, Atmos.-Ocean, 49, 67–94, doi:10.1080/07055900.2011.562470, 2011.

Feng, W., Chipperfield, M. P., Dorf, M., Pfeilsticker, K., and Ricaud, P.: Mid-latitude ozone changes: studies with a 3-D CTM forced by ERA-40 analyses, Atmos. Chem. Phys., 7, 2357–2369, doi:10.5194/acp-7-2357-2007, 2007.

Froidevaux, L., Livesey, N. J., Read, W. G., Salawitch, R. J., Waters, J. W., Drouin, B., MacKenzie, I. A., Pumphrey, H. C., Bernath, P., Boone, C., Nassar, R., Montzka, S., Elkins, J., Cunnold, D., and Waugh, D.: Temporal decrease in upper atmospheric chlorine, Geophys. Res. Lett., 33, L23812, doi:10.1029/2006GL027600, 2006.

Gardiner, T., Forbes, A., de Mazière, M., Vigouroux, C., Mahieu, E., Demoulin, P., Velazco, V., Notholt, J., Blumenstock, T., Hase, F., Kramer, I., Sussmann, R., Stremme, W., Mellqvist, J., Strandberg, A., Ellingsen, K., and Gauss, M.: Trend analysis of greenhouse gases over Europe measured by a network of ground-based remote FTIR instruments, Atmos. Chem. Phys., 8, 6719–6727, doi:10.5194/acp-8-6719-2008, 2008.

Goldman, A., Paton-Walsh, C., Bell, W., Toon, G. C., Blavier, J.-F., Sen, B., Coffey, M. T., Hannigan, J. W., and Mankin, W. G.: Network for the detection of stratospheric change Fourier transform infrared intercomparison at Table Mountain Facility, November 1996, J. Geophys. Res., 104, 30481–30503, 1999.

Griffith, D. W. T., Jones, N. B., and Matthews, W. A.: Interhemispheric ratio and Annual Cycle of Carbonyl Sulphide (OCS) Total Column from Ground-Based FTIR Spectra, J. Geophys. Res., 103, 8447–8454, 1998.

Hannigan, J. W., Coffey, M. T., and Goldman, A.: Semi-Autonomous FTS Observation System for Stratospheric and Tropospheric Gases, J. Atmos. Oceanic Technol., 26, 1814–1828, 2009.

Hase, F., Blumenstock, T., and Paton-Walsh, C.: Analysis of the instrumental lineshape of high-resolution Fourier transform IR spectrometers with gas cell measurements and new retrieval software, Appl. Optics, 38, 3417–3422, 1999.

Hase, F., Hannigan, J. W., Coffey, M. T., Goldman, A., Höpfner, M., Jones, N. B., Rinsland, C. P., and Wood, C. P.: Intercomparison of retrieval codes used for the analysis of high-resolution, ground-based FTIR measurements, J. Quant. Spectrosc. Ra., 87, 25–52, 2004.

Hossaini, R., Chipperfield, M. P., Monge-Sanz, B. M., Richards, N. A. D., Atlas, E., and Blake, D. R.: Bromoform and dibromomethane in the tropics: a 3-D model study of chemistry and transport, Atmos. Chem. Phys., 10, 719–735, doi:10.5194/acp-10-719-2010, 2010.

IPCC (Intergovernmental Panel on Climate Change): Climate Change 2001: Synthesis Report. A Contribution of Working Groups I, II and III to the Third Assessment Report of the Intergovernmental Panel on Climate Change, edited by: Watson, R. T. and the Core Writing Team, Cambridge University Press, Cambridge, UK, and New York, USA, 2001.

IPCC (Intergovernmental Panel on Climate Change): Climate Change 2007: Synthesis Report. A Contribution of Working Groups I, II and III to the Fourth Assessment Report of the Intergovernmental Panel on Climate Change, edited by: Core Writing Team, Pachauri, R. K., and Reisinger, A., IPCC, Geneva, Switzerland, 2007.

Jones, A., Urban, J., Murtagh, D. P., Sanchez, C., Walker, K. A., Livesey, N. J., Froidevaux, L., and Santee, M. L.: Analysis of HCl and ClO time series in the upper stratosphere using satellite data sets, Atmos. Chem. Phys., 11, 5321–5333, 2011, http://www.atmos-chem-phys.net/11/5321/2011/.

Jöckel, P., Sander, R., Kerkweg, A., Tost, H., and Lelieveld, J.: Technical Note: The Modular Earth Submodel System (MESSy) – a new approach towards Earth System Modeling, Atmos. Chem. Phys., 5, 433–444, doi:10.5194/acp-5-433-2005, 2005.

Jöckel, P., Tost, H., Pozzer, A., Brühl, C., Buchholz, J., Ganzeveld, L., Hoor, P., Kerkweg, A., Lawrence, M. G., Sander, R., Steil, B., Stiller, G., Tanarhte, M., Taraborrelli, D., van Aardenne, J., and Lelieveld, J.: The atmospheric chemistry general circulation model ECHAM5/MESSy1: consistent simulation of ozone from the surface to the mesosphere, Atmos. Chem. Phys., 6, 5067–5104, doi:10.5194/acp-6-5067-2006, 2006.

Kagawa, A., Kasai, Y., Jones, N. B., Yamamori, M., Seki, K., Murcray, F., Murayama, Y., Mizutani, K., and Itabe, T.: Characteristics and error estimation of stratospheric ozone and ozone-related species over Poker Flat (65° N, 147° W), Alaska observed by a ground-based FTIR spectrometer from 2001 to 2003, Atmos. Chem. Phys., 7, 3791–3810, doi:10.5194/acp-7-3791-2007, 2007.

Kinnersley, J. S.: The climatology of the stratospheric THIN AIR model, Q. J. Roy. Meteorol. Soc., 122, 219–252, 1996.

Kohlhepp, R., Barthlott, S., Blumenstock, T., Hase, F., Kaiser, I., Raffalski, U., and Ruhnke, R.: Trends of HCl, $ClONO_2$, and HF column abundances from ground-based FTIR measurements in Kiruna (Sweden) in comparison with KASIMA model calculations, Atmos. Chem. Phys., 11, 4669–4677, doi:10.5194/acp-11-4669-2011, 2011.

Kouker, W., Langbein, I., Reddmann, T., and Ruhnke, R.: The Karlsruhe Simulation Model of the Middle Atmosphere (KASIMA), Forschungszentrum Karlsruhe, Germany, Version 2, FZK Report 6278, 1999.

Lait, L., Newman, P., and Schoeberl, R.: Using the Goddard Automailer, available at: http://code916.gsfc.nasa.gov/Dataservices, 2005.

Lary, D. J., Waugh, D. W., Douglass, A. R., Stolarski, R. S., Newman, P. A., and Mussa, H.: Variations in stratospheric inorganic chlorine between 1991 and 2006, Geophys. Res. Lett., 34, L21811, doi:10.1029/2007GL030053, 2007.

Mahieu, E., Duchatelet, P., Demoulin, P., Walker, K. A., Dupuy, E., Froidevaux, L., Randall, C., Catoire, V., Strong, K., Boone, C. D., Bernath, P. F., Blavier, J.-F., Blumenstock, T., Coffey, M., De Mazière, M., Griffith, D., Hannigan, J., Hase, F., Jones, N., Jucks, K. W., Kagawa, A., Kasai, Y., Mebarki, Y., Mikuteit, S., Nassar, R., Notholt, J., Rinsland, C. P., Robert, C., Schrems, O., Senten, C., Smale, D., Taylor, J., Tétard, C., Toon, G. C., Warneke, T., Wood, S. W., Zander, R., and Servais, C.: Validation of ACE-FTS v2.2 measurements of HCl, HF, CCl3F and CCl2F2 using space-, balloon- and ground-based instrument observations, Atmos. Chem. Phys., 8, 6199–6221, doi:10.5194/acp-8-6199-2008, 2008.

Manzini, E., McFarlane, N. A., and McLandress, C.: Impact of the Doppler spread parameterization on the simulation of the middle atmosphere circulation using the MA/ECHAM4 general circulation model, J. Geophys. Res., 102, 25751–25762, 1997.

McPeters, R. D., Hofmann, D. J., Clark, M., Flynn, L., Froidevaux, L., Gross, M., Johnson, B., Koenig, G., Liu, X., McDermid, S., McGee, T., Murcray, F., Newchurch, M. J., Oltmans, A., Parrish, A., Schnell, R., Singh, U., Tsou, J. J., Walsh, T., and Zawodny, J. M.: Results from the 1995 Stratospheric Ozone Profile Intercomparison at Mauna Loa, J. Geophys. Res., 104, 30505–30514, 1999.

Meier, A., Paton-Walsh, C., Bell, W., Blumenstock, T., Hase, F., Goldman, A., Steen, A., Kift, R., Woods, P., and Kondo, Y.: Evidence of reduced measurement uncertainties from an FTIR instrument intercomparison at Kiruna, Sweden, J. Quant. Spectrosc. Ra., 96, 75–84, 2005.

Mikuteit, S.: Trendbestimmung stratosphärischer Spurengase mit Hilfe bodengebundener FTIR-Messungen, Wissenschaftliche Berichte, FZKA-Report No. 7385, Forschungszentrum Karlsruhe, Germany, 2008.

Molina, M. J. and Rowland, F. S.: Stratospheric sink for chlorofluoromethanes: chlorine atom-catalysed destruction of ozone, Nature 249, 810–812, 1974.

Monge-Sanz, B., Chipperfield, M. P., Simmons, A., and Uppala, S.: Mean age of air and transport in a CTM: Comparison of different ECMWF analyses, Geophys. Res. Lett., 34, L04801, doi:10.1029/2006GL028515, 2007.

Morgenstern, O., Giorgetta, M. A., Shibata, K., Eyring, V., Waugh, D. W., Shepherd, T. G., Akiyoshi, H., Austin, J., Baumgaertner, A. J. G., Bekki, S., Braesicke, P., Brühl, C., Chipperfield, M. P., Cugnet, D., Dameris, M., Dhomse, S., Frith, S. M., Garny, H., Gettelman, A., Hardiman, S. C., Hegglin, M. I., Jöckel, P., Kinnison, D. E., Lamarque, J.-F., Mancini, E., Manzini, E., Marchand, M., Michou, M., Nakamura, T., Nielsen, J. E., Olivié, D.,

Pitari, G., Plummer, D. A., Rozanov, E., Scinocca, J. F., Smale, D., Teyssèdre, H., Toohey, M., Tian, W., and Yamashita, Y.: Review of present-generation stratospheric chemistry-climate models and associated external forcings, J. Geophys. Res., 115, D00M02, doi:10.1029/2009JD013728, 2010.

Murata, I., Nakajima, H., Nakane, H., and Fukunishi, H.: Temporal variations of HCl, HF, O_3, and HNO_3 observed at Tsukuba with Fourier transform spectrometer, Proceedings of the 6th International Conference on Global Change: Connection to the Arctic, 59–62, 2005.

Nakicenovic, N., Alcamo, J., Davis, G., de Vries, B., Fenhann, J., Gaffin, S., Gregory, K., Grübler, A., Jung, T.Y., Kram, T., Lebre La Rovere, E., Michaelis, L., Mori, S., Morita, T., Pepper, W., Pitcher, H., Price, L., Riahi, K., Roehrl, A., Rogner, H.-H., Sankovski, A., Schlesinger, M., Shukla, P., Smith, S., Swart, R., van Rooijen, S., Victor, N., and Dadi, Z.: Special Report on Emissions Scenarios: A Special Report of Working Group III of the Intergovernmental Panel on Climate Change, Cambridge University Press, Cambridge, UK, 599 pp., available at: http://www.grida.no/climate/ipcc/emission/index.htm, 2000.

Newchurch, M. J., Yang, E.-S., Cunnold, D. M., Reinsel, G. C., Zawodny, J. M., and Russell, J. M. III: Evidence for slowdown in stratospheric ozone loss: First stage of ozone recovery, J. Geophys. Res., 108, 4507, doi:10.1029/2003JD003471, 2003.

Newman, P. A., Daniel, J. S., Waugh, D. W., and Nash, E. R.: A new formulation of equivalent effective stratospheric chlorine (EESC), Atmos. Chem. Phys., 7, 4537–4552, doi:10.5194/acp-7-4537-2007, 2007.

Notholt, J., Meier, A., and Peil, S.: Total Column Densities of Tropospheric and Stratospheric Trace Gases in the Undisturbed Arctic Summer Atmosphere, J. Atmos. Chem., 20, 311–332, 1995.

Notholt, J., von der Gathen, P., and Peil, S.: Heterogeneous conversion of HCl and $ClONO_2$ during the Arctic winter 1992/1993 initiating ozone depletion, J. Geophys. Res., 100, 11269–11274, 1995.

Paton-Walsh, C., Jones, N., Wilson, S., Meier, A., Deutscher, N., Griffith, D., Mitchell, R., and Campbell, S.: Trace gas emissions from biomass burning inferred from aerosol optical depth, Geophys. Res. Lett., 31, L05116, doi:10.1029/2003GL018973, 2004.

Paton-Walsh, C., Jones, N. B., Wilson, S. R., Haverd, V., Meier, A., Griffith, D. W. T., and Rinsland, C. P.: Measurements of trace gas emissions from Australian forest fires and correlations with coincident measurements of aerosol optical depth, J. Geophys. Res.-Atmos., 110, D24305, doi:10.1029/2005JD006202, 2005.

Reddmann, T., Ruhnke, R., and Kouker, W.: Three-dimensional model simulations of SF_6 with mesospheric chemistry, J. Geophys. Res., 106, 14525–14537, 2001.

Reisinger, A. R., Jones, N. B., Matthews, W. A., and Rinsland, C. P.: Southern hemisphere ground based measurements of carbonyl fluoride (COF_2) and hydrogen fluoride (HF): Partitioning between fluoride reservoir species, Geophys. Res. Lett., 21, 797–800, 1994.

Reisinger, A. R., Jones, N. B., Matthews, W. A., and Rinsland, C. P.: Southern hemisphere mid-latitude ground based measurements of $ClONO_2$, method of analysis, seasonal cycle, and long term trend, J. Geophys. Res., 100, 23183–23193, 1995.

Rinsland, C. P., Levine, J. S., Goldman, A., Sze, N. D., Ko, M. K. W., and Johnson, D.W .: Infrared measurements of HF and HCl total column abundances above Kitt Peak, 1977–1990: Seasonal cycles, long-term increases, and comparisons with model calculations, J. Geophys. Res., 96, 15523–15540, 1991.

Rinsland, C. P., Nicholas, B. J., Connor, B. J., Logan, J. A., Pougatchev, N. S., Goldman, A., Murcray, F. J., Stephen, T. M., Pine, A. S., Zander, R., Mahieu, E., and Demoulin, P.: Northern and southern hemisphere ground-based infrared spectroscopic measurements of tropospheric carbon monoxide and ethane, J. Geophys. Res., 103, 28197–28218, doi:10.1029/98JD02515, 1998.

Rinsland, C. P., Zander, R., Mahieu, E., Chiou, L. S., Goldman, A., and Jones, N. B.: Stratospheric HF column abundances above Kitt Peak (31.9° N latitude): trends from 1977 to 2001 and correlations with stratospheric HCl columns, J. Quant. Spectrosc. Ra., 74, 205–216, 2002.

Rinsland, C. P., Mahieu, E., Zander, R., Jones, N. B., Chipperfield, M. P., Goldman, A., Anderson, J., Russell III, J. M., Demoulin, P., Notholt, J., Toon, G. C., Blavier, J.-F., Sen, B., Sussmann, R., Wood, S. W., Meier, A., Griffith, D. W. T., Chiou, L. S., Murcray, F. J., Stephen, T. M., Hase, F., Mikuteit, S., Schulz, A., and Blumenstock, T.: Long-term trends of inorganic chlorine from ground-based infrared solar spectra: Past increases and evidence for stabilisation, J. Geophys. Res., 108, 4252, doi:10.1029/2002JD003001, 2003.

Rodgers, C. D.: Inverse Methods for Atmospheric Sounding: Theory and Practice, Series on Atmospheric, Oceanic and Planetary Physics, Vol. 2, World Scientific, Singapore, 2000.

Roeckner, E., Brokopf, R., Esch, M., Giorgetta, M., Hagemann, S., Koernblueh, L., Manzini, E., Schlese, U., and Schulzweida, U.: Sensitivity of simulated climate to horizontal and vertical resolution in the ECHAM5 atmosphere model, J. Climate, 19, 3771–3791, 2006.

Rothman, L. S., Gamache, R. R., Tipping, R. H., Rinsland, C. P., Smith, M. A. H., Chris Benner, D., Malathy Devi, V., Flaud, J.-M, Camy-Peyret, C., Perrin, A., Goldman, A., Massie, S. T., Brown, L. R., and Toth, R. A.: The HITRAN molecular database: editions of 1991 and 1992, J. Quant. Spectrosc. Ra., 48, 469–507, 1992.

Rothman, L. S., Rinsland, C. P., Goldman, A., Massie, S. T., Edwards, D. P., Flaud, J.-M., Perrin, A., Camy-Peyret, C., Dana, V., Mandin, J.-Y., Schroeder, J., Mccann, A., Gamache, R. R., Wattson, R. B., Yoshino, K., Chance, K. V., Jucks, K. W., Brown, L. R., Nemtchinov, V., and Varanasi, P.: The HITRAN molecular spectroscopic database and HAWKS (HITRAN atmospheric workstation): 1996 edition, J. Quant. Spectrosc. Ra., 60, 665–710, 1998.

Rothman, L. S., Barbe, A., Benner, D. C., Brown, L. R., Camy-Peyret, C., Carleer, M. R., Chance, K., Clerbaux, C., Dana, V., Devi, V. M., Fayt, A., Flaud, J.-M., Gamache, R. R., Goldman, A., Jacquemart, D., Jucks, K. W., Lafferty, W. J., Mandin, J.-Y., Massie, S. T., Nemtchinov, V., Newnham, D. A., Perrin, A., Rinsland, C. P., Schroeder, J., Smith, K. M., Smith, M. A. H., Tang, K., Toth, R. A., Vander Auwera, J., Varanasi, P., and Yoshino, K.: The HITRAN molecular spectroscopic database: edition of 2000 including updates through 2001, J. Quant. Spectrosc. Ra., 82, 5–44, 2003.

Rothman, L. S., Jacquemart, D., Barbe, A., Chris Benner, D., Birk, M., Brown, L. R., Carleer, M. R., Chackerian Jr., C., Chance, K., Coudert, L. H., Dana, V., Devi, V. M., Flaud, J.-M., Gamache, R. R., Goldman, A., Hartmann, J.-M., Jucks, K. W., Maki, A. G.,

Mandin, J.-Y., Massie, S. T., Orphal, J., Perrin, A., Rinsland, C. P., Smith, M. A. H., Tennyson, J., Tolchenov, R. N., Toth, R. A., Vander Auwera, J., Varanasi, P., and Wagner, G.: The HITRAN 2004 molecular spectroscopic database, J. Quant. Spectrosc. Ra., 96, 139–204, 2005.

Ruhnke, R., Kouker, W., and Reddmann, T.: The influence of the OH+NO_2+M reaction on the NOy partitioning in the late arctic winter 1992/1993 as studied with KASIMA, J. Geophys. Res., 104, 3755–3772, 1999.

Sander, S. P., Friedl, R. R., Golden, D. M., Kurylo, M. J., Huie, R. E., Orkin, V. L., Moortgat, G. K., Ravishankara, A. R., Kolb, C. E., and Molina, M. J.: Chemical Kinetics and Photochemical Data for Use in Atmospheric Studies. Evaluation Number 14, JPL Publication 02-25, 2002.

Sander, R., Kerkweg, A., Jöckel, P., and Lelieveld, J.: Technical note: The new comprehensive atmospheric chemistry module MECCA, Atmos. Chem. Phys., 5, 445–450, doi:10.5194/acp-5-445-2005, 2005.

Sander, S. P., Friedl, R. R., Golden, D. M., Kurylo, M. J., Moortgat, G. K., Keller-Rudek, H., Wine, P. H., Ravishankara, A. R., Kolb, C. E., Molina, M. J., Finlayson-Pitts, B. J., Huie, R. E., Orkin, V. L.: Chemical Kinetics and Photochemical Data for Use in Atmospheric Studies. Evaluation Number 15, JPL Publication 06-2, Jet Propulsion Laboratory, Pasadena, USA, 2006.

Schneider, M., Blumenstock, T., Chipperfield, M. P., Hase, F., Kouker, W., Reddmann, T., Ruhnke, R., Cuevas, E., and Fischer, H.: Subtropical trace gas profiles determined by ground-based FTIR spectroscopy at Izaña (28° N, 16° W): Five-year record, error analysis, and comparison with 3-D CTMs, Atmos. Chem. Phys., 5, 153–167, doi:10.5194/acp-5-153-2005, 2005.

Schraner, M., Rozanov, E., Schnadt Poberaj, C., Kenzelmann, P., Fischer, A. M., Zubov, V., Luo, B. P., Hoyle, C. R., Egorova, T., Fueglistaler, S., Brönnimann, S., Schmutz, W., and Peter, T.: Technical Note: Chemistry-climate model SOCOL: version 2.0 with improved transport and chemistry/microphysics schemes, Atmos. Chem. Phys., 8, 5957–5974, doi:10.5194/acp-8-5957-2008, 2008.

Senten, C., De Mazière, M., Dils, B., Hermans, C., Kruglanski, M., Neefs, E., Scolas, F., Vandaele, A. C., Vanhaelewyn, G., Vigouroux, C., Carleer, M., Coheur, P. F., Fally, S., Barret, B., Baray, J. L., Delmas, R., Leveau, J., Metzger, J. M., Mahieu, E., Boone, C., Walker, K. A., Bernath, P. F., and Strong, K.: Technical Note: New ground-based FTIR measurements at Ile de La Réunion: observations, error analysis, and comparisons with independent data, Atmos. Chem. Phys., 8, 3483–3508, doi:10.5194/acp-8-3483-2008, 2008.

Sinnhuber, B.-M., Sheode, N., Sinnhuber, M., Chipperfield, M. P., and Feng, W.: The contribution of anthropogenic bromine emissions to past stratospheric ozone trends: a modelling study, Atmos. Chem. Phys., 9, 2863–2871, doi:10.5194/acp-9-2863-2009, 2009.

SPARC CCMVal: SPARC Report on the Evaluation of Chemistry-Climate Models, edited by: Eyring, V., Shepherd, T. G., Waugh, D. W., SPARC Report No. 5, WCRP-132, WMO/TD-No. 1526, http://www.atmosp.physics.utoronto.ca/SPARC, 2010.

Stiller, G. P., von Clarmann, T., Höpfner, M., Glatthor, N., Grabowski, U., Kellmann, S., Kleinert, A., Linden, A., Milz, M., Reddmann, T., Steck, T., Fischer, H., Funke, B., López-Puertas, M., and Engel, A.: Global distribution of mean age of stratospheric air from MIPAS SF6 measurements, Atmos. Chem. Phys., 8, 677–695, doi:10.5194/acp-8-677-2008, 2008.

Struthers, H., Bodeker, G. E., Smale, D., Rozanov, E., Schraner, M., and Peter, T.: Evaluating how photochemistry and transport determine stratospheric inorganic chlorine in coupled chemistry-climate models, Geophys. Res. Lett., 36, L04805, doi:10.1029/2008GL036403, 2009.

Sussmann, R. and Schäfer, K.: Infrared spectroscopy of tropospheric trace gases: combined analysis of horizontal and vertical column abundances, Appl. Optics, 36, 735–741, 1997.

Taylor, J. R., Wunch, D., Midwinter, C., Wiacek, A., Drummond, J. R., and Strong, K.: An extended intercomparison of simultaneous ground-based Fourier transform spectrometer measurements at the Toronto Atmospheric Observatory, J. Quant. Spectrosc. Ra., 109, 2244–2260, 2008.

Vigouroux, C., De Mazière, M., Demoulin, P., Servais, C., Hase, F., Blumenstock, T., Kramer, I., Schneider, M., Mellqvist, J., Strandberg, A., Velazco, V., Notholt, J., Sussmann, R., Stremme, W., Rockmann, A., Gardiner, T., Coleman, M., and Woods, P.: Evaluation of tropospheric and stratospheric ozone trends over Western Europe from ground-based FTIR network observations, Atmos. Chem. Phys., 8, 6865–6886, doi:10.5194/acp-8-6865-2008, 2008.

Wallace, L. and Livingston, W.: Spectroscopic observations of atmospheric trace gases over Kitt Peak, 3, Long-term trends of hydrogen chloride and hydrogen fluoride from 1978 to 1990, J. Geophys. Res., 96, 15513–15521, 1991.

Wallace, L., Livingston, W., and Hall, D. N. B.: A twenty-five year record of stratospheric hydrogen chloride, Geophys. Res. Lett., 24, 2363–2366, 1997.

Wallace, L., and Livingston, W. C.: Thirty-five year trend of hydrogen chloride amount above Kitt Peak, Arizona, Geophys. Res. Lett., 34, L16805, doi:10.1029/2007GL030123, 2007.

Washenfelder, R. A., Toon, G. C., Blavier, J.-F., Yang, Z., Allen, N. T., Wennberg, P. O., Vay, S. A., Matross, D. M., and Daube, B. C.: Carbon dioxide column abundances at the Wisconsin Tall Tower site, J. Geophys. Res.-Atmos., 111, D22305, doi:10.1029/2006JD007154, 2006.

Waugh, D. W., Strahan, S. E., and Newman, P. A.: Sensitivity of stratospheric inorganic chlorine to differences in transport, Atmos. Chem. Phys., 7, 4935–4941, doi:10.5194/acp-7-4935-2007, 2007.

Weatherhead, E. C., Reinsel, G. C., Tiao, G. C., Meng, X.-L., Choi, D., Cheang, W.-K., Keller, T., DeLuisi, J., Wuebbles, D. J., Kerr, J. B., Miller, A. J., Oltmans, S. J., and Frederick, J. E.: Factors affecting the detection of trends: Statistical considerations and applications to environmental data, J. Geophys. Res., 103, 17149–17161, 1998.

Wiacek, A., Taylor, J. R., Strong, K., Saari, R., Kerzenmacher, T. E., Jones, N., and Griffith, D. W. T.: Ground-based solar absorption FTIR spectroscopy: a novel optical design instrument at a new NDSC complementary station, characterization of retrievals and first results, J. Atmos. Ocean. Technol., 24, 432–448, 2007.

WMO (World Meteorological Organization): Scientific Assessment of Ozone Depletion: 2002, Global ozone research and monitoring project, Report No. 47, Geneva, Switzerland, 2003.

WMO (World Meteorological Organization): Scientific Assessment of Ozone Depletion: 2006, Global Ozone Research and Monitoring Project, Report No. 50, Geneva, Switzerland, 2007.

WMO (World Meteorological Organization): Scientific Assessment of Ozone Depletion: 2010, Global Ozone Research and Monitoring Project, Report No. 52, Geneva, Switzerland, 2011.

Wunch, D., Taylor, J. R., Fu, D., Bernath, P., Drummond, J. R., Midwinter, C., Strong, K., and Walker, K. A.: Simultaneous ground-based observations of O_3, HCl, N_2O, and CH_4 over Toronto, Canada by three Fourier transform spectrometers with different resolutions, Atmos. Chem. Phys., 7, 1275–1292, doi:10.5194/acp-7-1275-2007, 2007.

Zander, R., Roland, G., Delbouille, L., Saval, A., Farmer, C. B., and Norton, R. H.: Column abundance and the long-term trend of hydrogen chloride (HCl) above the Jungfraujoch station, J. Atmos. Chem., 5, 395–404, 1987.

Zander, R., Mahieu, E., Demoulin, P., Duchatelet, P., Roland, G., Servais, C., De Mazière, M., Reimann, S., and Rinsland, C. P.: Our changing atmosphere: Evidence based on long-term infrared solar observations at the Jungfraujoch since 1950, Sci. Total Environ., 391, 184–195, 2008.

Journal of Quantitative Spectroscopy & Radiative Transfer 151 (2015) 88–96

Contents lists available at ScienceDirect

Journal of Quantitative Spectroscopy & Radiative Transfer

journal homepage: www.elsevier.com/locate/jqsrt

CO_2 line-mixing database and software update and its tests in the 2.1 μm and 4.3 μm regions

J. Lamouroux [a], L. Régalia [b], X. Thomas [b], J. Vander Auwera [c], R.R. Gamache [d], J.-M. Hartmann [a,*]

[a] Laboratoire Interuniversitaire des Systèmes Atmosphériques (LISA), CNRS (UMR 7583), Universités Paris Est Créteil et Paris Diderot, Institut P.-S. Laplace, Université Paris Est Créteil, 94010 Créteil Cedex, France
[b] Groupe de Spectrométrie Moléculaire et Atmosphérique, UMR CNRS 7331, U.F.R. Sciences, URCA, B.P. 1039, 51687 Reims Cedex 2, France
[c] Service de Chimie Quantique et Photophysique, C.P. 160/09, Université Libre de Bruxelles, 50 Avenue F. D. Roosevelt, B-1050 Brussels, Belgium
[d] Department of Environmental, Earth, and Atmospheric Sciences, University of Massachusetts Lowell, Lowell, MA 01854, USA

ARTICLE INFO

Article history:
Received 9 July 2014
Received in revised form
16 September 2014
Accepted 17 September 2014
Available online 28 September 2014

Keywords:
CO_2
Line-mixing
Database

ABSTRACT

An update of the former version of the database and software for the calculation of CO_2–air absorption coefficients taking line-mixing into account [Lamouroux et al. J Quant Spectrosc Radiat Transf 2010;111:2321] is described. In this new edition, the data sets were constructed using parameters from the 2012 version of the HITRAN database and recent measurements of line-shape parameters. Among other improvements, speed-dependent profiles can now be used if line-mixing is treated within the first order approximation. This new package is tested using laboratory spectra measured in the 2.1 μm and 4.3 μm spectral regions for various pressures, temperatures and CO_2 concentration conditions. Despite improvements at 4.3 μm at room temperature, the conclusions on the quality of this update are more ambiguous at low temperature and in the 2.1 μm region. Further tests using laboratory and atmospheric spectra are thus required for the evaluation of the performances of this updated package.

© 2014 Elsevier Ltd. All rights reserved.

1. Introduction

It is now well known that obtaining accurate retrieval of CO_2 atmospheric amounts in the Earth's atmosphere from ground-based (TCCON [1]) or satellite-based instruments (OCO-2 [2,3], GOSAT [4]) requires [5] one to take line-mixing (LM) effects [6] into account. For example, OCO-2 aims to quantify and map the CO_2 sources and sinks. Achieving this goal requires a precision better than 0.3% [7] on the spectra calculation, placing strong constraints on the theoretical models and spectroscopic and line-shape parameters used. In the 1.6 μm and 2.1 μm regions retained by GOSAT and OCO-2, LM essentially affects the troughs between the (P and R) lines with significant effects on the retrieved CO_2 amounts for optically thick paths [5]. The spectral modifications due to LM are even stronger in Q branches (*e.g.* [8,9], and those therein) with various consequences for retrievals of atmospheric state parameters (*e.g.* [6,10–12]). It is thus obvious that, since line mixing affects most regions of CO_2 spectra this process must be accurately modeled for numerous remote sensing applications.

A first update [13] of the LM database and software of [14] was made based on spectroscopic parameters taken from the HITRAN 2008 [15] and the CDSDs [16,17]

* Corresponding author.
E-mail address: jean-michel.hartmann@lisa.u-pec.fr (J.-M. Hartmann).

http://dx.doi.org/10.1016/j.jqsrt.2014.09.017
0022-4073/© 2014 Elsevier Ltd. All rights reserved.

databases. It included previously missing line-shape parameters (air-induced pressure shifts, broadening coefficients by H_2O and their temperature dependence, isotopologue dependence, *etc*). The resulting package is included in the HITRAN 2012 [18] database and has been widely used for atmospheric remote sensing [11,19–25]. However, although bringing [5] large improvements over calculations neglecting LM effects in the R and P branches of $\Sigma-\Sigma$ bands, it still does not always reach [20] the better than 0.3% targeted accuracy. This may result from several limitations of the data and model used. Firstly, the speed dependence of the pressure-broadening (and pressure-shifting) coefficients was disregarded, an approximation now known to have non-negligible consequences [26–31]. Note that many other subtle effects on the line shape may occur for which numerous models have been proposed [6]. Nevertheless, as far as CO_2 (in air) is considered, the speed-dependent line-mixing [32] is the only one that can be implemented for large scale spectra calculations due to missing data for the other models. Secondly, *a priori* approximate CO_2–air line-broadening coefficients [33] were used that can now be replaced using recent experimental determination [26–28]. Thirdly, the vibrational dependence of the broadening coefficients and the self-broadening were not taken into account. The study of Ref. [20] indicates that addressing some of these limitations may bring improvements.

The present paper describes a new package, constructed using HITRAN 2012 and laboratory measurements, in which these previous limitations are fixed and the line positions and intensities are updated. For the test of this new package, measurements have been made for CO_2–air mixtures in the 2.1 μm and 4.3 μm spectral regions, at 223 K and room temperature. The remainder of this paper is divided as follows. Section 2 describes the experiments while the updates of the spectroscopic parameters and software are presented in Section 3. The tests of the new package using the laboratory spectra are presented and discussed in Section 4. The article ends with an overall discussion and concluding remarks in Section 5.

2. Experiments

2.1. Measurements at 4.3 μm

Unapodized transmission spectra of CO_2 (with natural isotopic abundances) diluted in air at room temperature, stabilized by an air-conditioning system, and at 223 K have been recorded between 2200 and 2420 cm^{-1} at the Université Libre de Bruxelles, at a resolution of 0.01 cm^{-1} (maximum optical path difference of 90 cm), using a Bruker IFS 120 to 125 h upgraded Fourier transform spectrometer. The instrument was fitted with a Tungsten source, an entrance aperture diameter of 1.70 mm (at room temperature) or 1.30 mm (at 223 K), a CaF_2 beamsplitter, a band-pass filter with a transmission range of about 2010–2450 cm^{-1} and a 77 K InSb detector. The CO_2 (99.8% stated purity) and dry air samples were purchased from Sigma Aldrich. Mixtures of CO_2 with air were directly prepared in the 19.7 ± 0.2 cm long double-jacketed stainless steel absorption cell used, fitted with CaF_2 windows and located inside the evacuated spectrometer. Sample pressures were measured using two MKS Baratron gauges model 690A, of 1000 and 10 Torr full-scale ranges. At 223 K, the temperature of the cell was stabilized using a constant flow of methanol cooled by an external NESLAB model ULT-80 cryostat. The total and CO_2 pressures, and temperatures are listed in the upper part of Table 1. At room temperature, the temperature of the cell was measured using two TSic 301 sensors (IST Innovative Sensor Technology; stated accuracy ± 0.3 K in the 10–90 °C range) fixed on the outer cell wall. The temperature of the cold cell was measured using line intensities in the 2–0 band of $^{12}C^{16}O$ (Matheson), recorded twice at the same conditions as the CO_2+air recording. Transmittances were generated for all the spectra using empty cell spectra recorded at the same instrumental conditions, except for the resolution set to 0.1 cm^{-1}, before and after the CO_2+air spectra. The spectra were calibrated by matching to HITRAN 2008 [15] about 40 line positions in the ν_3 band of $^{12}C^{16}O_2$, measured in low pressure (~0.007 hPa) spectra of carbon dioxide recorded at the same instrumental conditions as the CO_2+air spectra and interpolated 8 times, with RMS deviations $\sim 5–7 \times 10^{-5}$ cm^{-1}.

2.2. Measurements at 2.1 μm

Four spectra were recorded with the Connes' type FTS [34] built at GSMA [35,36]. This instrument has a 3-m maximum optical path difference that corresponds to a non-apodized resolution of 0.0017 cm^{-1}. All the spectra were recorded with the following optical setup: a Tungsten source, a SiO_2 beamsplitter, some lenses and windows in BaF_2 and two InSb detectors to improve the signal to noise ratio and to reject signal fluctuations of the source. We used a optical filter ahead each detector to select the recording spectral range. A 50-m long White cell [37] coupled to the FTS has been used to achieve a path length of 1603.5 ± 0.8 m, recording absorption path length meters. During all recordings the FTS was maintained under vacuum and the pressure and temperature of the gas inside the cell were continuously monitored. Pressures were measured with two MKS Baratron capacitance manometers and temperature was measured with platinum-resistance

Table 1
Spectra ranges, total and CO_2 pressures (in hPa), and temperature (in K) used for each measurement. The numbers between parentheses represent the absolute uncertainty in the units of the last digit quoted. The uncertainty on the pressure is conservatively set to 0.5% of reading. Peak-to-peak variations of the total pressure during the recording of the spectra were 10 to 25 times smaller.

Region	P(CO_2)	P(total)	*T*
2200–2420 cm^{-1}	10.08 (5)	1043 (5)	295 (1)
	5.18 (3)	1091 (5)	295 (1)
	2.504 (13)	1015 (5)	295 (1)
	5.28 (3)	1011 (5)	223 (2)
	2.425 (12)	1009 (5)	223 (2)
	1.299 (6)	1009 (5)	223 (2)
4760–4921 cm^{-1}	14.41 (7)	977 (5)	291 (1)
	10.12 (5)	974 (5)	291 (1)
	7.05 (3)	973 (5)	291 (1)
	4.00 (2)	975 (5)	291 (1)

thermometers placed on the absorption cell. The FTS's room was air-conditioned and we did not observe any variation of temperature during the recordings. To ensure stabilization of gas pressures and temperatures, spectra were recorded several hours after filling the gases into the absorption cell (first CO_2 and then air) to make the mixture. The experimental conditions for the four spectra, recorded between 4760 and 4921 cm^{-1} are given in Table 1.

3. Update of the line-mixing database and software

The structures of the present updates of the database and associated software are quite similar to the previous ones [13]. No changes were made to the Energy Corrected Sudden approximation model [38,39] used for the calculations of the line-mixing relaxation matrix. However several fields were added in the spectroscopic data files and new subroutines were built in order to take the speed dependence (SD) of the broadening coefficients into account. Consequently the software is not compatible with the former versions of the database and *vice versa*. Note, all narrowing of spectral line is attributed to speed-dependent collisional broadening and Dicke narrowing is not considered. This approximation is valid for the pressures considered in this study for which the Lorentz width is much larger than the Doppler one. Besides there is, to our knowledge, no self-consistent and sufficiently complete set of data to calculate Dicke narrowed speed-dependent CO_2 line shapes.

3.1. Update of the database

As before [13,14], there is a spectroscopic file (or two in the case of asymmetric isotopologues [14]) for each band of each isotopologue. This file provides, together with new data, the same information as the HITRAN 2012 database, the parameters effectively used being, for each line: the position σ_0, the intensity S (at 296 K), the lower state energy E'', the rotational level identification J' and J'', the air-broadening coefficient ${}^{air}\gamma_{Voigt}$ (at 296 K) and its temperature dependence exponent n^{air}, and the air-induced line shift ${}^{air}\delta_{Voigt}$ (at 296 K). Note that ${}^{air}\gamma_{Voigt}$ and ${}^{air}\delta_{Voigt}$ *must be used with a Voigt profile*. In addition to these, the spectroscopic data files provide, as before [13], the self-broadening coefficient ${}^{CO_2}\gamma_{Voigt}$ (at 296 K), the broadening coefficient ${}^{H_2O}\gamma_{Voigt}$ of CO_2 lines by H_2O (at 296 K) and its temperature dependence exponent n^{H_2O}. The new parameters provided by this update are the temperature dependence of the self-broadening coefficient, and the speed-dependent broadening coefficient by air (${}^{air}\gamma^0_{SDV}$), CO_2 (${}^{CO_2}\gamma^0_{SDV}$), water (${}^{H_2O}\gamma^0_{SDV}$), and the ratios ${}^{X}\alpha_{SDV} = {}^{X}\gamma^2_{SDV}/\ {}^{X}\gamma^0_{SDV}$ (both at 296 K) describing the speed dependence of the broadening coefficients through [40]

$$ {}^{X}\gamma(v) = {}^{X}\gamma^0_{SDV}\left(1 + {}^{X}\alpha_{SDV}\left[\left(\frac{v}{\tilde{v}}\right)^2 - \frac{3}{2}\right]\right), \quad (1) $$

where X is the collisional partner (*i.e.* air, CO_2 or H_2O) and v and $\tilde{v}$ are the speed and the mean speed respectively. Obviously, these broadening coefficients and ratios *must be used with speed-dependent profiles*.

The values of σ_0, S, E'', J' and J'', n^{air} and ${}^{CO_2}\gamma_{SDV}$ (see discussion below on the broadening parameters in HITRAN 2012) were directly taken from the HITRAN 2012 database but not those of ${}^{air}\delta_{Voigt}$, ${}^{CO_2}\gamma_{Voigt}$ and ${}^{air}\gamma_{Voigt}$. For ${}^{air}\delta_{Voigt}$, we have generated their values as described in [41] because comparisons with measurements (as done in [41]) show that better agreement is obtained than with the HITRAN values. Regarding the self- and air-broadening coefficients in HITRAN, they have been calculated as described in [42–44] using intermolecular potential parameters adjusted in order to reproduce the speed-dependent Voigt (SDV) values of Devi et al. [45]. They thus do not correspond to ${}^{air}\gamma_{Voigt}$ and ${}^{CO_2}\gamma_{Voigt}$, as would be expected according to the database choices and description, but to ${}^{air}\gamma^0_{SDV}$ and ${}^{CO_2}\gamma^0_{SDV}$. Due to this inconsistency, we chose to build new sets of broadening coefficients (except for ${}^{CO_2}\gamma^0_{SDV}$), following the following procedure.

First, the values of ${}^{air}\gamma^0_{SDV}$ have been generated at 296 K by averaging the measurements of Refs. [26,27] and [28] for the 30012-00001 and 30013-00001 bands up to rotational quantum numbers of $J'' \approx 50$. The measured values above $J'' \approx 50$ were not considered due to the large scatter on the various measurements. Inter comparisons of the air-broadening coefficients of these references yield an estimated uncertainty of 0.5%. In order to extend the set to higher J'' values, the measurements of Ref. [46], made for the 00011-00001 band and analyzed with a Voigt profile, have been used. After scaling (by a factor of 1.033) in order to obtain agreement with the first set for $J'' < 50$, they provide values of ${}^{air}\gamma^0_{SDV}$ up to $J'' \approx 80$. In the absence of any measurement for higher rotational quantum numbers, Complex Robert–Bonamy calculations [42] have been used up to $J'' \approx 130$ after a proper scaling to insure the continuity of the values with J''. The final set was then smoothed and interpolated as a function of $J''+J'$. The value of ${}^{air}\alpha_{SDV}$ was fixed to the average of the values given in [26,27] (${}^{air}\alpha_{SDV} = 0.11$) and was considered temperature and vibrationally independent due to lack of data. Note that, according to [26,27] there seems to be a line-to-line dependence of ${}^{air}\alpha_{SDV}$ (between 0.08 and 0.15 for J'' between 0 and 60) but, the latter being moderate and having second order consequences on calculated spectra, it was neglected. At this step we thus have a complete set of SDV parameters [*i.e.*, ${}^{air}\gamma^0_{SDV}(296K)$ and ${}^{air}\alpha_{SDV}$, see Eq. (1)] for ^{16}O $^{12}C^{16}O$–air transitions of the $3\nu_1+\nu_2$ band at 296 K. These values of ${}^{air}\gamma^0_{SDV}$ are plotted in Fig. 1 *vs* $J'+J''$ for each $J' \leftarrow J''$ rotational transition together with the measurements used to generate them and the HITRAN 2012 air-broadening coefficients. As can be seen, the scaled measurements of [46] are in good agreement with the other experimental determinations [26–28] at low and intermediate $J'+J''$. This validates the procedure used for the generation the values for high rotational quantum numbers. However, after scaling the measurements of [46] (and our final set of values) disagree with the data in HITRAN for $J'+J''$ greater than 80, the disagreement reaching about

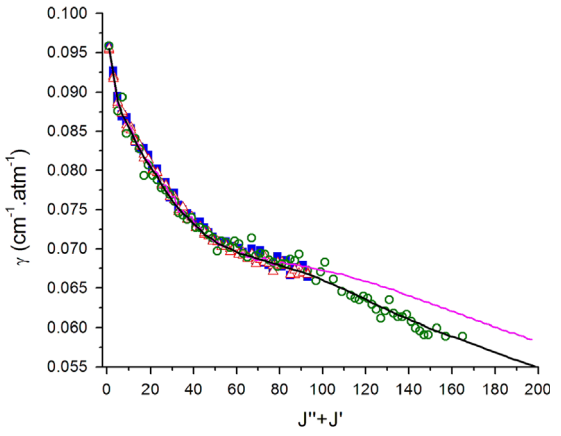

Fig. 1. Comparison of the generated (see text) speed-dependent Voigt air-broadening coefficients ${}^{air}\gamma^{0}_{SDV}$ (black line) with the HITRAN 2012 [18] data (magenta line) and the measurements of [46] (multiplied by 1.033) (open green circles), [28] (solid blue squares) and [26,27] (open red triangles). The broadening coefficients for both the 30012 and 30013 bands are shown for these two last references. (For interpretation of the references to color in this figure legend, the reader is referred to the web version of this article.)

5% for J'' around 80. Hence, one expects that using the HITRAN broadening coefficients will lead to significant deviations between calculated and experimental spectra, a result confirmed in Section 4.

Recall that the values constructed as explained above are for lines of the $3\nu_1+\nu_2$ band of $^{16}O^{12}C^{16}O$ in air. In order to complete the database, the half-widths for any other band of any isotopologue were then generated using the vibrational dependence predictions from Ref. [42,47] and the isotopologue dependence described in Appendix A of Ref. [13].

Starting from the now known values of ${}^{air}\gamma^{0}_{SDV}$, those of ${}^{air}\gamma_{Voigt}$ have been generated for all transitions by scaling ${}^{air}\gamma^{0}_{SDV}$ by 0.985 which is the line-averaged ratio of the Voigt to SDV air-broadening coefficients given in [28].

In order to account for the H_2O (and/or CO_2) broadening of CO_2 lines one needs to know the value of ${}^{H_2O}\gamma_{Voigt}$, ${}^{H_2O}\gamma^{0}_{SDV}$, ${}^{CO_2}\gamma_{Voigt}$, ${}^{CO_2}\gamma^{0}_{SDV}$ and the speed-dependence parameters ${}^{H_2O}\alpha_{SDV}$ and ${}^{CO_2}\alpha_{SDV}$ for Eq. (1). For the self-broadening, the values of ${}^{CO_2}\gamma^{0}_{SDV}$ were taken from HITRAN 2012 and ${}^{CO_2}\alpha_{SDV}={}^{air}\alpha_{SDV}$, *i.e.* ${}^{CO_2}\alpha_{SDV}=0.11$ [26,27] was assumed in the absence of relevant data. Note that this assumption was also made in [26,27]. From ${}^{CO_2}\gamma^{0}_{SDV}$, the corresponding Voigt values were obtained by a scaling factor of 0.978, a value determined from the average of the Voigt to SDV half-widths ratios from [29]. For water broadening, the values of ${}^{H_2O}\gamma_{Voigt}$ were taken from the previous update [13]. Due to lack of data, the SDV values ${}^{H_2O}\gamma^{0}_{SDV}$ were generated using the same average of Voigt to SDV broadening coefficients ratios than for air-broadening, *i.e.* 0.985, and ${}^{H_2O}\alpha_{SDV}=0.11$. Considering the relatively small contribution of CO_2–H_2O and CO_2–CO_2 collisions in the atmosphere, all these approximations are of negligible consequences.

Finally, the temperature dependence of self (n^{CO_2}) and water (n^{H_2O}) broadening were taken from [42] and [13] respectively. Note that n^{CO_2} was calculated for a temperature range of 200–350 K. For the three collisional partners, the temperature dependence of the Voigt and the speed-dependent Voigt broadening coefficients were assumed to be the same. Finally, the speed-dependence parameters α_{SDV} were considered temperature independent.

In addition to the spectroscopic files, the CO_2–air relaxation matrix (RM) files [13,14] have been updated. In HITRAN 2012, the lower state vibrational angular momentum ℓ''_2 and rotational quantum number J'' reach the values of 8 and 128 respectively, whereas the former package was limited to $\ell''_2=5$ and $J''=124$ only. Consequently, additional RM files have been generated (as explained in [14]) and added with all data extended up to $J''=128$. Note that, in the absence of a model for CO_2–H_2O, the relaxation matrices for CO_2–air are used for this system. Although a model exists for pure CO_2 [48] the same approximation is made, for simplicity, for CO_2–CO_2. These assumptions are obviously of negligible consequences due to the relatively small amounts of CO_2 and H_2O in air and to the relatively small effects of LM.

The file (BandInfo.dat) giving general information on the bands still provides the band identification, its overall integrated intensity, the maximum value of J'' for each branch, and the minimum and maximum wavenumbers between which the band contribution will be computed by the associated software (determined as described in [13]). The new database now contains more than 5300 bands (or sub-bands) from 10 isotopologues.

3.2. Update of the (FORTRAN) software

The partition functions have been updated using the most recent version of TIPS [49], which enables calculation for the 10 CO_2 isotopologues included in HITRAN 2012.

Changes have been made in order to take the self-broadening of CO_2 into account. This was done, despite its effect is negligible for the Earth atmosphere, in order to enable comparisons with laboratory measurements in which the relative CO_2 amount is not fully negligible (as in the ones used here, see Table 1).

The software has also been updated in order to offer the user the possibility to take speed-dependent effects into account. A new logical variable ("MixSDV") has been introduced as an input choice for the user who can set it to "false" or "true" in order to perform purely Voigt and LM calculations disregarding speed dependence effects (using ${}^{air}\gamma_{Voigt}$, ${}^{CO_2}\gamma_{Voigt}$, ${}^{H_2O}\gamma_{Voigt}$) or taking the latter into account (using ${}^{air}\gamma^{0}_{SDV}$ and ${}^{air}\alpha_{SDV}$, ${}^{CO_2}\gamma^{0}_{SDV}$ and ${}^{CO_2}\alpha_{SDV}$, ${}^{H_2O}\gamma^{0}_{SDV}$ and ${}^{H_2O}\alpha_{SDV}$) respectively. The SDV profile, first introduced by [50], was added to the software using the subroutine described in Ref. [51], built using the analytical development of [52,53]. Note that, since using speed-dependent relaxation matrices would be extremely costly, even when the speed dependence is restricted to the diagonal (broadening coefficients) terms, MixSDV="true" implies that the first order approach [14,54] (based on the coefficients Y_l) is automatically used. In this case, the "Mixfull" logical variable that conditions the full relaxation matrix calculation is thus automatically set to "false" by the software.

4. Tests of the update using laboratory spectra at 2.1 μm and 4.3 μm

4.1. Calculations and spectra analysis

For comparisons with each measured spectrum, three types of calculations have been performed. The first two ones considers LM effects, using either the database+software of Ref. [13] (LM but no SD) or the updated package (LM and SD). As the full relaxation matrix cannot be easily used with the SD broadening coefficients and in order to perform meaningful comparisons, all calculations were carried within the first order treatment of line-mixing using the associated coefficients Y_l [14,54]. The third type of calculation uses the present updated package and neglects LM (SDV).

Tests show that comparisons between measured spectra and those directly calculated for the stated experimental conditions lead to significant residuals. Their analysis indicates that they are essentially due to errors in the intensities of the lines and/or uncertainties on the CO_2 amount in the experimental samples but not to the line-shape parameters or the line-mixing model. These errors can be estimated to be 5% maximum, however whether this falls within the cumulated uncertainties on the measurement and spectroscopic data is a difficult question to answer due to the considerate amount of lines and bands contributing to the spectra. Since line-by-line empirical changes to the spectroscopic data are obviously beyond the scope of this paper and in order to test the quality of the spectral shape modeling, the CO_2 abundance was floated. It has been adjusted together with linear baselines for the 0% and 100% of transmission levels through least square fits of the calculated spectrum to the measured one. Due to the significant contribution of $^{16}O^{13}C^{16}O$ in the spectra, its amount was also fitted in addition to that of all other isotopologues. For these isotopologues, the natural relative isotopic ratios were assumed. Due to strong absorption of water in the 2.1 μm region (where laboratory air was used as buffer gas), its contribution was taken into account and its amount was fitted (note that the H_2O broadening of CO_2 lines was then taken into account). This nevertheless leaves significant residuals (likely due to spectroscopic knowledge) in the vicinity of H_2O lines. In order not to mask errors in the calculations of the CO_2 spectra, the spectral points where the H_2O transmittance was less than 0.91% have been removed, yielding a few "holes" in the corresponding plots but without significant consequences for the test of the CO_2 calculations. Finally, instrumental effects arising from the truncation of the interferogram and finite iris diameter were included as fixed contributions, through the proper instrument function.

4.2. Tests of the update near 4.3 μm

As a first test, three calculations taking LM effects into account but disregarding speed-dependence have been carried for the conditions of the most absorbing spectrum (the first in Table 1). The first one uses the former version of the database/software [13] while the second one uses the present update with the air-broadening coefficients from HITRAN 2012. Since, as mentioned above the latter actually correspond to $^{air}\gamma_{SDV}$ they were scaled by 0.985 [to generate $^{air}\gamma_{Voigt}$ (see Section 3.1)] for the third calculation. The measured-calculated spectra residuals from the fits using these three calculations are plotted in Fig. 2a–c. Before discussing the results, note that the $^{16}O^{12}C^{16}O$ and $^{16}O^{13}C^{16}O$ concentrations fitted from the three calculations are all about 6% larger and less than 2% smaller, respectively, than those expected and given in Table 1. This may result from experimental errors in the determination of the relatively small (about 1%) CO_2 amount in the mixture but also from the input spectroscopic data used.

Fig. 2b and c shows that the maximum amplitudes of the residuals with the HITRAN 2012 broadening coefficients are about twice larger than those obtained when using the former version of the package. This is particularly obvious above 2375 cm^{-1}, a region where lie high J'' lines ($J'' > 50$), whose broadening coefficients are significantly overestimated (see Fig. 1). Despite an improvement for this region when the scaled broadening coefficients are used (Fig. 2d), the measured-calculated deviations are still larger than with the former set of broadening coefficients [13].

A first test of the new package is presented in Fig. 3. The most absorbing experimental spectrum recorded at room temperature (294.8 K) is presented in Fig. 3a whereas the measured-calculated deviations obtained with a SD+LM and a SDV (*i.e.* no LM effects) profile are plotted in Fig. 3b

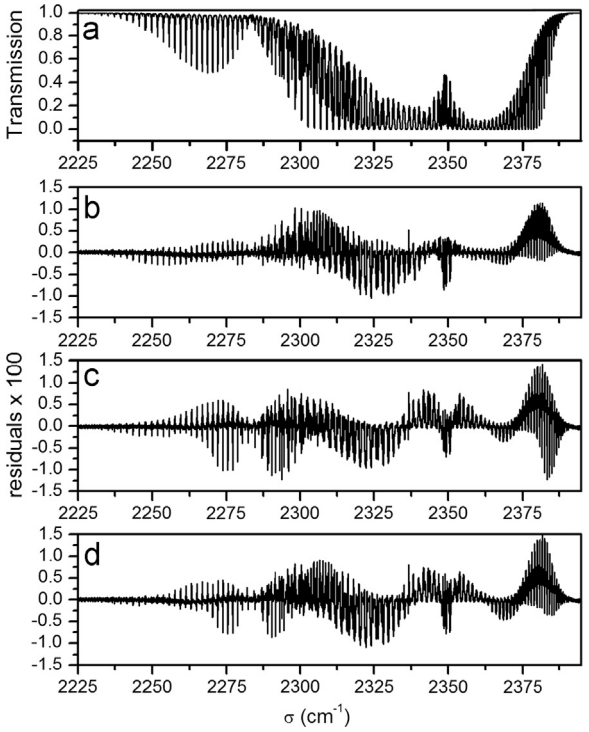

Fig. 2. (a) Measured transmission for the conditions of the first spectrum in Table 1 and measured-calculated residuals using (b) the former version of our database [13], (c) the HITRAN 2012 database and (d) the HITRAN 2012 database with air-broadening coefficients scaled by 0.985. All the calculations take line-mixing effects into account but disregard the speed dependence.

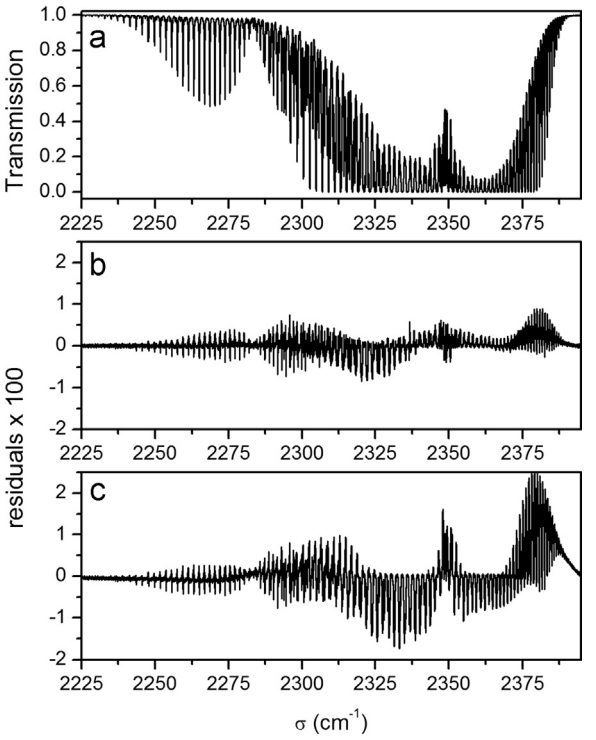

Fig. 3. (a) Measured transmission the conditions of the first spectrum in Table 1 and measured-calculated residuals using the new version of our database and software (b) with and (c) without line-mixing effects. All the calculations were carried taking speed dependence into account.

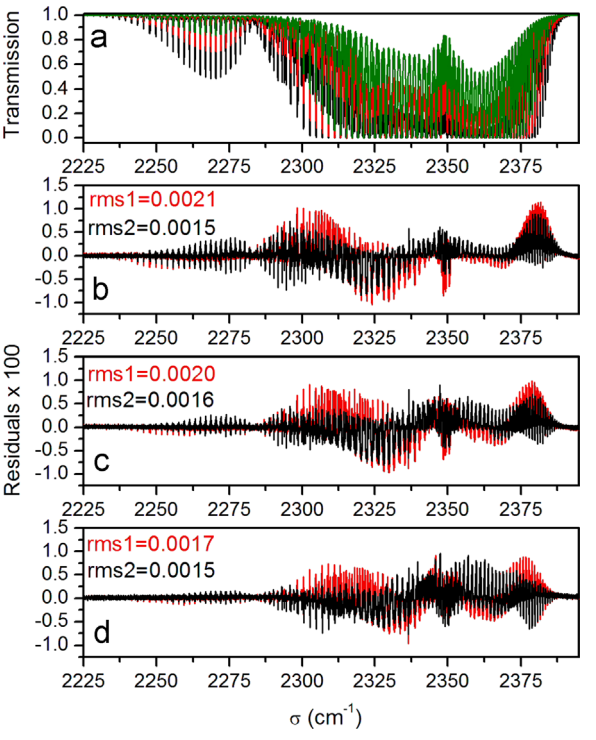

Fig. 4. (a) Room temperature (294.8 K) measured transmissions in the ν_3 band region for 0.97% (black curve), 0.48% (red curve) and 0.25% (olive curve) CO_2 in air at room temperature. Differences between these measured spectra and those calculated with the former (LM but no SD, red curves) and the new (SD+LM, black curves) version of our database and software are respectively plotted from (b) to (d), in order of highest to lowest to CO_2 molar fractions. The root mean square values are given for the former (*rms1*) and the new (*rms2*) calculations. (For interpretation of the references to color in this figure legend, the reader is referred to the web version of this article.)

and c respectively. The large residuals obtained when LM is neglected, which demonstrate their importance especially near the ν_3 band head (around 2380 cm^{-1}), are largely reduced when LM is taken into account. Discrepancies nevertheless remain in the whole absorption domain, even in regions that are not affected by LM, such as the P-branch of the ν_3 band of $^{16}O^{13}C^{16}O$ (between 2225 and 2280 cm^{-1}), a result for which we have no explanations yet and that will be discussed later.

The consequences of the present update can be tested by comparisons of the measured-calculated deviations obtained with the former and new version of the package. The obtained residuals are plotted for three different CO_2 concentrations in Fig. 4b–d. As can be seen, the use of the new package reduces the residuals on average, except in the $^{16}O^{13}C^{16}O$ region (2225–2280 cm^{-1}, as already shown in Fig. 2) where they indicate that the broadening coefficients used are too large. However the improvements brought by this update are smaller with decreasing CO_2 concentration. These results are confirmed by the analysis of the root mean square (*rms*) deviation between measured and calculated transmissions τ. The latter, were calculated over the spectral range of the plots from:

$$rms = \sqrt{\frac{1}{N}\sum_{i=1}^{N}\left((\tau_i^{meas}-\tau_i^{calc})^2\right)}, \quad (2)$$

and the values obtained for the calculations using the former (*rms1*) and the present update (*rms2*) are given in Fig.4. For all calculations *rms2* are the smallest, and the relative errors between *rms1* and *rms2* decrease as the CO_2 amount decreases. In all the cases, the values of the *rms* are about twice smaller than if LM effects are neglected.

Similar comparisons at low temperature (223 K), plotted in Fig. 5, lead to similar conclusions although the improvements are almost negligible as shown by the values of *rms1* and *rms2* given in the figure. This may be due to a compensation between errors on the room temperature air-broadening coefficients and on their temperature dependences.

In order to test the importance of speed dependence effects, LM calculations have been carried using the present update with (using ${}^{air}\gamma^0_{SDV}$ and ${}^{air}\alpha_{SDV}$, ${}^{CO_2}\gamma^0_{SDV}$ and ${}^{CO_2}\alpha_{SDV}$) and without speed dependence (using ${}^{air}\gamma_{Voigt}$ and ${}^{CO_2}\gamma_{Voigt}$). The results of this exercise are presented in Fig. 6 for the most absorbing spectrum (the first of Table 1). As can be seen, the introduction of SD yields an overall slight improvement although significant residuals remains that will be discussed in Section 5.

4.3. Tests of the update at 2.1 μm

Tests of the former and new packages, similar to those presented in the previous section, were also made in the

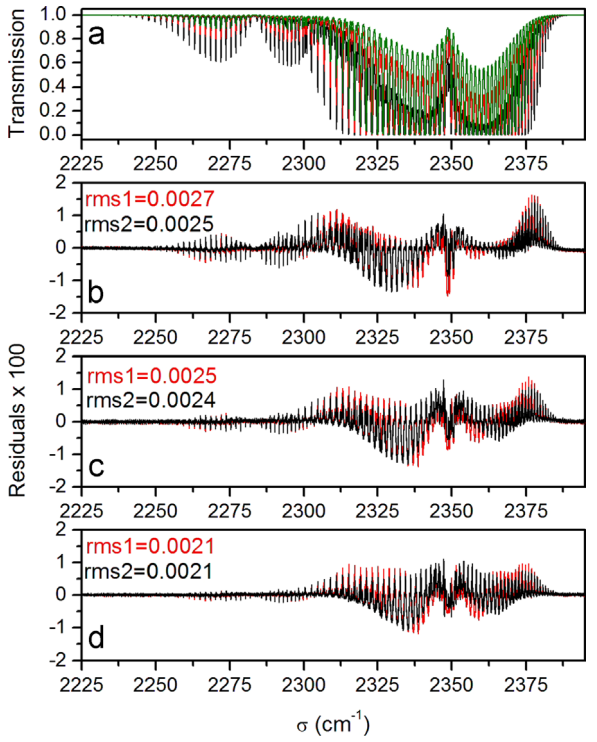

Fig. 5. Same as Fig. 4 for (b) 0.52%, (c) 0.24% and (d) 0.13% CO_2 in air at 223 K.

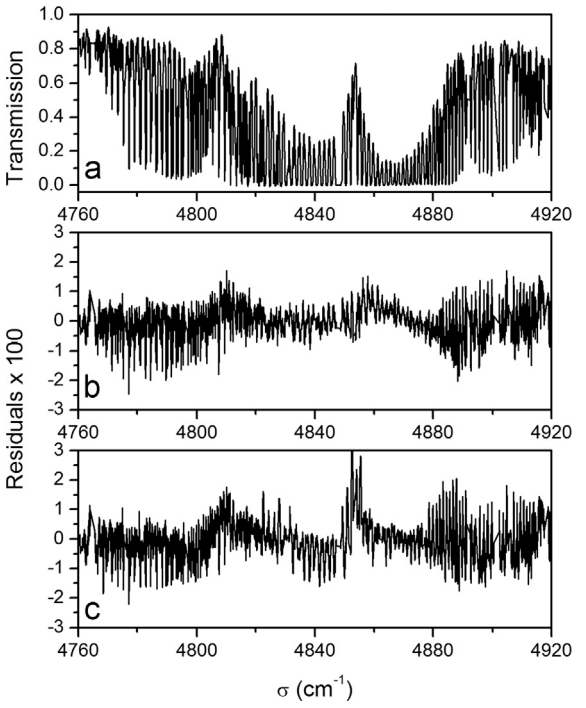

Fig. 7. Same as Fig. 3 for 1.5% CO_2 in air at 291 K. The "holes" in the experimental spectra and the residuals correspond to strong absorbing lines of H_2O.

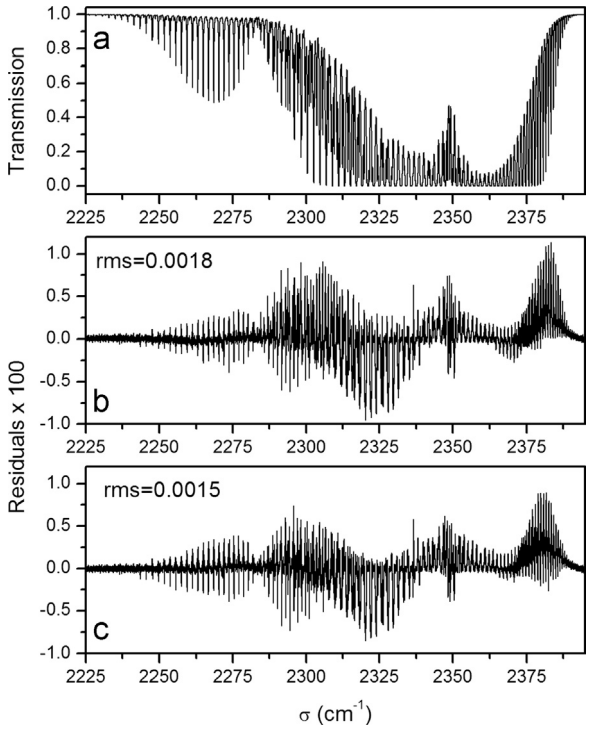

Fig. 6. (a) Room temperature (294.8 K) measured transmissions in the ν_3 band region for 0.97% (black curve) CO_2 in air at room temperature and comparison of the residuals obtained without (b) and with (c) speed dependence.

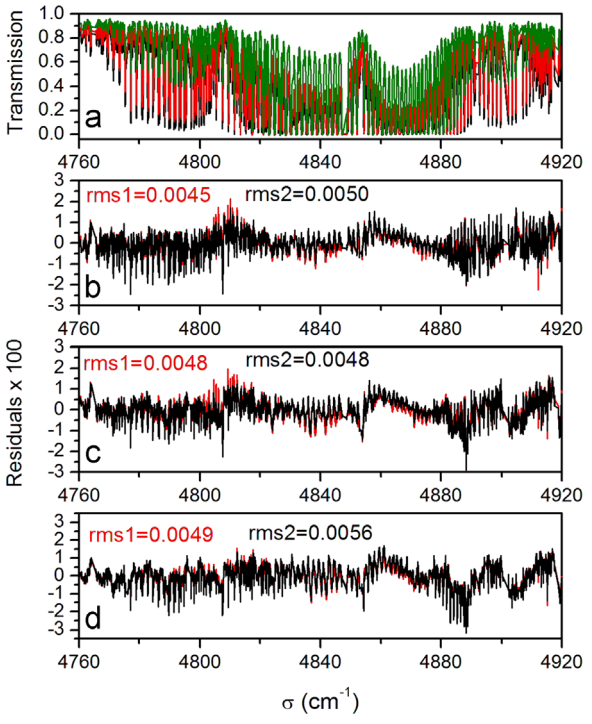

Fig. 8. Same as Fig. 4 for (b) 1.47%, (c) 1.04% and (d) 0.41% CO_2 in air at 291 K.

2.1 μm region at room temperature (291 K). An example of the results obtained is plotted in Fig. 7 where the residuals obtained with and without inclusion of LM effects are shown for the most absorbing spectrum (see Table 1). Again, many of the residuals are likely due to erroneous spectroscopic parameters (including those for H_2O lines). Nevertheless, as for the 4.3 μm region, neglecting LM effects leads to larger errors, with residuals in the affected regions (4820–4900 cm^{-1}) about twice larger than when LM is taken into.

The influence of the update can be seen in Fig. 8 where results obtained with the former and new versions are plotted. Contrary to the 4.3 μm region, the comparison of the residuals do not allow us to draw a clear conclusion about the improvements brought by the update, a result confirmed by the *rms* analysis. Possible reasons for this difference with the 4.3 μm region are the poorer signal to noise ratio and spectroscopic knowledge and the perturbing contribution of H_2O lines.

5. Discussion and conclusion

A new update of the database+software package for the calculation of the absorption coefficient of CO_2 (in air) infrared bands, that takes line-mixing effects into account, is proposed. Due to some inconsistency of the HITRAN 2012 line shape parameters, new sets of pressure broadening (and shifting) coefficients have been generated, based on accurate measurements from the literature. Furthermore, the speed dependence of the broadening is now included. In order to test this new package, transmission spectra have been recorded for various conditions in the 2.1 and 4.3 μm regions. Their analysis shows that, with respect to the former version, the proposed new data+software update brings improvements at 4.3 μm for room temperature conditions. This is much less obvious at 223 K and in the 2.1 μm region even though no degradation is observed. While much better agreement with measurements is obtained than when line-mixing is not taken into account, residuals of typically $\pm 0.5\%$ remain. This error is higher than that targeted for the satellite-based remote sensing of atmospheric CO_2 [3,4,7]. When compared with the results of [26–28] those of the present study raise a number of questions since our residuals are much larger than those in these references. A very likely explanation for part of this difference is inconsistencies in the line intensities (and positions) of the various bands contributing to our spectra. The differences in the line-mixing models may also be invoked although tests indicate that this should have small consequences. In any case, these explanations do not apply to the ν_3 band lines $^{16}O^{13}C^{16}O$ in our spectra since they are not affected by LM and since this isotopologue amount was adjusted. For these transitions, the analysis of the residuals shows that our calculation leads to lines that are too broad although their shapes were modeled with data from [26–28]. This points out a clear inconsistency between these studies and ours for which we have no explanation at this time. There is thus a strong need for further tests of the proposed new package using laboratory and atmospheric spectra for various spectral domains and experimental conditions of pressure and temperature. Since it will soon be available to the scientific community, the authors of the present work are looking forward to the feedback information that will be brought by future users.

Acknowledgments

J.L. thanks the French *Agence Nationale pour la Recherche* (ANR, France) for financial support through the Project ASGGRS (ANR-12-PDOC-0012-01). JVA acknowledges financial support from the Belgian Federal Science Policy Office (contract SD/CS/07A, Advanced exploitation of Ground-based measurements for Atmospheric Chemistry and Climate – II) and the *Groupe de Recherche International* (GDRI) HiResMIR (High resolution microwave infrared & Raman spectroscopy for molecules of atmospheric, planetologic and astrophysical interest). RRG is pleased to acknowledge support of this research by the National Science Foundation through Grant no. AGS-1156862.

References

[1] Wunch D, Toon GC, Blavier J-FL, Washenfelder RA, Notholt J, Connor BJ, et al. The total carbon column observing network. Philos Trans R Soc A: Math Phys Eng Sci 2011;369:2087–112.
[2] Crisp D, Atlas RM, Breon FM, Brown LR, Burrows JP, Ciais P, et al. The Orbiting Carbon Observatory (OCO) mission. Adv Space Res 2004;34:700–9.
[3] Crisp D, Miller C. The need for atmospheric carbon dioxide measurements from space: contributions from a rapid reflight of the orbiting carbon observatory; 2009⟨http://www.nasa.gov/pdf/363474main_OCO_Reflightpdf⟩.
[4] Yokomizo M. Greenhouse gases Observing SATellite (GOSAT) ground systems. FUJITSU Sci Tech J. 2008;44:410–7.
[5] Hartmann J-M, Tran H, Toon GC. Influence of line mixing on the retrievals of atmospheric CO_2 from spectra in the 1.6 and 2.1 μm regions. Atmos Chem Phys 2009;9:7303–12.
[6] Hartmann J-M, Boulet C, Robert D. Collisional effects on molecular spectra: laboratory experiments and models, consequences for applications. Amsterdam: Elsevier; 2008.
[7] Miller CE, Brown LR, Toth RA, Benner DC, Devi VM. Spectroscopic challenges for high accuracy retrievals of atmospheric CO_2 and the Orbiting Carbon Observatory (OCO) experiment. CR Phys Acad Sci 2005;6:876–87.
[8] Rodrigues R, Jucks KW, Lacome N, Blanquet G, Walrand J, Traub WA, et al. Model, software, and database for computation of line-mixing effects in infrared Q branches of atmospheric CO_2:I. Symmetric isotopomers. J Quant Spectrosc Radiat Transf 1999;61:153–84.
[9] Jucks KW, Rodrigues R, Le Doucen R, Claveau C, Traub WA, Hartmann J-M. Model, software, and database for computation of line-mixing effects in infrared Q branches of atmospheric CO_2: II Minor and asymmetric isotopomers. J Quant Spectrosc Radiat Transf 1999;63:31–48.
[10] Rinsland CP, Mahieu E, Demoulin P, Zander R, Servais C, Hartmann J-M. Decrease of the carbon tetrachloride (CCl4) loading above Jungfraujoch, based on high resolution infrared solar spectra recorded between 1999 and 2011. J Quant Spectrosc Radiat Transf 2012;113:1322–9.
[11] Alvarado MJ, Payne VH, Mlawer EJ, Uymin G, Shephard MW, Cady-Pereira KE, et al. Performance of the Line-By-Line Radiative Transfer Model (LBLRTM) for temperature, water vapor, and trace gas retrievals: recent updates evaluated with IASI case studies. Atmos Chem Phys 2013;13:6687–711.
[12] Niro F, Brizzi G, Carlotti M, Papandrea E, Ridolfi M. Precision improvements in the geo-fit retrieval of pressure and temperature from MIPAS limb observations by modeling CO_2 line- mixing. J Quant Spectrosc Radiat Transf 2007;103:14–26.
[13] Lamouroux J, Tran H, Laraia AL, Gamache RR, Rothman LS, Gordon IE, et al. Updated database plus software for line-mixing in CO_2

infrared spectra and their test using laboratory spectra in the 1.5–2.3 μm region. J Quant Spectrosc Radiat Transf 2010;111:2321–31.
[14] Niro F, Jucks K, Hartmann J-M. Spectra calculations in central and wing regions of IR bands. IV: software and database for the computation of atmospheric spectra. J Quant Spectrosc Radiat Transf 2005;95:469–81.
[15] Rothman LS, Gordon IE, Barbe A, Benner DC, Bernath PF, Birk M, et al. The HITRAN 2008 molecular spectroscopic database. J Quant Spectrosc Radiat Transf 2009;110:533–72.
[16] Tashkun SA, Perevalov VI, Teffo JL. CDSD-296, the high-precision carbon dioxide spectroscopic databank: version for atmospheric applications. In: Perrin A, Ben Sari-Zizi N, Demaison J, editors. Remote sensing of the atmosphere for environmental security. Netherlands: Springer; 2006. p. 161–9.
[17] Tashkun SA, Perevalov VI, Teffo JL, Bykov AD, Lavrentieva NN. CDSD-1000, the high-temperature carbon dioxide spectroscopic databank. J Quant Spectrosc Radiat Transfer 2003;82:165–96.
[18] Rothman LS, Gordon IE, Babikov Y, Barbe A, Chris Benner D, Bernath PF, et al. The HITRAN2012 molecular spectroscopic database. J Quant Spectrosc Radiat Transf 2013;130:4–50.
[19] Butz A, Guerlet S, Hasekamp OP, Kuze A, Suto H. Using ocean-glint scattered sunlight as a diagnostic tool for satellite remote sensing of greenhouse gases. Atmos Meas Tech 2013;6:2509–20.
[20] Thompson DR, Chris Benner D, Brown LR, Crisp D, Malathy Devi V, Jiang Y, et al. Atmospheric validation of high accuracy CO_2 absorption coefficients for the OCO-2 mission. J Quant Spectrosc Radiat Transf 2012;113:2265–76.
[21] Newman SM, Larar AM, Smith WL, Ptashnik IV, Jones RL, Mead MI, et al. The joint airborne IASI validation experiment: an evaluation of instrument and algorithms. J Quant Spectrosc Radiat Transf 2012;113:1372–90.
[22] Long DA, Hodges JT. On spectroscopic models of the O_2 A-band and their impact upon atmospheric retrievals. J Geophy Res Atmos 2012;117:D12309.
[23] Oshchepkov S, Bril A, Yokota T, Wennberg PO, Deutscher NM, Wunch D, et al. Effects of atmospheric light scattering on spectroscopic observations of greenhouse gases from space. Part 2: Algorithm intercomparison in the GOSAT data processing for CO_2 retrievals over TCCON sites. J Geophys Res Atmos 2013;118:1493–512.
[24] Yoshida Y, Ota Y, Eguchi N, Kikuchi N, Nobuta K, Tran H, et al. Retrieval algorithm for CO_2 and CH_4 column abundances from short-wavelength infrared spectral observations by the Greenhouse gases observing satellite. Atmos Meas Tech 2011;4:717–34.
[25] Morino I, Uchino O, Inoue M, Yoshida Y, Yokota T, Wennberg PO, et al. Preliminary validation of column-averaged volume mixing ratios of carbon dioxide and methane retrieved from GOSAT short-wavelength infrared spectra. Atmos Meas Tech 2011;4:1061–76.
[26] Devi VM, Benner DC, Brown LR, Miller CE, Toth RA. Line mixing and speed dependence in CO_2 at 6348 cm^{-1}: positions, intensities, and air- and self-broadening derived with constrained multispectrum analysis. J Mol Spectrosc 2007;242:90–117.
[27] Devi VM, Benner DC, Brown LR, Miller CE, Toth RA. Line mixing and speed dependence in CO_2 at 6227.9 cm^{-1}: constrained multispectrum analysis of intensities and line shapes in the 30013←00001 band. J Mol Spectrosc 2007;245:52–80.
[28] Predoi-Cross A, Liu W, Holladay C, Unni AV, Schofield I, McKellar ARW, et al. Line profile study of transitions in the 30012←00001 and 30013←00001 bands of carbon dioxide perturbed by air. J Mol Spectrosc 2007;246:98–112.
[29] Predoi-Cross A, Unni AV, Liu W, Schofield I, Holladay C, McKellar ARW, et al. Line shape parameters measurement and computations for self-broadened carbon dioxide transitions in the 30012←00001 and 30013←00001 bands, line mixing, and speed dependence. J Mol Spectrosc 2007;245:34–51.
[30] Hartmann J-M, Tran H, Ngo NH, Landsheere X, Chelin P, Lu Y, et al. *Abinitio* calculations of the spectral shapes of CO_2 isolated lines including non-Voigt effects and comparisons with experiments. Phys Rev A 2013;87:013403.
[31] Larcher G, Tran H, Schwell M, Chelin P, Landsheere X, Hartmann J-M, et al. CO_2 isolated line shapes by classical molecular dynamics simulations: influence of the intermolecular potential and comparison with new measurements. J Chem Phys 2014;140:084308.
[32] Ciuryło R, Pine AS. Speed-dependent line mixing profiles. J Quant Spectrosc Radiat Transf 2000;67:375–93.
[33] Rothman LS, Gamache RR, Tipping RH, Rinsland CP, Smith MAH, Benner DC, et al. The HITRAN molecular database: Editions of 1991 and 1992. J Quant Spectrosc Radiat Transf 1992;48:469–507.
[34] Connes P, Michel G. Astronomical Fourier spectrometer. Appl Opt 1975;14:2067–84.
[35] Plateaux JJ, Barbe A, Delahaigue A. Reims high resolution Fourier transform spectrometer. Data reduction for ozone. Spectrochim Acta Part A: Mol Biomol Spectrosc 1995;51:1153–69.
[36] Régalia L, Oudot C, Thomas X, Von der Heyden P, Decatoire D. FTS improvements and connection with a long white cell. Application: $H_2{}^{16}O$ intensity measurements around 1200 cm^{-1}. J Quant Spectrosc Radiat Transf 2010;111:826–42.
[37] White JU. Long optical paths of large aperture. J Opt Soc Am 1942;32:285.
[38] Niro F. Etudes théorique et expérimentale des profils collisionnels dans les centres et ailes des bandes infrarouges de CO_2. Applications à la simulation et à l'inversion de spectres atmosphériques. Paris: Université d'Orsay; 2003.
[39] Niro F, Boulet C, Hartmann JM. Spectra calculations in central and wing regions of CO_2 IR bands between 10 and 20 μm. I: model and laboratory measurements. J Quant Spectrosc Radiat Transf 2004;88:483–98.
[40] Rohart F, Mader H, Nicolaisen H-W. Speed dependence of rotational relaxation induced by foreign gas collisions: studies on CH_3F by millimeter wave coherent transients. J Chem Phys 1994;101:6475–86.
[41] Hartmann J-M. A simple empirical model for the collisional spectral shift of air-broadened CO_2 lines. J Quant Spectrosc Radiat Transf 2009;110:2019–26.
[42] Gamache RR, Lamouroux J. Predicting accurate line shape parameters for CO_2 transitions. J Quant Spectrosc Radiat Transf 2013;130:158–71.
[43] Lamouroux J, Gamache RR, Laraia AL, Hartmann J-M, Boulet C. Semiclassical calculations of half-widths and line shifts for transitions in the 30012←00001 and 30013←00001 bands of CO_2. II: Collisions with O_2 and air. J Quant Spectrosc Radiat Transf 2012;113:991–1003.
[44] Lamouroux J, Gamache RR, Laraia AL, Hartmann J-M, Boulet C. Semiclassical calculations of half-widths and line shifts for transitions in the 30012←00001 and 30013←00001 bands of CO_2. III: Self collisions. J Quant Spectrosc Radiat Transf 2012;113:1536–46.
[45] Devi VM, Benner DC, Miller CE, Predoi-Cross A. Lorentz half-width, pressure-induced shift and speed-dependent coefficients in oxygen-broadened CO_2 bands at 6227 and 6348 cm^{-1} using a constrained multispectrum analysis. J Quant Spectrosc Radiat Transf 2010;111:2355–69.
[46] Gulidova OS, Asfin RE, Grigoriev IM, Filippov NN. Air pressure broadening and shifting of high-J lines of (00011)←(00001) band of $^{12}C^{16}O_2$. J Quant Spectrosc Radiat Transf 2010;111:2315–20.
[47] Gamache RR, Lamouroux J. The vibrational dependence of half-widths of CO_2 transitions broadened by N_2, O_2, air, and CO_2. J Quant Spectrosc Radiat Transf 2013;117:93–103.
[48] Tran H, Boulet C, Stefani S, Snels M, Piccioni G. Measurements and modelling of high pressure pure CO_2 spectra from 750 to 8500 cm^{-1}. I-central and wing regions of the allowed vibrational bands. J Quant Spectrosc Radiat Transf 2011;112:925–36.
[49] Laraia AL, Gamache RR, Lamouroux J, Gordon IE, Rothman LS. Total internal partition sums to support planetary remote sensing. Icarus 2011;215:391–400.
[50] Berman PR. Speed-dependent collisional width and shift parameters in spectral profiles. J Quant Spectrosc Radiat Transf 1972;12:1331–42.
[51] Tran H, Ngo NH, Hartmann J-M. Efficient computation of some speed-dependent isolated line profiles. J Quant Spectrosc Radiat Transf 2013;129:199–203.
[52] Boone CD, Walker KA, Bernath PF. Speed-dependent Voigt profile for water vapor in infrared remote sensing applications. J Quant Spectrosc Radiat Transf 2007;105:525–32.
[53] Ngo NH, Lisak D, Tran H, Hartmann J-M. An isolated line-shape model to go beyond the Voigt profile in spectroscopic databases and radiative transfer codes. J Quant Spectrosc Radiat Transf 2013;129:89–100.
[54] Rosenkranz PW. Shape of the 5 mm oxygen band in the atmosphere. IEEE Trans Antennas Propag 1975;23:498–506.

Author's personal copy

Journal of Molecular Spectroscopy 267 (2011) 71–79

Contents lists available at ScienceDirect

Journal of Molecular Spectroscopy

journal homepage: www.elsevier.com/locate/jms

Toward the understanding of the high resolution infrared spectrum of C_2H_6 near 3.3 μm ☆

F. Lattanzi [a], C. di Lauro [a,*], J. Vander Auwera [b]

[a] Chimica Fisica, Università di Napoli Federico II, Via D. Montesano 49, I-80131 Naples, Italy
[b] Service de Chimie Quantique et Photophysique, C.P.160/09, Université Libre de Bruxelles, B-1050 Brussels, Belgium

ARTICLE INFO

Article history:
Available online 19 February 2011

Keywords:
Ethane
Internal rotation
Planetary atmospheres
Titan
High resolution infrared spectra
Vibration–rotation interactions

ABSTRACT

The Fourier transform infrared spectrum of ethane between 2860 and 3060 cm^{-1} has been re-investigated under high resolution at 229 K. The infrared absorption in this region is due mainly to the CH stretching fundamentals ν_5 (parallel band) and ν_7 (degenerate perpendicular band), and to the parallel combination system $\nu_8 + \nu_{11}$ (A_{4s}, A_{3s}). All the relevant perturbation mechanisms affecting the observed absorption patterns have been clarified. In particular, the main perturbers of the ν_7 state are identified to be the degenerate vibrational combination states $\nu_8 + \nu_{11}$ (l-type interaction) and $\nu_3 + 2\nu_4 + \nu_8$ (Fermi-type interaction). Because of the last interaction, the $K''\Delta K = -6$ transitions occur with intensities comparable to both the infrared active fundamental ν_7 and the almost dark combination $\nu_3 + 2\nu_4 + \nu_8$. The parallel combination system $\nu_8 + \nu_{11}$ (A_{4s}, A_{3s}) is overlapped and heavily perturbed by the nearby parallel system $\nu_4 + \nu_{11} + \nu_{12}$ (A_{4s}, A_{3s}), whose K-structure is spread by the strong z-Coriolis interaction of its two vibrational components. In this work, 95 new transitions to the perturbers of ν_7 have been assigned. They belong mostly to the degenerate vibrational states $\nu_8 + \nu_{11}$ (E_{1d}) and $\nu_3 + 2\nu_4 + \nu_8$ (E_{1d}), and to the parallel system $\nu_8 + \nu_{11}$ (A_{4s}, A_{3s}). A least squares fit calculation, limited to the ν_7 degenerate fundamental and its degenerate perturbers $\nu_8 + \nu_{11}$, $\nu_3 + 2\nu_4 + \nu_8$, $\nu_4 + \nu_{11} + \nu_{12}$, and $\nu_3 + 3\nu_4 + \nu_{12}$ was performed. From the results of this fit, we created a line-by-line database containing the molecular parameters for 4969 transitions in these five bands of $^{12}C_2H_6$. Finally, we identified the degenerate combination band $\nu_2 + \nu_8$ (62 observed transitions) to be the main perturber (x, y-Coriolis-type interaction) of the parallel fundamental ν_5.

© 2011 Elsevier Inc. All rights reserved.

1. Introduction

From the theoretical point of view, ethane is a key molecule because of its highly symmetric geometry, involving two coaxial identical internal rotors, and its peculiar large amplitude torsional dynamics, resulting in an extremely dense and complex rotational and torsional structure of its infrared bands. Apart from fundamental interest, the understanding of the spectroscopy of ethane is also of importance in various fields. For instance, ethane is present in various environments, including the Earth's atmosphere in which it is the second most abundant hydrocarbon, the atmospheres of outer planets, and comets.

The five infrared active fundamental transitions of ethane define three main spectral regions, around 12 μm, 6.2–7.5 μm, and 3.3 μm. The first two regions have been extensively studied. Numerical rotational analyses of the degenerate ν_9 fundamental occurring in the first region near 822 cm^{-1}, including torsional splittings caused by the interaction with the torsional system $3\nu_4$ (ν_4 near 289 cm^{-1} is the torsional mode of vibration), became available early in the 1980s [1–3]. However, a very accurate analysis of this region has been performed only recently [4]: it included the ν_9 band, the associated hot transitions $(\nu_4 + \nu_9) - \nu_4$, the infrared inactive C–C stretching fundamental ν_3 (near 995 cm^{-1}, activated by perturbations at resonance), the ν_{12}–ν_9 difference band near 385 cm^{-1} (ν_{12} is the symmetric CH_3 rock, near 1195 cm^{-1}), and the torsional bands ν_4, $2\nu_4$–ν_4 and $3\nu_4$. The second region is probably the most studied infrared region of ethane. It is dominated by the ν_8 fundamental band (degenerate antisymmetric deformation of the two methyl group, near 1472 cm^{-1}), perturbed by the ν_6 fundamental (mostly an asymmetric CH_3 umbrella vibration, near 1379 cm^{-1}) and the $2\nu_4 + \nu_{12}$ bands. However, the rotation-torsion analysis of this region proved to be difficult, because of the high density of spectral lines and anomalous line patterns caused by numerous perturbations. It is worth mentioning a tentative analysis of the ν_8 band performed by Susskind in 1974 using a grating spectrum with unresolved torsional structure [5], followed much later by the work of Lattanzi et al. [6], Hepp and Herman [7],

☆ Work presented at the 21st Colloquium on High-resolution Molecular Spectroscopy, Castellammare di Stabia, Italy, 2009.

* Corresponding author.
E-mail address: car.dilauro@gmail.com (C. di Lauro).

0022-2852/$ - see front matter © 2011 Elsevier Inc. All rights reserved.
doi:10.1016/j.jms.2011.02.003

Author's personal copy

and our work on the hot system $(\nu_4 + \nu_8) - \nu_8$ [8], all relying on Fourier transform spectra. However, a global numerical analysis of this spectral region was not performed until 2008, when we were able to analyze the interacting system ν_6, ν_8, $\nu_4 + \nu_{12}$, $2\nu_4 + \nu_9$, and the hot transitions from ν_4 to $\nu_4 + \nu_8$ [9]. Such a global analysis became feasible when we understood that all the complex and multiple resonances affecting this spectral region occur within the (ν_6, ν_8, $\nu_4 + \nu_{12}$, $2\nu_4 + \nu_9$) system only. Further work on this region is still in progress [10]. It led to the creation of the first line-by-line database containing the molecular parameters for over 20 000 $^{12}C_2H_6$ transitions at 7 μm [11].

The region around 3.3 μm, where the infrared active CH stretching fundamental vibrations ν_5 and ν_7 occur respectively near 2896 and 2985 cm^{-1}, is even more complex. It has not yet been analyzed by any model Hamiltonian, in spite of its relevance in applied spectroscopy. Indeed, the ν_7 band exhibits a series of very strong *Q*-branches, commonly used for the atmospheric monitoring of ethane [12,13]. Outstanding spectroscopic data on this spectral region were obtained by Pine and Lafferty [14], who studied a Doppler-limited absorption spectrum recorded at 119 K (Doppler FWHM = 0.0043 cm^{-1}) with a tunable difference-frequency laser spectrometer. These authors report extensive and very accurate assignments of rotation-torsion lines belonging to the vibrational bands ν_7 and ν_5, and the parallel band $\nu_8 + \nu_{11}$ (ν_{11} is the degenerate symmetric deformation of the two methyl group, near 1468 cm^{-1}), and several lines assigned to an unidentified perturber of ν_5. They also describe accurately the most prominent anomalies in the spectrum. However, the numerous and strong perturbations observed in this 3.3 μm region have never been clarified since then. The availability of this outstanding dataset prompted us to reinvestigate this spectral region, with the aim of improving the present knowledge and understanding of the mechanisms generating the observed complex spectral features. Note that infrared absorption cross sections have recently been measured in this range [15].

With the present contribution, we report results of a least squares fit of the transitions assigned to the fundamental ν_7 band and some of its perturbers, and propose perturbation mechanisms for the other bands observed in this region, that is the ν_5 fundamental band and the parallel components of the $\nu_8 + \nu_{11}$ combination band. With our analysis, we were able to assign 95 new transitions to the perturbers, which were added to the dataset generated by Pine and Lafferty [14].

2. Experimental details

Four unapodized absorption spectra of ethane have been recorded at a resolution of 0.0034 cm^{-1} (FWHM of the sinc function, maximum optical path difference = 180 cm) using a Bruker IFS125HR Fourier transform spectrometer, fitted with a Tungsten source, a CaF_2 beamsplitter, a low-pass filter with a cut-off near 5800 cm^{-1}, and an InSb detector. The sample was contained in a 19.7-cm long stainless steel cell, at pressures from 0.2 to 1.4 hPa and temperatures of 280 and 229 K. In addition, one spectrum was recorded at a resolution of 0.0039 cm^{-1}, the sample being in a 5.15-cm long aluminum cell, at 0.9 hPa and 296 K. This latter spectrum is shown in Fig. 1. Only the spectrum recorded at 229 K (pressure = 0.5 hPa) was used in the present analysis.

The positions of C_2H_6 lines were measured in the first four spectra by fitting the observed line shapes to a Voigt profile, including instrumental effects, using software written in Brussels [16]. They were calibrated using absorption lines in the ν_3 band of residual water vapor present in the evacuated instrument and the 2006 update of HITRAN 2004 as reference [17]. Their accuracy was estimated to be better than 0.0005 cm^{-1} by comparison of the calibrated positions of the same lines measured in the various spectra.

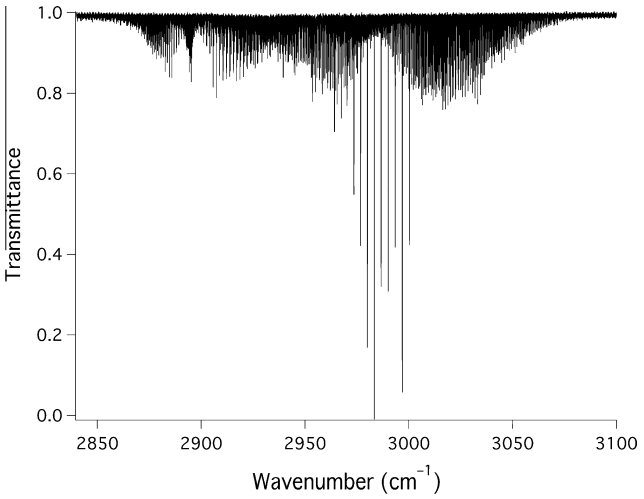

Fig. 1. Overview of the spectrum of ethane near 3.3 μm (0.9 hPa, 5.15 cm, 296 K), recorded at a resolution = 0.0039 cm^{-1} using a Fourier transform spectrometer.

Indeed, the RMS deviations in the six sets of differences, involving from 733 to 2147 differences, are in the range 1.8–3.3 × 10^{-4} cm^{-1}.

3. Description of the spectrum and corresponding energy levels structure

As Fig. 1 shows, the 3.3 μm region of the ethane spectrum is dominated by the ν_5 and ν_7 fundamental bands. The A_{4s} parallel component of the $\nu_8 + \nu_{11}$ combination band, centered between the two fundamentals, also contributes to the absorption in this region [14]. The nine narrow structures, standing out near the central part of ν_7, are *Q*-branches with $K''\Delta K$ from −4 to 4. Even at Doppler-limited resolution, they appear as narrow features with almost unresolved *J*-structure. The other *Q*-branches either appear to be broadened by strong perturbations or are weak, and are therefore hardly identified in the compressed spectrum shown in Fig. 1.

The vibrational states occurring in this region are schematized in Fig. 2. Their high density does in fact suggest that the spectral patterns have to be quite complex, because the ν_5 and ν_7 states can be perturbed by many states and these perturbers can be themselves affected by perturbations. These perturbations can additionally induce unpredictable irregularities in the rotation-torsion energy levels structure in these states.

Table 1 lists the ν_7, ν_5 and $\nu_8 + \nu_{11}$ states together with states (here called "perturbers") identified in the present work to perturb them through interaction mechanisms at least qualitatively understood. The symmetry species of the states under the G_{36}(EM) extended molecular group [18] are also given. The last two columns provide the values of the ζ *z*-Coriolis constant of the states, defined in Eq. (2) for the degenerate vibrational states and linking the A_{4s} and A_{3s} components of non-degenerate vibrational combination states. Note that interactions are also expected to occur among the perturbers. In fact, a strong interaction mainly due to the operator $(\boldsymbol{q}_{8-}\boldsymbol{p}_{12+} - \boldsymbol{p}_{8-}\boldsymbol{q}_{12+})\boldsymbol{J}_\gamma$ and its complex conjugate ($\boldsymbol{J}_\gamma$ is the torsional angular momentum operator, with γ being half the torsional angle) couples the perturbers in group 1 of Table 1 with those of group 3, the perturbers of groups 2 and 4, and those of groups 5 and 6.

4. The fundamental ν_7

The most obvious perturbation of the fundamental ν_7 band appears as a sudden change of the degradation of the *J*-structure for

Author's personal copy

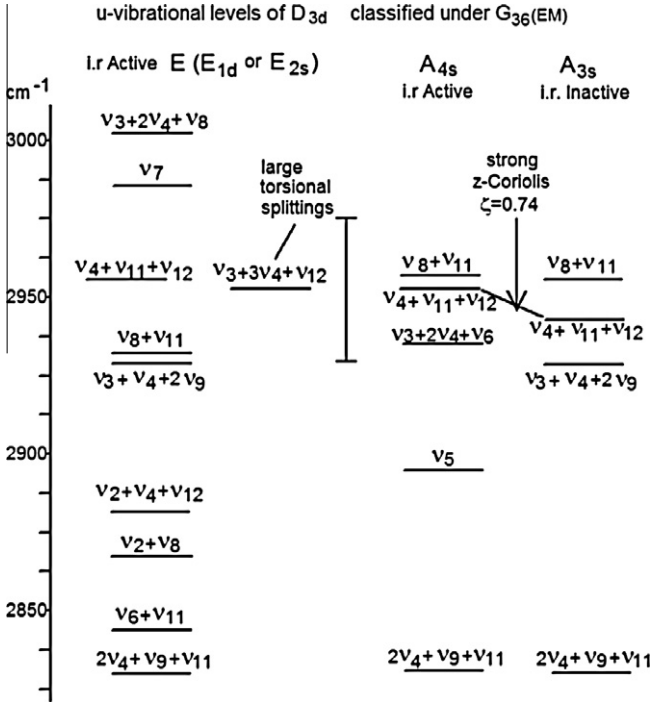

Fig. 2. Manifold of infrared active vibrational states of $^{12}C_2H_6$ in the region of the CH stretching fundamentals. The torsional components of the $\nu_3 + 3\nu_4 + \nu_{12}$ state are heavily split because of the high excitation of the torsional mode ν_4, and occur in a spectral range represented by the vertical line.

the sub-branches with $K''\Delta K = 5$ and 6. This can be seen in Fig. 3 for $^rQ_5$ and $^rQ_6$. We explain this perturbation as resulting from a *l*-type interaction with $\Delta l = \pm 2$ and $\Delta k = \mp 1$ [$l(2, -1)$ interaction] between the ν_7 state and the degenerate component of the combination state $\nu_8 + \nu_{11}$, identified by Hepp and Herman [19] using a slit jet cooled Fourier transform spectrum. Indeed, the vibrational frequency and Coriolis coefficient of that state are such that the $l(2, -1)$-resonance with ν_7 can be predicted to occur precisely where observed, that is for $K''\Delta K$ between 5 and 6. Note that the stronger torsional component of $^rQ_5$ is affected by a further resonance interaction, with *J*-crossing near $J = 20$–21, probably of the type $\Delta l = 0$, $\Delta k = \pm 3$ with the $\nu_3 + 3\nu_4 + \nu_{12}$ state. Its effects are clearly seen in Fig. 3: the relative positions of the *J*-pairs (19, 20) and (21, 22) are inverted.

To characterize the $l(2, -1)$ interaction between ν_7 and $\nu_8 + \nu_{11}$ (E_{1d} or E_{2s}), transitions to the latter need to be identified. We found it quite difficult to detect such transitions in our spectrum at 229 K, except for the $^rQ_0$-branch. This branch is clearly observed in the spectrum at 119 K printed in the article by Pine and Lafferty [14], who also report the corresponding line positions, without assignments. With the help of a slit jet cooled spectrum [19], we could assign transitions with $K''\Delta K$ from −1 to 1. These assignments are reported in Table 2.

The branches $K''\Delta K = -6$ of ν_7 consist of two vibrational components, as shown in Fig. 4 for the $^PQ_6$ branch. Each line of these two components is in turn split by the torsional tunneling mechanism, with the stronger torsional component appearing at energies lower than the weaker one. The latter is consistent with an excitation of the torsional mode ν_4 by an even number of quanta, which is easily found to be 2 from the magnitude of the torsional splittings (detected much better in the $^PP_6$ transitions than in the $^PQ_6$ shown here).

The perturber of the ν_7 state is identified to be the degenerate state $\nu_3 + 2\nu_4 + \nu_8$, in anharmonic resonance with ν_7. Pine and Lafferty [14] assigned the lower frequency component to ν_7 ($^PQ_6$ in Fig. 4), and the other component ($^PQ'_6$ in Fig. 4) remained unassigned. The fundamental ν_7 is the lower component at the low *J*, and the first few *J*-lines of the higher frequency component are not observed because the interacting levels are not yet close to resonance, and $\nu_3 + 2\nu_4 + \nu_8$ does not steal enough intensity from ν_7 (see Fig. 4). However, the interacting pairs of levels get closer as *J* increases, because the rotational parameter *B* is smaller in the perturber owing to the excitation of ν_4, and eventually a *J*-crossing occurs, at about $J' = 12$. In Table 3, we report wavenumbers and assignments for these transitions with $K''\Delta K = -6$.

5. Tentative analysis of the ν_7 band

5.1. Hamiltonian model

Owing to the extremely complex structure of this spectral region, only a rough attempt to a numerical analysis seemed to be feasible. We found that the perturbative effects of non-degenerate vibrational states on the degenerate state ν_7 could be disregarded in a first approximation. So, we restricted our analysis to the fundamental ν_7 and to the above mentioned degenerate perturber states $\nu_8 + \nu_{11}$ and $\nu_3 + 2\nu_4 + \nu_8$. In the course of the least squares fit calculations, we realized that the fit improved with an expanded model in which $\nu_8 + \nu_{11}$ interacts with $\nu_4 + \nu_{11} + \nu_{12}$, mainly through the operator $(\boldsymbol{q}_{8-}\boldsymbol{p}_{12+} - \boldsymbol{p}_{8-}\boldsymbol{q}_{12+})\boldsymbol{J}_\gamma$ and its complex conjugate (see Section 3, Table 1). For small torsional splittings, as in our case, this interaction can be treated as a simple Fermi-type

Table 1
Vibrational states, and their energy, identified in the present work in the CH stretching region of $^{12}C_2H_6$. The last 2 columns provide the values of the ζ *z*-Coriolis constant of the states (defined in Eq. (2) for the degenerate vibrational states and linking the A_{4s} and A_{3s} components of non-degenerate vibrational combinations).

	Vibrational state	ν_0 (cm^{-1})	Comments	ζ (A_{4s}, A_{3s})	ζ (E)
	ν_7 (E_{1d})	2985.04	Fundamental		0.116
	ν_5 (A_{4s})	2895.64	Fundamental		
1	$\nu_8 + \nu_{11}$ (E_{1d} or E_{2s})	2931.84	Observed for $K''\Delta K = -1$ to 1	0.01	0.554
	$\nu_8 + \nu_{11}$ (A_{4s})	2954.3	Observed for *K* up to 11		
	$\nu_8 + \nu_{11}$ (A_{3s})	2954.2			
2	$\nu_3 + 2\nu_4 + \nu_8$ (E_{1d})	3003.26	Observed for $K''\Delta K = -6$		−0.417
3	$\nu_4 + \nu_{11} + \nu_{12}$ (E_{1d} or E_{2s})	2952.7		0.74	−0.169
	$\nu_4 + \nu_{11} + \nu_{12}$ (A_{4s})	2952.2	Observed for $K = 1$ and 2		
	$\nu_4 + \nu_{11} + \nu_{12}$ (A_{3s})	2944.0			
4	$\nu_3 + 3\nu_4 + \nu_{12}$ (E_{1d})	2954	Large torsional splittings (about 40 cm^{-1})		0.413
5	$\nu_2 + \nu_8$ (E_{1d})	2863.1	Strong perturber of ν_5		−0.30
6	$\nu_2 + \nu_4 + \nu_{12}$ (E_{1d})	2880.3			0.41

Author's personal copy

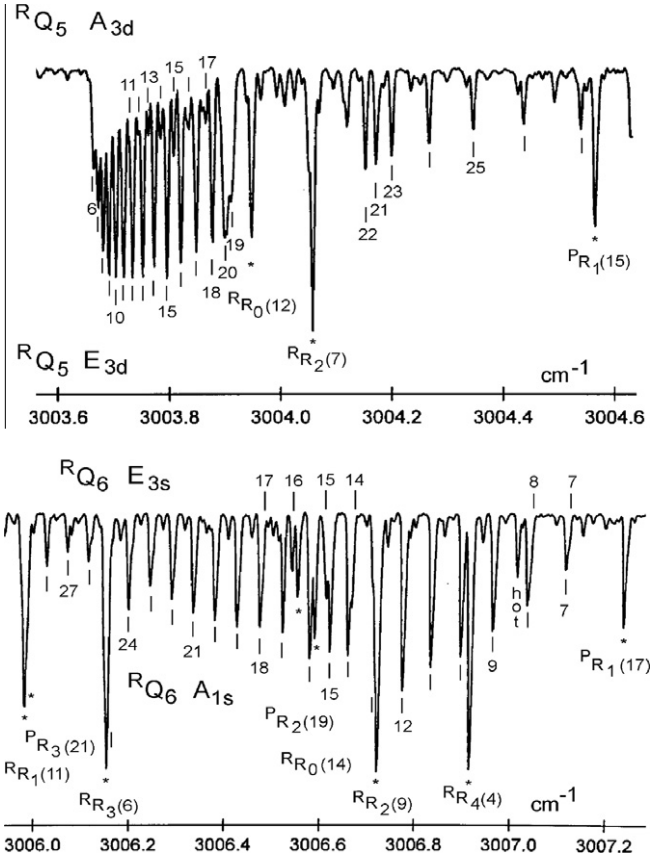

Fig. 3. The $^{r}Q_5$ and $^{r}Q_6$ branches of v_7, showing the opposite effects of a $l(2, -1)$ interaction with the degenerate component of $v_8 + v_{11}$, just before and after the K-crossing (see text for details).

coupling [9]. We also added the degenerate state $v_3 + 3v_4 + v_{12}$ to the Hamiltonian matrix, because the account of its Fermi-type and l-type interactions with v_7 improved the fit. This last state is also coupled to $v_3 + 2v_4 + v_8$ by the mentioned operators $(\boldsymbol{q}_{8-}\boldsymbol{p}_{12+} - \boldsymbol{p}_{8-}\boldsymbol{q}_{12+})\boldsymbol{J}_\gamma$ (see Section 3, Table 1), but calculations including this interaction proved to be poorly determined. This coupling was therefore disregarded, its effects being supposedly absorbed in the effective values of the other parameters of the two states. Thus, we used a model including five degenerate vibrational states: v_7, $v_8 + v_{11}$, $v_3 + 2v_4 + v_8$, $v_4 + v_{11} + v_{12}$, and $v_3 + 3v_4 + v_{12}$, all active by symmetry for electric dipole transitions from the ground state.

In the present analysis, small torsional splittings in the v_7, $v_8 + v_{11}$, $v_4 + v_{11} + v_{12}$ and ground states were accounted for by the usual one-parameter expression [20,21], that we write in the form:

$$v^0(\vec{v}, \Gamma_t) = v^0 - 2(-1)^{v_4} X_v \cos(\sigma 2\pi/6) \quad (1)$$

where $\vec{v}$ represents the ensemble of vibrational quantum numbers, inclusive of the torsional-vibration quantum number v_4, X_v is a generally positive parameter whose value increases rapidly with v_4, but depends also upon the excitation of the small amplitude vibrational modes, and $\sigma = 0$, 1, 2 and 3 for the components of torsional symmetries $\Gamma_t = A_{1s}$ (or A_{3s}), E_{3d}, E_{3s} and A_{3d} (or A_{1d}), using A_s and E_d vibrational basis states. For larger splittings (as observed in the $v_3 + 2v_4 + v_8$ and $v_3 + 3v_4 + v_{12}$ states), a vibrational energy v^0 has to be determined for each of the four torsional components. Note that the components A_{1s} and A_{3d} occur with the even values of v_4, whereas the components A_{3s} and A_{1d} occur with the odd values of v_4. Diagonal matrix elements are given as usual by

Table 2
Assignments of transitions in the degenerate $v_8 + v_{11}$ band. Line positions are from this work; the values between parentheses are from [14]. Numbers listed in column "A" are relative absorption line intensities, in arbitrary units. The ground state vibration–rotation-torsion symmetries in the G_{36}(EM) extended molecular group are also given. The ground state energies E'' were calculated using the constants reported in [2,23].

Line position (cm^{-1})	A	J'	K'	J''	K''	Sym.	E'' (cm^{-1})
2917.5216 - - - - - - -		8	0	9	1	G_s	61.6688
2918.7157 - - - - - - -		7	0	8	1	G_s	49.7373
2919.9217 - - - - - - -		6	0	7	1	G_s	39.1310
2921.1450 - - - - - - -		5	0	6	1	G_s	29.8501
2922.3730 - - - - - - -		4	0	5	1	G_s	21.8946
2923.6325 - - - - - - -		3	0	4	1	G_s	15.2649
2924.5337 (.5336)	16	4	2	5	1	G_s	21.8946
2924.9024 - - - - - - -		2	0	3	1	G_s	9.9609
2926.1969 - - - - - - -		1	0	2	1	G_s	5.9829
2928.8490 (.8472)	13	1	0	1	1	G_s	3.3308
2928.8804 (.8829)	10	2	0	2	1	G_s	5.9829
2929.0027 (.0096)	8	4	0	4	1	G_s	15.2649
2929.1005 (.0992)	18	5	0	5	1	G_s	21.8946
2929.2026 (.2016)	11	6	0	6	1	G_s	29.8501
2930.0259 (.0254)	14	3	1	3	0	A_{2s}	7.9524
2930.0865 (.0854)	7	4	1	4	0	A_{1s}	13.2564
2930.1602 (.1617)	23	5	1	5	0	A_{2s}	19.8862
2930.2509 (.2494)	8	6	1	6	0	A_{1s}	27.8416
2930.3610 (.3603)	21	7	1	7	0	A_{2s}	37.1226
2930.4815 (.4812)	21	8	1	8	0	A_{1s}	47.7290
2930.6189 (.6185)	21	9	1	9	0	A_{2s}	59.6605
2930.7714 (.7720)	14	10	1	10	0	A_{1s}	72.9169
2930.9375 (.9384)	29	11	1	11	0	A_{2s}	87.4981
2931.0472 - - - - - - - -	8	2	2	2	1	G_s	5.9829
2931.1067 (.1016)	13	3	2	3	1	G_s	9.9609
2931.1622 (.1604)	6	4	2	4	1	G_s	15.2649
2931.2354 (.2342)	6	5	2	5	1	G_s	21.8946
2931.3169 (.3195)	11	6	2	6	1	G_s	29.8501
2931.4342 (.4343)	9	7	2	7	1	G_s	39.1310
2933.6992 (.7074)		2	2	1	1	G_s	3.3308
2935.0847 (.0788)		3	2	2	1	G_s	5.9829
2936.4661 (.4654)		4	2	3	1	G_s	9.9609
2937.8652 (.8647)		5	2	4	1	G_s	15.2649
2939.2723 (.2680)		6	2	5	1	G_s	21.8946
2940.7151 - - - - - - - -		7	2	6	1	G_s	29.8501

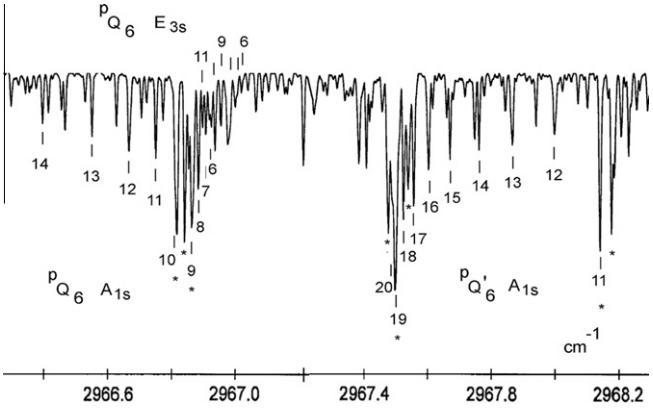

Fig. 4. The $^{p}Q_6$ branches of v_7 and $v_3 + 2v_4 + v_8$ in Fermi-type resonance. The lower frequency component corresponds to v_7 for the low values of J, then a J-crossing occurs (see text for details).

$$E[(\vec{v}, \Gamma_t, (\pm l), J, K] = v^0(\vec{v}, \Gamma_t) + (A - B)K^2 + BJ(J+1) - D_J J^2(J+1)^2 - D_{JK}J(J+1)K^2 - D_K K^4 \mp [2A\zeta - \eta_J J(J+1) - \eta_K K^2]K \quad (2)$$

K is the absolute value of the z-axis total angular momentum quantum number k, and the symbols $(+l)$ and $(-l)$ identify states with

Author's personal copy

Table 3
Assignments, positions and lower state energies for the $K''\Delta K = -6$ transitions to the resonating v_7 and $v_3 + 2v_4 + v_8$ states. Line positions are from this work; the values between parentheses are from [14]. Numbers listed in column "A" are relative absorption line intensities, in arbitrary units. Transitions to the higher energy vibrational component were observed but not assigned by Pine and Lafferty [14]. The ground state vibration–rotation-torsion symmetries in the G_{36}(EM) extended molecular group are also given. They are all single valued, therefore the "s" subscript to the symmetry species is omitted. The ground state energies E'' were calculated using the constants reported in [2,23]. See text for details.

Line position (cm^{-1})	A	J'	K'	J''	K''	Sym.	Vibrational component	E'' (cm^{-1})
2938.3734 (.3796)	15	21	5	22	6	$A_{1,2}$	Higher	407.4047
2939.6826 (.6831)	24	20	5	21	6	$A_{1,2}$	Higher	378.2796
2941.0161 (.0153)	23	19	5	20	6	$A_{1,2}$	Higher	350.4746
2941.8183 (.8178)	37	17	5	18	6	$A_{1,2}$	Lower	298.8271
2942.2012 (.2010)	13	17	5	18	6	$E_{3,4}$	Lower	298.8328
2942.3586 (.3579)	23	18	5	19	6	$A_{1,2}$	Higher	323.9903
2943.4278 (.4274)	23	16	5	17	6	$A_{1,2}$	Lower	274.9856
2943.7126 (.7121)	25	17	5	18	6	$A_{1,2}$	Higher	298.8271
2943.7911 (.8073)	12	16	5	17	6	$E_{3,4}$	Lower	274.9913
2945.0017 (.------)	16	15	5	16	6	$A_{1,2}$	Lower	252.4662
2945.3294 (.3291)	10	15	5	16	6	$E_{3,4}$	Lower	252.4718
2946.5172 (.5175)	24	14	5	15	6	$A_{1,2}$	Lower	231.2692
2946.7944 (.7942)	16	14	5	15	6	$E_{3,4}$	Lower	231.2749
2946.4711 (.4709)	26	15	5	16	6	$A_{1,2}$	Higher	252.4662
2947.8845 (.8839)	25	14	5	15	6	$A_{1,2}$	Higher	231.2692
2947.9964 (.9960)	21	13	5	14	6	$A_{1,2}$	Lower	211.3951
2948.2216 (.2221)	24	13	5	14	6	$E_{3,4}$	Lower	211.4008
2949.3120 (.3115)	25	13	5	14	6	$A_{1,2}$	Higher	211.3951
2949.4360 (.4349)	30	12	5	13	6	$A_{1,2}$	Lower	192.8443
2949.6144 (.6144)	26	12	5	13	6	$E_{3,4}$	Lower	192.8500
2950.7678 (.7667)	24	12	5	13	6	$A_{1,2}$	Higher	192.8443
2950.8433 (8420)	35	11	5	12	6	$A_{1,2}$	Lower	175.6171
2950.9900 (.9897)	31	11	5	12	6	$E_{3,4}$	Lower	175.6228
2952.2287 (.2277)	38	10	5	11	6	$A_{1,2}$	Lower	159.7139
2952.2345 (.2339)	24	11	5	12	6	$A_{1,2}$	Higher	175.6171
2952.3560 (.3546)	27	10	5	11	6	$E_{3,4}$	Lower	159.7195
2953.5973 (.5966)	56	9	5	10	6	$A_{1,2}$	Lower	145.1348
2953.6979 (.6965)	28	9	5	10	6	$E_{3,4}$	Lower	145.1405
2953.7287 (.7285)	23	10	5	11	6	$A_{1,2}$	Higher	159.7139
2954.9524 (.9516)	47	8	5	9	6	$A_{1,2}$	Lower	131.8803
2955.0472 (.0461)	33	8	5	9	6	$E_{3,4}$	Lower	131.8860
2955.1773 (.1766)	23	9	5	10	6	$A_{1,2}$	Higher	145.1348
2956.2998 (.2992)	45	7	5	8	6	$A_{1,2}$	Lower	119.9505
2956.3912 (.3912)	30	7	5	8	6	$E_{3,4}$	Lower	119.9562
2956.6422 (.6412)	14	8	5	9	6	$A_{1,2}$	Higher	131.8803
2957.6415 (.6402)	49	6	5	7	6	$A_{1,2}$	Lower	109.3457
2957.7365 (.7361)	27	6	5	7	6	$E_{3,4}$	Lower	109.3514
2958.9790 (.9778)	52	5	5	6	6	$A_{1,2}$	Lower	100.0717
2959.0831 (.0828)	29	5	5	6	6	$E_{3,4}$	Lower	100.0717
2959.6643 (.6635)	13	6	5	7	6	$A_{1,2}$	Higher	109.3457
2961.1335 (.1335)	33	5	5	6	6	$A_{1,2}$	Higher	100.0660
2966.1975 (.1969)	16	15	5	15	6	$A_{1,2}$	Lower	231.2692
2966.5259 (.5257)	10	15	5	15	6	$E_{3,4}$	Lower	231.2749
2966.5471 (.5470)	20	13	5	13	6	$A_{1,2}$	Lower	192.8443
2966.6645 (.6626)	25	12	5	12	6	$A_{1,2}$	Lower	175.6171
2966.7473 (.7471)	27	11	5	11	6	$A_{1,2}$	Lower	159.7139
2966.8504 (.8501)	30	9	5	9	6	$A_{1,2}$	Lower	131.8803
2966.8813 (.8809)	36	8	5	8	6	$A_{1,2}$	Lower	119.9505
2966.8937 (.8934)	18	11	5	11	6	$E_{3,4}$	Lower	159.7195
2966.9044 (.9034)	20	7	5	7	6	$A_{1,2}$	Lower	109.3457
2966.9221 (.9204)	18	6	5	6	6	$A_{1,2}$	Lower	100.0660
2966.9337 (.9343)	25	10	5	10	6	$E_{3,4}$	Lower	145.1405
2966.9518 (.9514)	17	9	5	9	6	$E_{3,4}$	Lower	131.8860
2966.9969 (.9967)	12	7	5	7	6	$E_{3,4}$	Lower	109.3514
2967.0166 (.0154)	8	6	5	6	6	$E_{3,4}$	Lower	100.0717
2967.5215 (.5205)	45	18	5	18	6	$A_{1,2}$	Higher	298.8271
2967.5539 (.5539)	42	17	5	17	6	$A_{1,2}$	Higher	274.9856
2967.6001 (.6003)	30	16	5	16	6	$A_{1,2}$	Higher	252.4662
2967.6677 (.6675)	27	15	5	15	6	$A_{1,2}$	Higher	231.2692
2967.7587 (.7583)	25	14	5	14	6	$A_{1,2}$	Higher	211.3951
2967.8629 (.8627)	23	13	5	13	6	$A_{1,2}$	Higher	192.8443
2967.9956 (.9936)	20	12	5	12	6	$A_{1,2}$	Higher	175.6171
2968.1382 (.1387)	54	11	5	11	6	$A_{1,2}$	Higher	159.7139
2968.4322 (.4311)	12	9	5	9	6	$A_{1,2}$	Higher	131.8803
2968.5719 (.5711)	8	8	5	8	6	$A_{1,2}$	Higher	119.9505

k and l (the quantum number associated with the diagonal vibrational contribution to the angular momentum, in general taken modulo 3) having identical or opposite signs, respectively.

The l-interactions with $\Delta k = \Delta(l \text{ modulo } 3) = \pm 2$ were taken into account within the states v_7 and $v_8 + v_{11}$, and between v_7 and $v_3 + 2v_4 + v_8$ and v_7 and $v_4 + v_{11} + v_{12}$, with matrix elements

Author's personal copy

$$\langle \vec{v}_r, \Gamma_t, l = \pm 1, J, k \pm 1 | \boldsymbol{H} | \vec{v}_s, \Gamma'_t, l = \mp 1, J, k \mp 1 \rangle = -2F_{r,s}\{[J(J+1) - k(k+1)][J(J+1) - k(k-1)]\}^{1/2} \quad (3)$$

where the subscripts r and s identify either different degenerate vibrational states or the same state (r = s, in which case these subscripts are not necessary). In this equation Γ'_t is equal to Γ_t if the quanta of v_4 excited in the two interacting states have the same parity, and Γ'_t is equal to $\Gamma_t \times A_{3s}$ if they have opposite parities. In particular, these l-type interactions of v_7 with $v_4 + v_{11} + v_{12}$ and $v_3 + 2v_4 + v_8$ improved the fit of locally perturbed regions of the v_7 state corresponding to transitions with $K''\Delta K = -4$ and 2, respectively.

Fermi-type and z-Coriolis interactions were accounted for with matrix elements of the form

$$\langle \vec{v}_r, \Gamma_t, (\pm l), J, k | \boldsymbol{H} | \vec{v}_s, \Gamma'_t, (\pm l), J, k \rangle = W_{r,s} + W_{Kl,r,s} kl + W_{J,r,s} J(J+1) \quad (4)$$

These interactions are found to be effective between v_7 and all the other four vibrational states, and between $v_8 + v_{11}$ and $v_4 + v_{11} + v_{12}$. Again Γ'_t is equal to Γ_t or to $\Gamma_t \times A_{3s}$, depending on whether the numbers of quanta of v_4 excited in the interacting states have the same parity or opposite parities.

The l-interactions with $\Delta k = \pm 1$ and $\Delta(l \text{ modulo } 3) = \mp 2$ were taken into account within and between the states v_7 and $v_8 + v_{11}$, between v_7 and $v_3 + 3v_4 + v_{12}$, and between v_7 and $v_4 + v_{11} + v_{12}$. The interaction between v_7 and $v_8 + v_{11}$ is responsible for extended perturbations of v_7, coming to resonance in the region shown in Fig. 3. The interaction between v_7 and $v_3 + 3v_4 + v_{12}$ is selective over the torsional components, owing to the large torsional splittings in the $v_3 + 3v_4 + v_{12}$ state (order of magnitude $\sim$40 cm^{-1}). It helps to improve the fit of the weaker torsional components of v_7, in a locally perturbed region corresponding to transitions with $K''\Delta K = 9$. The l-type interaction of v_7 with $v_4 + v_{11} + v_{12}$ improves the fit of transitions of v_7 with $K''\Delta K = 10$. The matrix elements of this l-type interaction were set in the form

$$\langle \vec{v}_r, \Gamma_t, l = \pm 1, J, k | \boldsymbol{H} | \vec{v}_s, \Gamma'_t, l = \mp 1, J, k \pm 1 \rangle = (E_{r,s} + K^2 E_{Kr,s} + J(J+1)E_{Jr,s})(2k+1)[J(J+1) - k(k \pm 1)]^{1/2} \quad (5)$$

where l is intended modulo 3. Γ'_t is equal to $\Gamma_t \times A_{3d}$ or to $\Gamma_t \times A_{1d}$, depending on whether the numbers of quanta of v_4 excited in the interacting states have the same parity or opposite parities.

Finally, we introduced a $\Delta k = \pm 3$ interaction between v_7 and $v_3 + 3v_4 + v_{12}$, which helped to improve the fit around a local perturbation affecting the strong component of the $K''\Delta K = 5$ transitions of v_7 (see Fig. 3). The matrix elements are

$$\langle \vec{v}_r, \Gamma_t, l, J, k | \boldsymbol{H} | \vec{v}_s, \Gamma_t \times A_{1d}, l, J, k \pm 3 \rangle = C_{r,s}\{[J(J+1) - k(k+1)][J(J+1) - (k+1)(k+2)][J(J+1) - (k+2)(k+3)]\}^{1/2} \quad (6)$$

The torsional symmetries Γ_t and Γ'_t occurring in the matrix elements of Eqs. (3)–(6) depend upon the specific cases, and have been determined according to the rules stated in Ref. [22]. However, for practical purposes, as for instance in writing a computer program where these matrix elements occur, the relation between the torsional symmetries in any interacting pair is automatically obeyed if the energy matrix is correctly factored into blocks, each corresponding to a given vibration–rotation–torsion symmetry.

5.2. Results

A body of 572 wavenumber data were treated by least squares fit calculations. They included ^pP and ^rR transitions in the v_7 band, with $K''\Delta K$ from -10 to 14 and a maximum J-value of 30, $^rQ_0$, $^pP_1$ and $^rR_1$ transitions in $v_8 + v_{11}$ (listed in Table 2), and $^pP_6$ transitions in $v_3 + 2v_4 + v_8$ (listed in Table 3). The best fit was obtained with the Hamiltonian model detailed above, with a root mean square deviation of about 0.018 cm^{-1} and the parameters reported in Tables 4 and 5.

Although we believe that all the relevant perturbations have been incorporated in the model, the fit remains unsatisfactory. In fact, a root mean square deviation of 0.018 cm^{-1} is quite large, as are the standard deviations determined for most of the parameters employed in the fit.

A serious difficulty in the analysis is caused by the fact that many perturbers are also affected by additional interactions that at present cannot be discerned because of the high density of lines and vibrational states in this region, and because of the lack of observable transitions to them. Thus their rotation-torsion level patterns are only roughly predictable. A further difficulty arises with those levels where the mode v_3 is excited, whose torsional structure can be heavily affected by interactions, also with excited levels of the torsional manifold [24]. This is due to the large value of the barrier derivative in the torsional potential energy term $0.5(\partial V_3/\partial Q_3)_0(\cos 3\tau + 1)Q_3$, [25]. Nevertheless, we believe that the results of this least squares calculation supports the soundness of the proposed perturbation model, with all the relevant interactions discussed here.

From exploratory calculations of the matrix elements of the $\cos 3\tau$ and $\sin 3\tau$ operators, in a basis of barrier hindered torsional states, we conclude that the interactions of vibrational modes with opposite behavior g or u under the D_{3d} point group (symmetry allowed in non-rigid ethane between the E-torsional components [21]) cannot be effective unless $v_4 \geqslant 3$ in one state at the least.

6. The parallel combination band $v_8 + v_{11}$

The anomalous structure of the absorption related to the $v_8 + v_{11}$ ($A_{4s} + A_{3s}$) parallel combination band (the A_{4s} component is IR allowed and the A_{3s} component is IR forbidden), showing the effects of a K-crossing at K between 1 and 2, has been accurately described by Pine and Lafferty [14]. Now we can explain the interaction mechanism. Strong Fermi-type interactions, with selection rules $A_{4s} \leftrightarrow A_{4s}$ and $A_{3s} \leftrightarrow A_{3s}$, and z-Coriolis type interactions, with selection rules $A_{4s} \leftrightarrow A_{3s}$, occur between the $v_8 + v_{11}$ ($A_{4s} + A_{3s}$) states and the corresponding parallel states $v_4 + v_{11} + v_{12}$ ($A_{4s} + A_{3s}$). The z-Coriolis interaction within the $v_8 + v_{11}$ system is weak ($\zeta \sim 0.01$), but it is strong within the $v_4 + v_{11} + v_{12}$ system ($\zeta \sim 0.74$, see Table 1). Thus the K-structure of the $v_4 + v_{11} + v_{12}$ system is spread by the z-Coriolis coupling its A_{4s} and A_{3s} components, and crosses the $v_8 + v_{11}$ system at K between 1 and 2. Several lines of the perturber $v_4 + v_{11} + v_{12}$ are in fact observed at these two values of K.

Fig. 5 shows the Q-branches of the $v_8 + v_{11}$ parallel system. The subbranch with $K = 1$, just before the crossing, lies far away at the higher wavenumbers, whereas the subbranch with $K = 2$ is the one most displaced to the lower wavenumbers. The sub-branches with K larger than 2 are progressively less and less displaced to the low wavenumbers, and eventually a K-turn occurs at $K = 4$. In fact, the K-structure tends eventually to degrade toward the lower wavenumbers, since the A constant in these vibrational states is smaller than in the ground state. The K-structure of all series of lines with given J does in fact show a turn at the high wavenumber side, at $K = 4$.

We were able to identify 35 transitions left unassigned by Pine and Lafferty [14]; they are listed in Table 6. Among them are several Q-branch lines, with K between 7 and 12, shown in Fig. 5.

The whole mechanism of perturbation of this system is very complex, and we were not able to perform reliable wavenumber

Author's personal copy

Table 4
Vibration–rotation-torsional parameters (in cm^{-1}) for the matrix elements occurring within vibrational states (Eqs. (1), (2), (3), and (5)). Parameters identical to those in the ground state are denoted 'g.s.' Numbers in parentheses are standard deviations in units of the last quoted digit. The ground state constants were held fixed to values reported in [2,23].

	v_7	$v_8 + v_{11}$	$v_3 + 2v_4 + v_8$	$v_4 + v_{11} + v_{12}$	$v_3 + 3v_4 + v_{12}$	Ground state
v^0	2985.040(5)	2931.84(6)		2952.71(3)		
X	0.0013(fixed)	g.s.		0.0767(fixed)		0.0189
$v^0(A_{1s}$ or $A_{3s})$			3002.95(4)		2953.8(2)	
$v^0(E_{3d})$			3003.17(6)		2938.0(2)	
$v^0(E_{3s})$			3003.38(5)		2915.4(2)	
$v^0(A_{3d}$ or $A_{1d})$			3003.52(6)		2906.9(2)	
A	2.68323(13)	2.6176(17)	2.614672	2.6107(35)	2.664(30)	2.669693
B	0.66292(2)	0.66988(16)	0.653007	0.6513(14)	0.6541(11)	0.66302901
10^5D_J	0.112(3)	g.s.	g.s.	g.s.	g.s.	0.103174
10^5D_{JK}	0.131(7)	g.s.	g.s.	g.s.	g.s.	0.26604
10^5D_K	0.86(10)	g.s.	g.s.	g.s.	g.s.	0.885
$A\zeta$	0.31108(60)	1.4495(4)	−1.090(6)	−0.442(30)	1.10(3)	
$10^3\eta_J$	−0.066(3)					
$10^3\eta_K$	−0.60(1)					
10^3F	0.152(3)	0.176(40)				
10^2E	−0.33(10)	0.116(50)				

Table 5
Vibration–rotation-torsion parameters for the interaction matrix elements (Eqs. (3)–(6)). The vibrational states are labeled with 1, 2, 3, 4, 5 corresponding to degenerate states v_7, $v_8 + v_{11}$, $v_3 + 2v_4 + v_8$, $v_4 + v_{11} + v_{12}$, $v_3 + 3v_4 + v_{12}$. Numbers in parentheses are standard deviations in units of the last quoted digit.

Symbol	Interaction	Equation	Value (cm^{-1})
$W_{1,2}$	v_7, $v_8 + v_{11}$	(4)	5.8237(322)
$W_{KI1,2}$	v_7, $v_8 + v_{11}$	(4)	−0.0786(99)
$W_{13,2}$	v_7, $v_8 + v_{11}$	(4)	−0.0028(3)
$W_{1,3}$	v_7, $v_3 + 2v_4 + v_8$	(4)	2.4200(161)
$W_{KI1,3}$	v_7, $v_3 + 2v_4 + v_8$	(4)	0.3172(21)
$W_{13,3}$	v_7, $v_3 + 2v_4 + v_8$	(4)	−0.00107(3)
$W_{1,4}$	v_7, $v_4 + v_{11} + v_{12}$	(4)	0.84(12)
$W_{1,5}$	v_7, $v_3 + 3v_4 + v_{12}$	(4)	0.1841(40)
$W_{2,4}$	$v_8 + v_{11}$, $v_4 + v_{11} + v_{12}$	(4)	2.888(49)
$10^3F_{1,2}$	v_7, $v_3 + 2v_4 + v_8$	(3)	0.306(15)
$10^3F_{1,4}$	v_7, $v_4 + v_{11} + v_{12}$	(3)	0.10(fixed)
$10^2E_{1,2}$	v_7, $v_8 + v_{11}$	(5)	0.7687(99)
$10^4E_{K1,2}$	v_7, $v_8 + v_{11}$	(5)	−0.457(16)
$10^3E_{1,5}$	v_7, $v_3 + 3v_4 + v_{12}$	(5)	0.614(40)
$10^2E_{1,4}$	v_7, $v_4 + v_{11} + v_{12}$	(5)	−0.214(8)
$10^4E_{13,4}$	v_7, $v_4 + v_{11} + v_{12}$	(5)	0.043(2)
$10^4C_{1,5}$	v_7, $v_3 + 3v_4 + v_{12}$	(6)	0.157(13)

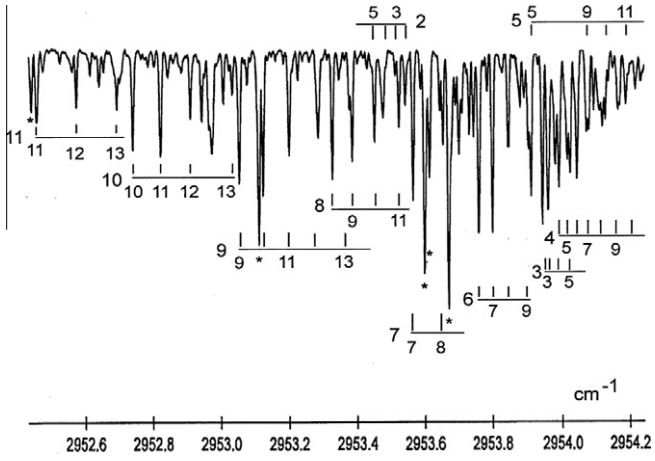

Fig. 5. ^qQ-branches of the parallel system $v_8 + v_{11}$ ($A_{4s} + A_{3s}$). The numbers above or below the horizontal bars are J-values, and those to the left or right are K-values. Some transition lines of the fundamental v_7 are marked by a star.

fit calculations. One of the main difficulties involved the determination of the relative energy order of the A_{4s} and A_{3s} components in both the $v_8 + v_{11}$ and $v_4 + v_{11} + v_{12}$ systems.

7. The fundamental v_5

The parallel fundamental v_5 is probably the most complicated band in this region. Pine and Lafferty [14] observed a strong perturbation with level crossing at K between 4 and 5. They also assigned 62 transitions to the perturber, all starting from $K = 4$ and 5 in the ground state. We identified the perturber to be the (+l)-levels of the perpendicular infrared active combination $v_2 + v_8$, on the basis of the values of its vibrational wavenumber and Coriolis coefficient. This state is strongly coupled to $v_2 + v_4 + v_{12}$ (see Fig. 2 and Table 1), whose vibrational energy is slightly higher and then closer to v_5, but the (+l)-levels of the two states cross as K increases because of the different values of ζ_8 (negative) and ζ_{12} (positive). Therefore the state which crosses v_5 at K between 4 and 5 is $v_2 + v_8$. Thus all the 62 assignments reported under label D in [14] should be attributed to $v_2 + v_8$, (+l)-side.

An intriguing observation by Pine and Lafferty [14] was that the torsional splittings in v_5 at J close to K are non-zero only for the even values of K. This should imply, among all the perturbations, the occurrence of a Fermi-type or z-Coriolis-type interaction sensible only for the even values of K. In principle, this is possible for the interaction with a vibrational state with quite large torsional splittings, so that only one torsional component would be close enough to interact with v_5. Since the torsional components occur in two pairs, one pair at the even values of K and the other one at the odd values of K, the component close to v_5 should be one of the first pair. Most presumably, interactions of this type may occur between v_5 (A_{4s}) and the parallel vibrational state $v_3 + 2v_4 + v_6$ (A_{4s}) (Fermi-type interaction), and between v_5 (A_{4s}) and the parallel vibrational state $v_3 + v_4 + 2v_9$ (A_{3s}) (z-Coriolis-type). In fact, both combinations lie slightly above v_5 (see Fig. 2) and, containing each one quantum of v_3, may show large torsional splittings because of the mechanism extensively treated in Ref. [24] and recalled at the end of Section 5.

Table 7 summarizes the assignments available in the 3.3 μm region. The different numbers of assignments in v_7 obtained in this work (229 K) and in Ref. [14] (119 K) are related to the different distributions of population at the two temperatures. In the v_7 band, we observe more transitions, reaching a higher value of $K''\Delta K$ (14 against 12) in the high frequency side. However, in the low frequency side, which is more perturbed, the less crowded spectrum at 119 K can be better analyzed. Therefore Pine and Lafferty [14] could reach the lowest $K''\Delta K$ value of −12 lower than ours ($K''\Delta K = -10$), in spite of the less favorable distribution of population.

Author's personal copy

Table 6
New assignments in the parallel system, $\nu_8 + \nu_{11}$ ($A_{4s} + A_{3s}$). Line positions are from this work; the values between parentheses are from [14]. Numbers listed in column "A" are relative absorption line intensities, in arbitrary units. The ground state vibration–rotation-torsion symmetries in the G_{36}(EM) extended molecular group are also given. They are all single valued, therefore the "s" subscript to the symmetry species can be omitted, as in the simpler G_{36} group. The ground state E'' energies were calculated using the constants reported in [2,23].

Line position (cm^{-1})	A	J'	K'	J''	K''	Sym.	E'' (cm^{-1})
2934.8276 (.8270)	14	13	9	14	9	$A_{1,2}$	301.6308
2935.6843 (.6835)	18	12	10	13	10	G	321.1685
2936.0577 (.0557)	16	12	9	13	9	$A_{1,2}$	283.0834
2936.9195 (.------)	8	11	10	12	10	G	303.9457
2937.2964 (.2962)	20	11	9	12	9	$A_{1,2}$	265.8593
2937.6198 (.6196)	14	11	8	12	8	G	231.7730
2938.5442 (.5439)	10	10	9	11	9	$A_{1,2}$	249.9589
2939.8079 (.8081)	16	9	9	10	9	$A_{1,2}$	235.3825
2941.3968 (.3967)	7	8	8	9	8	G	188.0411
2941.6823 (.6819)	12	8	7	9	7	G	157.9559
2942.9587 (.9582)	8	7	7	8	7	G	146.0268
2952.4541 (.4522)	20	11	11	11	11	G	330.1342
2952.5702 (.5693)	16	12	11	12	11	G	346.0321
2952.6898 (.6892)	16	13	11	13	11	G	363.2534
2952.7375 (.7375)	27	10	10	10	10	G	273.4712
2952.8193 (.8174)	28	11	10	11	10	G	288.0465
2952.9073 (.9067)	19	12	10	12	10	G	303.9457
2953.0302 (.0293)	13	13	10	13	10	G	321.1685
2953.0507 (.0506)	35	9	9	9	9	$A_{1,2}$	222.1304
2953.1203 (.1204)	37	10	9	10	9	$A_{1,2}$	235.3825
2953.1973 (.1970)	28	11	9	11	9	$A_{1,2}$	249.9589
2953.2829 (.2820)	23	12	9	12	9	$A_{1,2}$	265.8593
2953.3252 (.3257)	34	8	8	8	8	G	176.1126
2953.3752 (.3749)	17	13	9	13	9	$A_{1,2}$	283.0834
2953.3837 (.3835)	29	9	8	9	8	G	188.0411
2953.4490 (.4478)	24	10	8	10	8	G	201.2941
2953.5214 (.5215)	21	11	8	11	8	G	215.8715
2953.5628 (.5620)	38	7	7	7	7	G	135.4225
2953.6113 (.6108)	33	8	7	8	7	G	146.0268
2953.6506 (.6497)	25	9	7	9	7	G	157.9559
2966.3725 (.-----)	6	10	9	9	9	$A_{1,2}$	222.1304
2966.7022 (.7014)	15	10	8	9	8	G	188.0411
2967.7745 (.7736)	11	11	9	10	9	$A_{1,2}$	235.3825
2968.0987 (.0980)	12	11	8	10	8	G	201.2941
2969.1828 (.1819)	11	12	9	11	9	$A_{1,2}$	249.9589

8. First iteration of a database for the 3.3 μm region

The spectroscopic information available for the 3.3 μm region of the ethane spectrum in HITRAN 2008 [26] is rather limited. Indeed, it only includes parameters for the nine strong Q-branches of the ν_7 band: approximate parameters associated with artificial lines were obtained by Brown et al. [27] for eight of them and accurate parameters were determined by Pine and Rinsland [12] for $^pQ_3$ near 2976.8 cm^{-1} using subDoppler molecular-beam spectroscopy [28]. The GEISA database [29] only includes the latter information, i.e. the parameters of Pine and Rinsland [12] for the $^pQ_3$ branch.

Although the analysis carried out in the present work is far from complete, it can provide a significantly improved description of the ν_7 band. So, we combined positions, lower state energies and relative intensities of transitions (assuming that only ν_7 carries intensity) between 2900 and 3071 cm^{-1} from the present effort with recent N_2-broadening coefficients [30,31] to generate a database that could be useful for remote sensing. The database summarized in Table 8 is written in the format of HITRAN 2008 [26] and contains 4969 transitions involving five perpendicular bands ($\nu_8 + \nu_{11}$, ν_7, $\nu_3 + 3\nu_4 + \nu_{12}$, $\nu_4 + \nu_{11} + \nu_{12}$ and $\nu_3 + 2\nu_4 + \nu_8$).

Because of perturbations not accounted for in the Hamiltonian model, some line positions are not correctly predicted. To reduce the corresponding impact on the database, these calculated positions were recomputed using empirical upper state energies. These energies were obtained by adding to the measured positions of assigned lines the corresponding lower state energies, calculated using ground state ro-vibrational constants from [2,23], and were tabulated as a function of the ethane quantum numbers. In many cases, more than one unblended transition could be assigned to the same upper state level so that it was possible to obtain an averaged upper state value with a RMS precision of 0.0015 cm^{-1} or better. These empirical upper states improve the precision of many predicted positions in the range of quantum numbers summarized in Table 7. In the database, the altered positions are indicated by the HITRAN accuracy code = 4 (0.0001–0.001 cm^{-1}) [17], while a very conservative accuracy code = 2 (0.01–0.1 cm^{-1}) is set for the remaining predicted positions.

The predicted relative line intensities have been normalized by inspection of observed and calculated spectra. Their accuracy is therefore very conservatively characterized by a HITRAN code of 2 ("average or estimate") [17]. Self and N_2-broadening coefficients of C_2H_6 and their temperature dependences were estimated using the linear expressions reported by Devi et al. for ν_9 Q branch transitions at 822 cm^{-1} [30,31]. They have been applied to all the types of transitions (P, Q, R) in all the bands. The constants for the linear equations were applied from K'' = 0–3 for the broadening coefficients and K'' = 0–9 for their temperature dependence, the maximum K available being used for higher K transitions in the present database. The accuracies for broadening coefficients are conservatively set (HITRAN code = 2) with the warning that the uncertainty is unknown for $J > 31$. Finally, a constant value of −0.004 cm^{-1}/atm (HITRAN code = 1, "default or constant") was estimated for N_2-broadened pressure-induced shifts, from the average of two air-broadening measurements for $^rQ_0$ and $^pQ_3$ [28].

Table 8
Summary of the line-by-line database for $^{12}C_2H_6$ from 2900 to 3071 cm^{-1}. F_{min} and F_{max} are approximate beginning and ending wavenumbers (in cm^{-1}) of the range of transitions included in each band, along with the number of transitions. The maximum values of the quantum numbers J and K included are also provided. Note that 1468 of the line positions are recomputed using empirical upper state levels (see text).

Bands	ν_0 (cm^{-1})	F_{min}	F_{max}	#Lines	J_{max}	K_{max}
$\nu_8 + \nu_{11}$	2931.84	2902	3053	150	35	10
$\nu_4 + \nu_{11} + \nu_{12}$	2952.71	2936	3070	39	31	13
$\nu_3 + 3\nu_4 + \nu_{12}$	2928.5	2927	3044	51	32	10
ν_7	2985.040	2900	3071	4409	43	20
$\nu_3 + 2\nu_4 + \nu_8$	3003.26	2931	3069	320	38	8

Table 7
Summary of present C_2H_6 quantum assignments at 3.3 μm, and those reported by Pine and Lafferty [14] (given between parentheses).

Band	ν_0 (cm^{-1})	$K''\Delta K$	J_{max}	Number assigned
ν_7 (E_{1d})	2985.040	−10 to 14 (−12 to 12)	30 (26)	1103 (823)
$\nu_8 + \nu_{11}$ (E_{1d})	2931.84	−1 to 1	11	35
$\nu_3 + 2\nu_4 + \nu_8$ (E_{1d})	1480.558	−6	22	25
$\nu_8 + \nu_{11}$ (A_{4s}, A_{3s})	~2954	K up to 6 (up to 6)	21 (21)	311 (276)
ν_5 (A_{4s})	2895.6	(K up to 6)	(22)	(428)
$\nu_2 + \nu_8$ (E_{1d})	2863.1	4, 5 (4, 5)	15 (15)	62 (62)

Author's personal copy

9. Conclusion

Although we could not perform a global numerical analysis and fit of the whole infrared active CH stretching region of $^{12}C_2H_6$, we believe that this work represents a significant step toward the understanding of this part of the spectrum. We believe that we identified all the most important perturbers and interaction mechanisms responsible for the complex observed spectral patterns. We performed a numerical analysis limited to the ν_7 fundamental, accounting for the effect of four perturbing vibrational states. Moreover, we could find 95 new assignments in the perpendicular bands $\nu_8 + \nu_{11}$ and $\nu_3 + 2\nu_4 + \nu_8$, and in the parallel system $\nu_8 + \nu_{11}$, to be added to the sound and impressive body of assignments reported by Pine and Lafferty [14]. We also identified as $\nu_2 + \nu_8$ the perturber of ν_5 to whom we attributed the 62 perturber transitions, labeled D and correctly assigned by Pine and Lafferty [14] for what concerns rotational quantum numbers and torsional components.

The predictions from the present work provide quantum number assignments, lower state energies, and good line positions when computed from empirical upper state levels, while the recently measured absorption cross sections [15] characterize the intensity of the overall absorption with better accuracy. The present effort will eventually lead to a database for the 3.3 μm region of the ethane spectrum, to be combined to the database recently created for the 7 μm region [11], to form a new ethane compilation for the HITRAN and GEISA databases. However, further work is needed to improve the predicted line intensities in both spectral regions. All this may be relevant, owing to the importance of this spectral region in the applied research.

Acknowledgments

The authors are grateful to L.R. Brown for her constant support and helpful suggestions throughout this work. F.L. and C.dL. thank M. Herman for making his jet-cooled spectra available. J.V.D.A. acknowledges financial support from the *Fonds de la Recherche Scientifique* (FRS–FNRS, Belgium, contracts FRFC), the *Action de Recherches Concertées* of the *Communauté française de Belgique*, and the Belgian Federal Science Policy Office (contract SD/CS/07A, Advanced Exploitation of Ground-Based Measurements for Atmospheric Chemistry and Climate applications – II).

References

[1] J. Susskind, D.C. Reuter, D.E. Jennings, S.J. Daunt, W.E. Blass, G.W. Halsey, J. Chem. Phys. 77 (1982) 2728–2744.
[2] L. Henry, A. Valentin, W.J. Lafferty, J.T. Hougen, V. Malathy Devi, P.P. Das, K. Narahari Rao, J. Mol. Spectrosc. 100 (1983) 260–289.
[3] J. Susskind, L. Iredell, W.E. Blass, D.C. Reuter, G.W. Halsey, D.E. Jennings, J. Mol. Spectrosc. 192 (1983) 119–130.
[4] L. Borvayeh, N. Moazzen-Ahmadi, V.-M. Horneman, J. Mol. Spectrosc. 250 (2008) 51–56.
[5] J. Susskind, J. Mol. Spectrosc. 49 (1974) 331–342.
[6] F. Lattanzi, C. di Lauro, N. Legay-Sommaire, J. Mol. Spectrosc. 156 (1992) 227–236.
[7] M. Hepp, M. Herman, J. Mol. Spectrosc. 194 (1999) 87–94.
[8] F. Lattanzi, C. di Lauro, M. Herman, J. Vander Auwera, J. Mol. Spectrosc. 212 (2002) 308–314.
[9] F. Lattanzi, C. di Lauro, J. Vander Auwera, J. Mol. Spectrosc. 248 (2008) 134–145.
[10] F. Lattanzi, C. di Lauro, J. Vander Auwera, in preparation.
[11] C. di Lauro, F. Lattanzi, L.R. Brown, K. Sung, J. Vander Auwera, A.W. Mantz, M.A.H. Smith, Planet. Space Sci., in press.
[12] A.S. Pine, C.P. Rinsland, J. Quant. Spectrosc. Radiat. Transfer 62 (1999) 445–458.
[13] K. Magee-Sauer, M.J. Mumma, M.A. DiSanti, N. Dello Russo, E.L. Gibb, B.P. Boney, G.L. Villanueva, Icarus 194 (2008) 347–356.
[14] A.S. Pine, W.J. Lafferty, J. Res. Natl. Bur. Stand. 87 (1982) 237–256.
[15] J.J. Harrison, N.D.C. Allen, P.F. Bernath, J. Quant. Spectrosc. Radiat. Transfer 111 (2010) 357–363.
[16] M. Carleer, WSpectra: a Windows program to accurately measure the line intensities of high-resolution Fourier transform spectra, in: J.E. Russel, K. Shäfer, O. Lado-Bodowsky (Eds.), Remote Sensing of Clouds and the Atmosphere V, Proceedings of SPIE 4168, 2001, pp. 337–342.
[17] L.S. Rothman, D. Jacquemart, A. Barbe, D.C. Benner, M. Birk, L.R. Brown, M.R. Carleer, C. Chackerian Jr., K. Chance, L.H. Coudert, V. Dana, V.M. Devi, J.-M. Flaud, R.R. Gamache, A. Goldman, J.-M. Hartmann, K.W. Jucks, A.G. Maki, J.-Y. Mandin, S.T. Massie, J. Orphal, A. Perrin, C.P. Rinsland, M.A.H. Smith, J. Tennyson, R.N. Tolchenov, R.A. Toth, J. Vander Auwera, P. Varanasi, G. Wagner, J. Quant. Spectrosc. Radiat. Transfer 96 (2005) 139–204.
[18] P.R. Bunker, P. Jensen, Molecular Symmetry and Spectroscopy, second ed., NRC Research Press, Ottawa, 1998.
[19] M. Hepp, M. Herman, J. Mol. Spectrosc. 197 (1999) 56–63.
[20] J. Susskind, J. Mol. Spectrosc. 49 (1974) 1–17.
[21] J.T. Hougen, J. Mol. Spectrosc. 82 (1980) 92–116.
[22] C. di Lauro, F. Lattanzi, A. Valentin, Mol. Phys. 89 (1996) 663–676.
[23] F. Lattanzi, C. di Lauro, V.-M. Horneman, M. Herman, J. Vander Auwera, Mol. Phys. 105 (2007) 761–768.
[24] D. Bermejo, J. Santos, P. Cancio, J.M. Fernández-Sánchez, S. Montero, J. Chem. Phys. 97 (1992) 7055–7063.
[25] B. Kirtman, W.E. Palke, C.S. Ewig, J. Chem. Phys. 64 (1976) 1883–1890.
[26] L.S. Rothman, I.E. Gordon, A. Barbe, D.C. Benner, P.F. Bernath, M. Birk, V. Boudon, L.R. Brown, A. Campargue, J.-P. Champion, K. Chance, L.H. Coudert, V. Dana, V.M. Devi, S. Fally, J.-M. Flaud, R.R. Gamache, A. Goldman, D. Jacquemart, I. Kleiner, N. Lacome, W.J. Lafferty, J.-Y. Mandin, S.T. Massie, S. Mikhailenko, C.E. Miller, N. Moazzen-Ahmadi, O.V. Naumenko, A. Nikitin, J. Orphal, A. Predoi-Cross, V. Perevalov, A. Perrin, C.P. Rinsland, M. Rotger, M. Simeckova, M.A.H. Smith, K. Sung, S. Tashkun, J. Tennyson, R.A. Toth, A.C. Vandaele, J. Vander Auwera, J. Quant. Spectrosc. Radiat. Transfer 110 (2009) 533–572.
[27] L.R. Brown, C.B. Farmer, C.P. Rinsland, R.A. Toth, Appl. Opt. 26 (1987) 5154–5182.
[28] A.S. Pine, S.C. Stone, J. Mol. Spectrosc. 175 (1996) 21–30.
[29] N. Jacquinet-Husson, N.A. Scott, A. Chédin, L. Crépeau, R. Armante, V. Capelle, J. Orphal, A. Coustenis, A. Barbe, M. Birk, L.R. Brown, C. Camy-Peyret, C. Claveau, K. Chance, N. Christidis, C. Clerbaux, P.F. Coheur, V. Dana, L. Daumont, M.R. Debacker-Barilly, G. Di Lonardo, J.-M. Flaud, A. Goldman, A. Hamdouni, M. Hess, M.D. Hurley, D. Jacquemart, I. Kleiner, P. Köpke, J.-Y. Mandin, S. Massie, S. Mikhailenko, V. Nemtchinov, A. Nikitin, D. Newnham, A. Perrin, V.I. Perevalov, S. Pinnock, L. Régalia-Jarlot, C.P. Rinsland, A. Rublev, F. Schreier, L. Schult, K.M. Smith, S.A. Tashkun, J.-L. Teffo, R.A. Toth, V.G. Tyuterev, J. Vander Auwera, P. Varanasi, G. Wagner, J. Quant. Spectrosc. Radiat. Transfer 109 (2008) 1043–1059.
[30] V.M. Devi, C.P. Rinsland, D.C. Benner, R.L. Sams, T.A. Blake, J. Quant. Spectrosc. Radiat. Transfer 111 (2010) 1234–1251.
[31] V.M. Devi, D.C. Benner, C.P. Rinsland, M.A.H. Smith, R.L. Sams, T.A. Blake, J.-M. Flaud, K. Sung, L.R. Brown, A.W. Mantz, J. Quant. Spectrosc. Radiat. Transfer 111 (2010) 2481–2504.

Atmos. Meas. Tech., 7, 333–344, 2014
www.atmos-meas-tech.net/7/333/2014/
doi:10.5194/amt-7-333-2014
© Author(s) 2014. CC Attribution 3.0 License.

Atmospheric Measurement Techniques
Open Access

Spectrometric monitoring of atmospheric carbon tetrafluoride (CF_4) above the Jungfraujoch station since 1989: evidence of continued increase but at a slowing rate

E. Mahieu[1], R. Zander[1], G. C. Toon[2], M. K. Vollmer[3], S. Reimann[3], J. Mühle[4], W. Bader[1], B. Bovy[1], B. Lejeune[1], C. Servais[1], P. Demoulin[1], G. Roland[1], P. F. Bernath[5,6], C. D. Boone[7], K. A. Walker[8,7], and P. Duchatelet[1,*]

[1]Institute of Astrophysics and Geophysics of the University of Liège, Liège, Belgium
[2]Jet Propulsion Laboratory, California Institute of Technology, Pasadena, California, USA
[3]Empa, Laboratory for Air Pollution/Environmental Technology, Swiss Federal Laboratories for Materials Science and Technology, Duebendorf, Switzerland
[4]Scripps Institution of Oceanography, University of California at San Diego, La Jolla, California, USA
[5]Department of Chemistry and Biochemistry, Old Dominion University, Norfolk, Virginia, USA
[6]Department of Chemistry, University of York, York, UK
[7]Department of Chemistry, University of Waterloo, Ontario, Canada
[8]Department of Physics, University of Toronto, Toronto, Canada
[*]now at: Controlatom, Vilvoorde, Belgium

Correspondence to: E. Mahieu (emmanuel.mahieu@ulg.ac.be)

Received: 14 August 2013 – Published in Atmos. Meas. Tech. Discuss.: 21 August 2013
Revised: 22 November 2013 – Accepted: 17 December 2013 – Published: 31 January 2014

Abstract. The long-term evolution of the vertical column abundance of carbon tetrafluoride (CF_4) above the high-altitude Jungfraujoch station (Swiss Alps, 46.5° N, 8.0° E, 3580 m a.s.l.) has been derived from the spectrometric analysis of Fourier transform infrared solar spectra recorded at that site between 1989 and 2012. The investigation is based on a multi-microwindow approach, two encompassing pairs of absorption lines belonging to the R-branch of the strong ν_3 band of CF_4 centered at 1283 cm^{-1}, and two additional ones to optimally account for weak but overlapping HNO_3 interferences. The analysis reveals a steady accumulation of the very long-lived CF_4 above the Jungfraujoch at mean rates of $(1.38 \pm 0.11) \times 10^{13}$ molec cm^{-2} yr^{-1} from 1989 to 1997, and $(0.98 \pm 0.02) \times 10^{13}$ molec cm^{-2} yr^{-1} from 1998 to 2012, which correspond to linear growth rates of 1.71 ± 0.14 and 1.04 ± 0.02 % yr^{-1} respectively referenced to 1989 and 1998. Related global CF_4 anthropogenic emissions required to sustain these mean increases correspond to 15.8 ± 1.3 and 11.1 ± 0.2 Gg yr^{-1} over the above specified time intervals. Findings reported here are compared and discussed with respect to relevant northern mid-latitude results obtained remotely from space and balloons as well as in situ at the ground, including new gas chromatography mass spectrometry measurements performed at the Jungfraujoch since 2010.

1 Introduction

Carbon tetrafluoride (CF_4) or tetrafluoromethane is a perfluorocarbon (PFC-14) whose unambiguous presence in the earth's atmosphere, from the boundary layer (Rasmussen et al., 1979) to the stratosphere (Goldman et al., 1979), as well as its "near inertness" in the atmosphere (Cicerone, 1979) have raised increasing attention and concern among the scientific community since the 1980s.

Its main anthropogenic source is primary aluminum production, during which CF_4 is released through "anode effect" episodes (e.g., Penkett et al., 1981; Khalil et al., 2003). Since the 1980s, non-negligible CF_4 emissions have also been released increasingly by manufacturing of semiconductors and other electronic devices (e.g., "plasma etching"; Tsai

et al., 2002). The only known but poorly quantified natural sources of CF_4 are of lithospheric origin (e.g., Gassmann, 1974; Cicerone, 1979; Harnisch et al., 1996a; Harnisch and Eisenhauer, 1998; Harnisch, 2000). Recently, Deeds et al. (2008) presented the first in situ evidence for this lithospheric flux, which leads to a background contribution to atmospheric carbon tetrafluoride that lies between 35 and 45 ppt (parts per trillion dry air mole fraction) with the lower value favored on the basis of reported accuracies and precisions (for an overview, see Table 2 of Mühle et al., 2010).

PFCs are long-lived species with lifetimes of many thousand years (e.g., Ravishankara et al., 1993). With an atmospheric lifetime estimated to exceed 50 000 yr, CF_4 is by far the longest lived PFC (WMO-2010, 2011). Combined with a high global warming potential of at least 7390 on a 100 yr time horizon (WMO-2010, 2011), this compound is a strong greenhouse gas whose anthropogenic emissions are deservedly targeted for regulation under the Kyoto Protocol (IPCC, 2001). Because of the absence of atmospheric sinks, CF_4 shows a nearly constant mixing ratio profile throughout the atmosphere (e.g., Zander et al., 1992, 1996; Nassar et al., 2006) and its vertical gradient – as quantified, for example, by Fabian et al. (1996), and Harnisch et al. (1996b) using stratospheric balloon-borne cryogenic air sampling between 1987 and 1995 – is only caused by a delayed propagation of the ground-based emissions to higher altitudes. The presence of CF_4 in the stratosphere was first reported by Goldman et al. (1979) who identified the strong ν_3 band of CF_4 at 1283 cm^{-1} in a solar limb spectrum recorded in 1978 at 25 km altitude, from aboard a balloon platform. Its vertical profile between 15 and 50 km was derived by Zander et al. (1987) from ATMOS (Atmospheric Trace MOlecule Spectroscopy; Farmer, 1987) solar limb observations during the Spacelab 3 shuttle mission in 1985, from subsequent MkIV FTIR balloon flights (e.g., Toon, 1991; Sen et al., 1996), and from the satellite ACE-FTS instrument (Atmospheric Chemistry Experiment Fourier Transform Spectrometer, e.g., Bernath et al., 2005; Brown et al., 2011).

Recent ground-level air sampling and in situ measurements of CF_4 in both hemispheres (e.g., Khalil et al., 2003; Mühle et al., 2010) or remotely from space (e.g., Rinsland et al., 2006; Brown et al., 2011) have indicated a significant slowdown in the rate of increase of atmospheric CF_4, attributed to efforts undertaken by the aluminum industry to limit its emissions during "anode effect" episodes (International (Primary) Aluminium Institute, 1996, 2009). However, significant uncertainties remain, amongst others due to the increase of Chinese aluminum production and insufficiently defined emission factors for Chinese smelters (International Aluminium Institute, 2013). Additionally, the magnitude and temporal evolution of CF_4 emissions from the semi-conductor industry remain very unclear, despite efforts by the World Semiconductor Council to reduce their emissions (WSC, 2013). Based on the inversion with a 2-D box model of a selected subset of AGAGE (Advanced Global Atmospheric Gases Experiment) ground-level measurements in both hemispheres from the early 1970s to 2008, Mühle et al. (2010, Fig. 4) derived global CF_4 emissions which increased during the 1970s to reach their maximum during the early 1980s (17.5 ± 1 Gg yr^{-1}) and subsequently declined progressively to stabilize at about 11 Gg yr^{-1} by 2000 until 2008. We refer the reader to Mühle et al. (2010) and references therein, for a detailed and exhaustive discussion regarding the evolution of CF_4 in the global troposphere from 1973 to 2008.

This paper reports on the mean evolution of the vertical carbon tetrafluoride loading integrated over the free troposphere and stratosphere above the high-altitude Jungfraujoch station, derived from the spectrometric analysis of Fourier transform infrared (FTIR) solar observations made at that site between 1989 and 2012. Related findings are compared with relevant ones also obtained remotely from space- and balloon-borne solar observations, with new in situ gas chromatography mass spectrometry (GCMS) measurements performed by Empa (Laboratory for Air Pollution/Environmental Technology) at the Jungfraujoch since 2010, as well as with recently reconstructed in situ ground level baseline growth rates of CF_4 in both hemispheres, reported by Mühle et al. (2010). Our concluding remarks include recommendations for improving the relative accuracies of spectroscopic CF_4 line parameters which currently remain estimated at ± 6 %, as compared to the achieved 1–2 % for the in situ data.

Since 1990, the University of Liège research activities are performed within the frame of the Network for the Detection of Atmospheric Composition Change (NDACC; see http://www.ndacc.org).

2 Instrumentation and original data sets

2.1 FTIR remote-sensing measurements and retrieval strategy

The long-term CF_4 time series presented and analyzed in this study has been derived from the analysis of solar spectra recorded between January 1989 and December 2012 under clear-sky conditions at the high-altitude International Scientific Station of the Jungfraujoch (hereafter ISSJ; Swiss Alps, 46.5° N, 8.0° E; 3580 m a.s.l.). The recordings were made with two very high spectral resolution FTIR spectrometers, a "home-made" instrument primarily used until 1995, and progressively replaced by a faster, more sensitive commercial Bruker-120 HR instrument (Zander et al., 2008).

The initial database investigated here consists of over 5500 spectra recorded with an optical filter covering the 750 to 1400 cm^{-1} spectral region, thus encompassing the strongest infrared band of CF_4 – the ν_3 centered at 1283 cm^{-1}. Spectral resolutions (defined as the reciprocal of twice the maximum optical path difference) alternate between 0.004

and 0.006 cm^{-1}, depending on the rate of solar zenith angle variation during the day, and scanning time of successive recordings. Signal-to-noise (S/N) ratios vary between 150 to more than 2500 (average spectra resulting from several successive individual Bruker scans, predominantly around midday, when solar zenith angles vary slowly).

The spectral analyses were performed with the SFIT-2 v3.91 fitting algorithm, a code based on the optimal estimation formalism of Rodgers (1976) and specifically developed to retrieve vertical column abundances and mixing ratio profiles of atmospheric gases from FTIR observations (Connor et al., 1995; Rinsland et al., 1998). This code has been successfully intercompared with the PROFFIT retrieval algorithm (e.g., Hase et al., 2004; Duchatelet et al., 2010), the other tool in use by the NDACC FTIR community for monitoring numerous tropospheric and stratospheric target gases, worldwide.

Line parameters adopted in the spectral fitting process were taken from the HITRAN 2004 spectroscopic compilation (Rothman et al., 2005), including the August 2006 updates (e.g., Esposito et al., 2007). For CF_4, we selected a set of pseudo-lines whose intensities and temperature-dependent parameters were derived by one of us (G.C.T.) from a series of high-resolution and high-S/N laboratory spectra recorded by Nemtchinov and Varanasi (2003) under pressure and temperature conditions typical of those encountered in the atmosphere. These pseudo-lines were also used for all CF_4 remote sensing measurements intercompared in Sect. 3 with our ISSJ findings.

The model atmosphere adopted above the 3.58 km Jungfraujoch altitude consists of a 39 layer scheme with progressively increasing thicknesses to reach 100 km altitude. The pressure-temperature profiles are those specifically computed for the ISSJ location on a daily noontime basis by the National Centers for Environmental Prediction (NCEP, Washington, DC; see http://www.ncep.noaa.gov).

While most of the Q- and R-branch features of the ν_3 band of CF_4 can be used for remote sensing retrievals from space between about 15 and 50 km altitude (see Fig. 18 in Zander et al., 1987), strong absorptions by H_2O, HDO, N_2O, CO_2, CH_4, and weaker ones (i.e., by HNO_3, $ClONO_2$ and further H_2O isotopologues) combine to heavily interfere with CF_4 features in low altitude spectra. Consideration of the relative importance of these interferences in typical solar recordings at the high-altitude, rather dry ISSJ site led us to adopt as "RUN 1" the spectral interval from 1284.73 to 1285.15 cm^{-1} displayed in Fig. 1, which encompasses 6 of the strongest R-branch features of the CF_4 ν_3 band. Because of the poor fitting over the two middle CF_4 features, severely affected by H_2O and HDO interferences, we excluded from our initial database all spectra whose water vapor content exceeded 8×10^{21} molec cm^{-2}, as well as those observed at solar zenith angles larger than 75 degrees to also minimize line-wing depression by the strong N_2O line centered at 1284.7 cm^{-1}. In addition and as illustrated in Fig. 1, we restricted the subsequent "RUN2" to a composite window in which only the CF_4 profile was further adjusted. Frame B shows that the RMS (root mean square) residuals reduced by about a factor 2 in RUN 2 as compared to RUN 1. This RMS decrease was confirmed over the entire database, while the related CF_4 columns reduced by less than 0.7 % on average.

The a priori vertical concentration profile for the CF_4 target gas was set constant at 72 ppt throughout the atmosphere above ISSJ, consistent with values and associated uncertainties derived for the stratosphere (in the 15 to 45 km altitude range) from nearly 1400 solar occultations performed between February 2004 and mid-2012 in the 36.5 to 56.5° N latitude zone by the ACE-FTS instrument. As there is poor vertical information content in the individual spectra, the constant a priori profile was simply scaled during our fitting procedure.

For all interfering molecules, averaged mixing ratio profiles based on WACCM (the Whole Atmosphere Community Climate Model; e.g., Chang et al., 2008) model predictions for the 1980–2020 period and the ISSJ station were used as a priori. To reliably account for the weak interfering absorption features by HNO_3 (see Frame A of Fig. 1), its concentration profile was pre-retrieved for each spectrum from a simultaneous fit to two NDACC-dedicated spectral intervals (i.e., 867.05–870.00 and 872.25–874.00 cm^{-1}; see Wolff et al., 2008). It was then assumed in the consecutive fitting steps RUN 1 and RUN 2. During RUN 1, the vertical distributions of CF_4, CO_2, N_2O, HDO, H_2O, H_2O_2, $H_2{}^{17}O$ and $H_2{}^{18}O$ were independently scaled while in RUN 2, only the CF_4 profile was further adjusted. A S/N ratio of 500, commensurate with the noise level of most retained spectra, was adopted throughout the spectral fitting calculations. Inspection of an exo-atmospheric solar atlas by Farmer and Norton (1989) revealed only a very weak solar absorption feature at 1284.7666 cm^{-1}. It was neglected in the SFIT-2 retrievals, after verification that it had negligible influence on the CF_4 results.

After further exclusion of observations with S/N ratios lower than 300 and of high and low individual-carbon tetrafluoride-column outliers falling out of the $\pm 2.5\sigma$ confidence interval, the retained database upon which the results and discussion in Sect. 2.2 are based includes 3034 individual CF_4 column measurements above ISSJ, encompassing 1272 observational days.

Table 1 provides an error budget resulting from major instrumental and analytical uncertainties that may affect typical individual CF_4 column amounts above the site. They were evaluated according to referenced comments or perturbations to a representative subset of spectra. As is often the case when dealing with relatively "new anthropogenic" molecules (for which detailed fundamental spectroscopic laboratory studies are in progress and await validation), the largest systematic error in this work results from the CF_4 pseudo-line parameters (intensities and temperature dependences), which we set at ± 6 % on the basis of evaluations discussed by

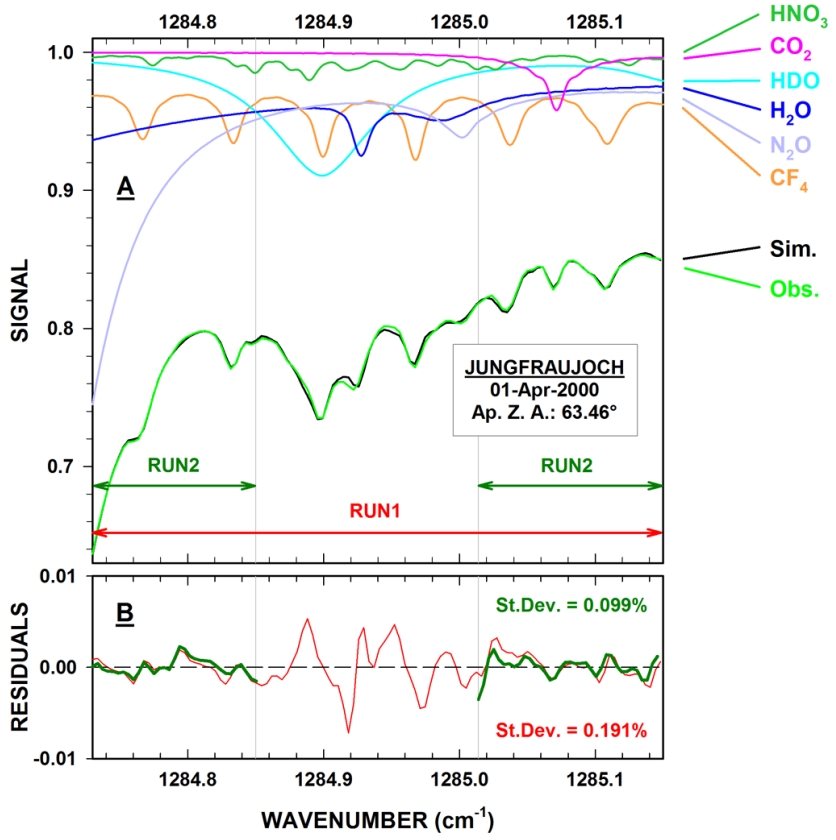

Fig. 1. Frame A displays the characteristic absorptions of CF_4 and the five most significant interfering gases in the "Run 1" micro-window selected for our CF_4 retrievals, computed for a typical ISSJ observation on 1 April 2000 (at 63.46° apparent solar zenith angle and 0.006 cm^{-1} resolution). Their combination results in the black simulation trace (labeled "Sim.") which, compared to the actual observation (green curve, labeled "Obs.") leads to the red residuals (observed minus calculated signals) in Frame B. Because of strong perturbations by the H_2O and HDO interferences, this initial "Run 1" was followed by a second composite "Run 2", with corresponding residuals displayed by the thick green trace in Frame B.

Irion et al. (2002). A "quality-test" performed with a synthetic line-list covering the R-branch of the CF_4 ν_3 band, recently released by Boudon et al. (2011), will be evoked in Sect. 3.

2.2 GCMS in situ measurements

The second original data set reported for the first time in this paper results from ground-based gas chromatography – mass spectrometry measurements conducted at ISSJ by Empa. The analyses are performed with a Medusa instrument described in detail by Miller et al. (2008), using 2 L of cryogenically trapped air alternated with measurements of a standard to calibrate the instrument. This leads to one air measurement every two hours. The CF_4 measurements at ISSJ began in 2008 but due to some instrumental difficulties, data are only reported here from 2010 onwards. Their precision is $\sim 0.4\,\%$ while the accuracy is estimated at 1–2 %. The measurements are based on the Scripps Institution of Oceanography (SIO) SIO-2005 calibration scale and are tightly linked into the AGAGE network.

3 Results and discussion

Figure 2 reproduces the daily mean vertical column abundances (expressed in numbers of CF_4 molecules per square cm; left vertical scale) derived above ISSJ between 1989 and 2012. They have been normalized to the mean local pressure monitored at the site during the past decades (i.e., 654 hPa) versus the daily surface pressure measured at noontime. The database reveals the relative sparseness and dispersion of the daily mean columns prior to about 1995, resulting from less frequent observations with the home-made instrument and their lower S/N ratios. However, as no statistically significant difference was observed between day-coincident CF_4 columns by both instruments, they have been merged in the post-1995 daily mean averages.

The right side scale of Fig. 2 reproduces the mean constant mixing ratio above ISSJ as returned by the SFIT-2 code on the basis of the physical P-T model atmosphere adopted for each day. The uncertainty on the conversion from left-to-right scale is less than $\pm 3\,\%$. These mixing ratios correspond to moist air values. However, correction factors to

Table 1. Major sources of random and systematic errors on typical individual CF_4 total column retrievals above the Jungfraujoch.

Error sources	Max. error (%)	Comments
	Random errors	
Spectra quality	4	Zero offset, S/N and instruments bias
H_2O and HDO a priori profiles	3	Changes by a factor 2 in a priori slope and local altitude variability
Temperature/pressure profile	4	± 4 K around NCEP noon profile; also column to mixing ratio conversion
Modeling of wing slopes	2	Water vapor and N_2O wing slopes affecting the local continuum
TOTAL	~ 7	
	Systematic errors	
CF_4 spectroscopy	6	According to Irion et al. (2002)
H_2O and HDO spectroscopy	2	Assuming the HITRAN-04 uncertainties
CF_4 profile	3	Mixing time uncertainty
Forward model	1	Retrieval algorithm-related
ILS	2	± 10 % misalignment and instruments bias
TOTAL	~ 7	

get dry air mole fractions would be very small, since only the driest observations were retained here (water vapor column of maximum 8×10^{21} molec cm^{-2}, for an air column of $\sim 1.4 \times 10^{25}$ molec cm^{-2} above ISSJ).

At first glance, two major features emerge from Fig. 2, namely

i. the large increase of the CF_4 column loading above ISSJ by 2.8×10^{14} molec cm^{-2} between 1989 and 2012, corresponding to +35 % when referenced to 1989. This increase is entirely of anthropogenic origin; it jumps to over 80 % when the "natural" background level of ~ 35 ppt, recently reported by Worton et al. (2007) and Mühle et al. (2010), is taken into account. As about one third of the atmospheric mass is located below the Jungfraujoch altitude (mean pressure = 654 hPa) and assuming that the very stable CF_4 gas is uniformly distributed through the atmosphere, its increase above ISSJ translates into a total column change above sea level equal to $+4.35 \times 10^{14}$ molec cm^{-2}, from 1989 to 2012. Globally, this has required a cumulated anthropogenic CF_4 emission at the ground totaling nearly 320 Gg over that time frame.

ii. a significant slowing of the rate of CF_4 accumulation which we first evaluated by splitting the entire database into two subsets, that is, before and after 1 January 1998, respectively, the blue and green plus (+) symbols in Fig. 2. Application of the statistical bootstrap re-sampling method developed by Gardiner et al. (2008; a tool based on a Fourier series that allows calculation, at the 2σ confidence level, of the long-term linear component as well as the seasonal modulation of a given data set), returned mean linear yearly increases above ISSJ of $(1.38 \pm 0.11) \times 10^{13}$ and $(0.98 \pm 0.02) \times 10^{13}$ molec cm^{-2}, respectively, for the periods 1989–1997 and 1998–2012. Extrapolation of these increases down to sea level, as done in the previous paragraph, translates into yearly total column changes above sea level equal to $(2.14 \pm 0.17) \times 10^{13}$ and $(1.50 \pm 0.03) \times 10^{13}$ molec cm^{-2}. Globally, these changes require CF_4 emission rates equal to (15.8 ± 1.25) Gg yr^{-1} and (11.1 ± 0.2) Gg yr^{-1} for the above mentioned periods.

When taking into account a reasonable lag time of three years for ground-level emissions to uniformly mix in the free troposphere and in the stratosphere (e.g., Fabian et al., 1996; Waugh and Hall, 2002; Anderson et al., 2000; Stiller et al., 2008; Diallo et al., 2012), these derived CF_4 emission rates are commensurate with the 1986 to 2009 time averaged global emission estimates reported by Mühle et al. (2010, Table 6, i.e., 14.6 and 10.8 Gg yr^{-1}, for the 1986–1994 and 1995–2009 periods, respectively). A noticeable CF_4 seasonal cycle (close to 2 %, peak-to-peak amplitude) also deduced with the bootstrap re-sampling tool (Gardiner et al., 2008) is essentially ascribable to the seasonal variation of temperature versus pressure ratios in our adopted layered model atmosphere and to resulting impacts upon temperature- and pressure-dependent line intensities and half widths.

In a second evaluation approach, the CF_4 database was "modeled" with both a second order function and a nonparametric least-squares fit, respectively displayed in Fig. 2 by the black- and red curves. For the red curve, a local smoothing technique is applied, assuming a Gaussian weighting function and sampling 20 % of the data points at once. The actual bandwidth progressively considers all the measurements along the x axis (see Rinsland et al., 2003; and reference therein). Discrete six-year time averaged trends determined from tangential derivatives to the black line at 1992.0,

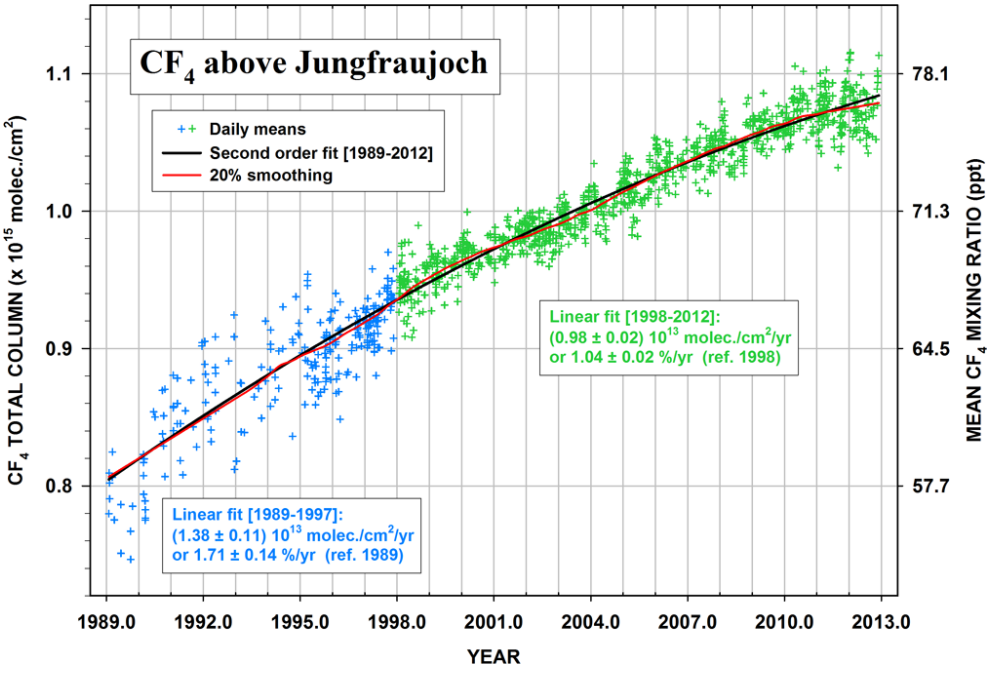

Fig. 2. FTIR time series of CF_4 daily mean vertical column abundances above the Jungfraujoch (expressed in numbers of CF_4 molecules per square cm), normalized to a mean local pressure of 654 hPa. The solid black and red curves correspond to a second order fit and a 20 % smoothing function to the data points, respectively. The coefficients of the second order black curve are (from the highest order to the independent term): −0.0194, 78.72 and −79835, in units of 10^{13} molec cm^{-2}. In the same units and rank, the coefficients of the linear regression are 1.385, −2675 and 0.979, −1862, for the 1989–1997 (blue) and 1998–2012 (green) time periods, respectively. The right side scale corresponds to the conversion of our measured columns into mean constant mixing ratios above the site, expressed in ppt (parts per trillion).

1998.0, 2004.0 and 2010.0, and related global emissions are provided in Table 2. The latter are in line with the significant slowing in the CF_4 emission rates at the ground that began during the late 1980s, amplified during the early 1990s and leveled off subsequently, as synthesized by Mühle et al. (2010, Fig. 4). The mean global emission of 17.6 Gg yr^{-1} derived here for the 1989 to 1994 time interval is in good agreement with the mean increase rate of 18 Gg yr^{-1} derived by Zander et al. (1996) from upper stratospheric CF_4 measurements made in the northern hemisphere by the ATMOS FTIR instrument during the shuttle missions that occurred between 1985 and 1994 (Gunson et al., 1996).

The small but noticeable differences between the red- and black curves in Fig. 2 are indicative of slow temporal growth regime changes by up to +/−1.5 Gg yr^{-1} around the second order fit.

A "quality-test" covering our entire database, performed by replacing the adopted CF_4 pseudo-lines by the synthetic line parameters of Boudon et al. (2011), as included in the "supplemental" section of the Hitran 2008 compilation (Rothman et al., 2009), led to the following appreciations: (i) the line positions are good; (ii) on average, the fitting residuals are ∼ 30 % higher; (iii) the retrieved CF_4 columns are consistently larger by ∼ 25 %. We believe that this last observed difference may result from the fact that the Boudon line list, currently restricted to the ν_3 R-branch, is only based on one high-resolution FTIR laboratory spectrum at 296 K and a low pressure of 0.17 torr, while the pseudo-lines were derived from a large set of spectra recorded at numerous typical pressure and temperature sets encountered throughout the atmosphere (Nemtchinov and Varanasi, 2003). However, another possible explanation is that this significant bias might also result from contributions, for example, by underlying hot bands of CF_4 not present in the Boudon line list (Rothman et al., 2009), while they are captured by cross-section measurements.

The conversion of our measured CF_4 column abundances into mean constant mixing ratios above ISSJ (see vertical scales in Fig. 2), assuming that this molecule is uniformly mixed throughout the entire atmosphere, allows some comparison with ground-level in situ- and FTIR solar occultation measurements from balloon- and space-based platforms. A few relevant examples, referring to data obtained at northern mid-latitudes, are displayed in Fig. 3, where the thick black line corresponds to the mixing ratios associated to the second order black curve fitted in Fig. 2 to our daily mean CF_4 columns above the site. The green curve reproduces an excerpt of the 1973 to 2010 assimilated monthly CF_4 mixing ratios for the northern extra-tropics (i.e., 30–90° N), based on AGAGE archived air samples and in situ measurements

Table 2. Discrete six-year time averaged CF_4 trends based on tangential derivatives to the black line of Fig. 2, and corresponding emissions at 1992.0, 1998.0, 2004.0, and 2010.0.

Data source	1989–1994	1995–2000	2001–2006	2007–2012
Columns above ISSJ in 10^{13} molec cm^{-2} yr^{-1}	1.53 ± 0.41	1.29 ± 0.11	1.05 ± 0.07	0.82 ± 0.08
Corresponding global emissions in Gg yr^{-1}	17.6 ± 4.7	14.8 ± 1.25	12.0 ± 0.8	9.4 ± 0.9
Emissions from in situ measurements in Gg yr^{-1}*	15.1 ± 0.7	12.4 ± 0.6	11.0 ± 0.6	10.6 ± 0.4

* from Mühle et al. (2010), assuming a lag time of 3 yr for ground-level emissions to propagate in the free troposphere and stratosphere.

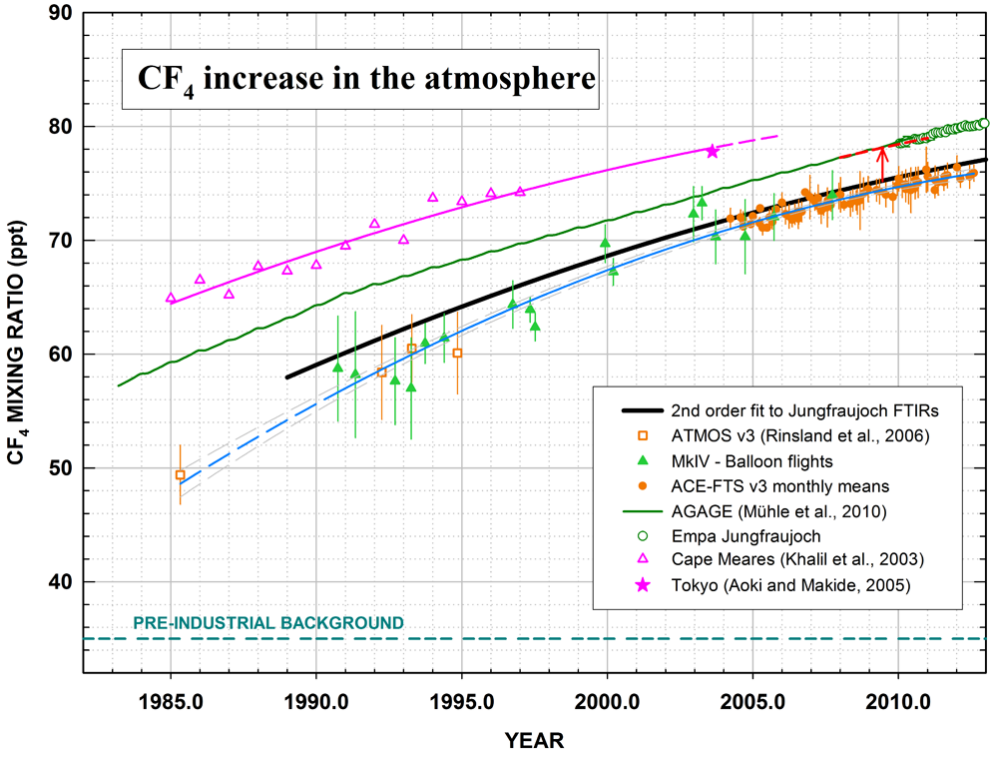

Fig. 3. Comparison between selected CF_4 mixing ratio time series and trends deduced from infrared remote-sensing and in situ surface measurements (see legend and text for their identification). The various data sets can all be reconciled in term of absolute concentration when accounting for the associated uncertainties affecting the retrieved quantities (calibration scales, line parameters) and time needed for a thorough mixing of CF_4 throughout the atmosphere. See text for details.

performed at Mace Head (Ireland) and at Trinidad Head (California, USA), and reported on the recent SIO-2005 calibration scale by Mühle et al. (2010) with a stated accuracy of $\sim$1 to 2 %. The green open circles show the monthly mean CF_4 mixing ratios at the ISSJ site measured by Empa within AGAGE, also reported on the SIO-2005 calibration scale, and in excellent agreement with the other AGAGE data. The pink open triangles correspond to yearly averaged CF_4 mixing ratios derived by Khalil et al. (2003) from clean air samples collected at Cape Meares (45.5° N; OR-USA) and reported on the MPAE 86 (Max Planck Institute for Aeronomy) calibration scale which has a stated uncertainty of $\sim$10 % (Fabian et al., 1996). The pink star corresponds to a CF_4 mixing ratio of 77.8 ± 0.6 ppt derived from one air sample collected in Tokyo (35.6° N) in August 2003, using a specific calibration approach based on the atmospheric ^{80}Kr abundance as reference; no calibration accuracy is reported (Aoki and Makide, 2005). The second order curve fitted to the pink triangles and the star is a typical representation of numerous ground-based monitoring efforts conducted in situ at northern mid-latitudes during the late 1970s onwards, as illustrated in Fig. 1 of Mühle et al. (2010). The latter showed that the MPAE 86 and UEA (University of East Anglia) calibration scales adopted during these earlier activities have reported uncertainties ranging by up to $\pm$ 15 % and that related measurements can thus be reconciled with the recent, much more accurate ones based on the SIO-2005 calibration scale (1–2 %).

The filled orange circles represent stratospheric monthly mean CF_4 mixing ratios between 20 and 45 km altitude,

Table 3. Annual rate of increase expressed in ppt yr^{-1} for atmospheric CF_4 computed for three reference times.

Data source	1990.0	2000.0	2010.0	Reference/Accuracy in %
Cape Meares	0.85	0.59	–	Khalil et al. (2003)/MPAE 86 (±10 %)
+ Tokyo				Aoki and Makida (2005)
AGAGE	1.08	0.69	0.67	Mühle et al. (2010)/SIO-05 (±1–2 %)
+ Empa	–	–	0.63	Empa/SIO-05 (±1–2 %)
ULg-FTIR	1.09	0.82	0.58	This work – see Table 1 (±7 %)
ATMOS+MkIV	1.40	0.95	–	Rinsland et al. (2006) (±11 %)
+ACE-FTS	–	–	0.60	This work (±7 %)

derived from over 1400 solar occultation measurements (Version 3 products; Boone et al., 2013) in the 36.5 to 56.5 northern latitude zone between 2004 and 2012 with the satellite-embarked ACE-FTS instrument (Bernath et al., 2005). The four orange square symbols reproduce updated mean stratospheric CF_4 mixing ratios between ∼ 20 to 40 km altitude, derived from the 1985, 1992, 1993 and 1994 ATMOS missions (Version 3; Irion et al., 2002) as reported by Rinsland et al. (2006). Finally, the filled green triangles correspond to the average mixing ratios between 10 and 35 km altitude derived from individual MkIV balloon flights performed over 1990 to 2007, between 33 and 68° N latitude (e.g., Sen et al., 1996). The error bars associated to the ATMOS, MkIV and ACE data points represent the standard deviations of the means. As all the space- and balloon-borne CF_4 retrievals were performed using the same cross-section parameters, not only for R-branch features but also for the strong Q-branch of the CF_4 ν_3 band, we assumed that they could reasonably be interlinked with a 2nd order fitting, represented in Fig. 3 by the blue curve. It clearly shows the significant but slowing increase of CF_4 throughout the stratosphere over the past decades. The limited number of spectra recorded by ATMOS during the short pioneering US shuttle flights, as compared to the ongoing ACE-FTS mission, clearly shows the advantage of regular, long-term monitoring approaches, which is also true for ground-based investigations. Table 3 provides mean annual mixing ratio increases determined by taking derivatives at 1990.0, 2000.0, and 2010.0 to the continuous curves displayed in Fig.3.

The dashed horizontal line in Fig. 3 corresponds to the natural background level of ∼ 35 ppt recently reported by Worton et al. (2007) and Mühle et al. (2010); it has been drawn here to better illustrate the relative anthropogenic contribution to the total CF_4 atmospheric burden which, since the turn into the 21st century, has overtaken the natural loading.

The differences between the various data sets displayed in Fig. 3 are obviously linked, at least partially, to atmospheric transport and can be ascribed to the fact that the instruments involved sound different layers of the atmosphere, namely the boundary layer for AGAGE and Empa as well as Cape Meares and Tokyo, the free troposphere and stratosphere for our FTIR observations, and the stratosphere only for the satellite and balloon data. Consequently, changes in the emissions of a long-lived gas at the ground will mix in the global troposphere within 1 to 2 yr, and propagate in the stratosphere by upwelling via the tropical pipe, reaching 20 km mid-latitudes within 3 to 5 yr (e.g., Elkins et al., 1996; Stiller et al., 2008). Examples of such time delays have also been reported by Anderson et al. (2000) who found that the inorganic chlorine and fluorine loadings in the upper stratosphere lag the related organic loadings at the ground by 4.5 to 5.5 yr. Inputs from the two-dimensional 12-box model of Mühle et al. (2010) indicate for 30–90° N a mean difference between the tropospheric and stratospheric mixing ratios of 2 ppt over the last decade and of more than 3 ppt in the early 1980s, when the CF_4 emissions were stronger. In order to assess the adequacy (and possible bias) of having adopted a constant distribution in our column retrieval calculations and mixing ratio conversion, we built an a priori profile accounting for the time needed for CF_4 emitted at the ground to propagate and mix in the stratosphere. Since the 12-box model only included a single stratospheric level, we based the construction of our a priori CF_4 distribution on a profile of mean age of stratospheric air parcels produced by Diallo et al. (2012), using ERA-Interim reanalyses and a Lagrangian model. Their findings have been confronted to satellite, aircraft and balloon observations, showing good agreement, including at northern mid-latitudes. For this region of the atmosphere of interest here, Figs. 2 and 6 of Diallo et al. (2012) provide profiles of mean age of air, with values close to 2 yr at 16 km, 3 yr at 18 km, 4 yr at 20 km and more than 6 yr above 25 km (i.e., showing a gradient of approximately 0.5 yr per km in the lower mid-latitude stratosphere). Assuming the CF_4 annual rate of change which prevailed over the last decade as derived by AGAGE (i.e., 0.7 ppt per year), our a priori profile was built such as to present a mixing ratio difference with the surface concentration of −1.4 ppt at 16 km, −2.1 ppt at 18 km, −2.8 ppt at 20 km, and so on, up to a constant difference of −4.5 ppt for altitudes above 25 km. All the observations of 2009 were refitted with this non-constant vertical distribution, returning total columns on average 2.5 % higher. Conversion of these columns into corresponding surface mixing

ratios resulted in values systematically higher by 3.7 %, or +2.9 ppt with respect to our standard run assuming a constant vertical distribution. Applying a vertical shift of +2.9 ppt to the FTIR function for 2009 brings it in very good agreement with the AGAGE and Empa time series, as indicated by the dashed red segment matching the green curve and open circles in Fig. 3. This result gives good credibility on the absolute scale (1–2 %) provided by the SIO-2005 calibration standard as well as by the CF_4 spectroscopic parameters used in our analyses.

Nonetheless, it remains that the uncertainties associated with the various CF_4 remote data sets presented in Fig. 3, namely 7 % for ISSJ (see Table 1), 11 % for ATMOS (Rinsland et al., 2006), 10 % for MkIV (Sen et al., 1996) and 7 % for the recent ACE-FTS data (Brown et al., 2011; Rinsland et al., 2006) have to be maintained as such, until further spectroscopic laboratory and related theoretical investigations narrow these uncertainties.

4 Summary and conclusions

Since the 1980s, the presence of carbon tetrafluoride (CF_4) in the earth's atmosphere has attracted increasing attention for three reasons, namely (i) its continued accumulation in our atmosphere, (ii) its extremely long lifetime, and (iii) its high global warming potential, 7390 times larger than that of CO_2, justifying priority recommendations by the Kyoto Protocol for CF_4 monitoring and regulation. In response to these recommendations, strongly endorsed by the Network for the Detection of Atmospheric Composition Change, we have reported the first spectrometric measurement from the ground of the atmospheric CF_4, and their comparison with recently reported ground-level in situ mixing ratios which have a quoted accuracy of 1 to 2 % (Mühle et al., 2010).

Owing to the location of the Jungfraujoch (3.58 km a.s.l.) above the polluted and wet boundary layer of the low troposphere, we have established a special retrieval procedure that minimizes the perturbations by numerous interfering atmospheric gases, in particular the residual H_2O and HDO above the site (see Fig. 1), and successfully determined with an accuracy of ± 7 % the loading of CF_4 throughout the free troposphere and the stratosphere (i.e., over two thirds of the total mass of the atmosphere) between 1989 and 2012. The spectrometric analysis of a subset of solar spectra recorded at ISSJ during this period (i.e., over 3000 spectra, encompassing 1272 days) has allowed, for the first time, the measurement of the long-term evolution of the CF_4 column abundance from ground-based remote FTIR observations.

As illustrated in Fig. 2, the yearly mean CF_4 column increase above ISSJ was found equal to $(1.38 \pm 0.11) \times 10^{13}$ molec cm^{-2} between 1989 and 1997, and $(0.98 \pm 0.02) \times 10^{13}$ molec cm^{-2} from 1998 to 2012. Globally, these increases require 15.8 ± 1.3 and 11.1 ± 0.2 Gg yr^{-1}, respectively, resulting from anthropogenic CF_4 emissions at the ground in the earlier part of the record, primarily from the aluminum industry, and in the latter part also from the manufacturing of electronic devices. The significant slowing in the rate of increase is probably the result of efforts undertaken by the aluminum industry to comply with recommendations from the Kyoto Protocol. Considering our uncertainty, which is almost entirely due to the quality of the CF_4 spectroscopic parameters adopted here (± 6 %), our findings are in good agreement with results derived by Mühle et al. (2010) based on selected ground level in situ measurements in the Northern Hemisphere from 1973 to 2008, and by new in situ GCMS measurements performed since 2010 by Empa at the Jungfraujoch. Moreover, we showed that the adoption of a vertical distribution for CF_4, accounting for the time needed for this very long-lived species to propagate and mix in the stratosphere, provided FTIR converted mixing ratios in very good agreement with the AGAGE data sets, giving good confidence in the absolute mixing ratios derived from the analyses involved here for both techniques.

We also note that the CF_4 FTIR time series is in excellent agreement (within 2 %) with solar occultation measurements made from satellites (ATMOS, ACE) and balloons (MkIV). This demonstrates the reliability of the spectral fitting procedures for retrieving CF_4 from the ground, in particular, the handling of the interfering H_2O lines (which are negligible in solar occultation retrievals above 10 km altitude).

During this study, we noticed that a synthetic CF_4 linelist produced by Boudon et al. (2011) was available in the formal HITRAN 2008 compilation (Rothman et al., 2009). Running our entire data set with these line-by-line parameters showed a reasonably good fit of the CF_4 line positions and contours. However, the retrieved column abundances were consistently larger by ~ 25 % than those derived with the pseudo-lines adopted here. This corroborates a conclusion by Boudon et al. (2011), stating that "the new linelist is still approximate concerning line intensities". We strongly encourage the continuation of such fundamental efforts aimed at improving the accuracy of line parameters for important atmospheric species.

Finally, we expect that the new in situ local measurements of CF_4 performed by Empa at the Jungfraujoch within AGAGE open interesting possibilities for in-depth statistical intercomparison with our FTIR time series. This side-by-side, high-mountain operation is currently unique, worldwide, and is complementary in terms of techniques involved, vertical atmospheric coverage and, hopefully, long-term regular operation.

Acknowledgements. This work was funded primarily by the Belgian Federal Science Policy Office (SSD AGACC-II and PRODEX A3C projects). The financial support of MeteoSwiss (Global Atmosphere Watch, GAW) is further acknowledged. We thank the International Foundation High Altitude Research Stations Jungfraujoch and Gornergrat (HFSJG, Bern) and the University

of Liège for supporting the facilities needed to perform the observations and their analyses. We are also grateful to the Fédération Wallonie-Bruxelles and the F.R.S. – FNRS for supporting mission expenses and laboratory developments, respectively. E. Mahieu is Research Associate with the F.R.S. – FNRS. The Liège team wishes to thank Olivier Flock for his excellent technical support. Thanks are also extended to all people having contributed to FTIR data acquisition at the Jungfraujoch, including colleagues from the Royal Observatory of Belgium and from the Belgian Institute for Space Aeronomy, Brussels. The GCMS Medusa measurements are conducted under the auspices of the Swiss national research project HALCLIM with financial support from the Swiss Federal Office for the Environment (FOEN). Collaboration within AGAGE is also acknowledged. The ACE mission is supported primarily by the Canadian Space Agency.

Edited by: G. Stiller

References

Anderson, J., Russell, J. M., Solomon, S., and Deaver, L. E.: Halogen Occultation Experiment confirmation of stratospheric chlorine decreases in accordance with the Montreal Protocol, J. Geophys. Res., 105, 4483–4490, 2000.

Aoki, N. and Makide, Y.: The concentration of krypton in the atmosphere – Its revision after half a century, Chem. Lett., 34, 1396–1397, 2005.

Bernath, P. F., McElroy, C. T., Abrams, M. C., Boone, C. D., Buttler, M., Camy-Peyret, C., Carleer, M., Clerbaux, C., Coheur, P.-F., Colin, R., DeCola, P., De Mazière, M., Drummond, J. R., Dufour, D., Evans, W. F. J., Fast, H., Fussen, D., Gilbert, K., Jennings, D. E., Llewellyn, E. J., Lowe, R. P., Mahieu, E., McConnell, J. C., McHugh, M., McLeod, S. D., Michaud, R., Midwinter, C., Nassar, R., Nichitiu, F., Nowlan, C., Rinsland, C. P., Rochon, Y. J., Rowlands, N., Semeniuk, K., Simon, P., Skelton, R., Sloan, J. J., Soucy, M.-A., Strong, K., Tremblay, P. Turnbull, D., Walker, K. A., Walkty, I., Wardle, D. A., Wehrle, V., Zander, R., and Zou, J.: Atmospheric Chemistry Experiment (ACE): mission overview, Geophys. Res. Lett., 32, L15S01, doi:10.1029/2005GL022386, 2005.

Boone, C. D., Walker, K. A., and Bernath, P. F.: Version 3 retrievals for the Atmospheric Chemistry Experiment Fourier Transform Spectrometer (ACE-FTS), in: the Atmospheric Chemistry Experiment ACE at 10: A solar Occultation Anthology, edited by: Bernath, P. F., ISBN 978-0-937194-54-9, A. Deepak Publishing, 103–127, 2013.

Boudon, V., Mitchell, J., Domanskaya, A., Maul, C., Georges, R., Benidar, A., and Harter, W. G.: High-resolution spectroscopy and analysis of the $\nu_3/2\nu_4$ dyad of CF_4, Mol. Phys., 109, 2273–2290, 2011.

Brown, A. T., Chipperfield, M. P., Boone, C. D., Wilson, C., Walker, K. A., and Bernath, P. F.: Trends in atmospheric halogen containing gases since 2004, J. Quant. Spectrosc. Ra., 112, 2552–2566, 2011.

Chang, L., Palo, S., Hagan, M., Richter, J., Garcia, R., Riggin, R., and Fritts, D.: Structure of the migrating diurnal tide in the Whole Atmosphere Community Climate Model (WACCM), Adv. Space. Res., 41, 1397–1406, 2008.

Cicerone, R. J.: Atmospheric carbon tetrafluoride – Nearly inert gas, Science, 206, 59–61, 1979.

Connor, B. J., Parrish, A., Tsou, J.-J., and McCormick, P.: Error analysis of the ground-based microwave ozone measurements during STOIC, J. Geophys. Res., 100, 9283–9291, 1995.

Deeds, D. A., Vollmer, M. K., Kulongoski, J. T., Miller, B. R., Mühle, J., Harth, C. M., Izbicki, J. A., Hilton, D. R., and Weiss, R. F.: Evidence for crustal degassing of CF_4 and SF_6 in Mojave Desert groundwaters, Geochim. Cosmochim. Acta, 72, 4, 999–1013, doi:10.1016/j.gca.2007.11.027, 2008.

Diallo, M., Legras, B., and Chédin, A.: Age of stratospheric air in the ERA-Interim, Atmos. Chem. Phys., 12, 12133–12154, doi:10.5194/acp-12-12133-2012, 2012.

Duchatelet, P., Demoulin, P., Hase, F., Ruhnke, R., Feng, W., Chipperfield, M. P., Bernath, P. F., Boone, C. D., Walker, K. A., and Mahieu, E.: Hydrogen fluoride total and partial column time series above the Jungfraujoch from long-term FTIR measurements: Impact of the line-shape model, characterization of the error budget and seasonal cycle, and comparison with satellite and model data, J. Geophys. Res., 115, D22306, doi:10.1029/2010JD014677, 2010.

Elkins, J. W., Fahey, D. W., Gilligan, J. M., Dutton, G. S., Baring, T. J., Volk, C. M., Dunn, R. E., Myers, R. C., Montzka, S. A., Wamsley, P. R., Hayden, A. H., Bulter, J. H., Thompson, T. M., Swanson, T. H., Dlugokencky, E. J., Novelli, P. C., Hurst, D. F., Lobert, J. M., Ciciora, S. J., McLaughlin, R. J., Thompson, T. L., Winkler, R. H., Fraser, P. J., Steele, L. P., and Lucarelli, M. P.: Air-borne gas chromatograph for in-situ measurements of long-lived species in upper troposphere and lower stratosphere, Geophys. Res. Let., 23, 347–350, 1996.

Esposito, F., Grieco, G., Masiello, G., Pavese, G., Restieri, R., Serio, C., and Cuomo, V.: Intercomparison of line-parameter spectroscopic databases using downwelling spectral radiance, Q. J. R. Meteorol. Soc., 133, 191–202, 2007.

Fabian, P., Borchers, R., Leifer, R., Subbaraya, B. H., Lal, S., and Boy, M.: Global stratospheric distribution of halocarbons, Atmos. Environ., 30, 1787–1796, 1996.

Farmer, C. B.: High resolution infrared spectroscopy of the sun and the Earth's atmosphere from space, Microchem. Acta, 3, 189–214, 1987.

Farmer, C. B. and Norton, R. H.: A high-resolution atlas of the infrared spectrum of the sun and the earth atmosphere from space, Vol. I The Sun, NASA Reference Publication 1224, 1989.

Gardiner, T., Forbes, A., de Mazière, M., Vigouroux, C., Mahieu, E., Demoulin, P., Velazco, V., Notholt, J., Blumenstock, T., Hase, F., Kramer, I., Sussmann, R., Stremme, W., Mellqvist, J., Strandberg, A., Ellingsen, K., and Gauss, M.: Trend analysis of greenhouse gases over Europe measured by a network of ground-based remote FTIR instruments, Atmos. Chem. Phys., 8, 6719–6727, doi:10.5194/acp-8-6719-2008, 2008.

Gassmann, M.: Freon-14 in pure Krypton and in Atmosphere, Naturwissenschaften, 61, 127–127, 1974.

Goldman, A., Murcray, D. G., Murcray, F. J., Cook, G. R., van Allen, J. W., Bonomo, F. S., and Blatherwick, R. D.: Identification of the ν_3 vibration-rotation band of CF_4 in infrared balloon-borne solar spectra, Geophys. Res. Lett., 6, 609–612, 1979.

Gunson, M. R., Abbas, M., Abrams, M. C., Allen, M., Brown, L. R., Brown, T. L., Chang, A. Y., Goldman, A., Irion, F. W., Lowes, L. L., Mahieu, E., Manney, G. L., Michelsen, H. A.,

Newchurch, M. J., Rinsland, C. P., Salawitch, R. J., Stiller, G. P., Toon, G. C., Yung, Y. L., and Zander, R.: The Atmospheric Trace Molecule Spectroscopy (ATMOS) experiment: Deployment on the ATLAS space shuttle missions, Geophys. Res. Lett., 23, 2333–2336, 1996.

Harnisch, J.: Atmospheric perfluorocarbons: sources and concentrations, in: Non-CO_2 greenhouse gases: scientific understanding, control and implementation, edited by: van Ham, J., Baede, A. P. M., Meyer, L. A., and Ybema, R., Kluwer Academic Publishers, Netherlands, 205–210, 2000.

Harnisch, J. and Eisenhauer, A.: Natural CF_4 and SF_6 on Earth, Geophys. Res. Lett., 25, 2401–2404, 1998.

Harnisch, J., Borchers, R., Fabian, P., Gäggeler, H. W., and Schotterer, U.: Effect of natural tetrafluoromethane, Nature, 384, p. 32, 1996a.

Harnisch, J., Borchers, R., Fabian, P., and Maiss, M.: Tropospheric trends for CF_4 and C_2F_6 since 1982 derived from SF_6 dated stratospheric air, Geophys. Res. Lett., 23, 1099–1102, 1996b.

Hase, F., Hannigan, J. W., Coffey, M. T., Goldman, A., Hopfner, M., Jones, N. B., Rinsland, C. P., and Wood, S. W.: Intercomparison of retrieval codes used for the analysis of high-resolution ground-based FTIR measurements, J. Quant. Spectrosc. Ra., 87, 25–52, 2004.

Intergovernmental Panel on Climate Change, in Climate Change 2001: The scientific basis, edited by: Houghton, J. T., Ding, Y., Griggs, D. J., Noguer, M., van der Linden, P. J., Dai, X., Maskell, K., and Johnson, C. A., Univ. of Cambridge Press, New York, 2001.

International Aluminium Institute: The International Aluminium Institute Report on the Aluminium Industry Global Perfluorocarbon Gas Emissions Reduction Programme – Results of the 2007 Anode Effect Survey, International Aluminium Institute, London, 2009.

International Aluminium Institute: The International Aluminium Institute Report on the Aluminium Industry's Global Perfluorocarbon Gas Emissions Reduction Programme – Results of the 2012 Anode Effect Survey, International Aluminium Institute, London, 2013.

International Primary Aluminium Institute: Anode effect and PFC emission survey 1990–1993, International Aluminium Institute, London, 1996.

Irion, F. W., Gunson, M. R., Toon, G. C., Brown, L. R., Chang, A. Y., Eldering, A., Mahieu, E., Manney, G. L., Michelsen, H. A., Moyer, E. J., Newchurch, M. J., Osterman, G. B., Rinsland, C. P., Salawitch, R. J., Sen, B., Yung, Y. L., and Zander, R.: The Atmospheric Trace Molecule Spectroscopy (ATMOS) experiment version 3 data retrievals, Appl. Opt., 41, 6968–6979, 2002.

Khalil, M. A. K., Rasmussen, R. A., Culbertson, J. A., Prins, J. M., Grimsrud, E. P., and Shearer, M. J.: Atmospheric perfluorocarbons, Environ. Sci. Technol., 37, 4358–4361, 2003.

Miller, B. R., Weiss, R. F., Salameh, P. K., Tanhua, T., Greally, B. R., Mühle, J., and Simmonds, P. G.: Medusa: A sample preconcentration and GC/MS detector system for in situ measurements of atmospheric trace halocarbons, hydrocarbons, and sulfur compounds, Anal. Chem., 80, 1536–1545, doi:10.1021/ac702084k, 2008.

Mühle, J., Ganesan, A. L., Miller, B. R., Salameh, P. K., Harth, C. M., Greally, B. R., Rigby, M., Porter, L. W., Steele, L. P., Trudinger, C. M., Krummel, P. B., O'Doherty, S., Fraser, P. J., Simmonds, P. G., Prinn, R. G., and Weiss, R. F.: Perfluorocarbons in the global atmosphere: tetrafluoromethane, hexafluoroethane, and octafluoropropane, Atmos. Chem. Phys., 10, 5145–5164, doi:10.5194/acp-10-5145-2010, 2010.

Nassar, R., Bernath, P. F., Boone, C. D., McLeod, S. D., Skelton, R., Walker, K. A., Rinsland, C. P., and Duchatelet, P.: A global inventory of stratospheric fluorine in 2004 based on Atmospheric Chemistry Experiment Fourier transform spectrometer (ACE-FTS) measurements, J. Geophys. Res., 111, D22313, doi:10.1029/2006JD007395, 2006.

Nemtchinov, V. and Varanasi, P.: Thermal infrared absorption cross-sections of CF_4 for atmospheric applications, J. Quant. Spectrosc. Ra., 82, 461–471, 2003.

Penkett, S. A., Prosser, N. D. J., Rasmussen, R. A., and Khalil, M. A. K.: Atmospheric measurements of CF_4 and other fluorocarbons containing the CF_3 grouping, J. Geophys. Res., 86, 5172–5178, 1981.

Rasmussen, R. A., Penkett, S. A., and Prosser, N.: Measurement of carbon tetrafluoride in the atmosphere, Nature, 277, 549–551, 1979.

Ravishankara, A. R., Solomon, S., Turnispeed, A. A., and Warren, R. F.: Atmospheric lifetimes of long-lived halogenated species, Science, 259, 194–199, 1993.

Rinsland, C. P., Jones, N. B., Connor, B. J., Logan, J. A., Pougatchev, N. S., Goldman, A., Murcray, F. J., Stephen, T. M., Pine, A. S., Zander, R., Mahieu, E., and Demoulin, P.: Northern and southern hemisphere ground-based infrared measurements of tropospheric carbon monoxide and ethane, J. Geophys. Res., 103, 28197–28218, 1998.

Rinsland, C. P., Mahieu, E., Zander, R., Jones, N. B., Chipperfield, M. P., Goldman, A., Anderson, J., Russell III, J. M., Demoulin, P., Notholt, J., Toon, G. C., Blavier, J.-F., Sen, B., Sussmann, R., Wood, S. W., Meier, A., Griffith, D. W. T., Chiou, L. S., Murcray, F. J., Stephen, T. M., Hase, F., Mikuteit, S., Schulz, A., and Blumenstock, T., Long-term trends of inorganic chlorine from ground-based infrared solar spectra: past increases and evidence for stabilization, J. Geophys. Res., 108, 4252, doi:10.1029/2002JD003001, 2003.

Rinsland, C. P., Mahieu, E., Zander, R., Nassar, R., Bernath, P. F., Boone, C. D., and Chiou, L. S.: Long-term stratospheric carbon tetrafluoride (CF_4) increase inferred from 1985–2004 space-based solar occultation measurements, Geophys. Res. Lett., 33, L02808, doi:10.1029/2005GL024709, 2006.

Rodgers, C. D.: Retrieval of atmospheric temperature and composition from remote measurements of thermal radiation, Rev. Geophys., 14, 609–624, 1976.

Rothman, L. S., Jacquemart, D., Barbe, A., Chris Benner, D., Birk, M., Brown, L. R., Carleer, M. R., Chackerian Jr., C., Chance, K., Coudert, L. H., Dana, V., Devi, V. M., Flaud, J.-M., Gamache, R. R., Goldman, A., Hartmann, J.-M., Jucks, K. W., Maki, A. G., Mandin, J.-Y., Massie, S. T., Orphal, J., Perrin, A., Rinsland, C. P., Smith, M. A. H., Tennyson, J., Tolchenov, R. N., Toth, R. A., Vander Auwera, J., Varanasi, P., and Wagner G.: The HITRAN 2004 molecular spectroscopic database, J. Quant. Spectrosc. Ra., 96, 139–204, 2005.

Rothman, L. S., Gordon, I. E., Barbe, A., Chris Benner, D., Bernath, P. F., Birk, M., Boudon, V., Brown, L. R., Campargue, A., Champion, J.-P., Chance, K., Coudert, L. H., Dana, V., Devi, V. M., Fally, S., Flaud, J.-M., Gamache, R. R., Gold-

man, A., Jacquemart, D., Kleiner, I., Lacome, N., Lafferty, W. J., Mandin, J.-Y., Massie, S. T., Mikhailenko, S. N., Miller, C. E., Moazzen-Ahmadi, N., Naumenko, O. V., Nikitin, A. V., Orphal, J., Perevalov, V. I., Perrin, A., Predoi-Cross, A., Rinsland, C. P., Rotger, M., Simeckova, M., Smith, M. A. H., Sung, K., Tashkun, S. A., Tennyson, J., Toth, R. A., Vandaele, A. C., and Vander Auwera, J.: The HITRAN 2008 molecular spectroscopic database, J. Quant. Spectrosc. Ra., 110, 533–572, 2009.

Sen, B., Toon, G. C., Blavier, J.-F., Fleming, E. L., and Jackman, C. H.: Balloon-borne observations of midlatitude fluorine abundance, J. Geophys. Res., 101, 9045–9054, 1996.

Stiller, G. P., von Clarmann, T., Höpfner, M., Glatthor, N., Grabowski, U., Kellmann, S., Kleinert, A., Linden, A., Milz, M., Reddmann, T., Steck, T., Fischer, H., Funke, B., López-Puertas, M., and Engel, A.: Global distribution of mean age of stratospheric air from MIPAS SF6 measurements, Atmos. Chem. Phys., 8, 677–695, doi:10.5194/acp-8-677-2008, 2008.

Toon, G. C.: The JPL MkIV interferometer, Opt. Photonics News, 2, 19–21, 1991.

Tsai, W.-T., Chen, H.-P., and Hsien, W.-Y.: A review of uses, environmental hazards and recovery/recycle technologies of perfluorocarbons (PFCs) emissions from the semiconductor manufacturing processes, J. Loss Prev. Process Ind., 15, 65–75, 2002.

Waugh, D. and Hall, T.: Age of stratospheric air: Theory, observations and models, Rev. Geophys., 40, 1010, doi:10.1029/2000RG000101, 2002.

WMO (World Meteorological Organization): Scientific Assessment of Ozone Depletion: 2010, Global Ozone Research and Monitoring Project, Report N° 52, Geneva, Switzerland, 2011.

Wolff, M. A., Kerzenmacher, T., Strong, K., Walker, K. A., Toohey, M., Dupuy, E., Bernath, P. F., Boone, C. D., Brohede, S., Catoire, V., von Clarmann, T., Coffey, M., Daffer, W. H., De Mazière, M., Duchatelet, P., Glatthor, N., Griffith, D. W. T., Hannigan, J., Hase, F., Höpfner, M., Huret, N., Jones, N., Jucks, K., Kagawa, A., Kasai, Y., Kramer, I., Küllmann, H., Kuttippurath, J., Mahieu, E., Manney, G., McElroy, C. T., McLinden, C., Mébarki, Y., Mikuteit, S., Murtagh, D., Piccolo, C., Raspollini, P., Ridolfi, M., Ruhnke, R., Santee, M., Senten, C., Smale, D., Tétard, C., Urban, J., and Wood, S.: Validation of HNO_3, $ClONO_2$, and N_2O_5 from the Atmospheric Chemistry Experiment Fourier Transform Spectrometer (ACE-FTS), Atmos. Chem. Phys., 8, 3529–3562, doi:10.5194/acp-8-3529-2008, 2008.

World Semiconductor Council: Joint Statement of the 16th Meeting of the World Semiconductor Council (WSC), Lisbon, Portugal, 2013.

Worton, D. R., Sturges, W. T., Gohar, L. K., Shine, K. P., Martinerie, P., Oram, D. E., Humphrey, S. P., Begley, P., Gunn, L., Barnola, J. M., Schwander, J., and Mulvaney, R.: Atmospheric trends and radiative forcing of CF_4 and C_2F_6 inferred from firn air, Environ. Sci. Technol., 41, 2184–2189, 2007.

Zander, R., Rinsland, C. P., Farmer, C. B., and Norton, R. H.: Infrared spectroscopic measurements of halogenated source gases in the stratosphere with the ATMOS instrument, J. Geophys. Res., 92, 9836–9850, 1987.

Zander, R., Gunson, M. R., Farmer, C. B., Rinsland, C. P., Irion, F. W., and Mahieu, E.: The 1985 chlorine and fluorine inventories in the stratosphere based on ATMOS observations at 30° north latitudes, J. Atmos. Chem., 15, 171–186, 1992.

Zander, R., Solomon, S., Mahieu, E., Goldman, A., Rinsland, C. P., Gunson, M. R., Abrams, M. C., Chang, A. Y., Salawitch, R. J., Michelsen, H. A., Newchurch, M. J., and Stiller, G. P.: Increase of stratospheric carbon tetrafluoride (CF_4) based on ATMOS observations from space, Geophys. Res. Lett., 23, 2353–2356, 1996.

Zander, R., Mahieu, E., Demoulin, P., Duchatelet, P., Roland, G., Servais, C., De Mazière, M., Reimann, S., and Rinsland, C. P.: Our changing atmosphere: Evidence based on long-term infrared solar observations at the Jungfraujoch since 1950, Sci. Total Environ.t, 391/2-3, 185–195, 2008.

Atmos. Chem. Phys., 11, 1989–2013, 2011
www.atmos-chem-phys.net/11/1989/2011/
doi:10.5194/acp-11-1989-2011
© Author(s) 2011. CC Attribution 3.0 License.

Atmospheric Chemistry and Physics

Importance of secondary sources in the atmospheric budgets of formic and acetic acids

F. Paulot[1], D. Wunch[1], J. D. Crounse[2], G. C. Toon[3], D. B. Millet[4], P. F. DeCarlo[5,12,*], C. Vigouroux[6], N. M. Deutscher[7,], G. González Abad[8], J. Notholt[9], T. Warneke[9], J. W. Hannigan[10], C. Warneke[11,12], J. A. de Gouw[11,12], E. J. Dunlea[12,13], M. De Mazière[6], D. W. T. Griffith[7], P. Bernath[8], J. L. Jimenez[12,13], and P. O. Wennberg[1]**

[1]Division of Engineering and Applied Sciences, California Institute of Technology, Pasadena, California, USA
[2]Division of Chemistry and Chemical Engineering, California Institute of Technology, Pasadena, California, USA
[3]Jet Propulsion Laboratory, California Institute of Technology, Pasadena, California, USA
[4]University of Minnesota, Department of Soil, Water and Climate, St. Paul, Minnesota, USA
[5]Department of Atmospheric and Oceanic Sciences, University of Colorado, Boulder, Colorado, USA
[6]Belgian Institute for Space Aeronomy, Brussels, Belgium
[7]School of Chemistry, University of Wollongong, Wollongong, Australia
[8]Department of Chemistry, University of York, York, UK
[9]Institute of Environmental Physics, Bremen, Germany
[10]National Center for Atmospheric Research, Boulder, Colorado, USA
[11]Earth System Research Laboratory, Chemical Sciences Division, NOAA, Boulder, Colorado, USA
[12]Cooperative Institute for Research in Environmental Sciences, University of Colorado, Boulder, Colorado, USA
[13]Department of Chemistry and Biochemistry, University of Colorado, Boulder, Colorado, USA
[*]now at: AAAS Science and Technology Policy Fellow hosted at the US EPA, Washington, DC, USA
[**]now at: Institute of Environmental Physics, Bremen, Germany

Received: 18 September 2010 – Published in Atmos. Chem. Phys. Discuss.: 20 October 2010
Revised: 23 February 2011 – Accepted: 25 February 2011 – Published: 4 March 2011

Abstract. We present a detailed budget of formic and acetic acids, two of the most abundant trace gases in the atmosphere. Our bottom-up estimate of the global source of formic and acetic acids are ∼1200 and ∼1400 Gmol yr^{-1}, dominated by photochemical oxidation of biogenic volatile organic compounds, in particular isoprene. Their sinks are dominated by wet and dry deposition. We use the GEOS-Chem chemical transport model to evaluate this budget against an extensive suite of measurements from ground, ship and satellite-based Fourier transform spectrometers, as well as from several aircraft campaigns over North America. The model captures the seasonality of formic and acetic acids well but generally underestimates their concentration, particularly in the Northern midlatitudes. We infer that the source of both carboxylic acids may be up to 50% greater than our estimate and report evidence for a long-lived missing secondary source of carboxylic acids that may be associated with the aging of organic aerosols. Vertical profiles of formic acid in the upper troposphere support a negative temperature dependence of the reaction between formic acid and the hydroxyl radical as suggested by several theoretical studies.

Correspondence to: F. Paulot
(paulot@caltech.edu)

1 Introduction

Formic (HCOOH, hereafter FA) and acetic (CH_3COOH, hereafter AA) acids are among the most abundant and ubiquitous trace gases in the atmosphere. They have been detected in remote, rural, polar, marine and urban environments in the gas-phase as well as in clouds and in aerosols (Keene and Galloway, 1988; Chebbi and Carlier, 1996; Khare et al., 1999).

Sources of FA and AA include direct emissions from biomass burning, biofuel, fossil fuel, soil, vegetation, as well as secondary production from gas-phase and aqueous photochemistry (Chebbi and Carlier, 1996; Khare et al., 1999). Measurements of the isotopic composition of FA and AA have shown that they are primarily composed of modern carbon (Glasius et al., 2000, 2001), consistent with major

biogenic and biomass burning sources. Furthermore, most field measurements show a remarkable correlation between FA and AA suggesting similar sources. The sources of FA and AA remain, however, very poorly understood and several investigations (Poisson et al., 2000; von Kuhlmann et al., 2003a; Ito et al., 2007) have pointed to large inconsistencies between measurements and model predictions.

Sinks of FA and AA are better understood. Both acids are relatively long-lived in the gas-phase with respect to OH photooxidation ($\tau_{FA} \simeq 25$ days and $\tau_{AA} \simeq 10$ days at $T = 260$ K and [OH]=10^6 molec cm^{-3}). Because both gases are very soluble, their primary atmospheric sink is thought to be deposition (Chebbi and Carlier, 1996). Irreversible uptake on dust can also be an important regional sink (Falkovich et al., 2004).

Better constraints on the budget of FA and AA are important to understand patterns of rain acidity particularly in remote regions (Galloway et al., 1982). More generally, since FA and AA are major trace gases in the atmosphere and have few anthropogenic sources, the study of their budget offers a glimpse at the interaction between the biosphere and the atmosphere.

In this work, we derive a detailed inventory of FA and AA sources and sinks. We then use a chemical transport model to evaluate the resulting budget against measurements from an extensive suite of ground, aircraft and satellite-based measurements. Major discrepancies between the model and the measurements are investigated and several avenues for further research are discussed.

2 Global budget

We use the GEOS-Chem global 3-D chemical transport model (Bey et al., 2001) to investigate the budget of FA and AA. In the standard GEOS-Chem mechanism (v8.3), photochemical sources of AA include ozonolysis of isoprene and reaction of peroxyacyl radicals with HO_2 and other peroxy radicals (RO_2) while sinks are limited to its reaction with OH. FA is not treated explicitly.

In the following, we describe the sources and sinks of FA and AA and their implementation into the GEOS-Chem framework. In this work, the model is driven by the GEOS-5 assimilated meteorology from the NASA Goddard Earth Observing System. The horizontal resolution is degraded here to $4^\circ \times 5^\circ$ and the vertical resolution to 47 vertical layers. The model is run from 2004 to 2008 following a one-year spin-up.

2.1 Emissions

2.1.1 Terrestrial vegetation

Terrestrial vegetation emits both FA and AA (e.g. Kesselmeier, 2001). Emissions by trees are triggered by light and are well correlated with the transpiration rate. In contrast, crops have been reported not to emit detectable amounts of FA or AA (Kesselmeier et al., 1998). FA emissions by plants are related to the C_1 pathway, ethene synthesis and photo-respiration (Kesselmeier and Staudt, 1999). The emission of AA by plants occurs as the result of the hydrolysis of acetyl-coA, a product of the degradation of fats and carbohydrates (Kesselmeier and Staudt, 1999).

We use the Model of Emissions of Gases and Aerosols from Nature (MEGAN) v2.1 (Guenther et al., 2006) implemented in GEOS-Chem as described by Millet et al. (2010) to compute biogenic emissions from each GEOS-Chem grid cell (E):

$$E = \gamma \sum_i \varepsilon_i \chi_i$$

where the sum is over the number of plant functional types with baseline emission factor, ε, and fractional coverage, χ. For both FA and AA, ε are 30 µg (m^{-2} h^{-1}) for trees and shrubs and 4.8 µg (m^{-2} h^{-1} for crops (Guenther et al., 2000, updated on the basis of recent measurements (A. Guenther, personal communication, 2010)). The emission activity factor, γ, accounts for the variability in the local environment (e.g., temperature, light, leaf area, soil moisture). In particular for FA and AA:

$$\gamma = \exp(\beta(T - 303))\,\gamma_{(\text{other})} \text{ with } \beta = 0.08 \text{ and } T \text{ inK}$$

where $\gamma_{(\text{other})}$ is described in Millet et al. (2010) and T is the current leaf temperature.

2.1.2 Biomass burning and biofuel

Both FA and AA have been measured in biomass burning plumes (Goode et al., 2000; Christian et al., 2003; Yokelson et al., 2009). We estimate biomass burning emissions of FA and AA from biomass burning emissions inventory (GFEDv2 Randerson et al., 2006) using the emission factors (EF) summarized in Table 1. Emissions from biofuels are calculated in the same way using the CO emission inventory from Yevich and Logan (2003).

We note that the emission factors used in this study are generally smaller than the ones reported by Andreae and Merlet (2001) for FA but larger for AA. These changes reflect the very large variability in the reported emission factors.

2.1.3 Fossil fuel

Emissions of FA and AA from motor vehicles were first measured by Kawamura et al. (1985). Here we estimate fossil fuel FA and AA from CO fossil fuel emissions (Duncan et al., 2007) scaled by the emission ratios derived by Talbot et al. (1988) at the Hampton Roads Bridge Tunnel (Virginia): 2.1×10^{-4} FA per CO and 4.2×10^{-4} AA per CO.

Table 1. Biomass burning emission factors for FA and AA (in g per kg of dry matter, Yokelson personal communication and Akagi et al. (2010)). Emission factors from Andreae and Merlet (2001) are indicated in parentheses.

	Savanna	Tropical	Boreal	Biofuel*
FA	0.18 (0.7)	0.42 (1.1)	0.80 (2.9 ± 2.4)	0.22 (0.13)
AA	1.58 (1.3)	3.11 (2.1)	4.05 (3.8 ± 1.8)	4.97 (0.4–1.4)

* Derived from open-cooking.

2.1.4 Agricultural emissions

Large emissions of acetic acid are associated with intensive animal farming (from both cattle and cattle waste Shaw et al., 2007). Ngwabie et al. (2008) used the correlation between AA and ammonia to derive emission factors (2×10^{-3}–$0.2\,gC/gNH_3$ and a global estimate of AA emissions from cattle (4–17 Gmol yr^{-1}). Using an emission factor of $0.1\,gC/gNH_3$ and the anthropogenic emissions of ammonia (Bouwman and Hoek, 1997) located on agricultural lands, we estimate the global soil emissions of AA to be ∼40 Gmol yr^{-1}.

Ethanol, which has nearly the same molecular weight as FA, is a major emission of cattle farming. This makes it difficult to quantify the emissions of FA by proton transfer mass spectrometry (PTRMS), the most common technique for these investigations. We assume that the emissions of FA (in moles) are equal to the emissions of AA. This corresponds to 40% of the upper estimate of ethanol global emissions by Ngwabie et al. (2008).

Both FA and, to a lesser extent, AA farming emission estimates are larger than those from Ngwabie et al. (2008) and probably represent upper estimates. However, the contribution of agricultural activities to the FA and AA budget is likely to be underestimated as one can expect FA and AA production from the photooxidation of volatile compounds emitted as a result of farming activities but not represented in the model.

2.1.5 Soil

FA and AA production by soil bacteria is well documented with soil concentrations ranging from 2 to 5 mol m^{-3} (Sposito, 1989, p. 66). The few studies of FA and AA emissions (Sanhueza and Andreae, 1991; Enders et al., 1992) suggest that soil emission is an important source of acids where production from terrestrial vegetation is low.

Sanhueza and Andreae (1991) reported emissions of FA (AA) of ∼0.4 nmol ($m^{-2}\,s^{-1}$) (0.2 nmol ($m^{-2}\,s^{-1}$)) at noon over dry savanna soil. Emissions of both acids were found to be temperature dependent. Here we approximate the temperature dependence reported by Sanhueza and Andreae (1991) using an exponential law:

$$E_{\mathrm{FA}}^{\mathrm{dry}}(\text{savanna}) = 1.7\times10^{-3}\times(\exp(0.119\times T)-1),$$

$$T > 0\,^{\circ}\mathrm{C}\ (R^2 = 0.66)$$

$$E_{\mathrm{AA}}^{\mathrm{dry}}(\text{savanna}) = 2.5\times10^{-3}\times(\exp(0.091\times T)-1),$$

$$T > 0\,^{\circ}\mathrm{C}\ (R^2 = 0.50)$$

where T is the soil temperature in °C and E_X is the emission of the acid in nmol ($m^{-2}\,s^{-1}$). This corresponds to an average emission of $\overline{E_{\mathrm{FA}}} = 1.8\times10^{-1}$ nmol ($m^{-2}\,s^{-1}$) and $\overline{E_{\mathrm{AA}}} = 8.4\times10^{-2}$ nmol ($m^{-2}\,s^{-1}$) over the 30 °C to 40 °C temperature range.

For a similar environment and using a much larger dataset, Yienger and Levy (1995) derived $\overline{E_{\mathrm{NO}}} = 1.89\times10^{-1}$ nmol ($m^{-2}\,s^{-1}$). We use the soil emissions of NO from Yienger and Levy (1995) in other environments to infer the emissions of FA and AA (Table 2). This assumes that the ratio between the emissions of FA (AA) and NO is independent of the environment type and that the emissions of FA and AA exhibit the same temperature dependence as the one measured by Sanhueza and Andreae (1991). Field measurements are clearly needed to assess these assumptions.

Because of the weak acidity of FA (pKa = 3.75) and AA (4.75), their soil emissions are likely to depend on soil pH under wet conditions. We assume that the emissions listed in Table 2 are at pH = pKa(FA/AA) and 30 °C, i.e. that they correspond to half of the maximum emissions under wet conditions. Under these assumptions, the wet emissions are thus obtained by scaling the baseline wet emission by the following factor:

$$\exp\left(-\frac{\Delta H_X}{R}\left(\frac{1}{T_{\mathrm{soil}}}-\frac{1}{303.15}\right)\right)\times\frac{2}{1+10^{\mathrm{pH}-\mathrm{pKa_X}}}$$

with $X = \{\mathrm{FA}, \mathrm{AA}\}$

where the soil pH is taken from the ISRIC World Soil Information Database (http://www.isric.org) and ΔH is the heat of dissolution at 298 K.

Sanhueza and Andreae (1991) also reported an increase in AA emissions after watering the soil, while FA emissions were suppressed. The AA emission increase hints at the existence of water-stressed AA-producing microorganisms, similar to denitrifying bacteria (Davidson, 1992). Here, we use the same pulsing factors for AA as the one derived by Yienger and Levy (1995) for the soil emissions of NO. AA pulsing increases AA soil emissions by ∼10% globally.

2.2 Photochemical sources of formic and acetic acids

2.2.1 Terrestrial biogenic precursors

The oxidation of biogenic compounds, and in particular their ozonolysis has been suggested to be a major source of FA and AA (Jacob and Wofsy, 1988; Neeb et al., 1997).

Table 2. Soil emissions of formic and acetic acids at $T_{soil} = 30\,°C$ in nmol $(m^{-2}\,s^{-1})$ for different land types.

Land Type*	Formic Acid		Acetic Acid	
	wet	dry	wet	dry
Agriculture (not Rice)	1.8×10^{-1}	–	1.1×10^{-1}	–
Agriculture (Rice)	5.9×10^{-3}	–	3.5×10^{-3}	–
Conifer and other deciduous	1.47×10^{-2}	4.9×10^{-3}	8.8×10^{-3}	2.9×10^{-3}
Desert	0	0	0	0
Drought deciduous	2.9×10^{-2}	8.9×10^{-3}	1.8×10^{-2}	5.4×10^{-3}
Grassland	1.8×10^{-1}	5.9×10^{-2}	1.1×10^{-1}	3.6×10^{-2}
Tropical rain forest	1.3	1.9×10^{-1}	7.7×10^{-1}	1.2×10^{-1}
Tundra	2.4×10^{-2}	8.2×10^{-3}	1.5×10^{-2}	5.0×10^{-3}
Woodland	8.3×10^{-2}	3.2×10^{-2}	5.0×10^{-2}	1.9×10^{-2}
Wetland	1.5×10^{-3}	–	8.8×10^{-4}	–

* Wang et al. (1998); Wang and Jacob (1998).

Here we update the photochemical oxidation mechanism of isoprene, a non methane hydrocarbon which accounts for ∼30–50% of biogenic emissions (Guenther et al., 2006), to include sources of FA from products of its photooxidation with OH: hydroxyacetone, glycolaldehyde and isoprene nitrates (Butkovskaya et al., 2006a,b; Paulot et al., 2009, cf. Supplement). Ozonolysis of methylvinylketone (MVK) and methacrolein (MACR), two major products of isoprene photooxidation, are also known to yield FA (Aschmann et al., 1996; Grosjean et al., 1993). In contrast, isoprene photochemistry has long been thought to be an insignificant source of AA (Jacob and Wofsy, 1988). Recent experimental evidence suggests, however, that the photooxidation of hydroxyacetone produces significant amounts of AA (Butkovskaya et al., 2006b) at low temperature. Isoprene is also a significant source of peroxy acetyl radical (PA), which reacts with HO_2 to yield AA with a yield of 15% (Hasson et al., 2004; Dillon and Crowley, 2008).

The OH-oxidation of methylbutenol (MBO), a volatile organic compound emitted in large quantities by coniferous trees (Harley et al., 1998), also yields glycolaldehyde and hydroxymethylpropanal (HMPR), a precursor of acetone (Carrasco et al., 2006), and thus of AA via PA. MBO ozonolysis has also been shown to yield FA as well as acetone and HMPR (Carrasco et al., 2007).

The OH-oxidation of various monoterpenes has been reported to produce FA. However, the yield remains very uncertain. For instance, reported FA yields from the OH-oxidation of α-pinene range from 7% (Orlando et al., 2000) to 28% (Larsen et al., 2001). Yields greater than 50% have been reported for limonene (Larsen et al., 2001). Ozonolysis of various monoterpenes also yields FA and AA (Lee et al., 2006). Monoterpenes are lumped into one species, MONX, in the GEOS-Chem chemical mechanism. We adopt a FA yield of 15.5% for the reaction of MONX with OH and a FA (AA) yield of 7.5% (8%) for its ozonolysis. The formation of carboxylic acids in the oxidation of MONX by OH has been ascribed to the reaction of stabilized α-hydroxyalkyl radicals with NO (Orlando et al., 2000; Larsen et al., 2001). However, Peeters et al. (2001) calculated that this reaction is only competitive with their thermal decomposition to aldehyde + HO_2 under laboratory conditions (NO ∼ 1–10 ppmv), suggesting that the yield of FA from the first steps of MONX photooxidation is negligible (Peeters et al., 2001; Capouet et al., 2004). Conversely, the very simplified representation of MONX secondary photochemistry in GEOS-Chem may result in an underestimate of their overall FA/AA forming potential.

The OH-oxidation of acetaldehyde, whose sources include large emissions from the terrestrial and marine biosphere (Millet et al., 2010), is an important source of AA via PA + HO_2. The modification to the GEOS-Chem mechanism are summarized in Table S4.

2.2.2 Marine precursors

Ozonolysis of marine biogenic emissions has been suggested to provide a source of FA and AA in the marine atmosphere (Arlander et al., 1990; Sanhueza et al., 1996; Baboukas et al., 2000).

In this study, we include monthly marine emissions of isoprene, acetaldehyde, ethene and larger alkenes. Acetaldehyde marine emissions (∼1.3 Tmol yr^{-1}) are from Millet et al. (2010) and isoprene sources are from Arnold et al. (2009) (top-down estimate : 28 Gmol yr^{-1}). Emissions of ethene (162 Gmol yr^{-1}) and larger alkenes (164 Gmol yr^{-1}) are inferred from isoprene emissions using the flux ratios observed by Broadgate et al. (1997).

2.2.3 Anthropogenic/biomass burning precursors

In addition to fresh emissions from biomass burning or anthropogenic sources, production of FA and AA within fire plumes has been measured in many (Goode et al., 2000; Gao et al., 2003; Yokelson et al., 2003; Herndon et al., 2007) but not all instances (de Gouw et al., 2006). Here, we include formation of FA and AA from the photooxidation of acetylene (Hatakeyama et al., 1986), ethene and propene (and higher alkenes).

Anthropogenic inventories for CO are described by Bey et al. (2001) and biofuel emissions by Yevich and Logan (2003). Recent updates of these inventories are described by Millet et al. (2010). Emissions and photooxidation of acetylene, propene and ethene, which are precursors of FA and AA, were recently included or updated by Fu et al. (2008) in the GEOS-Chem model. In addition we include biomass burning emission of hydroxyacetone and glycolaldehyde (Fu et al., 2008), two precursors of FA and AA.

2.3 Sources not treated

Graedel and Eisner (1988) estimate that emissions of FA from formicine ants could exceed motor vehicle and biomass burning emissions. The overall contribution of formicine ants to the FA budget is, however, likely to be limited (Chebbi and Carlier, 1996) but may be important in ecosystems where formicine ants are abundant (e.g., tropical forests).

Aqueous phase oxidation of formaldehyde within clouds has been proposed to be a non-negligible source of FA in remote environments (Chameides, 1984; Jacob, 1986). However Lelieveld and Crutzen (1991) argued that the very fast aqueous oxidation of FA would greatly diminish the role of cloud chemistry as a source of FA.

The source of FA and AA from enol photochemistry is not included in the model (Archibald et al., 2007). Enol are known intermediates in combustion (Taatjes et al., 2005) and could originate from keto-enol tautomerizations catalyzed by carboxylic acids (da Silva, 2010). However, the importance of these processes as a source of FA and AA is poorly known and additional experimental constraints are needed to include these processes in a global model.

2.4 Sinks

2.4.1 Photochemical

FA reacts with OH primarily via abstraction of the acidic hydrogen with a recommended temperature independent rate of 4.5×10^{-13}cm^3 (molec s^{-1}) (Atkinson et al., 2006). The uncertainty of this rate coefficient is relatively large ($\Delta\log=$ 0.15 at 298 K (Atkinson et al., 2006)) because of experimental challenges (dimerization of FA). To our knowledge, this rate coefficient has not been determined below 298 K. Theoretical calculations suggest, however, that the acidic (R1), dominant at ambient temperature, and formyl (R2) channels have opposite temperature dependence (Galano et al., 2002; Sun and Saeys, 2008).

$$\mathrm{HCOOH+OH \rightarrow HCOO^{\cdot}+H_2O} \quad \text{(R1)}$$

$$\rightarrow {}^{\cdot}\mathrm{COOH+H_2O} \quad \text{(R2)}$$

This results in a relatively "flat" temperature profile near 298 K where the laboratory investigations were conducted but a strong negative temperature dependence at lower temperature. This will be examined in Sect. 4.3.

In contrast, the AA reaction with OH has been studied over a much wider temperature range. The reaction follows a mechanism similar to FA (Butkovskaya et al., 2004) and exhibits a negative activation energy. The temperature dependence remains uncertain and we use the IUPAC recommendation, $4.2\times10^{-14}\exp(855/T)$ cm^3 (molec s^{-1}) ($\Delta\log=0.15$ at 298 K) (Atkinson et al., 2006), which is in excellent agreement with the two most recent determinations of this reaction rate coefficient (Butkovskaya et al., 2004; Huang et al., 2009).

2.4.2 Dry deposition

Dry deposition of oxidants and water soluble species is computed using a resistance-in-series model based on the formulation of Wesely (1989) implemented in GEOS-Chem by Wang and Jacob (1998). The dry deposition velocities of FA and AA depend on surface momentum and sensible heat fluxes, temperature, solar radiation as well as the effective Henry's constant of FA and AA ($\mathcal{H}$), which are calculated at a pH of 7, a reasonable assumption for most surfaces (Wesely, 1989). We use the median of the reported measurements: $\mathcal{H}_{\mathrm{FA}}=5400\,\mathrm{M\,atm^{-1}}$, $\mathcal{H}_{\mathrm{AA}}=5350\,\mathrm{M\,atm^{-1}}$ (Sander, 1999).

2.4.3 Wet deposition

Wet deposition is thought to be the most important sink of FA and AA (Chebbi and Carlier, 1996). The GEOS-Chem wet deposition scheme includes scavenging of soluble tracers in convective updrafts, as well as rainout and washout of soluble tracers (Mari et al., 2000; Liu et al., 2001). We assume a rain pH of 5 and that the acids are fully retained at freezing, as with HNO_3.

We modify the GEOS-Chem deposition scheme to include the uptake of FA and AA in ice clouds. Briefly, assuming equilibrium between the ice surface concentration $[X]_{\mathrm{s}}$ (molec cm^{-3}) and the gas-phase concentration $[X]_{\mathrm{g}}$ (molec cm^{-3}), non-dissociative uptake and non competitive adsorption, $[X]_{\mathrm{s}}$ can be related to the surface area of ice (S_{ice} (cm^2 cm^{-3})), the maximum number of molecules which can be adsorbed on the surface (N_{max} (molecules cm^{-2})) and the fractional coverage (θ) by:

$[X]_s = S_{ice} \theta N_{max}$

θ is given by the Hill-Langmuir equation:

$$\theta = \frac{\frac{K}{N_{max}}[X]_g}{1+\frac{K}{N_{max}}[X]_g}$$

where K (cm) is a temperature dependent partition coefficient: $K = \alpha \times \exp(\beta/T)$ with $\alpha_{FA} = 5.8 \times 10^{-11}$ cm, $\alpha_{AA} = 1.0 \times 10^{-10}$ cm and $\beta_{FA} = 6500$ K, $\beta_{AA} = 6600$ K (Marécal et al., 2010; Crowley et al., 2010).

2.4.4 Dust

Field measurements have identified formate and acetate on collected mineral aerosols (Lee et al., 2000, 2002; Russell et al., 2002; Falkovich et al., 2004). Falkovich et al. (2004) found that formate and acetate were the most abundant mono carboxylic anions in dust particles and that their uptake was facilitated at higher relative humidity (RH).

Consistent with these observations, efficient uptake of carboxylic acids on various components of dust (Usher et al., 2003) has been measured: FA on clay (montmorillonite) (Hatch et al., 2007) and $CaCO_3$ (Al-Hosney et al., 2005); AA on SiO_2, $\alpha-Al_2O_3$, $\alpha-Fe_2O_3$ (Carlos-Cuellar et al., 2003) and $CaCO_3$ (Prince et al., 2008). Increased water enhance the capacity of the mineral dust to take up carboxylic acids (Al-Hosney et al., 2005; Hatch et al., 2007; Prince et al., 2008) but does not change the accommodation coefficient (γ) significantly.

Surface saturation needs to be explicitly treated as it severely reduces the efficiency of this removal mechanism (Hatch et al., 2007). Accounting for the saturation limit, Hatch et al. (2007) estimated that up to 40% of gaseous AA could be removed during a dust storm.

In GEOS-Chem, dust is carried into four different size bins. Here we use emissions from the dust entrainment and deposition (DEAD) scheme (Zender et al., 2003; Fairlie et al., 2007). From Hatch et al. (2007), we use $\gamma_{FA} = 4 \times 10^{-4}$ and $\gamma_{AA} = 3 \times 10^{-4}$ for RH $< 30\%$; $\gamma_{FA} = 5.4 \times 10^{-4}$ and $\gamma_{AA} = 14 \times 10^{-4}$ for RH $\geq 30\%$. The dependence of surface saturation (S in mg(acid)/g(dust)) on RH is approximated by fitting an exponential to Hatch et al. (2007) measurements: $S_{FA} = 2 + 4.7 \times (1 - \exp(-8.6 \times 10^{-3} \times \text{RH}))$ and $S_{AA} = 2 + 5.8 \times (1 - \exp(-2.6 \times 10^{-2} \times \text{RH}))$. Heterogeneous degradation of FA (Al-Hosney et al., 2005) and AA (Prince et al., 2008) to CO_2 is not represented but may further enhance the uptake of FA and AA.

2.5 Simulated distribution

2.5.1 Formic acid

The total source of formic acid in the model is about 1200 Gmol yr^{-1} (Table 3). This is about twice as large as previous estimates (Ito et al., 2007; von Kuhlmann et al., 2003a). Modeled FA sources are dominated by photochemical production from the oxidation of biogenic precursors. More than a third of the FA photochemical source stems from glycolaldehyde and hydroxyacetone via the Butkovskaya's mechanism (Butkovskaya et al., 2006a,b). These sources were not included in previous estimates and account for much of the difference (Table 3). Other important sources include isoprene ozonolysis (14% of the photochemical production) and monoterpenes photooxidation (6%). Acetylene is the dominant non-biogenic precursor (6.5%).

Over three quarters of FA photochemical production is derived from isoprene photooxidation, many aspects of which remain uncertain. In particular, it is worth noting that the mechanism recently proposed by Peeters et al. (2009) results in large modifications of the distribution of isoprene photooxidation products determined from chamber experiments (including hydroxyacetone and glycolaldehyde). If correct, this could significantly affect the modeled budget of FA. Nevertheless, despite our incomplete knowledge of isoprene photooxidation, its representation in the GEOS-Chem mechanism is much more explicit than for most other biogenic volatile organic compounds. This probably results in an overestimation of the importance of isoprene as a precursor for FA as the photooxidation of other biogenic volatile organic compounds, such as the different monoterpenes, is much more simplified.

Direct emissions of FA are small ($\sim$15%) and dominated by terrestrial vegetation and biomass burning. Emissions from vehicles do not contribute significantly to the modeled FA budget, consistent with observations from de Gouw et al. (2005). Our modeled FA budget suggests, however, that more than 90% of FA is composed of modern carbon globally (Table S2). This percentage is lower in the northern mid and high latitudes, though FA is still predicted to be largely dominated by modern sources (Table S2), consistent with isotope studies in Europe (Glasius et al., 2001).

The enhancement in FA (ΔFA) in aged biomass burning plumes and its correlation with ΔCO has frequently been used to derive emission factors from ground or satellite based observations (e.g. Paton-Walsh et al., 2005; Rinsland et al., 2007; Gonzàlez Abad et al., 2009). Our study suggests that FA is rapidly removed from the boundary layer by wet and dry deposition, so that little FA emitted or formed in the boundary layer is advected over long distances or transported into the free troposphere. Therefore ΔFA observed in aged plumes is unlikely to represent direct emissions, as commonly assumed, but rather the production of FA from the photooxidation of biomass burning emitted precursors. Thus, ΔFA cannot be used, in general, to derive emission factors far away from emission regions.

FA sinks are dominated by depositions. Dust is not a significant sink globally but can result in a large decrease of acids in the vicinity of large deserts.

The modeled atmospheric lifetime of FA is 3.2 days, consistent with previous estimates (Chebbi and Carlier, 1996).

Table 3. Modeled global budget of atmospheric formic and acetic acids (2004–2008 average). Previous estimates are indicated in parentheses.

	Formic acid (τ = 3.2 days)	Acetic acid (τ = 2.3 days)
Total Sources (Gmol yr^{-1})	1232 (666[a], 587[b])	1424 (1550[a], 1217[b])
Photochemical production	1055 (370[a], 370[b])	976 (1250[a], 700[b], 2000[c])
Biogenic	917[d]	955[d]
Anthropogenic +Biomass burning	138	21
Emissions	177 (296[a], 217[b])	448 (300[a],517[b])
Anthropogenic	3.5	7
Biofuel Burning	6.5 (25[b])	114.5 (274[b])
Biomass Burning	32.5 (174[a], 183[b])	187 (243[a], 279[b])
Cattle	39.5 (25 – 100[f,g])	39.5 (4.2 – 16.8[f])
Soil	39	57
Terrestrial vegetation	56 (122[a], 125[h], 33 – 166[i], 20 – 130[j])	43 (56[a], 25[h],17 – 83[i], 10 – 33[j])
Total Sinks (Gmol yr^{-1})	1233	1426
Photochemical	229.5	413
Dry deposition	536	522
Wet deposition	437.5	451.5
Dust	30	39.5

[a] von Kuhlmann et al. (2003a,b).
[b] Ito et al. (2007).
[c] Baboukas et al. (2000).
[d] Neglect biomass burning contribution to hydroxyacetone and glycolaldehyde.
[e] Sum of biomass burning and biogenic emissions.
[f] Ngwabie et al. (2008).
[g] $C_2H_5OH + HCOOH$.
[h] Lathière et al. (2006).
[j] Kesselmeier et al. (1998).

The lifetime of FA in the boundary layer is about 1.6 days (excluding transport to the free troposphere).

The FA atmospheric mass is highest in the tropics (∼60% of the global burden Table S2) as a result of large biogenic and biomass burning emissions (Fig. 1). Modeled mixing ratios in the Northern midlatitudes are low and follow the seasonal cycle of biogenic emissions.

2.5.2 Acetic acid

The total source of acetic acid is about 1400 Gmol yr^{-1} (Table 3). Emissions of AA account for about one third of AA sources. The difference with FA stems from much larger direct emissions from biomass and biofuel burning. Secondary production from anthropogenic sources or biomass burning is small. AA production has, however, been observed in biomass burning plumes. For instance, Yokelson et al. (2003) observed $\Delta AA/\Delta CO$ increase by as much as 9% in some biomass burning plumes and noted that the secondary production of AA exceeds the measured direct emissions. This observation cannot, however, be generalized since other plumes did not exhibit production of AA (de Gouw et al., 2006; Yokelson et al., 2009, and references therein). Yokelson et al. (2009) also noted that the growth of FA and AA in the Yucatan biomass burning plumes cannot be accounted for by the photochemistry of their known precursors, pointing to unidentified high molecular weight precursors. The importance of these precursors as a source of FA and AA will be investigated in Sect. 4.2.

Photochemical production is dominated by the reaction of PA with HO_2 (53%) and other peroxy radicals (24%), with isoprene photochemistry and acetaldehyde oxidation the primary sources of PA. Our estimates are consistent with those of von Kuhlmann et al. (2003a) and Ito et al. (2007) but much lower than the estimate by Baboukas et al. (2000). von Kuhlmann et al. (2003a) pointed out that this is the result of the very high branching ratio for the production of AA from $PA + HO_2$ assumed by Baboukas et al. (2000), inconsistent with values reported in recent laboratory experiments (e.g., Dillon and Crowley, 2008).

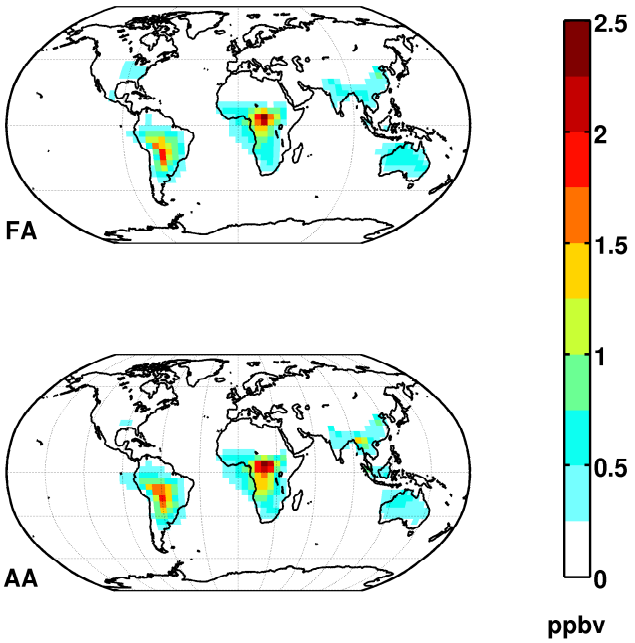

Fig. 1. Annual simulated distribution of FA and AA in the boundary layer. FA and AA maxima in the tropics reflect strong biogenic sources.

Similar to FA, deposition is the major sink of AA. Because AA is less soluble than FA and because its oxidation by OH is faster and has a negative temperature dependence, photooxidation of AA is much more important than for FA and contributes to the significantly shorter lifetime of AA in the atmosphere: 2.3 days (1.7 days in the boundary layer). AA is predicted to primarily consist of modern carbon globally (Table S3). The distribution follows patterns similar to FA with a stronger influence of biomass and biofuel burning.

3 Comparison with observations

In this section, we evaluate the GEOS-Chem simulation against upper tropospheric and total column measurements of FA by solar absorption spectrometry in the infrared using a Fourier transform spectrometer (FTS) as well as FA and AA aircraft measurements. The location of ground based stations, the ship cruises and aircraft-based measurements is indicated in 2.

3.1 FTS measurements

FA can be measured by FTS using the Q-branch of the ν_6 mode near 1105 cm^{-1}. In this section, we use FA total columns retrieved by ground-based stations of the Network for the Detection of Atmospheric Composition Change (NDACC, http://www.ndacc.org/, Kurylo and Solomon (1990)) as well as during several cruises by the German vessel Polarstern in the Atlantic ocean (Velazco et al., 2005). We also use upper tropospheric FA profiles measured by the space-borne Atmospheric Chemistry Experiment FTS (Bernath et al., 2005). All retrievals use the revised spectroscopic parameters for FA (Vander Auwera et al., 2007) contained in the HITRAN 2008 spectral database (Rothman et al., 2009).

3.1.1 Ground-based total column

Solar spectra in the vicinity of the ν_6 vibration have been obtained by several stations of the NDACC: Barcroft in the Inyo National Forest (California) at 3800 m, Bremen in northwestern Germany, La Réunion 700 km east of Madagascar, Paramaribo on the coast of Suriname, Thule in northwestern Greenland, and Wollongong, 100 km south of Sydney. The different measurement sites and the cruise ship tracks are depicted in Fig. 2. Measurement uncertainty is estimated to be ∼19%. The choice of the spectral microwindow used to retrieve FA could result in a systematic bias in the retrieved FA as large as $\pm 2.7 \times 10^{15}$ molec cm^{-2}. A more detailed description of the FTS retrievals can be found in the Supplement (Figs. S1 to S4 and Table S1).

Photooxidation of isoprene and other biogenic emissions: a major source of FA

The FA seasonal cycle at the mid-latitude stations, Wollongong (Fig. 3a, see also Fig. S5), Bremen (Fig. 4b, see also Fig. S6) and Barcroft (Fig. 4c, see also Figs. S7 to S9) is consistent with a major source of FA from terrestrial biogenic emissions and their photooxidation. At Wollongong, for instance, FA and biogenic emissions peak simultaneously in January. In contrast, CO and HCN total columns generally peak around October, at the height of the biomass burning season (Fig. S5). At Barcroft, the strong correlation between FA and CH_2O in the summer months (Fig. S7) also suggests a large influence of biogenic emissions on the FA budget. In contrast there is no correlation between FA and HCN. This interpretation is consistent with the conclusions of Zander et al. (2010) that FA seasonal variations above the Alpine plateau are the result of natural processes.

At all sites, the model predicts large contributions of biogenic photooxidation to the FA budget. The model performs best in regions and time periods impacted by large isoprene emissions such as in Wollongong (Fig. 3a) and La Réunion (Fig. 4a). Interestingly, the model predicts a biogenic peak in FA in May at La Réunion later than the maximum in isoprene emission in Southern Africa (Otter et al., 2002). Intense precipitations from January to April over La Réunion may explain this delay by efficiently scavenging FA (leading to a minimum in the modeled FA in January). As the climate becomes drier in May, the atmospheric lifetime of FA increases resulting in higher FA total columns in spite of lower

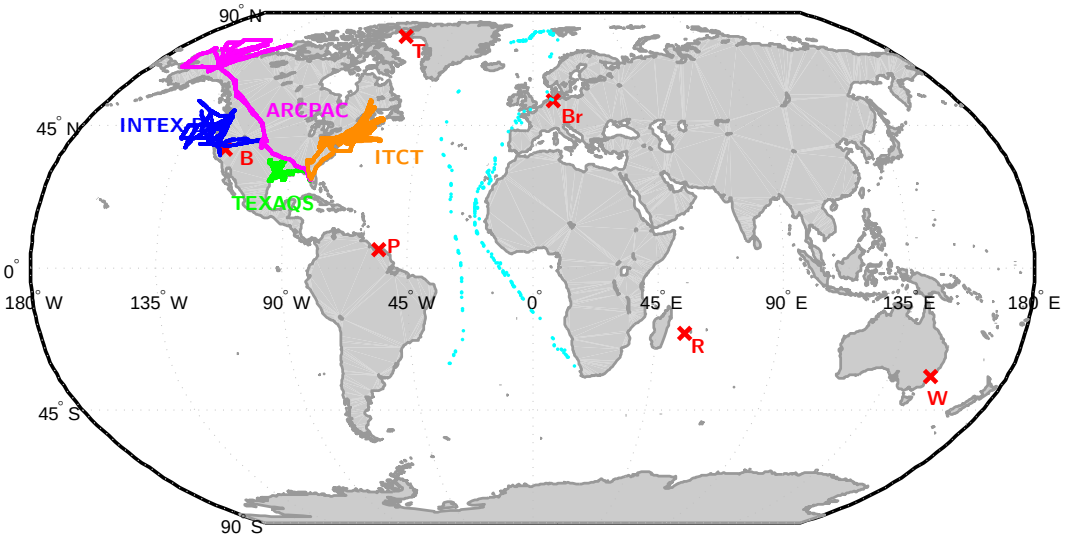

Fig. 2. Locations of the measurement sites used in this study. Red crosses: FTS ground stations (B: Barcroft, Br: Bremen, P: Paramaribo, R: La Réunion, T: Thule, W: Wollongong). Cyan dots: ship cruises. Blue, Magenta, Yellow and Green dots: aircraft missions flight tracks.

isoprene emissions. This illustrates the complicated interplay between FA sources and sinks in the tropics. The model suggests La Réunion is especially sensitive to this effect as the modeled FA total column is dominated by transport from Madagascar and Southern Africa.

In contrast, the model greatly underestimates FA at Bremen (Fig. 4b) and Barcroft (Fig. 4c). These stations exhibit a marked biogenic signature but are located in regions with lower isoprene emissions. This likely reflects a missing biogenic precursor of FA in the model. In these regions, FA production may be promoted by seasonal biotic emissions from cattle and crop farming (Karl et al., 2009) associated with elevated ozone due to anthropogenic activities. The anthropogenic contribution to FA is predicted to be low at both sites (less than 5%) consistent with the seasonal profile of FA and previous isotope measurements in Europe (Glasius et al., 2000, 2001).

We note that Barcroft data must be interpreted cautiously as the complicated topography of the region is not resolved in the model. In particular summer FA total columns show evidence for boundary layer incursions which are not captured at the coarse resolution used in this study. However, CH_2O seasonality is surprisingly well-captured in the model despite a low-bias in the summer (Fig. S8). Therefore, meteorology alone is unlikely to explain the large discrepancy between the model and the data over this site, and sources from the Central Valley (150 km to the west of Barcroft) are likely underestimated.

Missing biomass burning precursors

Evidence for a large but more localized and seasonal biomass burning source of FA can be found in the Wollongong and La Réunion records (Figs. 3a and 4a). In La Réunion, FA peaks in October. This peak is also observed in CO and CH_2O FTS measurements at the same location and is associated with biomass burning in Southern Africa (CO) and Madagascar (CO and CH_2O) (Vigouroux et al., 2009). In Wollongong, the anomalously high FA total column measured in December 2006, the largest on the record, is also associated with biomass burning, since (a) it clearly precedes the biogenic peak in FA observed in other years, (b) very large bush fires burned over 1 million acres from December 2006 to January 2007 in the Victorian Alps ∼450 km southwest of Wollongong, and (c) anomalously high CO and HCN columns are recorded during the same time period (Fig. S5). This is consistent with the work of Paton-Walsh et al. (2005) who reported a significant correlation between aerosol optical depth and FA at the same site during bush fires from 2001 to 2003 and inferred that biomass burning could result in a strong enhancement in FA total column at this site.

The model captures the timing of the biomass burning contribution to the FA column well but underestimates FA during biomass burning periods. The coarse resolution of the model is likely to contribute to this discrepancy due to the dilution of biomass burning plumes. However, the systematic discrepancy on a multi-year average at La Réunion may also indicate missing biomass burning sources of FA.

The discrepancy for marine sites (cruise (Fig. 5) and Paramaribo (Fig. 4d)) also hints at a missing biomass burning source of FA. Air masses affected by biomass burning

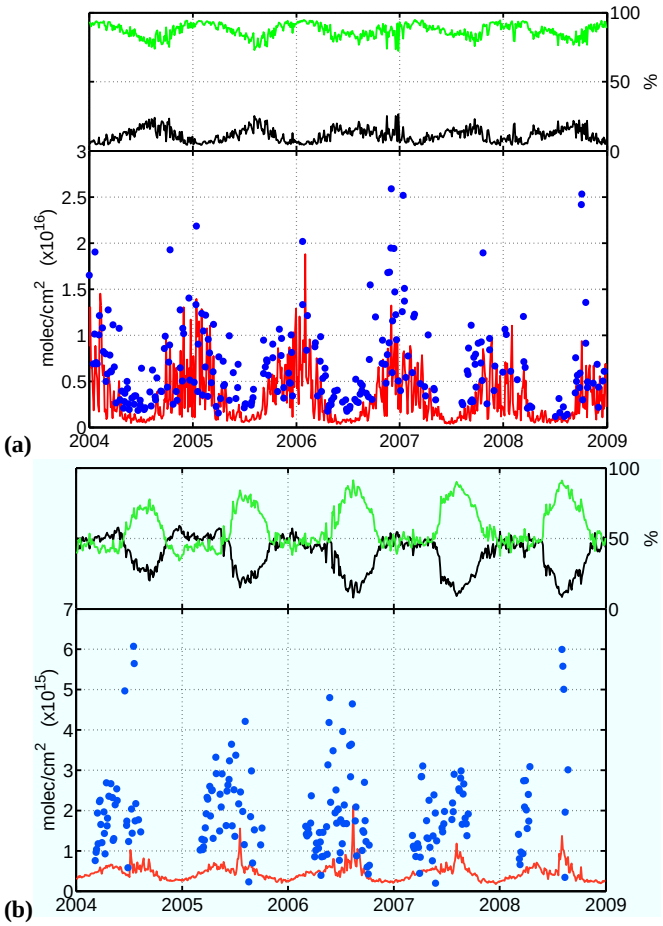

Fig. 3. The observed seasonal cycle of FA total column (blue, lower panel) is well captured by the model at (red, lower panel) at Wollongong, Australia (34.5° S, 150° E, 20 m a.s.l., **(a)**) and is consistent with a strong biogenic influence (green, upper panel). This is not the case in the high latitude site at Thule, Greenland (76.53° N, 68.75° W, 220 m a.s.l., **(b)**) where model under predicts measured FA. Upper panel: modeled contribution of biogenic sources (green: emission + photochemical production) and biomass burning (black: emissions + photochemical production) to FA total column. Lower panel: modeled (red) and measured (blue) FA total column. Measurements and model are averaged over a two day time period.

emissions are known to be advected aloft from Africa to South America and their impact has been measured over Paramaribo during the dry season from August to November (Peters et al., 2004; Petersen et al., 2008). High CO measured in the tropics during cruises is also well correlated with FA ($R = 0.64$, Fig. S10). The lifetime of FA is, however, incompatible with a large contribution of directly emitted FA to the FA total column over Paramaribo (transport time from Africa to Paramaribo has been estimated at 10 days by Peters et al. (2004)) and suggests a missing long-lived precursor from biomass burning. Sources of FA and AA from marine emissions are also likely to be underestimated since the model predicts surface concentrations which are 2 to 5 times lower than measurements made during cruises by Arlander et al. (1990) and Baboukas et al. (2000).

A local source in the polar regions

FA and AA account for a large fraction of the water-soluble organic carbon (gas + particle) over snow in polar regions (Anderson et al., 2008). Better constraints on the budget of FA and AA in these regions may help understand the large variations in FA and AA observed in the ice core record in the last 100 000 years (Legrand and De Angelis, 1996). These variations have been tentatively attributed to changes in the biosphere or biomass burning activity in boreal regions (Fuhrer and Legrand, 1997; Eichler et al., 2009).

Measured FA over Thule is about one order of magnitude lower than in Wollongong (Fig. 3b). The largest FA total columns are measured in the summers of 2004 and 2008. Both these periods are characterized by exceptional biomass burning in boreal regions (in North America in 2004 and in Asia in 2008) (Giglio et al., 2010), consistent with the hypothesis that FA anomalies may reflect large biomass burning events. In the absence of local sources, the modeled FA column is dominated by transport. This is reflected in the modeled vertical distribution of FA peaking in the free troposphere. The model predicts a strong seasonal cycle with maximum during the boreal summer, corresponding to the largest biogenic and biomass burning emissions. The model underestimates FA total column by a factor of 2 to 5. This discrepancy may in part reflect insufficient biomass burning emissions (Andreae and Merlet, 2001). We also note that the model predicts very low concentrations of FA at the surface (∼10 pptv). This is in sharp contrast with the measurements of Anderson et al. (2008) which report ∼1 ppbv of water-soluble organic carbon (primarily FA and AA) over Summit at 1.5 m above the snow. This discrepancy between model and observation in Thule may thus reflect missing local sources. Indeed, Dibb and Arsenault (2002) reported surface concentrations of FA and AA measured in the Arctic could not be sustained by transport alone but required a large source from snow photochemistry.

Missing winter sources

Mid latitude and low altitude sites (Bremen, Wollongong) show larger relative biases between the model and the data during the winter (Figs. 3a and 4b). This may point to large missing anthropogenic sources of FA (Talbot et al., 1988). Alternatively leaf decay may also contribute to the FA sources in the winter months (Kesselmeier et al., 1998). A missing biogenic contribution would be consistent with isotope measurements which showed that FA and AA are primarily made of modern carbon even in the winter (Glasius et al., 2001).

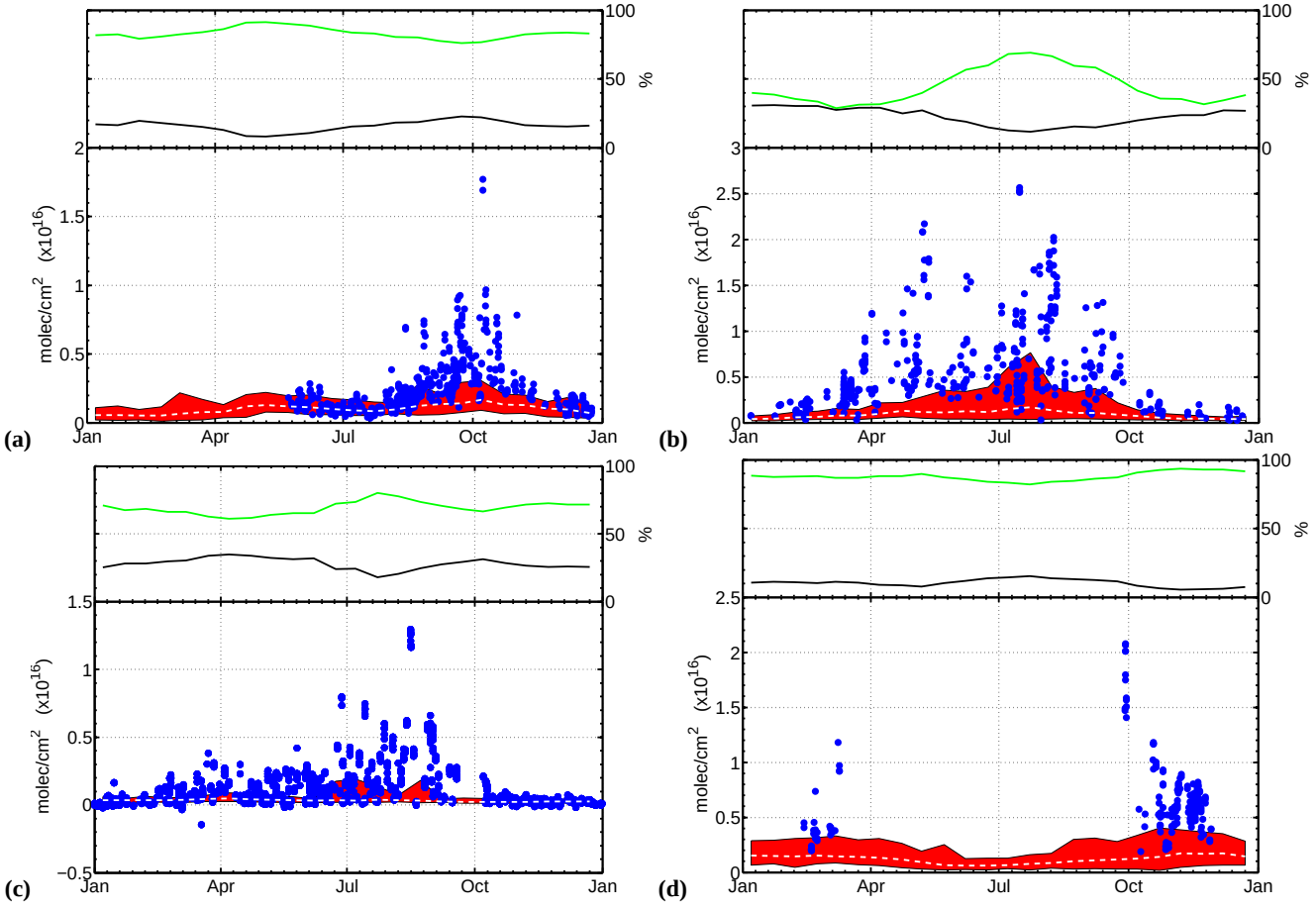

Fig. 4. **(a)** La Réunion, France (−20.9° N, 55.5° E, 10 m.as.l.). Measurements are from campaigns in 2004 (Aug–Oct), 2007 (May–June; Aug–Oct) and 2009 (May–Dec) and **(b)** Bremen, Germany (53.1° N, 8.9° E, 27 m a.s.l.). Measurements are from 2002 to 2010. **(c)** Barcroft, United States (37.6° N, −118.2° E, 3800 m a.s.l.). Measurements are from campaigns in 1994 (Aug), 1998 (Oct–Dec), 1999 (Jan–Jul), 2000 (Oct–Dec), 2001 and 2002 (Jan-Aug) and **(d)** Paramaribo, Suriname (5.8° N–55.2° W, 23 m a.s.l.). Measurements are from campaigns in 2004/2006 (Oct–Nov), 2005/2007 (Feb–Mar; Sep). Upper panels: same as Fig. 3. Lower panel: comparison between modeled and measured FA total columns. Individual total column measurements are indicated with blue dots. The 2004–2008 model range is indicated by the red shaded area and the model mean by the white dashed line.

3.1.2 ACE-FTS

The Atmospheric Chemistry Experiment (ACE) is a Canadian satellite that was launched by NASA on on 12 August 2003. FA is measured by high spectral resolution ($0.02\,cm^{-1}$) FTS operating from 2.2 to 13.3 µm. Using solar occultation, the altitude profile of temperature, pressure and various chemical compounds, including FA, CO and C_2H_2 are determined between 85° N and 85° S. Here, we are using version 3.0 of the ACE-FTS Level 2 data product.

Rinsland et al. (2006) and Gonzàlez Abad et al. (2009) have used the ACE-FTS spectra to retrieve mid and upper tropospheric FA. Even though most FA is located at low altitude and thus cannot be observed by ACE-FTS, these upper atmospheric profiles provide insights into the sinks, sources and transport of FA.

Figure 6 shows the average distribution of FA measured by ACE-FTS from 2004 to 2008. FA is highest from 10 to 50° S, probably reflecting large biogenic sources. The Northern hemisphere exhibits lower FA mixing ratios on average. FA mixing ratios decrease rapidly with altitude and away from the source region. High mixing ratios observed at high altitudes in the Southern Hemisphere may indicate efficient transport of FA or, more likely, its precursors from the boundary layer to the free troposphere.

The model captures mid tropospheric FA in the tropics and Southern mid latitudes relatively well. It is biased low north of 40° N (Fig. 7), mirroring the low modeled concentration of FA in the planetary boundary layer (Fig. 1) and consistent with the large underestimation of FA total column over Bremen. The model is biased high south of 50° S. This region experiences among the lowest concentrations of FA and it is unclear how significant this discrepancy is.

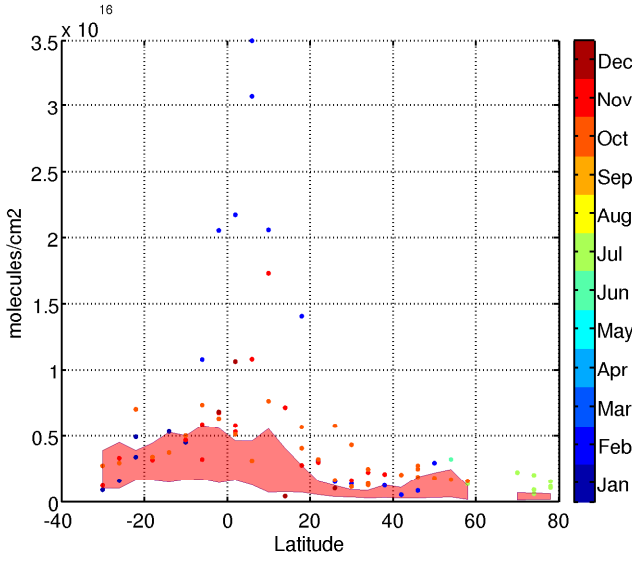

Fig. 5. Monthly FA total column measured during cruises in the Atlantic ocean in 1996, 1999, 2000, 2002, 2003 and 2005 (dots). The 2004–2008 model monthly mean range is indicated by the red shaded area. FA maximum in the tropics reflects biomass and biogenic sources.

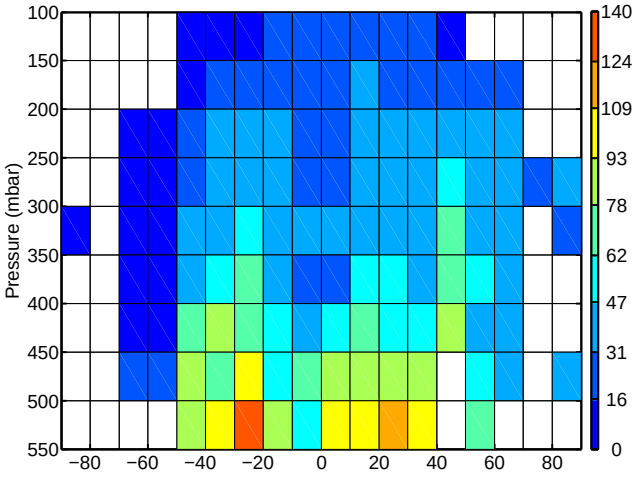

Fig. 6. Measured distribution of FA (pptv) by ACE-FTS from 2004 to 2008. Median of FA measurements is calculated in 10° latitude 50 mbar bins. Only cells with more than ten measurements are shown.

The model greatly underestimates the measured vertical gradient of FA in the free troposphere, underestimating FA at low altitude and overestimating it at high altitude (Fig. 7). The correlation plot between FA and CO reveals possible reasons for this discrepancy (Fig. 8). The model overestimates FA at low CO (40 to 60 ppbv) which primarily reflects the high bias of the model at high altitude where most of the ACE-FTS measurements are taken. ACE HCN measurements (not shown) imply that air masses with CO mixing ratios greater than 160 ppbv are strongly influenced by fresh biomass burning emissions. This is in part captured by the model which shows a strong enhancement of FA in this regime. The largest discrepancy is found for values of CO ranging from 120 to 150 ppbv. These air masses exhibit a weak biomass burning signature and are primarily located in the lower free troposphere at high northern latitudes. These air masses may be affected by boundary layer air, carrying high mixing ratios of FA or its precursors of biogenic or anthropogenic origins. Alternatively, they may be associated with aged biomass burning, which would support the existence of long-lived biomass burning precursors of FA.

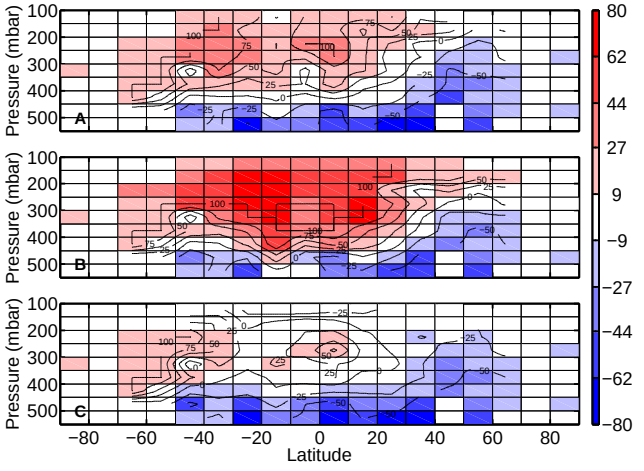

Fig. 7. Comparison of the simulated FA with observations by ACE-FTS suggests an altitude-dependent error. Increasing the reaction rate of OH with FA reduces the model high-bias in the upper troposphere **(C)** while injection of biomass burning in the free troposphere provides little improvement in the middle troposphere while degrading FA simulation in the upper troposphere **(B)**. Absolute difference between the model and the ACE-FTS measurement is shown in pptv with contours indicating the relative difference in % ((model-measurement)/measurement). Cells with no measurements are grayed. Panel **(A)** shows the comparison for the reference run (R1), Panel **(B)** for R2b and Panel **(C)** for R4 (see Sect. 4). The model is sampled at the location and time of the ACE-FTS measurement.

3.2 Aircraft measurements by mass spectrometry

From the previous section, large sources of FA appears to be missing in the Northern Hemisphere mid latitudes. Here we present data from several aircraft missions over North America to gain insights on these missing sources. We use measurements from the Intercontinental chemical transport experiment (INTEX-B/IMPEX April to May 2006 with a focus on the transport of pollution from Asia to the United States over the Pacific, Singh et al., 2009), the Second Texas Air Quality Study (TexAQS II – August to October 2006 Parrish et al., 2009), the Intercontinental Transport and Chemical Transformation experiment (ITCT 2k4 campaign over

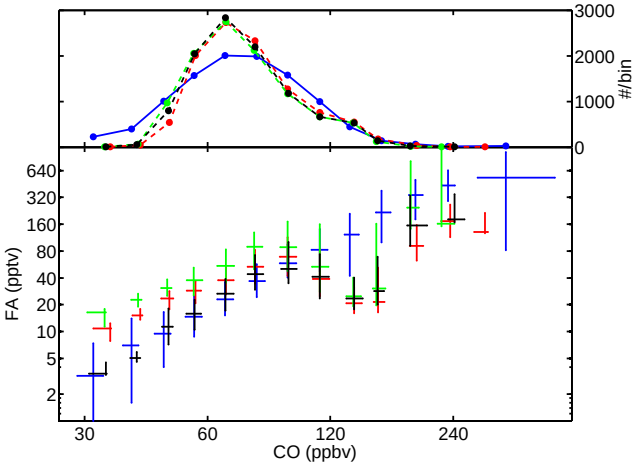

Fig. 8. The correlation between CO and FA observed by ACE-FTS (blue crosses) in the free troposphere is not well-captured by the model (green, red and blue crosses), suggesting a missing secondary source. Lower panel: correlation plot between FA and CO (lower panel) for the measurements (blue) and the model: R1 (red), R2b (green), R4 (black). Upper panel: distribution of measured and modeled CO. The extent of the error bars indicate the 25 and 75 percentiles. The model is sampled at the location and time of the ACE-FTS measurement.

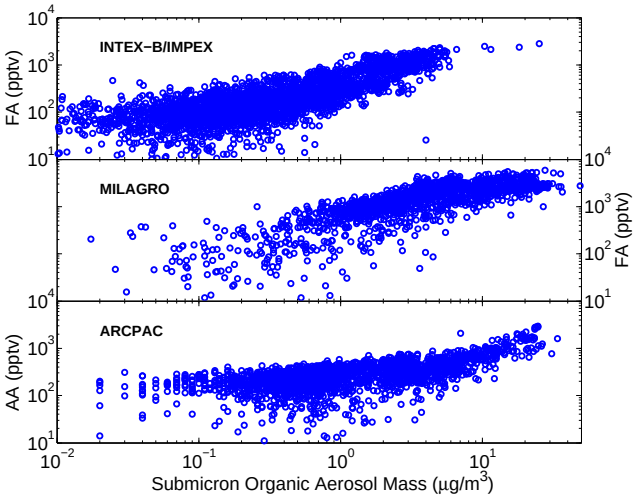

Fig. 9. In-situ measurements show strong correlation of FA and AA with the abundance of organic aerosol over the West Coast of the United States and the eastern Pacific (INTEX-B), in urban environments (MILAGRO) as well as in arctic regions (ARCPAC).

the Northeastern United States, Fehsenfeld et al., 2006) and the Aerosol, Radiation and Cloud Processes Affecting Arctic Climate study (ARCPAC 2008 over Alaska (Warneke et al., 2009)). FA and AA were measured by Chemical Ionization Mass Spectrometry during INTEX-B Crounse et al., 2006) and AA was measured by PTRMS during ITCT 2k4, ARCPAC 2008 and TexAQS II de Gouw and Warneke, 2007. Even though FA was not measured during these missions, it can be expected to correlate very well with AA (e.g., $R = 0.9$ for INTEX-B).

The model underestimates AA and FA in all missions, consistent with total column observations in the Northern mid and high latitudes (Bremen and Thule). Missions closer to large biogenic or anthropogenic sources (ITCT 2k4 and TexAQS II) exhibit a smaller discrepancy than INTEX-B (impacted by aged Asian pollution) or ARCPAC 2008 (impacted by biomass burning). This suggests a large missing long-lived precursor of FA and AA. Consistent with this hypothesis, air masses exhibiting a strong Asian pollution signature (as defined by Dunlea et al., 2009) exhibit a marked enhancement in FA and AA mixing ratio over other air masses sampled over the Pacific (Table 4). Since FA and AA emitted or formed in Asia are expected to be washed out as air is lifted out of the boundary layer, this enhancement hints at a secondary production of both acids. The correlation of FA with the organic fraction of the aerosols ($R = 0.83$, Fig. 9), which are predominantly of secondary origin (Dunlea et al., 2009) is consistent with this hypothesis. Similarly, in ARCPAC 2008, a strong correlation of AA with black carbon ($R = 0.86$) and the organic content of the aerosol ($R = 0.82$) hints at missing sources of AA from biomass burning.

Unrepresented precursors of FA and AA could also account for some of the discrepancy in INTEX-B (e.g. Sinreich et al., 2010). The discrepancy in the marine boundary layer for both acids is similar to the one reported by Baboukas et al. (2000) in the Atlantic ocean. Modeled marine sources of FA are a negligible fraction of FA photochemical production (∼2.5%) reflecting the low emissions of FA precursors. This is not true for AA as acetaldehyde emissions from marine sources are large, resulting in ∼8.5% of AA production over the ocean. The marked maximum in FA total column in the tropics is, however, consistent with an important role of transport from the continents (Fig. 5).

INTEX-B measurements over the California Central Valley (Table 4) also confirm that cattle and/or crop farming is accompanied by very large mixing ratios of FA and AA (5 times greater than in Asian plumes and 10 times greater than in the Pacific free troposphere). In contrast with measurements taken over the Pacific, AA appears to be produced/emitted more efficiently than FA in this environment.

Comparisons between the model and the data show lower discrepancies for TexAQS II and ITCT 2k4(∼2−3x, Fig. 10a and 10b). Correlations with anthropogenic markers (benzene: $R = 0.5$ for TexAQS II, $R = 0.75$ for ITCT 2k4 ; methoxyperoxyacetylnitrate: $R = 0.85$ for ITCT 2k4) suggests a source of AA may be associated with anthropogenic processes.

Table 4. The increase in the median measured (m) FA and AA in polluted air observed during INTEX-B/IMPEX reflects the importance of secondary sources in the budget of FA and AA. These sources are missing from the model (M). α is the slope of the linear fit: AA=αFA+β calculated using York's method (York et al., 2004) for the measurement (ordinary least square for the model). Characterization of the air masses follows the approach of Dunlea et al. (2009).

	FA (pptv)		AA (pptv)		$\alpha \pm 1\sigma$ (R^2)	
	m	M	m	M	m	M
Free troposphere (Asian pollution)	296	26	193	25	0.37 ± 0.16 (0.53)	0.42 (0.37)
Free troposphere (pristine + dilute Asian pollution)	108	26	86	26	0.62 ± 0.23 (0.52)	0.54 (0.51)
Boundary layer (California Central Valley)	1291	81	906	62	1.59 ± 0.16 (0.63)	0.40 (0.91)

3.3 Summary of model-measurement comparisons

The comparisons between measurements and model results have revealed that:

1. the model captures FA concentration and seasonality in regions with large biogenic emissions (ACE-FTS in the tropics, Wollongong, La Réunion)
2. FA and AA concentrations are largely underestimated when biomass burning (ARCPAC 2008, ACE-FTS, La Réunion) or anthropogenic influences (Bremen, INTEX-B) are strong. However, even in these instances, FA and AA seasonality (Bremen) suggests that a large fraction of FA and AA is associated with emission and photooxidation of biogenic compounds.
3. The rapid decrease in FA with altitude in the upper troposphere is not captured by the model.
4. FA and AA are greatly underpredicted in polar regions and in Northern midlatitude regions impacted by anthropogenic activities.

These observations are consistent with major secondary sources of FA and AA missing in the model. In the following, we use a series of sensitivity runs to examine the criteria a secondary source of FA and AA must meet to help bridge the gap between the model and the data. The reference simulation described in this section is referred to as R1 hereafter.

4 Sensitivity study

4.1 Biomass burning injection height

As a default in GEOS-Chem, biomass burning emissions are solely released in the boundary layer. However observations have shown that major fires can inject emissions well above the boundary layer (e.g. de Gouw et al., 2006; Vigouroux et al., 2009). Several modeling studies have also shown that observations of CO and aerosols downwind of fires could be best explained when a large fraction of the fire emissions is released above the boundary layer (e.g. Turquety et al., 2007). Injection of FA/AA or their precursors outside of the boundary layer is of great importance in their budget. Indeed a fast transport of carboxylic acids out of the boundary layer increases their lifetime by reducing the dry deposition sink and results in a large increase in their net lifetime. This in turn results in enhanced transport of FA and AA on larger scales. Furthermore biomass burning has been associated with a reduction of low-level precipitation (e.g. Andreae et al., 2004) which may further increase carboxylic acid lifetime.

Several studies have associated enhancements of FA in the free troposphere to biomass burning (Gonzàlez Abad et al., 2009). Here we examine whether injection of biomass burning emissions outside of the boundary layer can help bridge the gap between between model and observations at high CO. We use two different scenarios. In the first one (R2a), 60% of the biomass burning is emitted in the boundary layer while 35% is emitted in the mid troposphere (from the top of boundary layer to 400 hPa) and 5% in the upper troposphere (400 hPa to 200 hPa). In the second scenario (R2b), we adopt one of the scenarios used by Turquety et al. (2007) to investigate biomass burning over North America with 40% of the biomass burning emissions in the boundary layer, 30% in the mid troposphere and 30% in the upper troposphere. Since our goal is to examine the sensitivity of free tropospheric FA to biomass burning injection height, modifications of the injection height are applied globally, an important simplification (Val Martin et al., 2010, and references therein). Furthermore we assume that EF for FA and AA are independent of the the biomass burning injection height. This is another important simplification since (a) the injection of biomass burning in the free troposphere strongly depends on the fire intensity, and (b) EF for FA and AA exhibit some correlation with the modified combustion efficiency (MCE), an indicator of the combustion type (flaming or smoldering). Therefore, a more

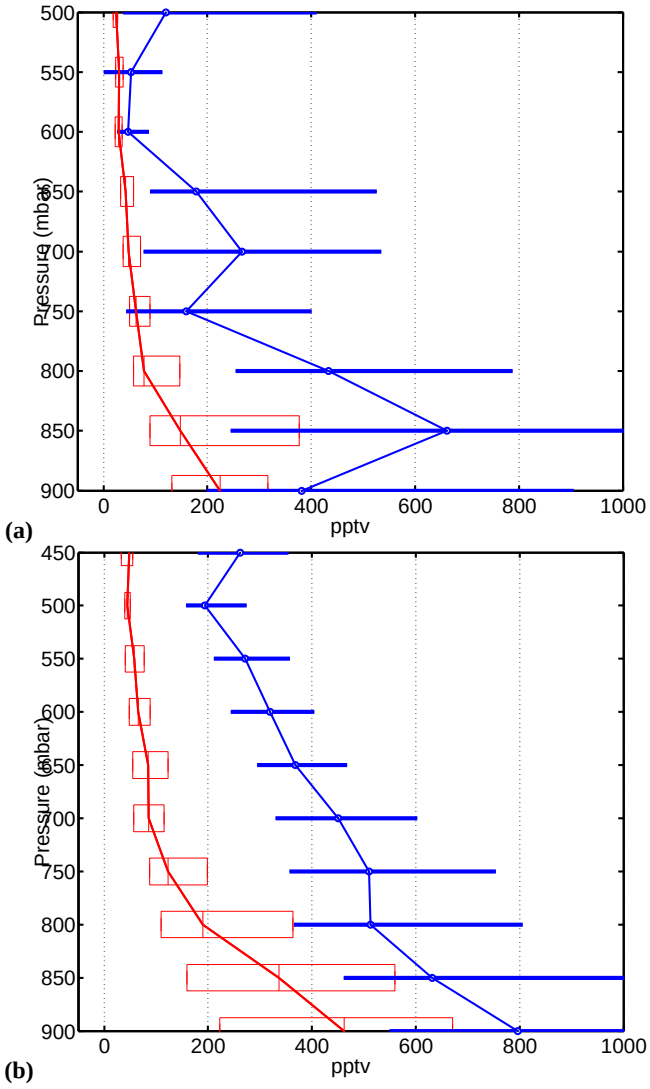

Fig. 10. **(a)** TexAQS II and **(b)** ITCT 2k4. Comparison between measured (blue) and modeled (red) vertical AA profiles. The box (thick line) extent represents the 25% and 75% percentiles.

quantitative study of the importance of biomass burning in the FA and AA budget would require an explicit description of the relationship between MCE and EF as well as MCE and injection height.

Both scenarios lead to an enhancement of FA in the mid troposphere (by 10% for R2a (not shown) and by 35% for R2b (Fig. 7 panel b)). The increase is especially large at high CO, greatly reducing the discrepancy between the model and the measurements (Fig. 8). This is remarkable since biomass burning emissions of FA and its precursors account for a relatively small fraction of FA sources in the model. This disproportionate effect highlights the strength of boundary layer sinks of FA which greatly hinder its transport to the free troposphere. The increase in FA induced by both scenarios is, however, insufficient to bridge the gap between the model and the data in the lower troposphere. In particular, it has no effect on the modeled FA in air masses with CO mixing ratios ranging from 120 to 150 ppbv. This is not surprising if these air masses are associated with aged biomass burning, as FA sinks (photooxidation and wet deposition) are faster than for CO. In contrast, the injection of FA into the free troposphere significantly amplifies the discrepancy between the model and the measurements in the upper troposphere. The very long lifetime of FA in the upper troposphere is responsible for this strong sensitivity. In R2b, FA is increased by almost 50% in the upper troposphere compared to the reference run, resulting in large discrepancies for CO between 40 and 120 ppbv (Fig. 7).

These observations suggest that the distribution of FA in the free troposphere is only sensitive to biomass burning injection height for fresh biomass burning plumes. As FA is removed from the free troposphere faster than CO, the correlation between FA and CO across the whole CO range can only be sustained if the photooxidation of long-lived unrepresented compounds (i.e., poorly soluble and reactive) produces FA. However, if such a source exists, the observed vertical gradient of FA indicates a large sink is missing from the model in the upper free troposphere.

4.2 Secondary source of FA and AA and organic aerosol aging

The positive correlation of FA and AA with submicron organic aerosol observed in several aircraft campaigns (Fig. 9) hints at a possible relationship between FA and AA production and aerosol aging, i.e., processes affecting aerosol composition.

Aerosol composition is very dynamic as evidenced by the positive correlation between the oxygen to carbon ratio and the residence time of aerosols (DeCarlo et al., 2008; Capes et al., 2008). Near sources, aging is thought to be dominated by gas-phase oxidation of semivolatiles (a), while, for longer residence time, heterogeneous oxidation (b) may become important (DeCarlo et al., 2008; George et al., 2008). The combined evolution of the oxygen to carbon ratio and of the hydrogen to carbon ratio during aerosol aging was recently showed to be consistent with the formation of carboxylic groups (Heald et al., 2010). This is not inconsistent with (a), even though we are not aware of direct evidence for the formation of either FA or AA from the photooxidation of semivolatiles. In contrast, laboratory experiments provide ample evidence for the volatilization of FA and AA (b) following the photolysis of aerosols (Walser et al., 2007; Pan et al., 2009) as well as their heterogeneous oxidation by O_3 (Eliason et al., 2003; Park et al., 2006) and OH (Eliason et al., 2004; Molina et al., 2004; Vlasenko et al., 2008). As heterogeneous oxidation operates on relatively long time scales (>4 days George et al., 2008), it could help account for observations during INTEX-B and at Paramaribo. It appears, however, to be too slow to provide a large source of FA and

AA near emission centers (DeCarlo et al., 2008). These observations suggest that aerosol aging and wall reactions could result in a significant source of FA and AA in chamber experiments that was not accounted for by Paulot et al. (2009).

Comparison between the data and the model suggests global sources of FA and AA may be underestimated by up to 50% for both acids, i.e., an additional $\sim$2 TmolC yr^{-1}. Estimates for the global flux of carbon from the photooxidation of aerosol range from 4 to 16.5 TmolC yr^{-1} (Kwan et al., 2006), suggesting FA and AA volatilization would need to account for a very large fraction of this flux (10–50%). However this estimate does not account for the probably large dynamic exchange of matter between the gas and aerosol phases driven by semivolatile volatilization and photooxidation (Robinson et al., 2007; Kroll et al., 2009; Jimenez et al., 2009).

Proper evaluation of the role of aerosol aging as a source of FA and AA requires detailed modeling of aerosol evolution (e.g., following the framework presented by Jimenez et al., 2009) informed by additional laboratory measurements. This is beyond the scope of this paper. Here, we do not explicitly model secondary organic aerosol but use organic aerosol (OA) to generate a diffuse source of FA and AA associated with aerosol aging (scenario R3). In GEOS-Chem, OA represents both emitted OA (primarily from biomass burning with an important contribution of anthropogenic sources in the Northern midlatitudes) and a small and simplified secondary production from the condensation of low volatility compounds from biogenic and anthropogenic sources (Park et al., 2003). The largest global source of OA is biomass burning globally. We assume that the reaction of OH with OA produces FA and AA according to:

$$\frac{d\mathrm{FA}}{dt} = \frac{d\mathrm{AA}}{dt} = \left(\frac{r_\mathrm{p}}{D_\mathrm{g}} + \frac{4}{v\gamma}\right)^{-1} A \times \mathrm{OH}$$

where r_p is the particle radius, γ the reaction probability (assumed to be 1 here), D_g the gas-phase diffusion coefficient, v the mean molecular velocity of OH and A the aerosol surface area. This reaction does not represent a physical process (OA is not lost via this reaction) but is meant to provide a diffuse source of FA and AA correlated with OA. Including this process results in an increase in the source of FA and AA by 320 Gmol yr^{-1}, about $\sim$25% ($\sim$0.95 TmolC yr^{-1}).

This large additional FA source greatly improves the agreement with La Réunion. The mean FA concentration increases by almost 60% in October (Fig. 11a). Similarly, the anomalously high FA measured in December 2006 in Wollongong is much better reproduced in the model with this hypothetical aerosol source (Fig. 11b). We note that it has little effect on the FA total columns for the other years, underlining the exceptional intensity of the 2006 bush fires. For both sites, a similar increase in biomass burning emissions of FA would not result in such a large improvement. This is because the lifetime of organic aerosol is longer than

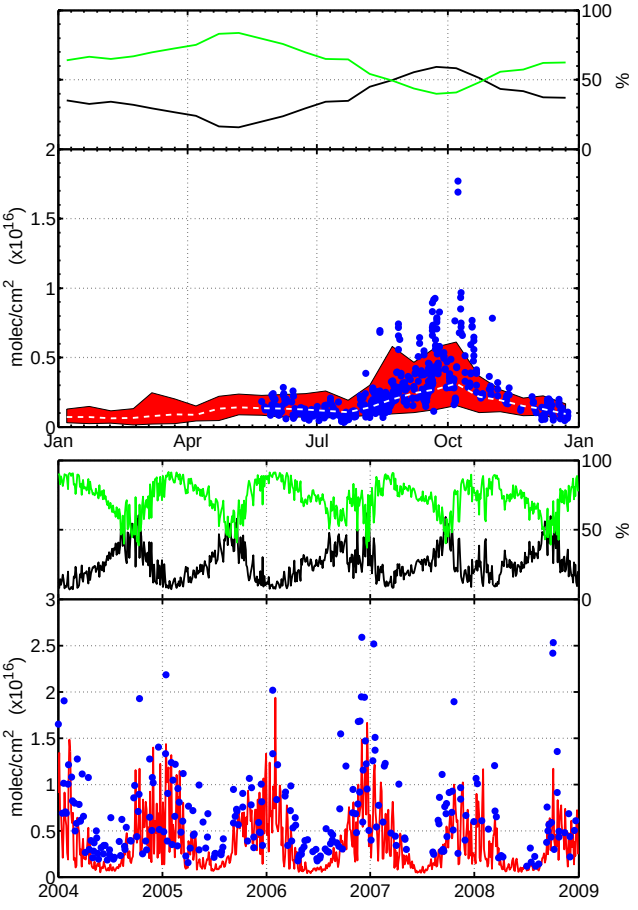

Fig. 11. A diffuse source of FA from aerosol aging (dominated by biomass burning (R3)) allows the model to reproduce the increase in FA during the biomass burning season in La Réunion **(a)** and Wollongong **(b)**. Color code as Fig. 3.

the lifetime of FA. This is evident in the comparison with the cruise measurements where a very large increase is observed in the tropics, reflecting the enhanced transport of FA biomass burning precursors away from their source regions (Fig. S11). Other locations impacted by biomass burning such as Thule see large increases in FA or AA though this remains insufficient to bridge the gap between model and measurements.

In the GEOS-Chem simulations used in this study, organic aerosol sources are dominated by biomass burning. Because of the lack of a proper representation of secondary organic aerosol (SOA) in our simulation, it is not surprising the discrepancy remains very large in locations where organic aerosols are dominated by SOA from biogenic or anthropogenic sources (e.g., Bremen (Fig. S13), INTEX-B). Future work will focus on assessing the role of semivolatiles as a source of FA and AA. In particular, the interaction between biotic emissions (biogenic and agricultural) and anthropogenic activities need to be properly represented, as it has been shown that this interaction could result in enhanced

secondary aerosol formation (de Gouw et al., 2005; Weber et al., 2007; Goldstein et al., 2009). If SOA aging is indeed a source of FA and AA, this could help explain the biogenic signature of FA and AA in polluted regions (seasonality and isotopic composition), as well as the similar magnitudes of Wollongong and Bremen FA total columns despite very different isoprene sources.

4.3 Upper tropospheric budget of FA

The ACE-FTS comparison revealed a high bias of the model in the upper troposphere. At these altitudes, wet deposition becomes small and FA sink is dominated by the reaction of OH with FA.

To examine the sensitivity of the FA profile to the temperature dependence of its reaction with OH, we use the temperature dependence derived theoretically by Galano et al. (2002) for the acidic (k_1) and formyl channels (k_2) and scale it to match the experimental rate of FA + OH determined at room temperature. The resulting rate constant of FA with OH ($k_{\mathrm{FA+OH}}$) is :

$$k_{\mathrm{FA+OH}} = k_1 + k_2 = 2.94 \times 10^{-14} \times \exp\left(\frac{786}{T}\right) + 9.85 \times 10^{-13} \times \exp\left(-\frac{1036}{T}\right)$$

At 220 K, this predicts the oxidation of FA is 2.3 times faster than at 298 K.

In the R4 simulation, we also include FA formation from organic aerosol (as in R3) as well as the injection of FA in the mid troposphere (as in R2a). The change in the reaction rate at cold temperature results in a dramatic decrease of FA in the upper troposphere (Fig. 7), because photooxidation is the dominant sink of FA in this region. This decrease is especially remarkable since mid troposphere FA is increased as a result of the injection of biomass burning in this regions. This result must be interpreted cautiously as the model may underestimate HO_x in the upper troposphere, especially in the tropics (Wennberg et al., 1998). The fate of FA in the upper troposphere deserves more study since FA could provide a useful proxy to investigate biomass burning injection in the free troposphere.

The discrepancy between model and observation of FA in the upper troposphere is further amplified if the equilibrium between $HOCH_2OO$ and $HCHO + HO_2$ is considered (Veyret et al., 1989).

$$HCHO + HO_2 \leftrightarrows HOCH2OO \quad \text{(R3)}$$

$$HOCH_2O_2 + HO_2 \rightarrow HOCH2OOH \quad \text{(R4)}$$

$$HOCH_2O_2 + HO_2 \rightarrow HOCH2O + OH + O_2 \quad \text{(R5)}$$

$$HOCH_2O_2 + HO_2 \rightarrow FA + H_2O \quad \text{(R6)}$$

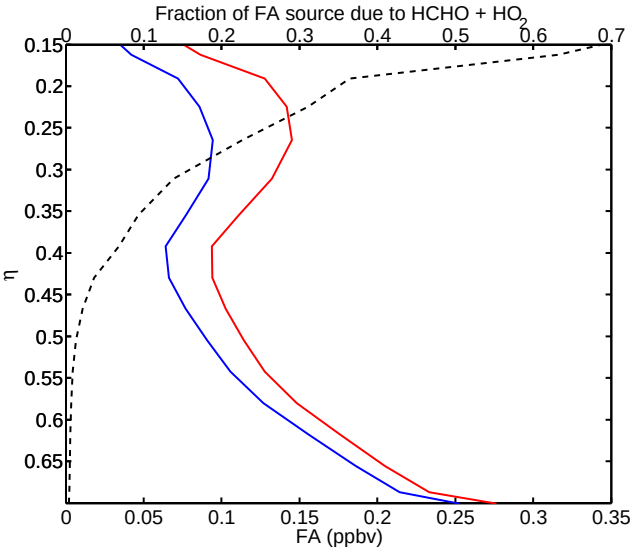

Fig. 12. Including a representation of $HCHO + HO_2$ chemistry increases FA in the upper troposphere by nearly 50% (red) compared to the reference run (blue). Such a source (black dashed line) would further amplify the high bias of the model with respect to ACE-FTS observations. Profile of FA at −14° N, 60° W July 2005.

$$HOCH_2O_2 + NO \rightarrow HOCH2O + NO_2 \quad \text{(R7)}$$

$$HOCH_2O + O_2 \rightarrow FA + HO_2 \quad \text{(R8)}$$

$$HOCH_2OOH \xrightarrow{S} FA \quad \text{(R9)}$$

$$HOCH_2OOH + OH \rightarrow FA + H_2O + OH \quad \text{(R10)}$$

$$HOCH_2OOH + OH \rightarrow HOCH_2OO \quad \text{(R11)}$$

$$HOCH_2OOH + h\nu \rightarrow HOCH_2O + OH \quad \text{(R12)}$$

Reaction of $HOCH_2OO$ with NO results in FA formation. Jenkin et al. (2007) reported than (R5) and (R6) account for 20% and 30% of the reaction of $HOCH_2OO$ with HO_2. The photooxidation of hydroxymethylhydroperoxide ($HOCH_2OOH$) is also expected to form FA with high yield from photolysis, reaction with OH and heterogeneous decomposition (Neeb et al., 1997). Therefore we assume that the reaction of HO_2 with $HOCH_2OO$ results in FA formation with a yield of 1. As shown on Fig. 12, $HO_2 + HCHO$ chemistry significantly increases FA in the upper troposphere where the lifetime of $HOCH_2OO$ is long enough for the reaction of $HOCH_2OO$ with NO and HO_2 to compete with $HOCH_2OO$ decomposition. As pointed by Hermans et al. (2005), proper assesment of $HCHO + HO_2$ importance as a sink of formaldehyde and source of FA requires very precise knowledge of the temperature dependence of (R3). Recent measurements of $HOCH_2OO \rightarrow HO_2 + CH_2O$ by Pinceloup et al. (2003) are significantly slower than the recommended IUPAC value (Atkinson et al., 2006) used in this simulation. This suggests the source of FA from $HCHO + HO_2$ in the free

troposphere may be even larger than shown on Fig. 12. FA observations in the upper troposphere thus provide a much needed test of the representation of $HCHO + HO_2$ in models.

5 Conclusions

We have derived a detailed bottom-up inventory of FA and AA in the atmosphere. Our updated source of FA is more than twice as large as previous estimates, reflecting the formation of FA from the photooxidation of isoprene and its products by OH. Both carboxylic acids are predicted to originate primarily from the photooxidation of biogenic compounds with biomass burning a significant seasonal source in many environments.

Despite these larger sources, the model remains biased low, especially in the Northern mid latitudes and in air masses affected by biomass burning. This discrepancy cannot be solely resolved by increasing biomass burning emissions of FA and AA.

We propose that a long-lived secondary source of FA and AA of order $\sim 2\,\mathrm{TmolC\,yr^{-1}}$ has yet to be identified. We hypothesize that the strong correlation of aerosol organic content with FA and AA hints at the possible relationship between aerosol aging and carboxylic acid production. If this relationship is demonstrated, FA and AA could prove very valuable to investigate aerosol aging, composition and sources. A realistic treatment of SOA (especially the missing SOA in polluted regions, including through anthropogenic-biogenic interactions), may help reduce the discrepancy in the mid latitudes where the biomass burning source of organic aerosol is limited.

The comparison between ACE-FTS mid and upper tropospheric measurements also reveals that strong enhancements in FA are consistent with injection of biomass burning emissions outside of the boundary layer (though FA is most likely associated with secondary production). FA may be used as a proxy to track biomass burning injection in the free troposphere, a very uncertain parameter in chemical transport models.

Finally even though the data set presented in this study offers the first long-term overview of the global distribution of FA, many regions of interest (in particular Africa and Asia), remain very poorly sampled. Ongoing efforts to retrieve FA from TES, IASI (Clerbaux et al., 2009; Razavi et al., 2011) or MIPAS-ENVISAT (Grutter et al., 2010) are thus particularly promising.

Supplementary material related to this article is available online at: http://www.atmos-chem-phys.net/11/1989/2011/acp-11-1989-2011-supplement.pdf.

Acknowledgement. The authors thank two anonymous referees and T. Stavrakou for their constructive comments. FP is supported by a NASA Earth and Space Science fellowship. GGA is supported by the Wild Fund and the National Center for Earth Observation (NCEO). DBM acknowledges support from NASA under Grant NNX10AG65G. The National Center for Atmospheric Research is supported by the National Science Foundation. The NCAR FTS observation program at Thule (GR) is supported under contract by the National Aeronautics and Space Administration (NASA). This work is also supported by the NSF Office of Polar Programs (OPP). PFD, EJD and JLJ were supported by NASA NNX08AD39G and NOAA NA08OAR4310565. The authors wish to thank the Danish Meteorological Institute for support at the Thule site. JN acknowledges funding by the grant from the Deutsche Forschungsgemeinschaft (DFG) NO 404/14-1. NMD and DWTG acknowledge support from the Australian Department of Innovation, Industry, Science and Research, Internation Science Linkage under Grant CG130014. CV and MDM acknowledge the PRODEX project SECPEA and the project AGACC from the Belgian Science Policy Office (contracts SD/AT/O1A and SD/AT/01B) for supporting the FTIR experiment at La Réunion. Part of this work was performed at the Jet Propulsion Laboratory, California Institute of Technology, under contract with NASA. The ACE mission is supported primarily by the Canadian Space Agency. Some support was also provided by the UK Natural Environment Research Council (NERC), through the National Centre for Earth Observation (NCEO). Measurements of FA and AA during the INTEX-B and Milagro missions were supported by NASA under Grant NNG06GB32B. The authors are grateful to Stephen Arnold and Dominick Spracklen for providing the marine isoprene fluxes, and to Sheryl Akagi and Robert Yokelson for providing updated biomass burning and biofuel emission factors. The numerical simulations for this research were performed on Caltech's Division of Geological and Planetary Sciences Dell cluster.

Edited by: J. P. D. Abbatt

References

Akagi, S. K., Yokelson, R. J., Wiedinmyer, C., Alvarado, M. J., Reid, J. S., Karl, T., Crounse, J. D., and Wennberg, P. O.: Emission factors for open and domestic biomass burning for use in atmospheric models, Atmos. Chem. Phys. Discuss., 10, 27523–27602, doi:10.5194/acpd-10-27523-2010, 2010.

Al-Hosney, H. A., Carlos-Cuellar, S., Baltrusaitis, J., and Grassian, V. H.: Heterogeneous uptake and reactivity of formic acid on calcium carbonate particles: a Knudsen cell reactor, FTIR and SEM study, Phys. Chem. Chem. Phys., 7, 3587–3595, doi:10.1039/b510112c, 2005.

Anderson, C. H., Dibb, J. E., Griffin, R. J., Hagler, G. S., and Bergin, M. H.: Atmospheric water-soluble organic carbon measurements at Summit, Greenland, Atmos. Environ., 42, 5612–5621, doi:10.1016/j.atmosenv.2008.03.006, 2008.

Andreae, M. O. and Merlet, P.: Emission of trace gases and aerosols from biomass burning, Global Biogeochem. Cy., 15, 955–966, doi:10.1029/2000GB001382, 2001.

Andreae, M. O., Rosenfeld, D., Artaxo, P., Costa, A. A., Frank, G. P., Longo, K. M., and Silva-Dias, M. A. F.: Smok-

ing Rain Clouds over the Amazon, Science, 303, 1337–1342, doi:10.1126/science.1092779, 2004.

Archibald, A. T., McGillen, M. R., Taatjes, C. A., Percival, C. J., and Shallcross, D. E.: Atmospheric transformation of enols: A potential secondary source of carboxylic acids in the urban troposphere, Geophys. Res. Lett., 34, L21 801, doi:10.1029/2007GL031032, 2007.

Arlander, D. W., Cronn, D. R., Farmer, J. C., Menzia, F. A., and Westberg, H. H.: Gaseous oxygenated hydrocarbons in the remote marine troposphere, J. Geophys. Res., 95, 16391–16403, doi:10.1029/JD095iD10p16391, 1990.

Arnold, S. R., Spracklen, D. V., Williams, J., Yassaa, N., Sciare, J., Bonsang, B., Gros, V., Peeken, I., Lewis, A. C., Alvain, S., and Moulin, C.: Evaluation of the global oceanic isoprene source and its impacts on marine organic carbon aerosol, Atmos. Chem. Phys., 9, 1253–1262, doi:10.5194/acp-9-1253-2009, 2009.

Aschmann, S. M., Arey, J., and Atkinson, R.: OH radical formation from the gas-phase reactions of O_3 with methacrolein and methyl vinyl ketone, Atmos. Environ., 30, 2939 – 2943, doi:10.1016/1352-2310(96)00013-1, 1996.

Atkinson, R., Baulch, D. L., Cox, R. A., Crowley, J. N., Hampson, R. F., Hynes, R. G., Jenkin, M. E., Rossi, M. J., Troe, J., and IUPAC Subcommittee: Evaluated kinetic and photochemical data for atmospheric chemistry: Volume II - gas phase reactions of organic species, Atmos. Chem. Phys., 6, 3625–4055, doi:10.5194/acp-6-3625-2006, 2006.

Baboukas, E. D., Kanakidou, M., and Mihalopoulos, N.: Carboxylic acids in gas and particulate phase above the Atlantic Ocean, J. Geophys. Res., 105, 14459–14472, doi:10.1029/1999JD900977, 2000.

Bernath, P. F., McElroy, C. T., Abrams, M. C., Boone, C. D., Butler, M., Camy-Peyret, C., Carleer, M., Clerbaux, C., Coheur, P., Colin, R., DeCola, P., DeMazière, M., Drummond, J. R., Dufour, D., Evans, W. F. J., Fast, H., Fussen, D., Gilbert, K., Jennings, D. E., Llewellyn, E. J., Lowe, R. P., Mahieu, E., McConnell, J. C., McHugh, M., McLeod, S. D., Michaud, R., Midwinter, C., Nassar, R., Nichitiu, F., Nowlan, C., Rinsland, C. P., Rochon, Y. J., Rowlands, N., Semeniuk, K., Simon, P., Skelton, R., Sloan, J. J., Soucy, M., Strong, K., Tremblay, P., Turnbull, D., Walker, K. A., Walkty, I., Wardle, D. A., Wehrle, V., Zander, R., and Zou, J.: Atmospheric Chemistry Experiment (ACE): Mission overview, Geophys. Res. Lett., 32(15), L15S01, doi:10.1029/2005GL022386, 2005.

Bey, I., Jacob, D. J., Yantosca, R. M., Logan, J. A., Field, B. D., Fiore, A. M., Li, Q., Liu, H. Y., Mickley, L. J., Schultz, M. G.: Global modeling of tropospheric chemistry with assimilated meteorology- Model description and evaluation, J. Geophys. Res., 106, 23073–23095, doi:10.1029/2001JD000807, 2001.

Bouwman, A. F. and Hoek, K. W. V. D.: Scenarios of animal waste production and fertilizer use and associated ammonia emission for the developing countries, Atmos. Environ., 31, 4095–4102, doi:10.1016/S1352-2310(97)00288-4, 1997.

Broadgate, W. J., Liss, P. S., and Penkett, S. A.: Seasonal emissions of isoprene and other reactive hydrocarbon gases from the ocean, Geophys. Res. Lett., 24, 2675–2678, doi:10.1029/97GL02736, 1997.

Butkovskaya, N. I., Kukui, A., Pouvesle, N., and Le Bras, G.: Rate constant and mechanism of the reaction of OH radicals with acetic acid in the temperature range of 229-300 K, J. Phys. Chem. A, 108, 7021–7026, doi:10.1021/jp048444v, 2004.

Butkovskaya, N. I., Pouvesle, N., Kukui, A., and Bras, G. L.: Mechanism of the OH-initiated oxidation of glycolaldehyde over the temperature range 233-296 K., J. Phys. Chem. A, 110, 13492–13499, doi:10.1021/jp064993k, 2006a.

Butkovskaya, N. I., Pouvesle, N., Kukui, A., Mu, Y., and Le Bras, G.: Mechanism of the OH-initiated oxidation of hydroxyacetone over the temperature Range 236-298 K, J. Phys. Chem. A, 110, 6833–6843, doi:10.1021/jp056345r, 2006b.

Capes, G., Johnson, B., McFiggans, G., Williams, P. I., Haywood, J., and Coe, H.: Aging of biomass burning aerosols over West Africa: Aircraft measurements of chemical composition, microphysical properties, and emission ratios, J. Geophys. Res. Atmos., 113, D00C15, doi:10.1029/2008JD009845, 2008.

Capouet, M., Peeters, J., Nozière, B., and Müller, J.-F.: Alpha-pinene oxidation by OH: simulations of laboratory experiments, Atmos. Chem. Phys., 4, 2285–2311, doi:10.5194/acp-4-2285-2004, 2004.

Carlos-Cuellar, S., Li, P., Christensen, A. P., Krueger, B. J., Burrichter, C., and Grassian, V. H.: Heterogeneous uptake kinetics of volatile organic compounds on oxide surfaces using a Knudsen cell reactor: Adsorption of acetic acid, formaldehyde, and methanol on α-Fe_2O_3, α-Al_2O_3, and SiO_2, J. Phys. Chem. A, 107, 4250–4261, doi:10.1021/jp0267609, 2003.

Carrasco, N., Doussin, J.-F., Picquet-Varrault, B., and Carlier, P.: Tropospheric degradation of 2-hydroxy-2-methylpropanal, a photo-oxidation product of 2-methyl-3-buten-2-ol: Kinetic and mechanistic study of its photolysis and its reaction with OH radicals, Atmos. Environ., 40, 2011–2019, doi:10.1016/j.atmosenv.2005.11.042, 2006.

Carrasco, N., Doussin, J., O'Connor, M., Wenger, J., Picquet-Varrault, B., Durand-Jolibois, R., and Carlier, P.: Simulation chamber studies of the atmospheric oxidation of 2-methyl-3-buten-2-ol: Reaction with hydroxyl radicals and ozone under a variety of conditions, J. Atmos. Chem., 56, 33–55, doi:10.1007/s10874-006-9041-y, 2007.

Chameides, W. L.: The photochemistry of a remote marine stratiform cloud, J. Geophys. Res., 89, 4739–4755, doi:10.1029/JD089iD03p04739, 1984.

Chebbi, A. and Carlier, P.: Carboxylic acids in the troposphere, occurrence, sources, and sinks: A review, Atmos. Environ., 30, 4233–4249, doi:10.1016/1352-2310(96)00102-1, 1996.

Christian, T. J., Kleiss, B., Yokelson, R. J., Holzinger, R., Crutzen, P. J., Hao, W. M., Saharjo, B. H., and Ward, D. E.: Comprehensive laboratory measurements of biomass-burning emissions: 1. Emissions from Indonesian, African, and other fuels, J. Geophys. Res., 108, 4719, doi:10.1029/2003JD003704, 2003.

Clerbaux, C., Boynard, A., Clarisse, L., George, M., Hadji-Lazaro, J., Herbin, H., Hurtmans, D., Pommier, M., Razavi, A., Turquety, S., Wespes, C., and Coheur, P.-F.: Monitoring of atmospheric composition using the thermal infrared IASI/MetOp sounder, Atmos. Chem. Phys., 9, 6041–6054, doi:10.5194/acp-9-6041-2009, 2009.

Crounse, J. D., McKinney, K. A., Kwan, A. J., and Wennberg, P. O.: Measurement of gas-phase hydroperoxides by chemical ionization mass spectrometry., Anal. Chem., 78, 6726–6732, doi:10.1021/ac0604235, 2006.

Crowley, J. N., Ammann, M., Cox, R. A., Hynes, R. G., Jenkin, M. E., Mellouki, A., Rossi, M. J., Troe, J., and Wallington, T. J.:

Evaluated kinetic and photochemical data for atmospheric chemistry: Volume V - heterogeneous reactions on solid substrates, Atmos. Chem. Phys., 10, 9059–9223, doi:10.5194/acp-10-9059-2010, 2010.

da Silva, G.: Carboxylic Acid Catalyzed Keto-Enol Tautomerizations in the Gas Phase, Angew. Chem., 49, 7523–7525, doi:10.1002/anie.201003530, 2010.

Davidson, E.: Pulses of nitric oxide and nitrous oxide flux following wetting of dry soil: An assessment of probable sources and importance relative to annual fluxes, Ecol. Bull., 149–155, 1992.

de Gouw, J. A. and Warneke, C.: Measurements of volatile organic compounds in the earth's atmosphere using proton-transfer-reaction mass spectrometry, Mass Spectrom. Rev., 26, 223–257, doi:10.1002/mas.20119, 2007.

de Gouw, J. A., Middlebrook, A. M., Warneke, C., Goldan, P. D., Kuster, W. C., Roberts, J. M., Fehsenfeld, F. C., Worsnop, D. R., Canagaratna, M. R., Pszenny, A. A. P., Keene, W. C., Marchewka, M., Bertman, S. B., and Bates, T. S.: Budget of organic carbon in a polluted atmosphere: Results from the New England Air Quality Study in 2002, J. Geophys. Res. Atmos., 110, 16305, doi:10.1029/2004JD005623, 2005.

de Gouw, J. A., Warneke, C., Stohl, A., Wollny, A. G., Brock, C. A., Cooper, O. R., Holloway, J. S., Trainer, M., Fehsenfeld, F. C., Atlas, E. L., Donnelly, S. G., Stroud, V., and Lueb, A.: Volatile organic compounds composition of merged and aged forest fire plumes from Alaska and western Canada, J. Geophys. Res. Atmos., 111, 10303, doi:10.1029/2005JD006175, 2006.

DeCarlo, P. F., Dunlea, E. J., Kimmel, J. R., Aiken, A. C., Sueper, D., Crounse, J., Wennberg, P. O., Emmons, L., Shinozuka, Y., Clarke, A., Zhou, J., Tomlinson, J., Collins, D. R., Knapp, D., Weinheimer, A. J., Montzka, D. D., Campos, T., and Jimenez, J. L.: Fast airborne aerosol size and chemistry measurements above Mexico City and Central Mexico during the MILAGRO campaign, Atmos. Chem. Phys., 8, 4027–4048, doi:10.5194/acp-8-4027-2008, 2008.

Dibb, J. E. and Arsenault, M.: Shouldn't snowpacks be sources of monocarboxylic acids?, Atmos. Environ., 36, 2513–2522, doi:10.1016/S1352-2310(02)00131-0, 2002.

Dillon, T. J. and Crowley, J. N.: Direct detection of OH formation in the reactions of HO_2 with $CH_3C(O)O_2$ and other substituted peroxy radicals, Atmos. Chem. Phys., 8, 4877–4889, http://www.atmos-chem-phys.net/8/4877/2008/, 2008.

Duncan, B. N., Logan, J. A., Bey, I., Megretskaia, I. A., Yantosca, R. M., Novelli, P. C., Jones, N. B., and Rinsland, C. P.: Global budget of CO, 1988-1997: Source estimates and validation with a global model, J. Geophys. Res. Atmos., 112, 22301, doi:10.1029/2007JD008459, 2007.

Dunlea, E. J., DeCarlo, P. F., Aiken, A. C., Kimmel, J. R., Peltier, R. E., Weber, R. J., Tomlinson, J., Collins, D. R., Shinozuka, Y., McNaughton, C. S., Howell, S. G., Clarke, A. D., Emmons, L. K., Apel, E. C., Pfister, G. G., van Donkelaar, A., Martin, R. V., Millet, D. B., Heald, C. L., and Jimenez, J. L.: Evolution of Asian aerosols during transpacific transport in INTEX-B, Atmos. Chem. Phys., 9, 7257–7287, doi:10.5194/acp-9-7257-2009, 2009.

Eichler, A., Brütsch, S., Olivier, S., Papina, T., and Schwikowski, M.: A 750 year ice core record of past biogenic emissions from Siberian boreal forests, Geophys. Res. Lett., 36, 18813, doi:10.1029/2009GL038807, 2009.

Eliason, T. L., Aloisio, S., Donaldson, D. J., Cziczo, D. J., and Vaida, V.: Processing of unsaturated organic acid films and aerosols by ozone, Atmos. Environ., 37, 2207–2219, doi:10.1016/S1352-2310(03)00149-3, 2003.

Eliason, T. L., Gilman, J. B., and Vaida, V.: Oxidation of organic films relevant to atmospheric aerosols, Atmos. Environ., 38, 1367–1378, doi:10.1016/j.atmosenv.2003.11.025, 2004.

Enders, G., Dlugi, R., Steinbrecher, R., Clement, B., Daiber, R., Eijk, J., Gäb, S., Haziza, M., Helas, G., Herrmann, U., Kessel, M., Kesselmeier, J., Kotzias, D., Kourtidis, K., Kurth, H.-H., McMillen, R., Roider, G., Schürmann, W., Teichmann, U., and Torres, L.: Biosphere/Atmosphere interactions: Integrated research in a European coniferous forest ecosystem, Atmospheric Environment. Part A. General Topics, 26, 171–189, doi:10.1016/0960-1686(92)90269-Q, 1992.

Fairlie, T. D., Jacob, D. J., and Park, R. J.: The impact of transpacific transport of mineral dust in the United States, Atmos. Environ., 41, 1251–1266, doi:10.1016/j.atmosenv.2006.09.048, 2007.

Falkovich, A. H., Schkolnik, G., Ganor, E., and Rudich, Y.: Adsorption of organic compounds pertinent to urban environments onto mineral dust particles, J. Geophys. Res. Atmos., 109, D02208, doi:10.1029/2003JD003919, 2004.

Fehsenfeld, F. C., Ancellet, G., Bates, T. S., Goldstein, A. H., Hardesty, R. M., Honrath, R., Law, K. S., Lewis, A. C., Leaitch, R., McKeen, S., Meagher, J., Parrish, D. D., Pszenny, A. A. P., Russell, P. B., Schlager, H., Seinfeld, J., Talbot, R., and Zbinden, R.: International Consortium for Atmospheric Research on Transport and Transformation (ICARTT): North America to Europe-Overview of the 2004 summer field study, J. Geophys. Res. Atmos., 111, D23S01, doi:10.1029/2006JD007829, 2006.

Fu, T., Jacob, D. J., Wittrock, F., Burrows, J. P., Vrekoussis, M., and Henze, D. K.: Global budgets of atmospheric glyoxal and methylglyoxal, and implications for formation of secondary organic aerosols, J. Geophys. Res. Atmos., 113, 15 303, doi:10.1029/2007JD009505, 2008.

Fuhrer, K. and Legrand, M.: Continental biogenic species in the Greenland Ice Core Project ice core: Tracing back the biomass history of the North American continent, J. Geophys. Res., 102, 26735–26746, doi:10.1029/97JC01299, 1997.

Galano, A., Alvarez-Idaboy, J., Ruiz-Santoyo, M., and Vivier-Bunge, A.: Rate coefficient and mechanism of the gas phase OH hydrogen abstraction reaction from formic acid: A quantum mechanical approach, J. Phys. Chem. A, 106, 9520–9528, doi:10.1021/jp020297i, 2002.

Galloway, J. N., Likens, G. E., Keene, W. C., and Miller, J. M.: The composition of precipitation in remote areas of the world, J. Geophys. Res., 87, 8771–8786, doi:10.1029/JC087iC11p08771, 1982.

Gao, S., Hegg, D., Hobbs, P., Kirchstetter, T., Magi, B., and Sadilek, M.: Water-soluble organic components in aerosols associated with savanna fires in southern Africa: Identification, evolution, and distribution, J. Geophys. Res., 108, 8491, doi:10.1029/2002JD002324, 2003.

George, I. J., Slowik, J., and Abbatt, J. P. D.: Chemical aging of ambient organic aerosol from heterogeneous reaction with hydroxyl radicals, Geophys. Res. Lett., 35, 13811, doi:10.1029/2008GL033884, 2008.

Giglio, L., Randerson, J. T., van der Werf, G. R., Kasibhatla, P. S., Collatz, G. J., Morton, D. C., and DeFries, R. S.: Assess-

ing variability and long-term trends in burned area by merging multiple satellite fire products, Biogeosciences, 7, 1171–1186, doi:10.5194/bg-7-1171-2010, 2010.

Glasius, M., Wessel, S., Christensen, C., Jacobsen, J., Jørgensen, H., Klitgaard, K., Petersen, L., Rasmussen, J., Stroyer Hansen, T., Lohse, C., Boaretto, E., and Heinemeier, J.: Sources to formic acid studied by carbon isotopic analysis and air mass characterization, Atmos. Environ., 34, 2471–2479, doi:10.1016/S1352-2310(99)00416-1, 2000.

Glasius, M., Boel, C., Bruun, N., Easa, L. M., Hornung, P., Klausen, H. S., Klitgaard, K. C., Lindeskov, C., Møller, C. K., Nissen, H., Petersen, A. P. F., Kleefeld, S., Boaretto, E., Hansen, T. S., Heinemeier, J., and Lohse, C.: Relative contribution of biogenic and anthropogenic sources to formic and acetic acids in the atmospheric boundary layer, J. Geophys. Res., 106, 7415–7426, doi:10.1029/2000JD900676, 2001.

Goldstein, A. H., Koven, C. D., Heald, C. L., and Fung, I. Y.: Biogenic carbon and anthropogenic pollutants combine to form a cooling haze over the southeastern United States, P. Natl. Acad. Sci. USA, 106, 8835–8840, doi:10.1073/pnas.0904128106, 2009.

Gonzàlez Abad, G., Bernath, P. F., Boone, C. D., McLeod, S. D., Manney, G. L., and Toon, G. C.: Global distribution of upper tropospheric formic acid from the ACE-FTS, Atmos. Chem. Phys., 9, 8039–8047, doi:10.5194/acp-9-8039-2009, 2009.

Goode, J. G., Yokelson, R. J., Ward, D. E., Susott, R. A., Babbitt, R. E., Davies, M. A., and Hao, W. M.: Measurements of excess O_3, CO_2, CH_4, C_2H_4, C_2H_2, HCN, NO, NH_3, HCOOH, CH_3COOH, HCHO, and CH_3OH in 1997 Alaskan biomass burning plumes by airborne Fourier transform infrared spectroscopy (AFTIR), J. Geophys. Res., 105, 22147–22166, doi:10.1029/2000JD900287, 2000.

Graedel, T. E. and Eisner, T.: Atmospheric formic acid from formicine ants: a preliminary assessment, Tellus B, 40, 335–339, doi:10.1111/j.1600-0889.1988.tb00107.x, 1988.

Grosjean, D., Williams, E. L., and Grosjean, E.: Atmospheric chemistry of isoprene and of its carbonyl products, Environ. Sci. Technol., 27, 830–840, doi:10.1021/es00042a004, 1993.

Grutter, M., Glatthor, N., Stiller, G. P., Fischer, H., Grabowski, U., Höpfner, M., Kellmann, S., Linden, A., and von Clarmann, T.: Global distribution and variability of formic acid as observed by MIPAS-ENVISAT, J. Geophys. Res. Atmos., 115, 10303, doi:10.1029/2009JD012980, 2010.

Guenther, A., Geron, C., Pierce, T., Lamb, B., Harley, P., and R., F.: Natural emissions of non-methane volatile organic compounds, carbon monoxide, and oxides of nitrogen from North America, Atmos. Environ., 34, 2205–2230, doi:10.1016/S1352-2310(99)00465-3, 2000.

Guenther, A., Karl, T., Harley, P., Wiedinmyer, C., Palmer, P. I., and Geron, C.: Estimates of global terrestrial isoprene emissions using MEGAN (Model of Emissions of Gases and Aerosols from Nature), Atmos. Chem. Phys., 6, 3181–3210, doi:10.5194/acpd-6-107-2006, 2006.

Harley, P., Fridd-Stroud, V., Greenberg, J., Guenther, A., and Vasconcellos, P.: Emission of 2-methyl-3-buten-2-ol by pines- A potentially large natural source of reactive carbon to the atmosphere, J. Geophys. Res., 103(25), 25479–25486, doi:10.1029/98JD00820, 1998.

Hasson, A. S., Tyndall, G. S., and Orlando, J. J.: A product yield study of the reaction of HO_2 radicals with ethyl peroxy ($C_2H_5O_2$), acetyl peroxy (CH_3 $C(O)O_2$), and acetonyl peroxy ($CH_3C(O)CH_2O_2$) radicals, J. Phys. Chem. A, 108, 5979–5989, doi:10.1021/jp048873t, 2004.

Hatakeyama, S., Washida, N., and Akimoto, H.: Rate constants and mechanisms for the reaction of hydroxyl (OD) radicals with acetylene, propyne, and 2-butyne in air at 297 ± 2 K, J. Phys. Chem., 90, 173–178, doi:10.1021/j100273a039, 1986.

Hatch, C. D., Gough, R. V., and Tolbert, M. A.: Heterogeneous uptake of the C_1 to C_4 organic acids on a swelling clay mineral, Atmos. Chem. Phys., 7, 4445–4458, http://www.atmos-chem-phys.net/7/4445/2007/, 2007.

Heald, C. L., Kroll, J. H., Jimenez, J. L., Docherty, K. S., DeCarlo, P. F., Aiken, A. C., Chen, Q., Martin, S. T., Farmer, D. K., and Artaxo, P.: A simplified description of the evolution of organic aerosol composition in the atmosphere, Geophys. Res. Lett., 37, 8803, doi:10.1029/2010GL042737, 2010.

Hermans, I., Müller, J. F., Nguyen, T. L., Jacobs, P., and Peeters, J.: Kinetics of-Hydroxy-alkylperoxyl Radicals in Oxidation Processes. HO_2 Initiated Oxidation of Ketones/Aldehydes near the Tropopause, J. Phys. Chem. A, 109, 4303–4311, 2005.

Herndon, S. C., Zahniser, M. S., Nelson, D. D., Shorter, J., McManus, J. B., Jiménez, R., Warneke, C., and de Gouw, J. A.: Airborne measurements of HCHO and HCOOH during the New England Air Quality Study 2004 using a pulsed quantum cascade laser spectrometer, J. Geophys. Res. Atmos., 112, D10S03, doi:10.1029/2006JD007600, 2007.

Huang, Y. W., Dransfield, T. J., Miller, J. D., Rojas, R. D., Castillo, X. G., and Anderson, J. G.: Experimental Study of the Kinetics of the Reaction of Acetic Acid with Hydroxyl Radicals from 255 to 355 K, J. Phys. Chem. A, 113, 423–430, doi:10.1021/jp808627w, 2009.

Ito, A., Sillman, S., and Penner, J. E.: Effects of additional nonmethane volatile organic compounds, organic nitrates, and direct emissions of oxygenated organic species on global tropospheric chemistry, J. Geophys. Res., 112, D06309, doi:10.1029/2005JD006556, 2007.

Jacob, D. J.: Chemistry of OH in remote clouds and its role in the production of formic acid and peroxymonosulfate, J. Geophys. Res., 91, 9807–9826, doi:10.1029/JD091iD09p09807, 1986.

Jacob, D. J. and Wofsy, S. C.: Photochemistry of biogenic emissions over the Amazon forest, J. Geophys. Res., 93, 1477–1486, doi:10.1029/JD093iD02p01477, 1988.

Jenkin, M. E., Hurley, M. D., and Wallington, T. J.: Investigation of the radical product channel of the CH_3 C (O) $O_2 + HO_2$ reaction in the gas phase, Phys. Chem. Chem. Phys., 9, 3149–3162, 2007.

Jimenez, J. L., Canagaratna, M. R., Donahue, N. M., Prevot, A. S. H., Zhang, Q., Kroll, J. H., DeCarlo, P. F., Allan, J. D., Coe, H., Ng, N. L., Aiken, A. C., Docherty, K. S., Ulbrich, I. M., Grieshop, A. P., Robinson, A. L., Duplissy, J., Smith, J. D., Wilson, K. R., Lanz, V. A., Hueglin, C., Sun, Y. L., Tian, J., Laaksonen, A., Raatikainen, T., Rautiainen, J., Vaattovaara, P., Ehn, M., Kulmala, M., Tomlinson, J. M., Collins, D. R., Cubison, M. J., E., Dunlea, J., Huffman, J. A., Onasch, T. B., Alfarra, M. R., Williams, P. I., Bower, K., Kondo, Y., Schneider, J., Drewnick, F., Borrmann, S., Weimer, S., Demerjian, K., Salcedo, D., Cottrell, L., Griffin, R., Takami, A., Miyoshi, T., Hatakeyama, S., Shimono, A., Sun, J. Y., Zhang, Y. M., Dzepina, K., Kimmel, J. R., Sueper, D., Jayne, J. T., Herndon, S. C., Trim-

born, A. M., Williams, L. R., Wood, E. C., Middlebrook, A. M., Kolb, C. E., Baltensperger, U., and Worsnop, D. R.: Evolution of Organic Aerosols in the Atmosphere, Science, 326, 1525–1529, doi:10.1126/science.1180353, 2009.

Karl, M., Guenther, A., Köble, R., Leip, A., and Seufert, G.: A new European plant-specific emission inventory of biogenic volatile organic compounds for use in atmospheric transport models, Biogeosciences, 6, 1059–1087, doi:10.5194/bg-6-1059-2009, 2009.

Kawamura, K., Ng, L., and Kaplan, I.: Determination of organic acids (C1–C10) in the atmosphere, motor exhausts, and engine oils, Environ. Sci. Technol., 19, 1082–1086, doi:10.1021/es00141a010, 1985.

Keene, W. C. and Galloway, J. N.: The biogeochemical cycling of formic and acetic acids through the troposphere - An overview of current understanding, Tellus B, 40, 322–334, doi:10.1111/j.1600-0889.1988.tb00106.x, 1988.

Kesselmeier, J.: Exchange of short-chain oxygenated volatile organic compounds (VOCs) between plants and the atmosphere: A compilation of field and laboratory studies, J. Atmos. Chem., 39, 219–233, doi:10.1023/A:1010632302076, 2001.

Kesselmeier, J. and Staudt, M.: Biogenic Volatile Organic Compounds (VOC): An Overview on Emission, Physiology and Ecology, J. Atmos. Chem., 33, 23–88, doi:10.1023/A:1006127516791, 1999.

Kesselmeier, J., Bode, K., Gerlach, C., and Jork, E.: Exchange of atmospheric formic and acetic acids with trees and crop plants under controlled chamber and purified air conditions, Atmos. Environ., 32, 1765–1775, doi:10.1016/S1352-2310(97)00465-2, 1998.

Khare, P., Kumar, N., Kumari, K. M., and Srivastava, S. S.: Atmospheric formic and acetic acids: An overview, Rev. Geophys., 37, 227–248, doi:10.1029/1998RG900005, 1999.

Kroll, J. H., Smith, J. D., Che, D. L., Kessler, S. H., Worsnop, D. R., and Wilson, K. R.: Measurement of fragmentation and functionalization pathways in the heterogeneous oxidation of oxidized organic aerosol, Phys. Chem. Chem. Phys., 11, 8005o, doi:10.1039/b905289e, 2009.

Kurylo, M. and Solomon, S.: Network for the detection of stratospheric change: a status and implementation report, NASA and NOAA Special Report, 1990.

Kwan, A. J., Crounse, J. D., Clarke, A. D., Shinozuka, Y., Anderson, B. E., Crawford, J. H., Avery, M. A., McNaughton, C. S., Brune, W. H., Singh, H. B., and Wennberg, P. O.: On the flux of oxygenated volatile organic compounds from organic aerosol oxidation, Geophys. Res. Lett., 33, L15815, doi:10.1029/2006GL026144, 2006.

Larsen, B. R., Di Bella, D., Glasius, M., Winterhalter, R., Jensen, N. R., and Hjorth, J.: Gas-phase OH oxidation of monoterpenes: Gaseous and particulate products, J. Atmos. Chem., 38, 231–276, doi:10.1023/A:1006487530903, 2001.

Lathière, J., Hauglustaine, D. A., Friend, A. D., De Noblet-Ducoudré, N., Viovy, N., and Folberth, G. A.: Impact of climate variability and land use changes on global biogenic volatile organic compound emissions, Atmos. Chem. Phys., 6, 2129–2146, doi:10.5194/acp-6-2129-2006, 2006.

Lee, A., Goldstein, A. H., Keywood, M. D., Gao, S., Varutbangkul, V., Bahreini, R., Ng, N. L., Flagan, R. C., and Seinfeld, J. H.: Gas-phase products and secondary aerosol yields from the ozonolysis of ten different terpenes, J. Geophys. Res., 111, D07302, doi:10.1029/2005JD006437, 2006.

Lee, M., Heikes, B. G., and O'Sullivan, D. W.: Hydrogen peroxide and organic hydroperoxide in the troposphere: a review, Atmos. Environ., 34, 3475–3494, doi:10.1016/S1352-2310(99)00432-X, 2000.

Lee, S., Murphy, D. M., Thomson, D. S., and Middlebrook, A. M.: Chemical components of single particles measured with Particle Analysis by Laser Mass Spectrometry (PALMS) during the Atlanta SuperSite Project: Focus on organic/sulfate, lead, soot, and mineral particles, J. Geophys. Res., 107, 4003, doi:10.1029/2000JD000011, 2002.

Legrand, M. and De Angelis, M.: Light carboxylic acids in Greenland ice: A record of past forest fires and vegetation emissions from the boreal zone, J. Geophys. Res., 101, 4129–4146, doi:10.1029/95JD03296, 1996.

Lelieveld, J. and Crutzen, P.: The role of clouds in tropospheric photochemistry, J. Atmos. Chem., 12, 229–267, doi:10.1007/BF00048075, 1991.

Liu, H., Jacob, D. J., Bey, I., and Yantosca, R. M.: Constraints from ^{210}Pb and ^{7}Be on wet deposition and transport in a global three-dimensional chemical tracer model driven by assimilated meteorological fields, J. Geophys. Res., 106, 12109–12128, doi:10.1029/2000JD900839, 2001.

Marécal, V., Pirre, M., Rivière, E. D., Pouvesle, N., Crowley, J. N., Freitas, S. R., and Longo, K. M.: Modelling the reversible uptake of chemical species in the gas phase by ice particles formed in a convective cloud, Atmos. Chem. Phys., 10, 4977–5000, doi:10.5194/acp-10-4977-2010, 2010.

Mari, C., Bechtold, P., and Jacob, D.: Transport and scavenging of soluble gases in a deep convective cloud, J. Geophys. Res., 105, 22255–22268, doi:10.1029/2000JD900211, 2000.

Millet, D. B., Guenther, A., Siegel, D. A., Nelson, N. B., Singh, H. B., de Gouw, J. A., Warneke, C., Williams, J., Eerdekens, G., Sinha, V., Karl, T., Flocke, F., Apel, E., Riemer, D. D., Palmer, P. I., and Barkley, M.: Global atmospheric budget of acetaldehyde: 3-D model analysis and constraints from in-situ and satellite observations, Atmos. Chem. Phys., 10, 3405–3425, http://www.atmos-chem-phys.net/10/3405/2010/, 2010.

Molina, M. J., Ivanov, A. V., Trakhtenberg, S., and Molina, L. T.: Atmospheric evolution of organic aerosol, Geophys. Res. Lett., 31, 22 104, doi:10.1029/2004GL020910, 2004.

Neeb, P., Sauer, F., Horie, O., and Moortgat, G. K.: Formation of hydroxymethyl hydroperoxide and formic acid in alkene ozonolysis in the presence of water vapour, Atmos. Environ., 31, 1417–1423, doi:10.1016/S1352-2310(96)00322-6, 1997.

Ngwabie, N. M., Schade, G. W., Custer, T. G., Linke, S., and Hinz, T.: Abundances and flux estimates of volatile organic compounds from a dairy cowshed in Germany, J. Environ. Qual., 37, 565–573, doi:10.2134/jeq2006.0417, 2008.

Orlando, J. J., Nozière, B., Tyndall, G. S., Orzechowska, G. E., Paulson, S. E., and Rudich, Y.: Product studies of the OH- and ozone-initiated oxidation of some monoterpenes, J. Geophys. Res., 105, 11 561–11 572, doi:10.1029/2000JD900005, 2000.

Otter, L. B., Guenther, A., and Greenberg, J.: Seasonal and spatial variations in biogenic hydrocarbon emissions from southern African savannas and woodlands, Atmos. Environ., 36, 4265–4275, doi:10.1016/S1352-2310(02)00333-3, 2002.

Pan, X., Underwood, J. S., Xing, J.-H., Mang, S. A., and Nizkorodov, S. A.: Photodegradation of secondary organic aerosol gen-

erated from limonene oxidation by ozone studied with chemical ionization mass spectrometry, Atmos. Chem. Phys., 9, 3851–3865, doi:10.5194/acp-9-3851-2009, 2009.

Park, R. J., Jacob, D. J., Chin, M., and Martin, R. V.: Sources of carbonaceous aerosols over the United States and implications for natural visibility, J. Geophys. Res. Atmos., 108, 4355, doi:10.1029/2002JD003190, 2003.

Park, J., Gomez, A. L., Walser, M. L., Lin, A., and Nizkorodov, S. A.: Ozonolysis and photolysis of alkene-terminated self-assembled monolayers on quartz nanoparticles: implications for photochemical aging of organic aerosol particles, Phys. Chem. Chem. Phys., 8, 2506, doi:10.1039/b602704k, 2006.

Parrish, D. D., Allen, D. T., Bates, T. S., Estes, M., Fehsenfeld, F. C., Feingold, G., Ferrare, R., Hardesty, R. M., Meagher, J. F., Nielsen-Gammon, J. W., Pierce, R. B., Ryerson, T. B., Seinfeld, J. H., and Williams, E. J.: Overview of the Second Texas Air Quality Study (TexAQS II) and the Gulf of Mexico Atmospheric Composition and Climate Study (GoMACCS), J. Geophys. Res. Atmos., 114, D00F13, doi:10.1029/2009JD011842, 2009.

Paton-Walsh, C., Jones, N. B., Wilson, S. R., Haverd, V., Meier, A., Griffith, D. W. T., and Rinsland, C. P.: Measurements of trace gas emissions from Australian forest fires and correlations with coincident measurements of aerosol optical depth, J. Geophys. Res. Atmos., 110, 24305, doi:10.1029/2005JD006202, 2005.

Paulot, F., Crounse, J. D., Kjaergaard, H. G., Kroll, J. H., Seinfeld, J. H., and Wennberg, P. O.: Isoprene photooxidation: new insights into the production of acids and organic nitrates, Atmos. Chem. Phys., 9, 1479–1501, http://www.atmos-chem-phys.net/9/1479/2009/, 2009.

Peeters, J., Vereecken, L., and Fantechi, G.: The detailed mechanism of the OH-initiated atmospheric oxidation of α-pinene: a theoretical study, Phys. Chem. Chem. Phys., 3, 5489–5504, doi:10.1039/b106555f, 2001.

Peeters, J., Nguyen, T., and Vereecken, L.: HO_x radical regeneration in the oxidation of isoprene, Phys. Chem. Chem. Phys., 11, 5935–5939, doi:10.1039/b908511d, 2009.

Peters, W., Krol, M. C., Fortuin, J. P. F., Kelder, H. M., Thompson, A. M., Becker, C. R., Lelieveld, J., and Crutzen, P. J.: Tropospheric ozone over a tropical Atlantic station in the Northern Hemisphere: Paramaribo, Surinam (6° N, 55° W), Tellus B, 56, 21–34, doi:10.1111/j.1600-0889.2004.00083.x, 2004.

Petersen, A. K., Warneke, T., Lawrence, M. G., Notholt, J., and Schrems, O.: First ground-based FTIR observations of the seasonal variation of carbon monoxide in the tropics, Geophys. Res. Lett., 35, 3813, doi:10.1029/2007GL031393, 2008.

Pinceloup, S., Laverdet, G., Maguin, F., Doussin, J. F., Carlier, P., and Bras, G. L.: Laboratory investigation of the photooxidation of formaldehyde combining FTIR analysis of stable species and HO2 detection by the chemical amplifier technique, J. Photochem. Photobiol., A, 157, 275–281, doi:10.1016/S1010-6030(03)00066-2, 2003.

Poisson, N., Kanakidou, M., and Crutzen, P. J.: Impact of Non-Methane Hydrocarbons on Tropospheric Chemistry and the Oxidizing Power of the Global Troposphere: 3-Dimensional Modelling Results, J. Atmos. Chem., 36, 157–230, doi:10.1023/A:1006300616544, 2000.

Prince, A., Kleiber, P., Grassian, V., and Young, M.: Reactive uptake of acetic acid on calcite and nitric acid reacted calcite aerosol in an environmental reaction chamber, Phys. Chem. Chem. Phys., 10, 142–152, doi:10.1039/b712915g, 2008.

Randerson, J. T., van der Werf, G. R., Giglio, L., Collatz, G. J., and Kasibhatla, P. S.: Global Fire Emissions Database, Version 2 (GFEDv2), Tech. rep., Oak Ridge National Laboratory Distributed Active Archive Center, Oak Ridge, TN, USA, doi:10.3334/ORNLDAAC/834, 2006.

Razavi, A., Karagulian, F., Clarisse, L., Hurtmans, D., Coheur, P. F., Clerbaux, C., Müller, J. F., and Stavrakou, T.: Global distributions of methanol and formic acid retrieved for the first time from the IASI/MetOp thermal infrared sounder, Atmos. Chem. Phys., 11, 857–872, doi:10.5194/acp-11-857-2011, 2011.

Rinsland, C. P., Boone, C. D., Bernath, P. F., Mahieu, E., Zander, R. , Dufour, G., Clerbaux, C., Turquety, S., Chiou, L., Mc-Connell, J. C., Neary, L., and Kaminski, J. W.: Atmospheric Chemistry Experiment austral spring 2004 and 2005 Southern Hemisphere tropical-mid-latitude upper tropospheric measurements, Geophys. Res. Lett, 33, L23804, doi:10.1029/2006GL027128, 2006.

Rinsland, C. P., Dufour, G., Boone, C. D., Bernath, P. F., Chiou, L., Coheur, P.-F., Turquety, S., and Clerbaux, C.: Satellite boreal measurements over Alaska and Canada during June-July 2004: Simultaneous measurements of upper tropospheric CO, C_2H_6, HCN, CH_3Cl, CH_4, C_2H_2, CH_3OH, HCOOH, OCS, and SF_6 mixing ratios, Global Biogeochem. Cy., 21, B3008, doi:10.1029/2006GB002795, 2007.

Robinson, A. L., Donahue, N. M., Shrivastava, M. K., Weitkamp, E. A., Sage, A. M., Grieshop, A. P., Lane, T. E., Pierce, J. R., and Pandis, S. N.: Rethinking Organic Aerosols: Semivolatile Emissions and Photochemical Aging, Science, 315, 1259, doi:10.1126/science.1133061, 2007.

Rothman, L. S., Gordon, I. E., Barbe, A., Benner, D. C., Bernath, P. F., Birk, M., Boudon, V., Brown, L. R., Campargue, A., Champion, J.-P., Chance, K., Coudert, L. H., Dana, V., Devi, V. M., Fally, S., Flaud, J.-M., Gamache, R. R., Goldman, A., Jacquemart, D., Kleiner, I., Lacome, N., Lafferty, W. J., Mandin, J.-Y., Massie, S. T., Mikhailenko, S. N., Miller, C. E., Moazzen-Ahmadi, N., Naumenko, O. V., Nikitin, A. V., Orphal, J., Perevalov, V. I., Perrin, A., Predoi-Cross, A., Rinsland, C. P., Rotger, M., Simeckov, M., Smith, M. A. H., Sung, K., Tashkun, S. A., Tennyson, J., Toth, R. A., Vandaele, A. C., and Auwera, J. V.: The HITRAN 2008 molecular spectroscopic database, J. Quant. Spectrosc. Ra., 110, 533–572, doi:10.1016/j.jqsrt.2009.02.013, 2009.

Russell, L. M., Maria, S. F., and Myneni, S. C. B.: Mapping organic coatings on atmospheric particles, Geophys. Res. Lett., 29, 1779, doi:10.1029/2002GL014874, 2002.

Sander, R.: Compilation of Henry's Law Constants for Inorganic and Organic Species of Potential Importance in Environmental Chemistry (Version 3), Tech. rep., 1999.

Sanhueza, E. and Andreae, M. O.: Emission of formic and acetic acids from tropical savanna soils, Geophys. Res. Lett., 18, 1707–1710, doi:10.1029/91GL01565, 1991.

Sanhueza, E., Figueroa, L., and Santana, M.: Atmospheric formic and acetic acids in Venezuela, Atmos. Environ., 30, 1861–1873, doi:10.1016/1352-2310(95)00383-5, joint 8th CAGCP and 2nd IGAC Conference on Global Atmospheric Chemistry, 1996.

Shaw, S., Mitloehner, F., Jackson, W., DePeters, E., Fadel, J., Robinson, P., Holzinger, R., and Goldstein, A.: Volatile organic compound emissions from dairy cows and their waste as mea-

sured by proton-transfer-reaction mass spectrometry, Environ. Sci. Technol, 41, 1310–1316, doi:10.1021/es061475e, 2007.

Singh, H. B., Brune, W. H., Crawford, J. H., Flocke, F., and Jacob, D. J.: Chemistry and transport of pollution over the Gulf of Mexico and the Pacific: spring 2006 INTEX-B campaign overview and first results, Atmos. Chem. Phys., 9, 2301–2318, doi:10.5194/acp-9-2301-2009,
2009.

Sinreich, R., Coburn, S., Dix, B., and Volkamer, R.: Ship-based detection of glyoxal over the remote tropical Pacific Ocean, Atmos. Chem. Phys., 10, 11359–11371, doi:10.5194/acp-10-11359-2010, 2010.

Sposito, G.: The Chemistry of Soils, Oxford University. Press, 1989.

Sun, W. and Saeys, M.: first principles Study of the Reaction of Formic and Acetic Acids with Hydroxyl Radicals, J. Phys. Chem. A, 112, 6918–6928, doi:10.1021/jp802017q, 2008.

Taatjes, C. A., Hansen, N., McIlroy, A., Miller, J. A., Senosiain, J. P., Klippenstein, S. J., Qi, F., Sheng, L., Zhang, Y., Cool, T. A., Wang, J., Westmoreland, P. R., Law, M. E., Kasper, T., and Kohse-Höinghaus, K.: Enols Are Common Intermediates in Hydrocarbon Oxidation, Science, 308, 1887–1889, doi:10.1126/science.1112532, 2005.

Talbot, R. W., Beecher, K. M., and Harriss, R. C.: Atmospheric geochemistry of formic and acetic acids at a mid-latitude temperate site, J. Geophys. Res., 93, 1638–1652, doi:10.1029/JD093iD02p01638, 1988.

Turquety, S., Logan, J. A., Jacob, D. J., Hudman, R. C., Leung, F. Y., Heald, C. L., Yantosca, R. M., Wu, S., Emmons, L. K., Edwards, D. P., and Sachse, G. W.: Inventory of boreal fire emissions for North America in 2004: Importance of peat burning and pyroconvective injection, J. Geophys. Res. Atmos., 112, D12S03, doi:10.1029/2006JD007281, 2007.

Usher, C. R., Michel, A. E., and Grassian, V. H.: Reactions on mineral dust, Chem. Rev, 103, 4883–4940, doi:10.1021/cr020657y, 2003.

Val Martin, M., Logan, J. A., Kahn, R. A., Leung, F.-Y., Nelson, D. L., and Diner, D. J.: Smoke injection heights from fires in North America: analysis of 5 years of satellite observations, Atmos. Chem. Phys., 10, 1491–1510, doi:10.5194/acp-10-1491-2010,
2010.

Vander Auwera, J., Didriche, K., Perrin, A., and Keller, F.: Absolute line intensities for formic acid and dissociation constant of the dimer, J. Chem. Phys., 126, 124311–124320, doi:10.1063/1.2712439, 2007.

Velazco, V., Notholt, J., Warneke, T., Lawrence, M., Bremer, H., Drummond, J., Schulz, A., Krieg, J., and Schrems, O.: Latitude and altitude variability of carbon monoxide in the Atlantic detected from ship-borne Fourier transform spectrometry, model, and satellite data, J. Geophys. Res. Atmos., 110, 9306, doi:10.1029/2004JD005351, 2005.

Veyret, B., Lesclaux, R., Rayez, M. T., Rayez, J. C., Cox, R. A., and Moortgat, G. K.: Kinetics and mechanism of the photo-oxidation of formaldehyde. 1. Flash photolysis study, J. Phys. Chem., 93, 2368–2374, 1989.

Vigouroux, C., Hendrick, F., Stavrakou, T., Dils, B., De Smedt, I., Hermans, C., Merlaud, A., Scolas, F., Senten, C., Vanhaelewyn, G., Fally, S., Carleer, M., Metzger, J.-M., Müller, J.-F., Van Roozendael, M., and De Mazière, M.: Ground-based FTIR and MAX-DOAS observations of formaldehyde at Réunion Island and comparisons with satellite and model data, Atmos. Chem. Phys., 9, 9523–9544, doi:10.5194/acp-9-9523-2009, 2009.

Vlasenko, A., George, I. J., and Abbatt, J. P. D.: Formation of Volatile Organic Compounds in the Heterogeneous Oxidation of Condensed-Phase Organic Films by Gas-Phase OH, J. Phys. Chem. A, 112, 1552–1560, doi:10.1021/jp0772979, 2008.

von Kuhlmann, R., Lawrence, M., Crutzen, P., and Rasch, P.: A model for studies of tropospheric ozone and nonmethane hydrocarbons: Model evaluation of ozone-related species, J. Geophys. Res.-Atmos., 108, 4729, doi:10.1029/2002JD003348, 2003a.

von Kuhlmann, R., Lawrence, M. G., Crutzen, P. J., and Rasch, P. J.: A model for studies of tropospheric ozone and nonmethane hydrocarbons: Model description and ozone results, J. Geophys. Res. Atmos., 108, 4294, doi:10.1029/2002JD002893, 2003b.

Walser, M. L., Park, J., Gomez, A. L., Russell, A. R., and Nizkorodov, S. A.: Photochemical Aging of Secondary Organic Aerosol Particles Generated from the Oxidation of d-Limonene, J. Phys. Chem. A, 111, 1907–1913, doi:10.1021/jp066293l, 2007.

Wang, Y. and Jacob, D.: Anthropogenic forcing on tropospheric ozone and OH since preindustrial times, J. Geophys. Res., 103, 31123–31136, doi:10.1029/1998JD100004, 1998.

Wang, Y., Jacob, D. J., and Logan, J. A.: Global simulation of tropospheric O_3-NO_x-hydrocarbon chemistry 1. Model formulation, J. Geophys. Res., 103, 10713–10726, doi:10.1029/98JD00158, 1998.

Warneke, C., Bahreini, R., Brioude, J., Brock, C. A., de Gouw, J. A., Fahey, D. W., Froyd, K. D., Holloway, J. S., Middlebrook, A., Miller, L., Montzka, S., Murphy, D. M., Peischl, J., Ryerson, T. B., Schwarz, J. P., Spackman, J. R., and Veres, P.: Biomass burning in Siberia and Kazakhstan as an important source for haze over the Alaskan Arctic in April 2008, Geophys. Res. Lett., 36, 2813, doi:10.1029/2008GL036194, 2009.

Weber, R. J., Sullivan, A. P., Peltier, R. E., Russell, A., Yan, B., Zheng, M., de Gouw, J., Warneke, C., Brock, C., Holloway, J. S., Atlas, E. L., and Edgerton, E.: A study of secondary organic aerosol formation in the anthropogenic-influenced southeastern United States, J. Geophys. Res. Atmos., 112, 13302, doi:10.1029/2007JD008408, 2007.

Wennberg, P. O., Hanisco, T. F., Jaeglé;, L., Jacob, D. J., Hintsa, E. J., Lanzendorf, E. J., Anderson, J. G., Gao, R.-S., Keim, E. R., Donnelly, S. G., Negro, L. A., Fahey, D. W., McKeen, S. A., Salawitch, R. J., Webster, C. R., May, R. D., Herman, R. L., Proffitt, M. H., Margitan, J. J., Atlas, E. L., Schauffler, S. M., Flocke, F., McElroy, C. T., and Bui, T. P.: Hydrogen Radicals, Nitrogen Radicals, and the Production of O_3 in the Upper Troposphere, Science, 279, 49–53, doi:10.1126/science.279.5347.49, 1998.

Wesely, M. . L.: Parameterization of surface resistances to gaseous dry deposition in regional-scale numerical models, Atmos. Environ., 23, 1293–1304, doi:10.1016/j.atmosenv.2007.10.058, 1989.

Wiedinmyer, C., Guenther, A., Harley, P., Hewitt, N., Geron, C., Artaxo, P., Steinbrecher, R., and Rasmussen, R.: Global Organic Emissions from Vegetation (in Emissions of Atmospheric Trace Compounds), 18 of Advances in Global Change Research, Springer, 2004.

Yevich, R. and Logan, J. A.: An assessment of biofuel use and

burning of agricultural waste in the developing world., Global Biogeochem. Cy., 17, 1095, doi:10.1029/2002GB001952, 2003.

Yienger, J. J. and Levy, H.: Empirical model of global soil-biogenic NOx emissions, J. Geophys. Res., 100, 11447–11464, doi:10.1029/95JD00370, 1995.

Yokelson, R. J., Bertschi, I. T., Christian, T. J., Hobbs, P. V., Ward, D. E., and Hao, W. M.: Trace gas measurements in nascent, aged, and cloud-processed smoke from African savanna fires by airborne Fourier transform infrared spectroscopy (AFTIR), J. Geophys. Res., 108, 8478, doi:10.1029/2002JD002322, 2003.

Yokelson, R. J., Crounse, J. D., DeCarlo, P. F., Karl, T., Urbanski, S., Atlas, E., Campos, T., Shinozuka, Y., Kapustin, V., Clarke, A. D., Weinheimer, A., Knapp, D. J., Montzka, D. D., Holloway, J., Weibring, P., Flocke, F., Zheng, W., Toohey, D., Wennberg, P. O., Wiedinmyer, C., Mauldin, L., Fried, A., Richter, D., Walega, J., Jimenez, J. L., Adachi, K., Buseck, P. R., Hall, S. R., and Shetter, R.: Emissions from biomass burning in the Yucatan, Atmospheric Chemistry and Physics, 9, 5785–5812, doi:10.5194/acp-9-5785-2009, 2009.

York, D., Evensen, N. M., Martínez, M. L., and Delgado, J. D. B.: Unified equations for the slope, intercept, and standard errors of the best straight line, Am. J. Phys., 72, 367–375, doi:10.1119/1.1632486, 2004.

Zander, R., Duchatelet, P., Mahieu, E., Demoulin, P., Roland, G., Servais, C., Auwera, J. V., Perrin, A., Rinsland, C. P., and Crutzen, P. J.: Formic acid above the Jungfraujoch during 1985–2007: observed variability, seasonality, but no long-term background evolution, Atmos. Chem. Phys., 10, 10047–10065, doi:10.5194/acp-10-10047-2010, 2010.

Zender, C. S., Bian, H., and Newman, D.: Mineral Dust Entrainment and Deposition (DEAD) model: Description and 1990s dust climatology, J. Geophys. Res. Atmos., 108, 4416, doi:10.1029/2002JD002775, 2003.

Atmos. Meas. Tech., 6, 167–185, 2013
www.atmos-meas-tech.net/6/167/2013/
doi:10.5194/amt-6-167-2013
© Author(s) 2013. CC Attribution 3.0 License.

Atmospheric Measurement Techniques
Open Access

MAX-DOAS formaldehyde slant column measurements during CINDI: intercomparison and analysis improvement

G. Pinardi[1], M. Van Roozendael[1], N. Abuhassan[4], C. Adams[2], A. Cede[4], K. Clémer[1,*], C. Fayt[1], U. Frieß[5], M. Gil[6], J. Herman[4], C. Hermans[1], F. Hendrick[1], H. Irie[7,], A. Merlaud[1], M. Navarro Comas[6], E. Peters[8], A. J. M. Piters[9], O. Puentedura[6], A. Richter[8], A. Schönhardt[8], R. Shaiganfar[3], E. Spinei[10], K. Strong[2], H. Takashima[7,***], M. Vrekoussis[8,11], T. Wagner[3], F. Wittrock[8], and S. Yilmaz[5]**

[1]Department of Physics, University of Toronto, Ontario, Canada
[2]BIRA-IASB – Belgian Institute for Space Aeronomy, Brussels, Belgium
[3]Max Planck Institute for Chemistry, Mainz, Germany
[4]NASA/Goddard Space Flight Center, GSFC, Greenbelt, MD, USA
[5]Institute of Environmental Physics, University of Heidelberg, Heidelberg, Germany
[6]National Institute for Aerospace technology, INTA, Madrid, Spain
[7]Research Institute for Global Change, JAMSTEC, Yokohama, Japan
[8]Institute of Environmental Physics, University of Bremen, Bremen, Germany
[9]Royal Netherlands Meteorological Institute, KNMI, De Bilt, The Netherlands
[10]Laboratory for Atmospheric Research, Washington State University, Pullman, WA, USA
[11]Energy, Environment and Water Research Center, The Cyprus Institute, Nicosia, Cyprus
[*]now at: Instituut voor Sterrenkunde, Katholieke Universiteit Leuven, Leuven, Belgium
[**]now at: Center for Environmental Remote Sensing, Chiba University, Chiba, Japan
[***]now at: Department of Earth System Science, Faculty of Science, Fukuoka University, Fukuoka, Japan

Correspondence to: G. Pinardi (gaia.pinardi@aeronomie.be)

Received: 23 July 2012 – Published in Atmos. Meas. Tech. Discuss.: 18 September 2012
Revised: 12 December 2012 – Accepted: 3 January 2013 – Published: 31 January 2013

Abstract. We present intercomparison results for formaldehyde (HCHO) slant column measurements performed during the Cabauw Intercomparison campaign of Nitrogen Dioxide measuring Instruments (CINDI) that took place in Cabauw, the Netherlands, in summer 2009. During two months, nine atmospheric research groups simultaneously operated MAX-DOAS (MultiAXis Differential Optical Absorption Spectroscopy) instruments of various designs to record UV-visible spectra of scattered sunlight at different elevation angles that were analysed using common retrieval settings. The resulting HCHO data set was found to be highly consistent, the mean difference between instruments generally not exceeding 15 % or 7.5×10^{15} molec cm^{-2}, for all viewing elevation angles. Furthermore, a sensitivity analysis was performed to investigate the uncertainties in the HCHO slant column retrieval when varying key input parameters such as the molecular absorption cross sections, correction terms for the Ring effect or the width and position of the fitting interval. This study led to the identification of potentially important sources of errors associated with cross-correlation effects involving the Ring effect, O_4, HCHO and BrO cross sections and the DOAS closure polynomial. As a result, a set of updated recommendations was formulated for HCHO slant column retrieval in the 336.5–359 nm wavelength range. To conclude, an error budget is proposed which distinguishes between systematic and random uncertainties. The total systematic error is estimated to be of the order of 20 % and is dominated by uncertainties in absorption cross sections and related spectral cross-correlation effects. For a typical integration time of one minute, random uncertainties range between 5 and 30 %, depending on the noise level of individual instruments.

Published by Copernicus Publications on behalf of the European Geosciences Union.

1 Introduction

Formaldehyde (HCHO) is the most abundant organic carbonyl compound in the atmosphere. Being a short-lived oxidation product of a large number of volatile organic compounds (VOCs), its abundance can be closely related to VOC emissions of natural origin or from human activities. In particular, the variability of HCHO over continents is dominated by local production from non-methane volatile organic compounds (NMVOCs) (Millet et al., 2006; Stavrakou et al., 2009a,b and references therein), originating from biogenic, pyrogenic or anthropogenic sources. These emissions, through their involvement in tropospheric ozone chemistry, are important in controlling air quality. Over Europe, satellite observations reveal a marked seasonal cycle, with a summer maximum and a winter minimum (Curci et al., 2010).

Tropospheric formaldehyde has been observed from nadir UV backscatter satellite sensors (Chance et al., 2000; Palmer et al., 2003; Wittrock et al., 2006; De Smedt et al., 2008, 2010; Millet et al., 2008; Marbach et al., 2009; Vrekoussis et al., 2010; Curci et al., 2010), as well as from airborne and ground-based in situ instruments (e.g. Hak et al., 2005; Fried et al., 2011 and references therein) and ground-based remote-sensing Fourier transform infrared spectrometers (e.g. Demoulin et al., 1999; Jones et al., 2009; Vigouroux et al., 2009). In the UV, HCHO can be measured using active and passive Differential Optical Absorption Spectroscopy (DOAS) (see Platt and Stutz, 2008, for a review). Among the category of passive DOAS systems, the Multiaxis DOAS (MAX-DOAS) technique can be used for tropospheric trace gas monitoring (Van Roozendael et al., 2003; Hönninger et al., 2004; Sinreich et al., 2005). The MAX-DOAS technique has been successfully applied to NO_2, HCHO, SO_2, BrO, and CHOCHO detection (e.g. Bobrowski et al., 2003; Wittrock et al., 2004; Heckel et al., 2005; Sinreich et al., 2007; Pikelnaya et al., 2007; Theys et al., 2007; Clémer et al., 2009; Vlemmix et al., 2010, 2011a; Irie et al., 2011; Wagner et al., 2011).

MAX-DOAS instruments perform quasi-simultaneous observations of scattered sunlight in a range of viewing directions scanned from the horizon to the zenith. Measurements made at low elevation angles have a higher sensitivity to lower tropospheric layers, since in this geometry the photons travel longer paths through these layers than photons sampled at larger elevation angles. This results in an increased sensitivity to atmospheric absorbers that are located near the surface, such as HCHO. It has been shown that the MAX-DOAS technique can be used to to retrieve information on the vertical distribution of both trace gases and aerosols (Wagner et al., 2004; Frieß et al., 2006; Irie et al., 2008, 2009; Clémer et al., 2010; Li et al., 2010). These advantages, combined with the fact that measurements can be made automatically year-round, with a good/frequent temporal sampling, make the MAX-DOAS method suitable for long-term monitoring of atmospheric composition. Moreover, due to their spatial representativeness in both vertical and horizontal axes (Irie et al., 2011; Wagner et al., 2011), MAX-DOAS measurements are also particularly well suited to make the link between satellite observations, chemical transport model calculations, and in situ measurements in a validation context (Brinksma et al., 2008; Vlemmix et al., 2011b).

The first reported MAX-DOAS measurements of HCHO were performed in the Italian Po Valley, in summers 2002 and 2003 (Heckel et al., 2005; Wagner et al., 2011). Soon after, Hak et al. (2005) reported on an intercomparison exercise including the chromatographic technique, long-path (LP) DOAS, Fourier Transform InfraRed (FTIR), MAX-DOAS, and Hantzsch-type in situ instruments, showing good consistency between the different techniques. In 2006, Wittrock et al. published a study on global HCHO mapping from the SCIAMACHY (SCanning Imaging Absorption spectroMeter for Atmospheric CHartographY) nadir satellite instrument including comparisons with two MAX-DOAS systems (in Kenya and the Netherlands), and found good agreement within the estimated uncertainties. Pikelnaya et al. (2007) and Inomata et al. (2008) also compared MAX-DOAS HCHO with LP-DOAS and PTR-MS data, respectively, and Vigouroux et al. (2009) compared SCIAMACHY, MAX-DOAS and FTIR HCHO total columns in a tropical remote region. Recently, Fried et al. (2011) presented a comparison of ground-based MAX-DOAS and aircraft HCHO measurements during the INTEX-B (INtercontinental chemical Transport EXperiment) campaign and showed good agreement between both data sets.

Although the aforementioned studies have largely demonstrated the capabilities of MAX-DOAS systems for HCHO detection, no effort has been devoted so far to intercompare and harmonize instruments and retrieval methods. Such activities are an essential prerequisite for the reliable retrieval of vertical columns and profiles from MAX-DOAS HCHO measurements. The Cabauw Intercomparison campaign of Nitrogen Dioxide measuring Instruments (CINDI) in the Netherlands in June–July 2009 (Roscoe et al., 2010; Piters et al., 2012), where a number of MAX-DOAS instruments were jointly operated, presented the opportunity to assess for the first time the consistency of these HCHO measuring systems. The Cabauw site is located in a semi-rural area of the Netherlands where formaldehyde concentrations are expected to be between one and several tens of ppbv, which are typical background levels in the continental boundary layer and urban regions, respectively (Hak et al., 2005; Fried et al., 2011). In their study on multi-component MAX-DOAS retrievals during CINDI, Irie et al. (2011) reported median HCHO vertical mixing ratios (VMRs) of around 2.5 ppbv, and peak values of up to 8 ppbv. The CINDI data set is therefore ideally suited for an HCHO intercomparison exercise.

This paper is structured as follows. Section 2 gives an overview of the CINDI campaign, the data recorded, the instruments, and the settings used by the different groups. Results from the HCHO slant column intercomparison are then presented in Sect. 3. In Sect. 4, we focus on sensitivity tests

performed to assess the stability of the HCHO retrievals. Results are used to derive an error budget for slant column retrievals. Conclusions and perspectives are given in Sect. 5.

2 Data analysis

2.1 The CINDI intercomparison campaign

The CINDI campaign took place at the Cabauw Experimental Site for Atmospheric Research (CESAR site; Russchenberg et al., 2005), a semi-rural area in the Netherlands. Although the campaign mainly focused on tropospheric NO_2, aerosols were also monitored with in situ systems, sun photometers and a lidar (Piters et al., 2012; Zieger et al., 2011; Irie et al., 2011). To complement the atmospheric composition measurements, the site offered a large ensemble of meteorological observations. A detailed description of the CINDI campaign and an overview of first results can be found in Piters et al. (2012).

Instruments were installed and tested between 8 and 14 June 2009 and a formal semi-blind intercomparison of NO_2 and O_4 Differential Slant Column Densities (DSCDs) took place from 15 to 30 June 2009 (Roscoe et al., 2010). After that date, additional measurements were performed by several groups until 24 July, focusing on other species, such as HCHO, BrO, and CHOCHO. The goal of the formal semi-blind NO_2 and O_4 intercomparison was to characterize the current level of consistency of multi-axis instruments, as previously done for the zenith-sky instruments of the Network for the detection of atmospheric composition change (NDACC; e.g. Roscoe et al., 1999; Vandaele et al., 2005). During CINDI, 22 NO_2 measuring systems were intercompared, and most of them were shown to meet the criteria for endorsement by NDACC (Roscoe et al., 2010).

2.2 Instruments

The present work focuses on HCHO measurements from MAX-DOAS instruments. Nine groups participated in this exercise, as reported in Table 1. In addition, NIWA (National institute for Water and Atmospheric Research, New Zealand) and KNMI (Koninklijk Nederlands Meteorologisch Instituut, the Netherlands) performed a few HCHO measurements during the campaign. However, these data were too sparse to include in the intercomparison.

A comprehensive description of the CINDI MAX-DOAS instruments can be found in Piters et al. (2012) and Roscoe et al. (2010), and additional references relevant for the present study are given in Table 1. All systems that operated during CINDI recorded spectra at a set of prescribed elevation angles (2, 4, 8, 15, 30° and the zenith), and at a fixed azimuth angle of 287° relative to north. A full cycle of MAX-DOAS measurements was generally obtained within half an hour. For the intercomparison of HCHO, only measurements recorded at a solar zenith angle (SZA) less than 75° were used in order to exclude error-prone twilight measurements that are not relevant for the present study.

As can be seen in Table 1, the characteristics of the various instruments were quite diverse, ranging from commercial mini-DOAS systems to state-of-the-art scientific grade instruments equipped with thermoelectrically cooled CCD array detectors of large dimension. Accordingly, the stability and noise levels were expected to differ considerably from one system to another, with a direct impact on corresponding HCHO measurements. Another important point is that some instruments were set up to record spectra in both UV and visible ranges simultaneously, while others had to alternate between these two wavelength regions. As a result, some systems (e.g. INTA and Toronto) could only measure HCHO after 30 June, at the end of the formal period of the NO_2 intercomparison exercise described in Roscoe et al. (2010). Others' instruments (WSU, NASA) switched their wavelength range repeatedly over time, alternating the two types of measurements throughout the campaign. It should be noted that the MAX-DOAS instrument of the Toronto group was tested in multi-axis mode for the first time during this campaign, and only a few days of data were available.

2.3 HCHO analysis settings

Formaldehyde presents structured absorption bands in the UV spectral region, between 240 and 360 nm. Because of the increased ozone absorption below 320 nm, only the bands above 320 nm are generally used for the spectral retrieval of HCHO. In this region, the HCHO DSCDs are retrieved from measured spectra by applying the DOAS technique (Platt and Stutz, 2008, and references therein). The wavelength interval for fitting is generally optimized so as to (1) maximize the sensitivity to HCHO, (2) minimize the fitting residuals and the scatter of the retrieved HCHO slant columns, and (3) minimize the interferences with other absorbers. Figure 1 displays the absorption cross sections of the trace gases that need to be considered in the 320–370 nm wavelength region. Based on experience and heritage from past studies on ground-based (e.g. Heckel et al., 2005; Vigouroux et al., 2009) and satellite instruments (Wittrock et al., 2006; De Smedt et al., 2008, 2009), standardized analysis settings were defined and prescribed for use in the present intercomparison exercise. These baseline settings are summarized in Table 2. Note that all absorption cross sections were convolved to the resolution of the individual instruments using slit function information provided by each group. In the case of the O_3 and NO_2 cross sections, a solar I_0 correction was applied (Aliwell et al., 2002).

For the retrievals, daily reference spectra were taken from the zenith observations around 11:40 UT. Figure 2 presents an example of HCHO fitting results obtained with the BIRA-IASB (Belgian Institute for Space Aeronomy)instrument on 30 June 2009, at 4° elevation angle and 43° SZA. The corresponding residuals (approximately 10^{-4} RMS) are typical

Table 1. Primary characteristics of the spectrometers taking part in the HCHO intercomparison campaign.

Institute	Measurement period for HCHO	FWHM (nm)	Sampling ratio (pixel/ FWHM)	Detector characteristics	Integration time	Reference
BIRA	13 Jun–22 Jul	0.4	9	back-illuminated CCD, 2048×512 pixels ($-30\,^{\circ}$C)	60 s	Clémer et al. (2010)
INTA, Instituto Nacional de Tecnica Aeroespacial	7 Jul–24 Jul	0.4	3.6	UV enhanced CCD, 1024×256 pixels ($-40\,^{\circ}$C)	90 s	Roscoe et al. (2010)
Bremen	8 Jun–21 Jul	0.4	11.8	back-illuminated CCD, 2048×256 pixels ($-35\,^{\circ}$C)	40 s	Wittrock et al. (2004)
Heidelberg	17 Jun–24 Jul	0.5	6.5	back-illuminated CCD, 2048×256 pixels ($-30\,^{\circ}$C)	60 s	Frieß et al. (2011)
JAMSTEC, Japan Agency for Marine-Earth Science and Technology	8 Jun–24 Jul	0.7	8 3648 pixels	uncooled CCD,	5 min (2011)	Irie et al.
NASA	22 Jun–20 Jul	0.6	5	uncooled CCD, 2048×14 pixels	16 s	Herman et al. (2009)
WSU, Washington State University	21 Jun–5 Jul	0.83	8	back-illuminated CCD, 2048×512 pixels ($-70\,^{\circ}$C)	Typical 1.2 s	Herman et al. (2009)
Toronto	30 Jun–4 Jul	0.2–0.8	7–12	back-illuminated CCD, 2048×512 pixels ($-72\,^{\circ}$C)	~ 2 min	Fraser et al. (2009)
Mainz	21 Jun–10 Jul	0.6	8	stabilised CCD, 2048 pixels ($4\,^{\circ}$C)	60 s	Shaiganfar et al. (2011)

Table 2. Baseline DOAS analysis settings used for HCHO slant column retrieval during the intercomparison exercise.

Parameter	Specification
Fitting interval	336.5–359 nm
Wavelength calibration	Calibration based on reference solar atlas (Chance and Kurucz, 2010)
Cross sections	
HCHO	Meller and Moortgat (2000), 293 °K
O_3	Bogumil et al. (2003), 223 and 243 °K, I_0-corrected
NO_2	Vandaele et al. (1996), 298 °K, I_0-corrected
BrO	Fleischmann et al. (2004), 223 °K
O_4	Hermans et al. (2003) (http://spectrolab.aeronomie.be/o2.htm)
Ring effect	Chance and Spurr (1997)
Closure term	Polynomial of order 3 (corresponding to 4 coefficients)
Intensity offset	Linear correction
Wavelength adjustment	All spectra shifted and stretched against reference spectrum

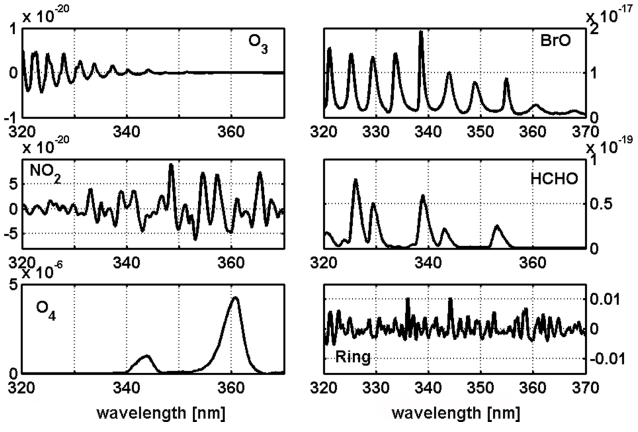

Fig. 1. Absorption cross sections of the main trace gases absorbing in the 320–370 nm spectral range and of the Ring effect. All absorption cross sections are expressed in cm^2 $molec^{-1}$, except O_4 ($\times 10^{-40}$ cm^5 $molec^{-2}$) and have been smoothed to match the resolution of the BIRA-IASB instrument (0.38 nm FWHM).

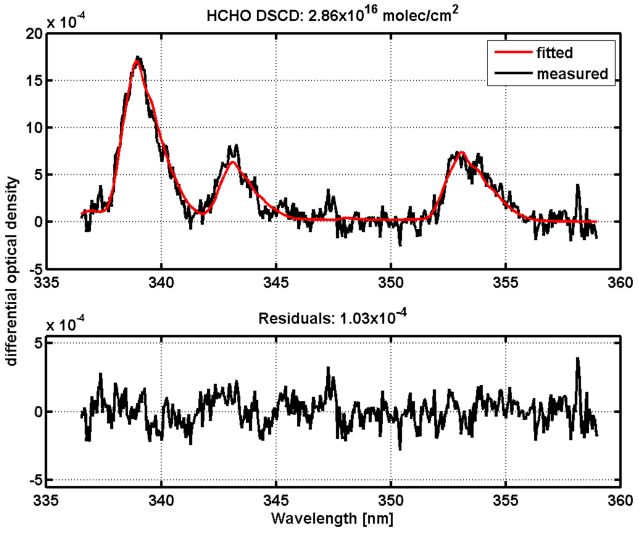

Fig. 2. Example of a HCHO slant column fit obtained with the BIRA-IASB instrument on 30 June 2009, around 14:30 UT, at 4° elevation angle and 43° solar zenith angle. The first panel shows the measured (black) and the fitted (red) values, and the second panel shows the residual of the DOAS fit.

of low-noise scientific grade instruments. Under similar conditions, residuals can be an order of magnitude larger when using compact mini-DOAS systems.

2.4 Results

Figure 3a shows an example of HCHO measurements obtained during CINDI. HCHO DSCDs measured by the BIRA-IASB MAX-DOAS instrument at 30° elevation were converted into equivalent vertical columns (VCDs) using a simple geometrical approximation (Hönninger et al., 2004; Ma et al., 2012). The time series of HCHO VCDs covers approximately one month during summer. Comparing the retrieved columns with measurements of the ambient temperature (Fig. 3a), one can see that the HCHO variations are strongly correlated with corresponding changes in the temperature. This feature was reported by Irie et al. (2011) and is consistent with a background HCHO source, mainly due to the oxidation of biogenic NMVOCs. In contrast, the HCHO peak values as observed on several days in July are probably related to anthropogenic emission sources. In Fig. 3b, the complete VCD data set was binned and plotted as a function of the local time. As can be seen from the standard deviations, the natural variability of HCHO is large, but the diurnal variation consistently peaks in the afternoon, which is likely related to the progressive oxidation of the NMVOCs emitted during the day.

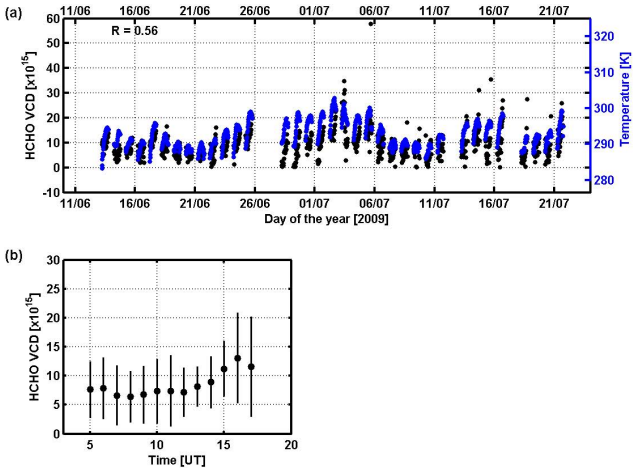

Fig. 3. HCHO vertical columns (molec cm^{-2}) retrieved from BIRA-IASB MAX-DOAS measurements at 30° elevation using a geometrical approximation. **(a)** Time series of observations performed during June and July 2009. Ambient temperature measurements are superimposed in blue. **(b)** Corresponding mean diurnal variation of the HCHO vertical column. Error bars denote the one sigma standard deviations around the mean values.

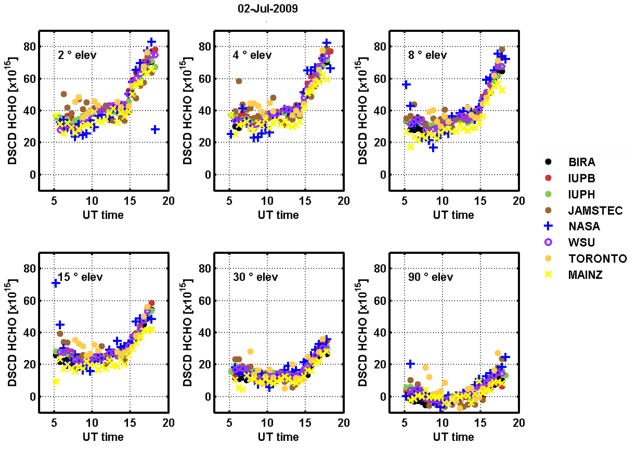

Fig. 4. Diurnal evolution of the HCHO DSCD measured on 2 July 2009 and averaged in 30-min bins, for the different instruments involved in the intercomparison. Units are molec cm^{-2}.

3 Slant column intercomparison results

We follow the method introduced in Roscoe et al. (2010) for the NO_2 and O_4 slant column measurement intercomparison. HCHO DSCDs retrieved by each group using the baseline analysis settings defined in Table 2, are averaged over periods of 30 min. This procedure minimizes the impact of the temporal and spatial variability of HCHO and of the differences in read-out noise between instruments. An example of the diurnal evolution of the resampled HCHO DSCDs is shown in Fig. 4 for different elevation angles and for SZA $< 75°$, on 2 July 2009. This day was chosen because

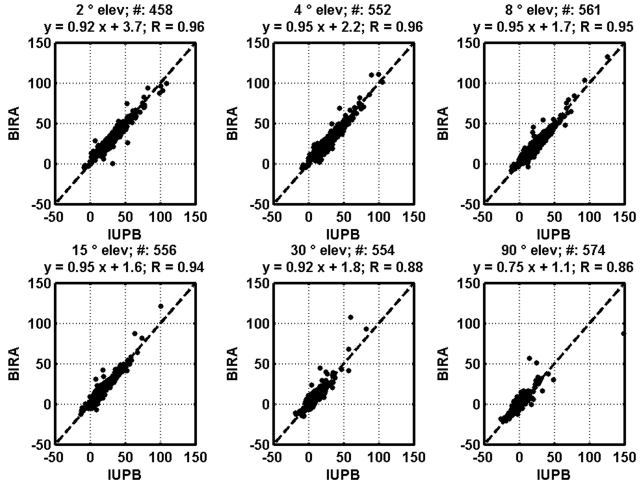

Fig. 5. Scatter plots of the HCHO DSCD (10^{15} molec cm^{-2}) measured by BIRA against those measured by IUP Bremen. Data from the whole campaign were averaged in 30-min bins. Statistical parameters derived from each regression plot (number of points #, linear regression equation and correlation coefficients R) are given for each elevation above the corresponding subplots. The dashed line is the $y = x$ line.

almost all instruments were in operation and the HCHO concentrations had a smooth variation over time. As can be seen, the HCHO DSCDs are consistently larger at low elevation due to the enhanced light path in the near-surface HCHO layer; good agreement is observed between various data sets.

To proceed further, the measurements from each group were first compared to the Bremen data set, which has the most complete time series, very frequent measurements and smooth behaviour. In the second step, a reference data set was created by grouping the instruments that presented the best mutual agreement. To illustrate this procedure, Fig. 5 displays the BIRA HCHO DCSDs plotted against those of Bremen, for different elevation angles. Relevant statistical parameters (correlation coefficient, slope and intercept of the linear regression fit) are indicated. As can be seen, the scatter plots are compact, and the slopes and correlation coefficients are close to unity, confirming the good agreement between the Bremen and BIRA instruments. Statistical parameters at 30 and 90° elevation are slightly smaller, due to the smaller dynamical range of the DSCDs at those elevations (see Fig. 4). Similar agreement was found with INTA, and therefore a reference data set was created by averaging data from the Bremen, BIRA and INTA instruments. The scatter plots displayed in Fig. 6 illustrate, for the 4° elevation case, the results of the final comparison where data from each individual instrument are compared to the merged reference. Although the number of coincident points can differ greatly depending on instruments, the data of most of the groups agree quite well with the reference. Figure 7 presents the final results of the statistical analysis, constructed using the

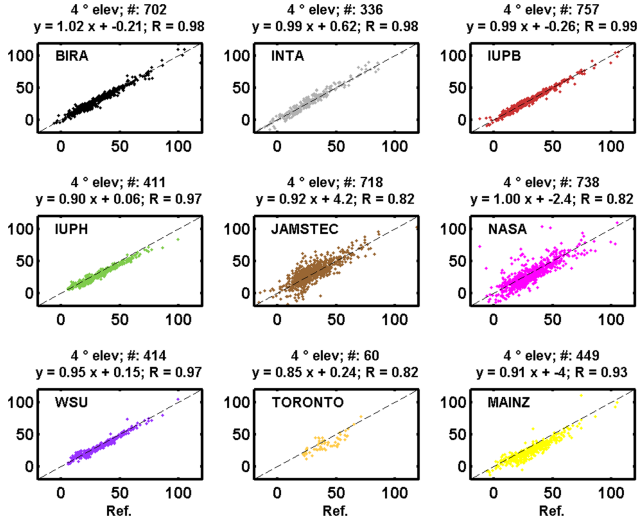

Fig. 6. Scatter plots of HCHO DSCDs (10^{15} molec cm^{-2}) measured by each instrument compared to the campaign reference data set (see text), for the case of measurements at the 4° elevation angle. Statistical parameters derived from the regressions (number of points #, linear regression equation and correlation coefficients R) are given on top of each subplot. The dashed line is the $y = x$ line.

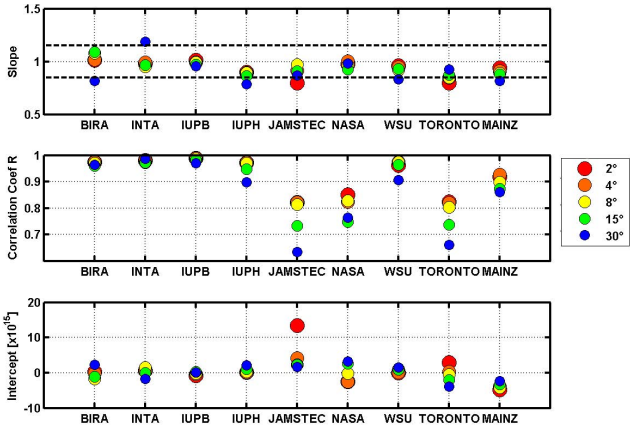

Fig. 7. Straight-line slopes, correlation coefficients and intercepts of HCHO slant columns against those of the reference, for each instrument and all off-axis elevation angles. The dotted lines in the first panel correspond to values of 1.15 and 0.85.

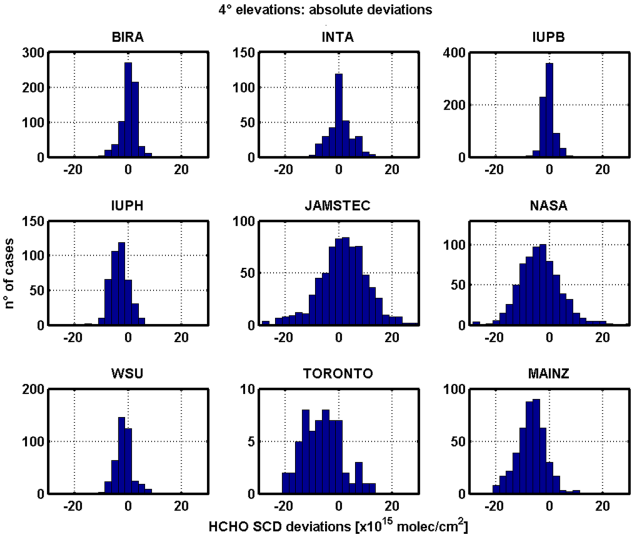

Fig. 8. Histograms of the HCHO DSCD absolute deviations (10^{15} molec cm^{-2}) of each instrument's data compared to the reference set, for the case of measurements at the 4° elevation angle, and for the whole campaign.

whole ensemble of off-axis measurements (2, 4, 8, 15 and 30°). Most instruments compare relatively well with the reference for most of the elevation angles: correlation coefficients are close to unity (illustrating the compactness of the scatter plot with respect to the reference), slopes deviate by no more than 15 % from the reference, and intercepts are close to zero. Note that larger relative differences against the reference are systematically obtained at 30° elevations due to the lower HCHO DSCDs at this elevation angle (see Fig. 4). Also, smaller values for the correlation coefficients and larger intercept values and corresponding uncertainties are found for the JAMSTEC, NASA and Toronto data sets, which might possibly be connected to the larger noise of the corresponding instruments with respect to others (see Fig. 6). A test with an orthogonal regression (instead of linear) shows similar results.

For each instrument, the histograms of the absolute HCHO DSCDs deviations are presented in Fig. 8. Only the results at 4° elevation are shown, but similar conclusions can be drawn at other elevations. All instruments, except the Toronto one, have a symmetric and quasi-Gaussian shape for the 4° elevation, but large differences in the Gaussian FWHM (full width at half maximum). Largest FWHM values are found for JAMSTEC, NASA and Mainz, consistent with the noise level of those instruments. Some of the groups (IUPH, JAMSTEC, NASA, Toronto and Mainz) also display a small but significant bias compared to the reference. It should be mentioned again that the first three instruments (BIRA, INTA and Bremen) were used to construct the reference data set and thus a better agreement with the reference is expected due to this choice. For the Mainz instrument, the negative bias might be related to the position of the instrument, at an altitude of 20 m on the Cabauw tower, where measurements probably loose sensitivity to HCHO present at the surface. In case of the Toronto instrument, the statistical results should be interpreted with care since there were only five days of measurements.

The HCHO intercomparison exercise presented here should be connected to the NO_2 and O_4 comparisons performed by Roscoe et al. (2010). They reported fitted slopes for the visible MAX-DOAS instruments within 10% of unity at almost all non-zenith elevations, with most instruments

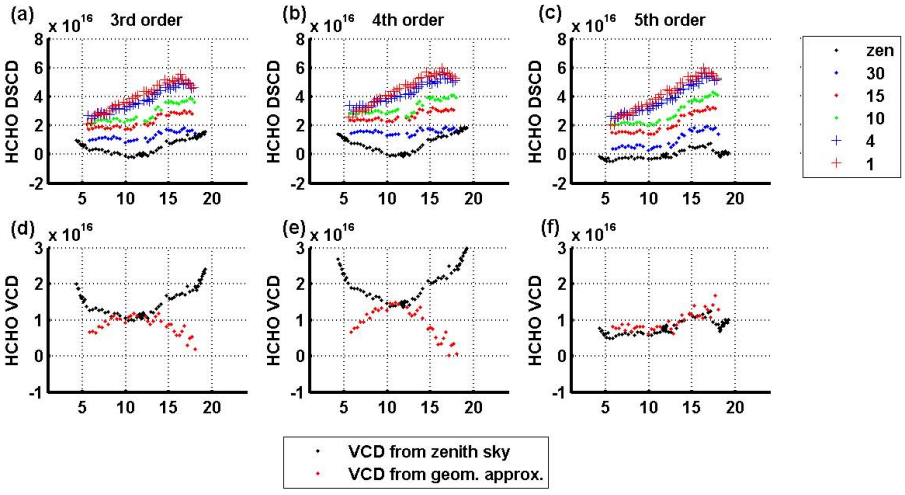

Fig. 9. Effect of the choice of the polynomial order used in the DOAS fit. **(a)–(c)**: Impact on the HCHO DSCDs (molec cm^{-2}) for the different elevation angles; **(d)–(f)** impact on the corresponding HCHO VCDs (molec cm^{-2}) obtained using two different methods described in the text.

within 5 %; similarly, values of 12 and 7 %, were found for the UV sensors. The 15 % deviation from unity slope derived in our study for the HCHO columns in the UV are thus a good result, considering that retrieving HCHO DSCDs is more challenging than retrieving NO_2, because of the smaller optical thickness of HCHO.

4 Sensitivity study

The intercomparison study presented in Sect. 3 has been conducted using standardized retrieval settings consistently applied by each participating group. This harmonization procedure allowed us to concentrate on instrument-specific differences, and to draw conclusions on the overall level of consistency between HCHO measuring systems operated during CINDI. We now concentrate on evaluating the sensitivity of HCHO results to possible changes in the retrieval settings using representative spectra from the BIRA instrument recorded on a clear day (4 July 2009). As will be illustrated hereafter, these sensitivity tests highlight possible optimizations in the HCHO slant column retrieval parameters and lead to the recommendation of new analysis settings. Sensitivity test results are shown both on DSCDs and on dDSCDs, i.e. the difference of the off-axis DSCDs with the zenith DSCDs of the scan (the closest in time), since this is the information used in the profile inversions.

4.1 Degree of closure polynomial and Ring effect

When performing a DOAS retrieval, an important free parameter is the degree of the polynomial function that is used to account for the smooth part of the attenuation spectrum. To avoid oscillations that may correlate with trace gas absorption features, the degree of this polynomial is generally restricted to values less than 5. For the baseline retrievals, a 3rd order polynomial was selected. However, during our sensitivity tests, we noticed that any changes to these polynomial settings had a strong impact on the diurnal behaviour of the HCHO DSCD, especially for high elevation angles, including zenith, as can be seen in Fig. 9a–c. This raised the following two questions: (1) Why such a dependence on the polynomial order, and (2) which one of the tested settings is the most satisfactory? In order to answer the second question, we decided to investigate the consistency of VCDs estimates as follows. In a first approximation, the HCHO VCD can be derived from measured DSCDs in two different simple ways: first, from the difference between 30° elevation off-axis and zenith observations using the so-called geometrical approximation (Hönninger et al., 2004; Ma et al., 2012), and second, from direct conversion of the zenith-sky observations using appropriate AMFs. For one given observation, the AMF represents the geometrical enhancement factor that results from the geometry of the (MAX)DOAS observation and from the scattering properties of the atmosphere. AMFs are calculated using radiative transfer models accounting for multiple scattering and earth sphericity. They allow for conversion of the measured slant columns into equivalent vertical columns. For the present analysis, and considering that our test data were recorded under clear-sky aerosol-free conditions, zenith-sky HCHO AMFs were calculated using the UVspec/DISORT (DIScrete Ordinate Radiative Transfer) model (Mayer and Kylling, 2005; Hendrick et al., 2006) at the wavelength of 346 nm and for a typical HCHO profile peaking in the boundary layer. The HCHO content in the noon reference spectrum was derived using the geometrical approximation, so that both VCD evaluations (geometrical approximation and zenith-sky conversion) were constrained to agree at the time of the noon reference spectrum. The resulting time series of

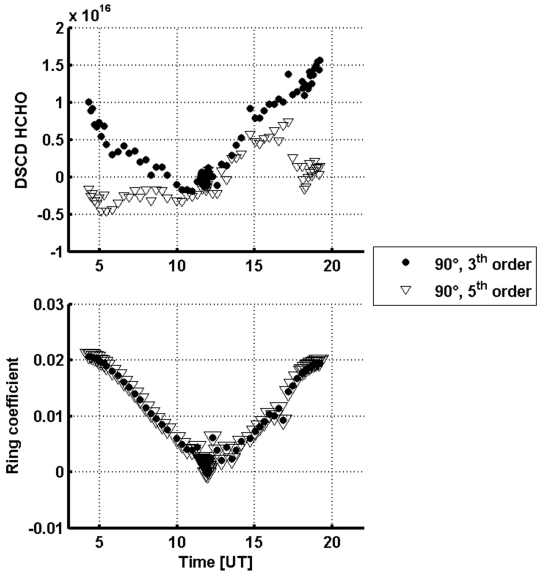

Fig. 10. Daily variation of the zenith HCHO DSCD columns (molec cm^{-2}) and of the Ring coefficients for retrievals with a 3rd and 5th order polynomial. A strong correlation is observed for HCHO and Ring when a 3rd order polynomial is used in the DOAS retrieval.

retrieved HCHO VCDs are displayed in Fig. 9d–f for the same three polynomial settings. As can be seen, only the third case, i.e. the DOAS evaluation using a 5th order polynomial, leads to consistent retrievals of HCHO VCDs using both geometrical approximation and zenith-sky conversion.

Although these results strengthen our confidence in the corresponding HCHO DSCDs, the question remains: What is causing the observed dependence on the polynomial order? The curvature of the zenith-sky daily variation observed when using polynomials of order 3 and 4 (black dots in the first two upper plots of Fig. 9) is striking, and suggests an interference problem involving another absorber. As can be seen in Fig. 10, the Ring effect clearly displays a similar curved pattern. Additional tests showed that none of the other parameters involved in the HCHO retrieval produces a similar shape.

The Ring effect (Grainger and Ring, 1962) is a well-known phenomenon responsible for filling-in of the solar and telluric lines in scattered sunlight spectra (e.g. Grainger and Ring, 1962; Wagner et al., 2009 and references therein). This effect is large in comparison to the faint absorption features of HCHO, and it can, therefore, produce interferences if not well corrected in the DOAS evaluation. To investigate further, the sensitivity of our HCHO DSCDs to uncertainties in the Ring effect, additional test analyses were performed using different sources for the Ring cross sections:

– Baseline case: cross section calculated according to Chance and Spurr (1997)

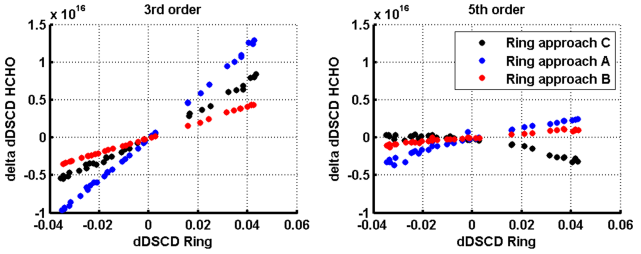

Fig. 11. Sensitivity of HCHO dDSCD (molec cm^{-2}) to changes in the Ring cross section used in the DOAS fitting procedure, expressed as the difference to the baseline scenario, for data recorded on 4 July 2009. The two panels present the results for different orders of the polynomial used in the DOAS fit.

– Case A: normalised cross section generated according to Wagner et al. (2009)

– Case B: cross section derived from SCIATRAN radiative transfer calculations in a Rayleigh atmosphere (A. Richter, personal communication, 2005)

– Case C: two cross sections generated from principal component analysis of a range of SCIATRAN calculations in an ozone containing atmosphere, according to Vountas et al. (1998).

Figure 11 shows the relation between changes in HCHO DSCDs and corresponding changes in the Ring fit coefficients when using different Ring cross sections. One can see that HCHO dDSCD changes compared to the baseline (delta dDSCDs = dDSCD(new setting) – dDSCD(baseline)) are linearly related to changes in the Ring fit coefficients. Comparing the retrieval cases using, respectively, a 3rd and a 5th order polynomial, it is also clear that the interference between HCHO and the Ring effect is much stronger when a 3rd order polynomial is used (Fig. 11a). This suggests that, for our analysis conditions, the use of a 3rd order polynomial introduces a misfit that activates the correlation between Ring and HCHO differential absorption features. In order to further test the stability of our retrievals, with respect to this issue, a number of combinations of polynomials and Ring effect cross sections were investigated and are summarized in Fig. 12. For each case, the root mean square of the differences between HCHO VCDs retrieved using our two alternative VCD calculation methods are displayed. Overall, one can see that the sensitivity to the choice of the Ring effect cross section is smallest when using a polynomial of order 5, for which more consistent results are obtained when changing the Ring data sets.

4.2 O_4 absorption cross section

Another important interfering species in the HCHO fitting interval is the collisional dimer of molecular oxygen (O_4). Its absorption cross sections are still poorly characterised

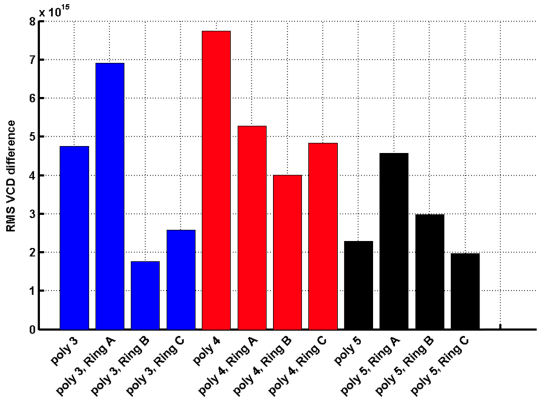

Fig. 12. Root mean square of HCHO VCD differences (molec cm^{-2}) obtained using two alternative methods for the calculation of vertical columns (see text and Fig. 9). Various choices of retrieval settings are tested using polynomials of degree 3 (blue), 4 (red) and 5 (black), respectively, and different Ring effect cross sections. Optimal stability (corresponding to smallest HCHO VCD differences and larger coherence between the results with different Ring choices) is obtained for cases using a polynomial of degree 5.

due to the difficulty of measuring them in laboratory under pressures and temperatures representative of atmospheric conditions. The Greenblatt et al. (1990) cross sections are known to suffer from wavelength registration errors and have been measured under unsuitable high pressure conditions, not present in the ambient atmosphere. Alternatively, the Hermans et al. (2003) data set provides cross sections of overall better quality, however significant uncertainties still remain, particularly in the UV region below 360 nm. We tested both data sets, and came to the conclusion that significant interferences take place between O_4, HCHO and BrO absorption features in the 336.5–359 nm interval. Figure 13 shows the HCHO and BrO DSCDs, as retrieved from MAX-DOAS measurements using the Hermans et al. (2003) and the Greenblatt et al. (1990) O_4 cross sections. As can be seen, the Hermans data set (our initial baseline for the intercomparison exercise) leads to larger HCHO columns but also to a larger spread in the BrO DSCDs retrieved at different viewing elevations, a feature that is not expected for a stratospheric absorber like BrO. In contrast, the BrO DSCDs derived using the Greenblatt O_4 cross section appear to be more consistent. Similarly to the case of the polynomial discussed before, this suggests that a misfit to the O_4 absorption (larger in this case using the Hermans et al, 2003, data set) activates a correlation between HCHO and BrO DSCDs. We will revisit the origin of these correlations in the next section. The linear relationship between HCHO, BrO and O_4 DSCDs changes when switching from the Hermans et al. (2003) to the Greenblatt et al. cross sections, as is clearly apparent from Fig. 14. Based on these considerations, we conclude that the Greenblatt et al. (1990) O_4 cross section, so far, remains the better choice for HCHO retrieval in the 336.5–359 nm region.

4.3 DOAS fitting interval

As already mentioned, the baseline HCHO fitting interval selected for the present study extends from 336.5 to 359 nm. This wavelength region, which includes three strong absorption bands of HCHO, has generally been recommended for HCHO DSCD retrievals. However, the absorption structures of HCHO and BrO are to some extent correlated in this wavelength interval, which has been identified as an issue for satellite BrO retrievals (Theys et al., 2011). Figure 15b graphically displays the correlation matrix of the different absorption cross sections used in the HCHO fit. As can be seen, HCHO and BrO present the largest coefficient of correlation (around 0.55), which can be easily explained by the similarities of their differential absorption cross sections (see Fig. 15a). In comparison, other species are less correlated. However, the coefficient of correlations between HCHO and O_3 and for other combinations involving O_3, O_4, BrO, NO_2 and Ring are not negligible. Such correlations may be expected to be dependent on the wavelength interval considered for the analysis. Therefore, in an attempt to identify the settings that would minimize the correlation matrix, calculations were performed for a range of fitting intervals starting between 332 and 338 nm and ending between 352 and 360 nm, in steps of 0.25 nm, in a similar way than what was done in Vogel et al. (2012). For each case, the root mean square of the non-diagonal elements of the correlation matrix was reported in Fig. 15c. Smaller correlations are clearly found for fitting intervals starting at short wavelengths. From visual inspection of Fig. 15c, one can conclude that the 333–358 nm wavelength range presents a local minimum of correlation, likely because of the addition of a BrO band at 334 nm in a region free of HCHO absorption. Note that this wavelength interval is similar to the one selected in Theys et al. (2011) for their satellite retrievals of BrO.

To further explore the potential of this extended fitting interval on our HCHO MAX-DOAS retrievals, additional sensitivity tests were performed. Results again show large instabilities with respect to the Ring effect interference. This is illustrated in Fig. 16a–c, where the HCHO DSCD retrieved in the 333–358 nm interval with a 5th order polynomial and O_4 Greenblatt et al. (1990) data set, is displayed for different elevation angles and for different choices of the Ring cross sections. As can be seen, the diurnal behaviour of the retrieved HCHO DSCDs has a large dependence on the source of the Ring cross section used in the DOAS fit, and the corresponding HCHO VCDs calculated using the two methods introduced in section Sect. 4.1 are generally inconsistent. These results suggest that the extended fitting interval that minimizes the BrO–HCHO interference is also more sensitive to Ring effect misfits. Therefore, any attempt to use this interval should be made with great care.

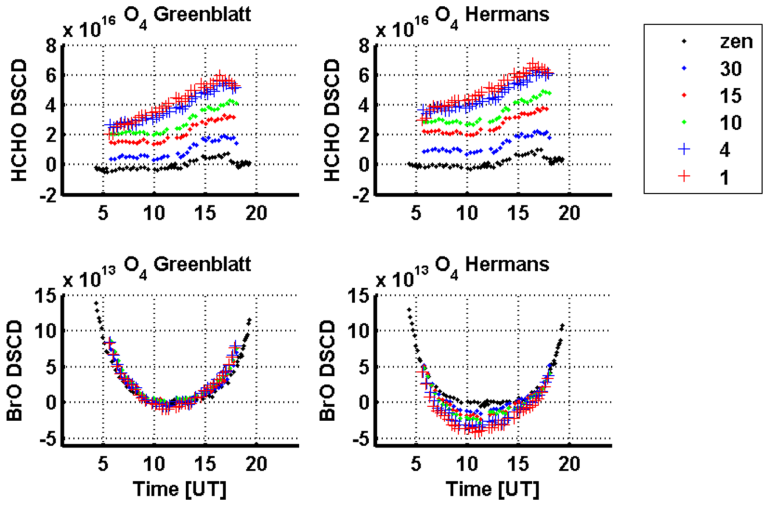

Fig. 13. Effect of the choice of the O_4 cross section used in the DOAS fit, on HCHO and BrO DSCD columns (molec cm^{-2}). Results **(a)** and **(c)** are obtained with the Greenblatt et al. (1990) cross sections while **(b)** and **(d)** are obtained using the Hermans et al. (2003) cross sections.

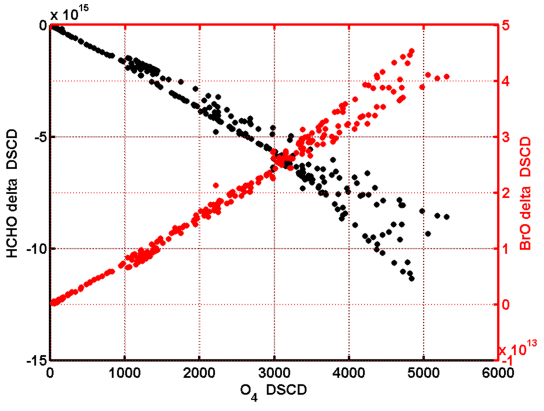

Fig. 14. Change in retrieved HCHO (black) and BrO DSCDs (red) (delta dDSCDs = dDSCD (new setting) – dDSCD (baseline); in molec cm^{-2}) when exchanging the Hermans et al. (2003) O_4 absorption cross section for the Greenblatt et al. (1990) data set, expressed as a function of the O_4 DSCD values (in 10^{40} $molec^2$ cm^{-5}).

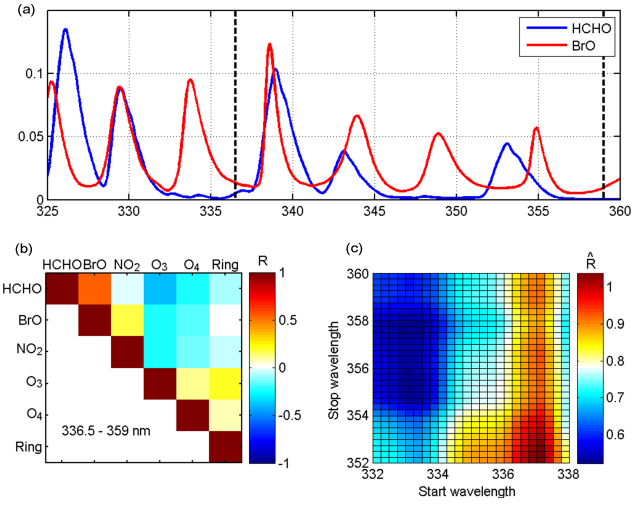

Fig. 15. (a) HCHO and BrO absorption cross sections in the 325–360 nm wavelength range convolved at the resolution of the BIRA instrument (0.38 nm FWHM) and normalized in arbitrary units. **(b)** Correlation matrix of the absorption cross sections used for HCHO DOAS retrievals in the 336.5–359 nm interval. **(c)** Overall correlation (expressed as the root mean square of the non-diagonal elements of the correlation matrix) for different wavelength intervals in the 332–360 nm wavelength range.

4.4 Recommended analysis settings

The sensitivity studies, performed on BIRA data of 4 July 2009, revealed several possible optimisations of the HCHO DOAS retrieval, in order to minimise interferences and misfits related to polynomial order, Ring effect and O_4 and BrO absorption cross sections. Compared to the settings used during the intercomparison exercise and presented in Table 2, the use of a 5th degree polynomial and the wavelength corrected O_4 Greenblatt et al. (1990) cross section is recommended. Applied in the 336.5–359 nm wavelength interval, these changes reduce instabilities related to the Ring effect and lead to more consistent BrO DSCDs. Sensitivity tests involving other parameters revealed a comparatively small impact on the HCHO evaluations. This is further discussed in the next section, where the systematic and random uncertainties on HCHO DSCD retrievals are reviewed in more detail.

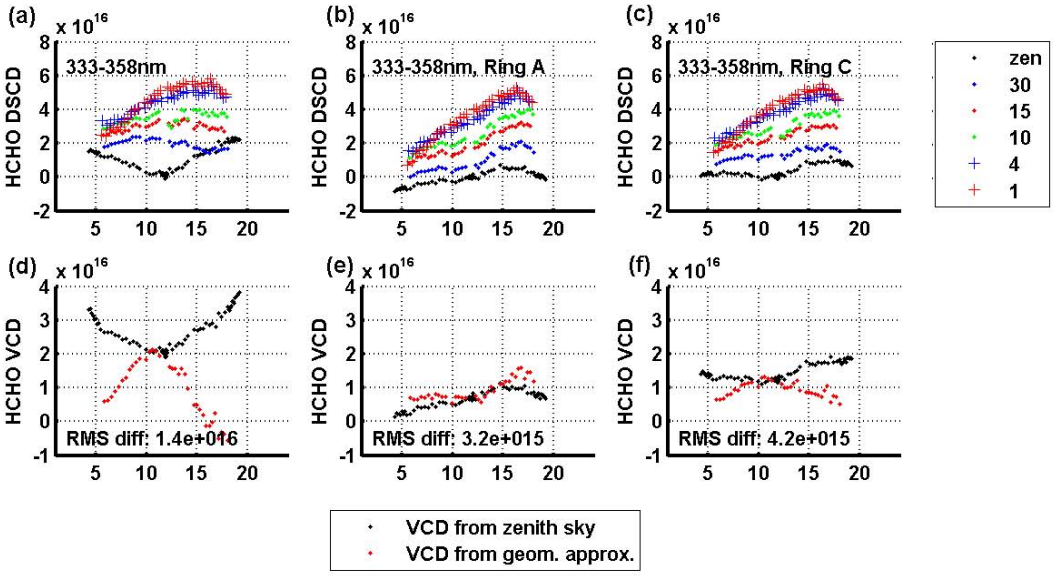

Fig. 16. Same as Fig. 9, but for an analysis in the 333–358 nm wavelength region, with a 5th order polynomial and the O_4 Greenblatt et al. (1990) data set, and for different choices of the Ring cross sections. Both DSCDs and VCDs are expressed in molec cm^{-2}.

5 Error budget

The total uncertainties on the HCHO DSCDs retrieval can be divided into two categories: (1) the random errors mostly caused by measurement noise, and (2) errors affecting the slant columns in a systematic way.

5.1 Random uncertainties

Random errors in DOAS observations are primarily related to the measurement noise which, for silicon array detectors, is generally limited by the photon shot noise. Assuming that the errors of the individual detector pixels are uncorrelated and that the DOAS fit residuals are dominated by instrumental noise, the random contribution to the DSCD error can be derived from the DOAS least-squares fit error propagation (e.g. Stutz and Platt, 1996). Random errors are then adequately represented by the slant column fit errors. Any deviation with respect to these assumptions generally results in an overestimation of the random error, so one can consider to a first approximation that the DOAS DSCD error constitutes an upper limit of the true random error. For the instruments involved in this exercise, slant column errors varying between $\sim 1 \times 10^{15}$ molec cm^{-2} and $\sim 2 \times 10^{16}$ molec cm^{-2} were reported by the different groups as illustrated in Fig. 17a for 4 July 2009 at SZA less than 75°. As expected, scientific grade instruments (BIRA, Bremen, IUPH, WSU) display small errors of the order of 1×10^{15} molec cm^{-2}, while mini-DOAS types of instruments (e.g. Mainz) are significantly noisier, typical errors reaching 5×10^{15} molec cm^{-2} or more. In order to better compare the actual performances of the different instruments, the DSCD errors were further

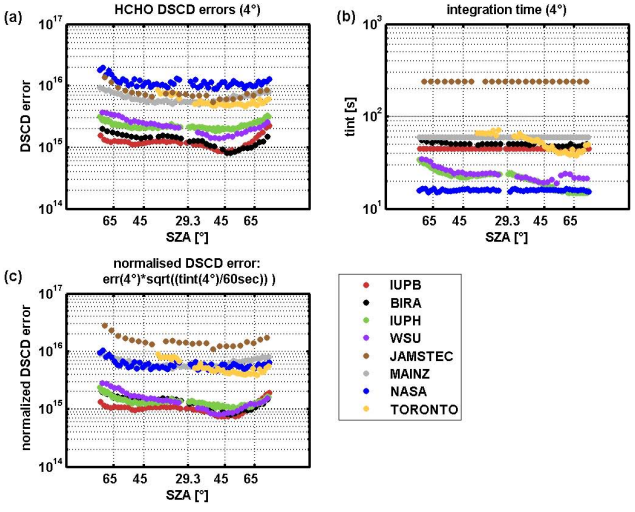

Fig. 17. Comparison of HCHO DSCD errors (molec cm^{-2}) retrieved by each participating group for the case of 4° elevation, based on measurements from 4 July 2009. **(a)** DSCD errors from DOAS evaluations, **(b)** corresponding integration times, **(c)** DSCD errors normalized by their integration exposure times.

normalised to a common integration time of 1 min. As can be seen in Fig. 17c, this largely improves the consistency between the scientific-grade instruments, which all display similar noise levels. The NASA and Mainz instruments, which use small and uncooled or less cooled detectors (see Table 1) have larger errors as is to be expected. More surprisingly, the Toronto data appear to display a similar level of noise, despite the fact that this instrument was using a large 2-D cooled array detector. This is likely related to a mechanical

slit problem having occurred during the campaign that reduced the signal to 25 % of normal values. Also, temperature instabilities have led to systematic features in the residuals that affected DSCD error estimates reported by this group. During part of the campaign, the Bremen instrument had a high frequency structure in the residuals which could be accounted for by using an empirical correction. The problem could not be reproduced in the laboratory after the campaign and appears not to have impacted the NO_2 and HCHO retrievals. The INTA instrument (not on Fig. 17 because it was not measuring on 4 July) is showing similar level of noise. When normalised to the same integration time as the other instruments, JAMSTEC appears to have been the noisiest system operated during the campaign.

5.2 Systematic uncertainties

Several important sources of systematic uncertainty have already been discussed in depth as part of our sensitivity analysis, which led us to propose optimised HCHO retrieval settings that minimise interference effects involving the polynomial closure term, Ring effect, O_4, BrO and HCHO cross sections. In this section, additional uncertainties are treated with the aim of providing a comprehensive error budget for dDSCDs, as these are the main input parameters for retrieving profile information. This includes the impact of systematic uncertainties in absorption cross sections as well as errors due to calibration uncertainties, in particular the slit function and the wavelength calibration, which are key parameters for DOAS retrievals.

5.2.1 Absorption cross sections

HCHO

Two sources of HCHO absorption cross sections have been used in the literature, the Cantrell et al. (1990) spectrum and the Meller and Moortgat (2000) data set. The latter was adopted for our baseline. HITRAN recommends the use of the Cantrell data set, rescaled to correct for its systematically low bias (Chance and Orphal, 2011). In the 336.5–359 nm interval and at the resolution of the BIRA spectrometer, the cross sections differ by approximately 9 %, a difference which was found to propagate directly to the slant column retrievals. The temperature dependence of the HCHO absorption cross section is small, of the order of $0.05\,\%\,K^{-1}$ (De Smedt, 2011) and its effect was neglected here since the Meller and Moortgat cross section was measured at 293 °K, a temperature representative of ambient conditions during CINDI.

BrO

Two main sources of BrO cross sections can be found in the literature: Wilmouth et al. (1999) and Fleischmann et al. (2004). These data sets are highly consistent in shape and their use was found to result in very small differences in the HCHO dDSCD, of the order of a few 10^{14} molec cm^{-2}. For a median dDSCD of 3.8×10^{16} molec cm^{-2} at 4° elevation, the difference is therefore less than 2 %.

Ozone

The baseline intercomparison settings used the Bogumil et al. (2003) ozone absorption cross sections. We have tested the impact of using the alternative data set from Brion, Daumont and Malicet (BDM, Daumont et al., 1992; Malicet et al., 1995). The resulting HCHO dDSCDs were found to be larger by approximately 5×10^{15} molec cm^{-2}. For a median dDSCD of 3.8×10^{16} molec cm^{-2} at 4° elevation, the difference is on the order of 13 % during the day.

Ring effect

Although the cross-talk between HCHO and the Ring effect has been strongly reduced using the new baseline settings defined in Sect. 4 (see Fig. 10), some level of correlation persists between these parameters. As a result, HCHO uncertainties are expected to be linked to the strength of the Ring effect, which itself is a function of the geometry, SZA and aerosol content (Wagner et al., 2009). When considering the Ring cross section that leads to the larger differences, (in most cases approach A), typical uncertainties on the HCHO DSCD reaches up to 5 to 12 %.

NO_2

The baseline intercomparison settings used the Vandaele et al. (1996) NO_2 absorption cross sections at 298 °K. Switching to the alternative data set of Burrows et al. (1998) HCHO DSCDs are found to vary by 2 to 5 %, depending on the NO_2 content.

O_4

The choice of the O_4 cross section has been already largely discussed in Sect. 4.2. Adopting the Greenblatt et al. (1990) data set, which minimises inconsistencies in the BrO slant columns, we further neglect residual errors related to O_4. It should be noted that in this study, a wavelength axis corrected version of the Greenblatt et al. (1990) data set has been used (see e.g. Wagner et al., 2002), with a shift of -0.2 nm.

5.2.2 Instrumental slit function and wavelength calibration

Uncertainties in key instrumental calibration parameters may also be important. For example, imperfect characterisation of the slit function can lead to errors in the HCHO retrieval due to inappropriate convolution of the laboratory absorption cross sections. This effect was tested by changing slightly the width of the measured slit function of the BIRA instrument

(changes of $\pm$ 0.04 nm around the measured value of 0.38 nm Gaussian FWHM). This led, for example, to changes in the HCHO dDSCD at 4° elevation of 1×10^{15} molec cm^{-2}, corresponding to relative differences of around 2 %. In addition, small perturbations to the wavelength registration of the spectra were introduced in order to test the sensitivity of the retrievals to known uncertainties in the wavelength calibration procedure. Results indicate changes of the order of 2×10^{15} molec cm^{-2} for the 4° dDSCD (around 5 %) for shifts of 0.02 nm. We therefore conclude that uncertainties in the instrumental slit function and the wavelength calibration have a minor impact.

Another potentially important source of error already identified in the CINDI NO_2 study by Roscoe et al. (2010) is the accuracy of the pointing direction. This issue was addressed early in the campaign, before the HCHO intercomparison was started, checking the alignment of each instrument and minimizing the pointing errors (Roscoe et al., 2010). Moreover, since this error source does not affect directly the DOAS evaluations, but more the determination of the corresponding air mass factors, we do not treat it explicitly here. It should, of course, be considered for a full error analysis of vertical column and/or profile concentration retrieval of HCHO.

5.3 Overall error budget

Based on the results discussed above, an overall assessment of the total uncertainties on HCHO dDSCDs has been generated, including the main contributions of systematic and random errors, and is shown in Fig. 18. The figure summarises the main results from the sensitivity study for an elevation angle of 4° with a typical dDSCD of 3.8×10^{16} molec cm^{-2}, which is the median value during 4 July 2009. For most cases, the retrieved HCHO dDSCDs fall within 15 % of the values obtained with the optimised settings defined in Sect. 4. Assuming that the different effects are sufficiently uncorrelated with each other, we can sum all deviations in quadrature to obtain an estimate of the overall systematic uncertainty, which is represented by the black line in Fig. 18. On this basis, we estimate the total systematic uncertainties on HCHO dDSCDs to be of approximately 20 % for measurements at 4° elevation, with a weak dependence on the SZA. Since some of the effects considered in our study are likely to be partly correlated, these values could be considered as upper limits, however, despite our efforts to include the most important sources of uncertainties in our sensitivity analysis, the need for possible additional terms cannot be excluded a-priori. Moreover, the results presented here are based on a single day of measurements and are influenced by the atmospheric conditions on that day. Therefore, arguably, the uncertainties reported here are to be interpreted as realistic conservative values.

In Fig. 18, the random error is estimated for a typical integration time of one minute. We distinguish between two

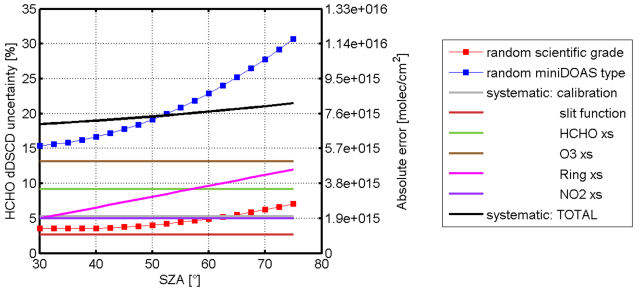

Fig. 18. Summary assessment of the error budget on HCHO dDSCD at 4° elevation, as a function of the SZA. Random uncertainties are typical of low-noise scientific grade instruments (red dots) and of mini-DOAS types of instruments (blue dots) for a typical integration exposure time of 1 min.

typical cases corresponding to low-noise scientific grade instruments and to mini-DOAS types of instruments, respectively. As can be seen for scientific grade instruments, the total errors on individual measurements are largely dominated by the systematic part. For mini-DOAS instruments, both random and systematic uncertainties contribute similarly. As already mentioned, the random uncertainty can be reduced by means of longer integration time and, for less sensitive mini-DOAS instruments, a trade-off between error and temporal resolution has to be made.

6 Conclusions

HCHO differential slant columns were retrieved from nine different MAX-DOAS instruments jointly operated during the CINDI campaign in Cabauw, the Netherlands, from June to July 2009. This exercise complements the formal semi-blind NO_2 and O_4 slant column intercomparison performed during the same campaign (Roscoe et al., 2010). To reduce the impact of uncertainties on retrieval parameters, common DOAS analysis settings were used by the different groups. In addition, 30-min averages were taken to reduce differences in temporal sampling. The HCHO differential slant columns retrieved by the different groups generally agree within 15 %, which is very satisfactory and almost as good as the agreement obtained for the NO_2 and O_4 intercomparison (Roscoe et al., 2010). This exercise shows that a large variety of MAX-DOAS instruments of different grades and sensitivities can consistently measure HCHO columns within acceptable errors. However, while scientific grade instruments clearly demonstrate their ability to provide low-noise measurements at high temporal resolution (less than 30 min), less sensitive mini-DOAS instruments display significantly larger noise, which probably compromises their ability to deliver vertical profile information at the same temporal resolution.

A number of sensitivity tests was performed to investigate the sensitivity of HCHO retrievals to changes in DOAS analysis settings and input data sets. The study highlights the

role of cross-correlation effects involving Ring effect, O_4, BrO and HCHO absorption cross sections and the order of the DOAS closure polynomial. Optimised retrieval settings are proposed with the aim to minimise correlation effects. Furthermore, systematic and random uncertainties are estimated for typical observation conditions. The largest systematic errors are found to be related to the Ring effect and to the uncertainties in HCHO and O_3 absorption cross sections. We conclude that the overall systematic uncertainty on the HCHO DSCD retrievals is of the order of 20 % with a weak dependence on the solar zenith angle. Total errors are dominated by systematic effects for the scientific grade instruments, while both systematic and random uncertainties contribute at the same level for mini-DOAS-like instruments.

Finally, it must be pointed out that issues already identified during the semi-blind NO_2 and O_4 intercomparison (Roscoe et al., 2010) remain largely valid for the present study on HCHO. In particular, the accuracy of slant column measurements crucially depends (especially for low elevation angles) on the accuracy of the pointing direction, which should therefore be checked on a regular basis. Also, the temporal variability in tropospheric signals can be large, even if this variability is expected to be less important for HCHO than for NO_2. For future MAX-DOAS intercomparisons, a better synchronisation of the measurements should be considered to minimise the scatter possibly introduced by differences in measurement time.

Acknowledgements. The authors wish to thank the KNMI staff at Cabauw for their technical assistance and for the infrastructure that was offered during the campaign. The CINDI Campaign was funded by ESA and EU, through the CEOS and ACCENT-AT2 projects, respectively. We further acknowledge the support of the EU via the GEOMON Integrated Project and via the FP 7 project NORS (284421), and of the Belgian Science Policy via the AGACC-II project. We also thank Isabelle De Smedt and Nicolas Theys for helpful discussions during the preparation of this manuscript. The participation of the Toronto team was supported by the Canadian Foundation for Climate and Atmospheric Science and the Centre for Global Change Science at the University of Toronto; the instrument was funded by the Natural Sciences and Engineering Research Council and the Canadian Foundation for Innovation, and is usually operated at the Polar Environment Atmospheric Research Laboratory (PEARL) by the Canadian Network for the Detection of Atmospheric Change (CANDAC).

Edited by: J. Stutz

References

Aliwell, S. R., Van Roozendael, M., Johnston, P. V., Richter, A., Wagner, T., Arlander, D. W., Burrows, J. P., Fish, D. J., Jones, R. L., Tørnkvist, K. K., Lambert, J.-C., Pfeilsticker, K., and Pundt, I.: Analysis for BrO in zenith-sky spectra: An intercomparison exercise for analysis improvement, J. Geophys. Res., 107, D140, doi:10.1029/2001JD000329, 2002.

Bobrowski, N., Hönninger, G., Galle, B., and Platt, U.: Detection of bromine monoxide in a volcanic plume, Nature, 423, 273–276, doi:10.1038/nature01625, 2003.

Bogumil, K., Orphal, J., Homann, T., Voigt, S., Spietz, P., Fleischmann, O. C., Vogel, A., Hartmann, M., Bovensmann, H., Frerik, J., and Burrows, J. P.: Measurements of molecular absorption spectra with the SCIAMACHY Pre-Flight Model: Instrument characterization and reference spectra for atmospheric remote sensing in the 230–2380 nm region, J. Photochem. Photobiol. A, 157, 167–184, 2003.

Brinksma, E. J., Pinardi, G., Volten, H., Braak, R., Richter, A., Schoenhardt, A., Van Roozendael, M., Fayt, C., Hermans, C., Dirksen, R. J., Vlemmix, T., Berkhout, A. J. C., Swart, D. P. J., Oetjes, H., Wittrock, F., Wagner, T., Ibrahim, O., de Leeuw, G., Moerman, M., Curier, R. L., Celarier, E. A., Cede, A., Knap, W. H., Veefkind, J. P., Eskes, H. J., Allaart, M., Rothe, R., Piters, A. J. M., and Levelt, P. F.: The 2005 and 2006 DANDELIONS NO_2 and aerosol intercomparison campaigns, J. Geophys. Res., 113, D16S46, doi:10.1029/2007JD008988, 2008.

Burrows, J. P., Dehn, A., Deters, B., Himmelmann, S., Richter, A., Voigt, S., and Orphal, J.: Atmospheric remote-sensing reference data from GOME: Part 1. Temperature-dependent absorption cross-sections of NO2 in the 231–794 nm range, J. Quant. Spectrosc. Ra., 60, 1025–1031, 1998.

Cantrell, C. A., Davidson, J. A., McDaniel, A. H., Shetter, R. E., and Calvert, J. G.: Temperature-dependent formaldehyde cross sections in the near ultraviolet spectra region, J. Phys. Chem., 94, 3902–3908, 1990.

Chance, K. and Kurucz, R. L.: An improved high-resolution solar reference spectrum for Earth's atmosphere measurements in the ultraviolet, visible, and near infrared, http://www.cfa.harvard.edu/atmosphere (last access: July 2011), 2010.

Chance, K. and Orphal, J.: Revised ultraviolet absorption cross sections of H_2CO for the HITRAN database, J. Quant. Spectrosc. Ra., 112, 1509–1510, doi:10.1016/j.jqsrt.2011.02.002, 2011.

Chance, K., Palmer, P. I., Spurr, R. J., Martin, R. V., Kurosu, T. P., and Jacob, D. J.: Satellite observations of formaldehyde over North America from GOME, Geophys. Res. Lett., 27, 3461–3464, 2000.

Chance, K. V. and Spurr, R. J. D.: Ring effect studies: Rayleigh scattering, including molecular parameters for rotational Raman scattering, and the Fraunhofer spectrum, Appl. Optics, 36, 5224–5230, 1997.

Clémer, K., Fayt, C., Hendrick, F., Hermans, C., Pinardi, G., and Van Roozendael, M.: The simultaneous retrieval of tropospheric aerosol extinction and NO_2 vertical profiles from MAXDOAS measurements in Beijing, in: Proceedings of the 8th International Symposium on Tropospheric Profiling, 19–23 October 2009, Delft, The Netherlands, 2009.

Clémer, K., Van Roozendael, M., Fayt, C., Hendrick, F., Hermans, C., Pinardi, G., Spurr, R., Wang, P., and De Mazière, M.: Multiple wavelength retrieval of tropospheric aerosol optical properties from MAXDOAS measurements in Beijing, Atmos. Meas. Tech., 3, 863–878, doi:10.5194/amt-3-863-2010, 2010.

Curci, G., Palmer, P. I., Kurosu, T. P., Chance, K., and Visconti, G.: Estimating European volatile organic compound emissions using satellite observations of formaldehyde from the Ozone Monitoring Instrument, Atmos. Chem. Phys., 10, 11501–11517, doi:10.5194/acp-10-11501-2010, 2010.

Daumont, M., Brion, J., Charbonnier, J., and Malicet, J.: Ozone UV spectroscopy, I: Absorption cross-sections at room temperature, J. Atmos. Chem., 15, 145–155, 1992.

Demoulin, P., Zander, R., Melen, F., Mahieu, E., and Servais, C.: Column abundance measurements of formaldehyde above the Jungfraujoch, in: Proceedings of "Atmospheric Spectroscopy Applications 1999", 1–3 September 1999, Reims, France, 59–62, 1999.

De Smedt, I.: Long-Term Global Observations of Tropospheric Formaldehyde Retrieved from Spaceborne Nadir UV Sensors, PhD Thesis, ULB – Université Libre de Bruxelles, Brussels, 2011.

De Smedt, I., Müller, J.-F., Stavrakou, T., van der A, R., Eskes, H., and Van Roozendael, M.: Twelve years of global observations of formaldehyde in the troposphere using GOME and SCIAMACHY sensors, Atmos. Chem. Phys., 8, 4947–4963, doi:10.5194/acp-8-4947-2008, 2008.

De Smedt, I., Stavrakou, T., Müller, J.-F., Hao, N., Valks, P., Loyola, D., and Van Roozendael, M.: H_2CO columns retrieved from GOME-2: first scientific results and progress towards the development of an operational product, in: Proceedings of the 2009 EUMETSAT Meteorological Satellite Conference, 20–25 September 2009, Bath, UK, 2009.

De Smedt, I., Stavrakou, T., Müller, J.-F., van Der A, R. J., and Van Roozendael, M.: Trend detection in satellite observations of formaldehyde tropospheric columns, Geophys. Res. Lett., 37, L18808, doi:10.1029/2010GL044245, 2010.

Fleischmann, O. C., Hartmann, M., Burrows, J. P., and Orphal, J.: New ultraviolet absorption cross-sections of BrO at atmospheric temperatures measured by time-windowing Fourier transform spectroscopy, J. Photochem. Photobiol. A, 168, 117–132, 2004.

Fraser, A., Adams, C., Drummond, J. R., Goutail, F., Manney, G., and Strong, K.: The Polar Environment Atmospheric Research Laboratory UV-Visible Ground-Based Spectrometer: First Measurements of O_3, NO_2, BrO, and OClO Columns. J. Quant. Spectrosc. Ra., 110, 986–1004, doi:10.1016/j.jqsrt.2009.02.034, 2009.

Fried, A., Cantrell, C., Olson, J., Crawford, J. H., Weibring, P., Walega, J., Richter, D., Junkermann, W., Volkamer, R., Sinreich, R., Heikes, B. G., O'Sullivan, D., Blake, D. R., Blake, N., Meinardi, S., Apel, E., Weinheimer, A., Knapp, D., Perring, A., Cohen, R. C., Fuelberg, H., Shetter, R. E., Hall, S. R., Ullmann, K., Brune, W. H., Mao, J., Ren, X., Huey, L. G., Singh, H. B., Hair, J. W., Riemer, D., Diskin, G., and Sachse, G.: Detailed comparisons of airborne formaldehyde measurements with box models during the 2006 INTEX-B and MILAGRO campaigns: potential evidence for significant impacts of unmeasured and multigeneration volatile organic carbon compounds, Atmos. Chem. Phys., 11, 11867–11894, doi:10.5194/acp-11-11867-2011, 2011.

Frieß, U., Monks, P. S., Remedios, J. J., Rozanov, A., Sinreich, R., Wagner, T., and Platt, U.: MAX-DOAS O_4 measurements: a new technique to derive information on atmospheric aerosols: 2. Modeling studies, J. Geophys. Res., 111, D14203, doi:10.1029/2005JD006618, 2006.

Frieß, U., Sihler, H., Sander, R., Pöhler, D., Yilmaz, S., and Platt, U.: The vertical distribution of BrO and aerosols in the Arctic: Measurements by active and passive differential optical absorption spectroscopy, J. Geophys. Res., 116, D00R04, doi:10.1029/2011JD015938, 2011.

Grainger, J. F. and Ring, J.: Anomalous Fraunhofer line profiles, Nature, 193, 762, doi:10.1038/193762a0, 1962.

Greenblatt, G. D., Orlando, J. J., Burkholder, J. B., and Ravishankara, A. R.: Absorption measurements of oxygen between 330 and 1140 nm, J. Geophys. Res., 95, 18577–18582, 1990.

Hak, C., Pundt, I., Trick, S., Kern, C., Platt, U., Dommen, J., Ordóñez, C., Prévôt, A. S. H., Junkermann, W., Astorga-Lloréns, C., Larsen, B. R., Mellqvist, J., Strandberg, A., Yu, Y., Galle, B., Kleffmann, J., Lörzer, J. C., Braathen, G. O., and Volkamer, R.: Intercomparison of four different in-situ techniques for ambient formaldehyde measurements in urban air, Atmos. Chem. Phys., 5, 2881–2900, doi:10.5194/acp-5-2881-2005, 2005.

Heckel, A., Richter, A., Tarsu, T., Wittrock, F., Hak, C., Pundt, I., Junkermann, W., and Burrows, J. P.: MAX-DOAS measurements of formaldehyde in the Po-Valley, Atmos. Chem. Phys., 5, 909–918, doi:10.5194/acp-5-909-2005, 2005.

Hendrick, F., Van Roozendael, M., Kylling, A., Petritoli, A., Rozanov, A., Sanghavi, S., Schofield, R., von Friedeburg, C., Wagner, T., Wittrock, F., Fonteyn, D., and De Mazière, M.: Intercomparison exercise between different radiative transfer models used for the interpretation of ground-based zenith-sky and multi-axis DOAS observations, Atmos. Chem. Phys., 6, 93–108, doi:10.5194/acp-6-93-2006, 2006.

Herman, J., Cede, A., Spinei, E., Mount, G., Tzortziou, M., and Abuhassan, N.: NO_2 column amounts from ground-based Pandora and MFDOAS spectrometers using the direct-sun DOAS technique: Intercomparisons and application to OMI validation, J. Geophys. Res., 114, D13307, doi:10.1029/2009JD011848, 2009.

Hermans, C., Vandaele, A. C., Fally, S., Carleer, M., Colin, R., Coquart, B., Jenouvrier, A., and Mérienne, M.-F.: Absorption cross-section of the collision-induced bands of oxygen from the UV to the NIR, in: Proceedings of the NATO Advanced Research Workshop, Weakly Interacting Molecular Pairs: Unconventional Absorbers of Radiation in the Atmosphere, Fontevraud, France, 24 April–2 May 2002, edited by: Camy-Peyret, C. and Vigasin, A. A., NATO Science Series IV Earth and Environmental Sciences, vol. 27, Kluwer Academic Publishers, Boston, 193–202, 2003.

Hönninger, G., von Friedeburg, C., and Platt, U.: Multi axis differential optical absorption spectroscopy (MAX-DOAS), Atmos. Chem. Phys., 4, 231–254, doi:10.5194/acp-4-231-2004, 2004.

Inomata, S., Tanimoto, H., Kameyama, S., Tsunogai, U., Irie, H., Kanaya, Y., and Wang, Z.: Technical Note: Determination of formaldehyde mixing ratios in air with PTR-MS: laboratory experiments and field measurements, Atmos. Chem. Phys., 8, 273–284, doi:10.5194/acp-8-273-2008, 2008.

Irie, H., Kanaya, Y., Akimoto, H., Iwabuchi, H., Shimizu, A., and Aoki, K.: First retrieval of tropospheric aerosol profiles using MAX-DOAS and comparison with lidar and sky radiometer measurements, Atmos. Chem. Phys., 8, 341–350, doi:10.5194/acp-8-341-2008, 2008.

Irie, H., Kanaya, Y., Akimoto, H., Iwabuchi, H., Shimizu, A., and Aoki, K.: Dual-wavelength aerosol vertical profile measurements by MAX-DOAS at Tsukuba, Japan, Atmos. Chem. Phys., 9, 2741–2749, doi:10.5194/acp-9-2741-2009, 2009.

Irie, H., Takashima, H., Kanaya, Y., Boersma, K. F., Gast, L., Wittrock, F., Brunner, D., Zhou, Y., and Van Roozendael, M.: Eight-component retrievals from ground-based MAX-DOAS observations, Atmos. Meas. Tech., 4, 1027–1044, doi:10.5194/amt-4-1027-2011, 2011.

Jones, N. B., Riedel, K., Allan, W., Wood, S., Palmer, P. I., Chance, K., and Notholt, J.: Long-term tropospheric formaldehyde concentrations deduced from ground-based fourier transform solar infrared measurements, Atmos. Chem. Phys., 9, 7131–7142, doi:10.5194/acp-9-7131-2009, 2009.

Li, X., Brauers, T., Shao, M., Garland, R. M., Wagner, T., Deutschmann, T., and Wahner, A.: MAX-DOAS measurements in southern China: retrieval of aerosol extinctions and validation using ground-based in-situ data, Atmos. Chem. Phys., 10, 2079–2089, doi:10.5194/acp-10-2079-2010, 2010.

Ma, J. Z., Beirle, S., Jin, J. L., Shaiganfar, R., Yan, P., and Wagner, T.: Tropospheric NO_2 vertical column densities over Beijing: results of the first three-years of ground-based MAX-DOAS measurements (2008–2011) and satellite validation, Atmos. Chem. Phys. Discuss., 12, 26719–26781, doi:10.5194/acpd-12-26719-2012, 2012.

Malicet, J., Daumont, D., Charbonnier, J., Parisse, C., Chakir, A., and Brion, J.: Ozone UV spectroscopy, II. Absorption crosssections and temperature dependence, J. Atmos. Chem., 21, 263–273, 1995.

Marbach, T., Beirle, S., Platt, U., Hoor, P., Wittrock, F., Richter, A., Vrekoussis, M., Grzegorski, M., Burrows, J. P., and Wagner, T.: Satellite measurements of formaldehyde linked to shipping emissions, Atmos. Chem. Phys., 9, 8223–8234, doi:10.5194/acp-9-8223-2009, 2009.

Mayer, B. and Kylling, A.: Technical note: The libRadtran software package for radiative transfer calculations – description and examples of use, Atmos. Chem. Phys., 5, 1855–1877, doi:10.5194/acp-5-1855-2005, 2005.

Meller, R. and Moortgat, G. K.: Temperature dependence of the absorption cross sections of formaldehyde between 223 and 323 K in the wavelength range 225–375 nm, J. Geophys. Res., 105, 7089–7101, 2000.

Millet, D., Jacob, D. J., Turquety, S., Hudman, R. C., Wu, S., Fried, A., Walega, J., Heikes, B. G., Blake, D. R., Singh, H. B., Anderson, B. E., and Clarke, A. D.: Formaldehyde distribution over North America: Implications for satellite retrievals of formaldehyde columns and isoprene emissions, J. Geophys. Res., 111, D24S02, doi:10.1029/2005JD006853, 2006.

Millet, D. B., Jacob, D. J., Boersma, K. F., Fu, T.-M., Kurosu, T. P., Chance, K. V., Heald, C. L., and Guenther, A.: Spatial distribution of isoprene emissions from North America derived from formaldehyde column measurements by the OMI satellite sensor, J. Geophys. Res., 113, 1–18, doi:10.1029/2007JD008950, 2008.

Palmer, P. I., Jacob, D. J., Fiore, A. M., Martin, R. V., Chance, K., and Kurosu, T. P.: Mapping isoprene emissions over North America using formaldehyde column observations from space, J. Geophys. Res., 108, 4180, doi:10.1029/2002JD002153, 2003.

Pikelnaya, O., Hurlock, S. C., Trick, S., and Stutz, J.: Intercomparison of multiaxis and long-path optical absorption spectroscopy measurements in the marine boundary layer, J. Geophys. Res., 112, D10S01, doi:10.1029/2006JD007727, 2007.

Piters, A. J. M., Boersma, K. F., Kroon, M., Hains, J. C., Van Roozendael, M., Wittrock, F., Abuhassan, N., Adams, C., Akrami, M., Allaart, M. A. F., Apituley, A., Beirle, S., Bergwerff, J. B., Berkhout, A. J. C., Brunner, D., Cede, A., Chong, J., Clémer, K., Fayt, C., Frieß, U., Gast, L. F. L., Gil-Ojeda, M., Goutail, F., Graves, R., Griesfeller, A., Großmann, K., Hemerijckx, G., Hendrick, F., Henzing, B., Herman, J., Hermans, C., Hoexum, M., van der Hoff, G. R., Irie, H., Johnston, P. V., Kanaya, Y., Kim, Y. J., Klein Baltink, H., Kreher, K., de Leeuw, G., Leigh, R., Merlaud, A., Moerman, M. M., Monks, P. S., Mount, G. H., Navarro-Comas, M., Oetjen, H., Pazmino, A., Perez-Camacho, M., Peters, E., du Piesanie, A., Pinardi, G., Puentedura, O., Richter, A., Roscoe, H. K., Schönhardt, A., Schwarzenbach, B., Shaiganfar, R., Sluis, W., Spinei, E., Stolk, A. P., Strong, K., Swart, D. P. J., Takashima, H., Vlemmix, T., Vrekoussis, M., Wagner, T., Whyte, C., Wilson, K. M., Yela, M., Yilmaz, S., Zieger, P., and Zhou, Y.: The Cabauw Intercomparison campaign for Nitrogen Dioxide measuring Instruments (CINDI): design, execution, and early results, Atmos. Meas. Tech., 5, 457–485, doi:10.5194/amt-5-457-2012, 2012.

Platt, U. and Stutz, J.: Differential Optical Absorption Spectroscopy, Principles and Applications, Springer, Berlin, 2008.

Roscoe, H. K., Johnston, P. V., Van Roozendael, M., Richter, A., Preston, K., Lambert, J.-C., Hermans, C., de Cuyper, W., Dzenius, S., Winterath, T., Burrows, J., Sarkissian, A., Goutail, F., Pommereau, J.-P., d'Almeida, E., Hottier, J., Coureul, C., Ramond, D., Pundt, I., Bartlet, L. M., Kerr, J. E., Elokhov, A., Giovanelli, G., Ravegnani, F., Premudan, M., Kostadinov, M., Erle, F., Wagner, T., Pfeilsticker, K., Kenntner, M., Marquand, L. C., Gil, M., Puentedura, O., Arlander, W., Kastad-Hoiskar, B. A., Tellefsen, C. W., Heese, C. W., Jones, R. L., Aliwalle, S. R., and Freswater, R. A.: Slant column measurements of O_3 and NO_2 during the NDSC intercomparison of zenith-sky UV-visible spectrometers in June 1996, J. Atmos. Chem., 32, 281–314, 1999.

Roscoe, H. K., Van Roozendael, M., Fayt, C., du Piesanie, A., Abuhassan, N., Adams, C., Akrami, M., Cede, A., Chong, J., Clémer, K., Friess, U., Gil Ojeda, M., Goutail, F., Graves, R., Griesfeller, A., Grossmann, K., Hemerijckx, G., Hendrick, F., Herman, J., Hermans, C., Irie, H., Johnston, P. V., Kanaya, Y., Kreher, K., Leigh, R., Merlaud, A., Mount, G. H., Navarro, M., Oetjen, H., Pazmino, A., Perez-Camacho, M., Peters, E., Pinardi, G., Puentedura, O., Richter, A., Schönhardt, A., Shaiganfar, R., Spinei, E., Strong, K., Takashima, H., Vlemmix, T., Vrekoussis, M., Wagner, T., Wittrock, F., Yela, M., Yilmaz, S., Boersma, F., Hains, J., Kroon, M., Piters, A., and Kim, Y. J.: Intercomparison of slant column measurements of NO_2 and O_4 by MAX-DOAS and zenith-sky UV and visible spectrometers, Atmos. Meas. Tech., 3, 1629–1646, doi:10.5194/amt-3-1629-2010, 2010.

Russchenberg, H., Bosveld, F., Swart, D., ten Brink, H., de Leeuw, G., Uijlenhoet, R., Abresser-Rastburg, B., van der Marel, H., Ligthart, L., Boers, R., and Apituley, A.: Ground-based atmospheric remote sensing in The Netherlands; European outlook, IEICE T. Commun., E88-B, 2252–2258, doi:10.1093/ietcom/e88-b.6.2252, 2005.

Shaiganfar, R., Beirle, S., Sharma, M., Chauhan, A., Singh, R. P., and Wagner, T.: Estimation of NO_x emissions from Delhi using Car MAX-DOAS observations and comparison with OMI satellite data, Atmos. Chem. Phys., 11, 10871–10887, doi:10.5194/acp-11-10871-2011, 2011.

Sinreich, R., Friess, U., Wagner, T., and Platt, U.: Multi axis differential optical absorption spectroscopy (MAX-DOAS) of gas and aerosol distributions, Faraday Discuss., 130, 153–164, 2005.

Sinreich, R., Volkamer, R., Filsinger, F., Frieß, U., Kern, C., Platt, U., Sebastián, O., and Wagner, T.: MAX-DOAS detection of glyoxal during ICARTT 2004, Atmos. Chem. Phys., 7, 1293–1303, doi:10.5194/acp-7-1293-2007, 2007.

Stavrakou, T., Müller, J.-F., De Smedt, I., Van Roozendael, M., van der Werf, G. R., Giglio, L., and Guenther, A.: Evaluating the performance of pyrogenic and biogenic emission inventories against one decade of space-based formaldehyde columns, Atmos. Chem. Phys., 9, 1037–1060, doi:10.5194/acp-9-1037-2009, 2009a.

Stavrakou, T., Müller, J.-F., De Smedt, I., Van Roozendael, M., van der Werf, G. R., Giglio, L., and Guenther, A.: Global emissions of non-methane hydrocarbons deduced from SCIAMACHY formaldehyde columns through 2003–2006, Atmos. Chem. Phys., 9, 3663–3679, doi:10.5194/acp-9-3663-2009, 2009b.

Stutz, J. and Platt, U.: Numerical analysis and error estimation of differential optical absorption spectroscopy measurements with least-squares methods, Appl. Optics, 35, 6041–6053, 1996.

Theys, N., Van Roozendael, M., Hendrick, F., Fayt, C., Hermans, C., Baray, J.-L., Goutail, F., Pommereau, J.-P., and De Mazière, M.: Retrieval of stratospheric and tropospheric BrO columns from multi-axis DOAS measurements at Reunion Island (21° S, 56° E), Atmos. Chem. Phys., 7, 4733–4749, doi:10.5194/acp-7-4733-2007, 2007.

Theys, N., Van Roozendael, M., Hendrick, F., Yang, X., De Smedt, I., Richter, A., Begoin, M., Errera, Q., Johnston, P. V., Kreher, K., and De Mazière, M.: Global observations of tropospheric BrO columns using GOME-2 satellite data, Atmos. Chem. Phys., 11, 1791–1811, doi:10.5194/acp-11-1791-2011, 2011.

Van Roozendael, M., Fayt, C., Post, P., Hermans, C., and Lambert, J.-C.: Retrieval of BrO and NO_2 from UV-Visible observations, in: Sounding the Troposphere from Space: a New Era for Atmospheric Chemistry, edited by: Borrell, P. M., Burrows, J. P., and Platt, U., Springer, Heidelberg, 155–165, 2003.

Vandaele, A. C., Hermans, C., Simon, P. C., Van Roozendael, M., Guilmot, J. M., Carleer, M., and Colin, R.: Fourier transform measurement of NO_2 absorption cross-section in the visible range at room temperature, J. Atmos. Chem., 25, 289–305, 1996.

Vandaele, A. C., Fayt, C., Hendrick, F., Hermans, C., Humbled, F., Van Roozendael, M., Gil, M., Navarro, M., Puentedura, O., Yela, M., Braathen, G., Stebel, K., Tørnkvist, K., Johnston, P., Kreher, K., Goutail, F., Mieville, A., Pommereau, J.-P., Khaikine, S., Richter, A., Oetjen, H., Wittrock, F., Bugarski, S., Friess, U., Pfeilsticker, K., Sinreich, R., Wagner, T., Corlett, G., and Leigh, R.: An intercomparison campaign of ground-based UV-visible measurements of NO_2, BrO, and OClO slant columns: Methods of analysis and results for NO_2, J. Geophys. Res., 110, D08305, doi:10.1029/2004JD005423, 2005.

Vigouroux, C., Hendrick, F., Stavrakou, T., Dils, B., De Smedt, I., Hermans, C., Merlaud, A., Scolas, F., Senten, C., Vanhaelewyn, G., Fally, S., Carleer, M., Metzger, J.-M., Müller, J.-F., Van Roozendael, M., and De Mazière, M.: Ground-based FTIR and MAX-DOAS observations of formaldehyde at Réunion Island and comparisons with satellite and model data, Atmos. Chem. Phys., 9, 9523–9544, doi:10.5194/acp-9-9523-2009, 2009.

Vlemmix, T., Piters, A. J. M., Stammes, P., Wang, P., and Levelt, P. F.: Retrieval of tropospheric NO_2 using the MAX-DOAS method combined with relative intensity measurements for aerosol correction, Atmos. Meas. Tech., 3, 1287–1305, doi:10.5194/amt-3-1287-2010, 2010.

Vlemmix, T., Piters, A. J. M., Berkhout, A. J. C., Gast, L. F. L., Wang, P., and Levelt, P. F.: Ability of the MAX-DOAS method to derive profile information for NO_2: can the boundary layer and free troposphere be separated?, Atmos. Meas. Tech., 4, 2659–2684, doi:10.5194/amt-4-2659-2011, 2011a.

Vlemmix, T., Eskes, H. J., Piters, A. J. M., Kelder, H., and Levelt, P. F.: MAX-DOAS tropospheric nitrogen dioxide column measurements compared with the Lotos-Euros air quality model, Atmos. Chem. Phys. Discuss., 11, 28895–28944, doi:10.5194/acpd-11-28895-2011, 2011b.

Vogel, L., Sihler, H., Lampel, J., Wagner, T., and Platt, U.: Retrieval interval mapping, a tool to optimize the spectral retrieval range in differential optical absorption spectroscopy, Atmos. Meas. Tech. Discuss., 5, 4195–4247, doi:10.5194/amtd-5-4195-2012, 2012.

Vountas, M., Rozanov, V. V., and Burrows, J. P.: Ring effect: Impact of rotational Raman scattering on radiative transfer in earth's atmosphere, J. Quant. Spectrosc. Ra., 60, 943–961, 1998.

Vrekoussis, M., Wittrock, F., Richter, A., and Burrows, J. P.: GOME-2 observations of oxygenated VOCs: what can we learn from the ratio glyoxal to formaldehyde on a global scale?, Atmos. Chem. Phys., 10, 10145–10160, doi:10.5194/acp-10-10145-2010, 2010.

Wagner, T., von Friedeburg, C., Wenig, M., Otten, C., and Platt, U.: UV-visible observations of atmospheric O_4 absorptions using direct moonlight and zenith-scattered sunlight for clear-sky and cloudy sky conditions, J. Geophys. Res., 107, D204424, doi:10.1029/2001JD001026, 2002.

Wagner, T., Dix, B., Friedeburg, C. V., Frieß, U., Sanghavi, S., Sinreich, R., and Platt, U.: MAX-DOAS O_4 measurements – a new technique to derive information on atmospheric aerosols, (I) Principles and information content, J. Geophys. Res., 109, D22205, doi:10.1029/2004JD004904, 2004.

Wagner, T., Beirle, S., and Deutschmann, T.: Three-dimensional simulation of the Ring effect in observations of scattered sun light using Monte Carlo radiative transfer models, Atmos. Meas. Tech., 2, 113–124, doi:10.5194/amt-2-113-2009, 2009.

Wagner, T., Beirle, S., Brauers, T., Deutschmann, T., Frieß, U., Hak, C., Halla, J. D., Heue, K. P., Junkermann, W., Li, X., Platt, U., and Pundt-Gruber, I.: Inversion of tropospheric profiles of aerosol extinction and HCHO and NO_2 mixing ratios from MAX-DOAS observations in Milano during the summer of 2003 and comparison with independent data sets, Atmos. Meas. Tech. Discuss., 4, 3891–3964, doi:10.5194/amtd-4-3891-2011, 2011.

Wilmouth, D. M., Hanisco, T. F., Donahue, N. M., and Anderson, J. G.: Fourier transform ultraviolet spectroscopy of the A(2_3/2)_(2_3/2) transition of BrO, J. Phys. Chem., 103, 8935–8944, 1999.

Wittrock, F., Oetjen, H., Richter, A., Fietkau, S., Medeke, T., Rozanov, A., and Burrows, J. P.: MAX-DOAS measurements of atmospheric trace gases in Ny-Ålesund – Radiative transfer studies and their application, Atmos. Chem. Phys., 4, 955–966, doi:10.5194/acp-4-955-2004, 2004.

Wittrock, F., Richter, A., Oetjen, H., Burrows, J. P., Kanakidou, M., Myriokefalitakis, S., Volkamer, R., Beirle, S., Platt, U., and Wagner, T.: Simultaneous global observations of glyoxal and formaldehyde from space, Geophys. Res. Lett., 33, L16804, doi:10.1029/2006gl026310, 2006.

Zieger, P., Weingartner, E., Henzing, J., Moerman, M., de Leeuw, G., Mikkilä, J., Ehn, M., Petäjä, T., Clémer, K., van Roozendael, M., Yilmaz, S., Frieß, U., Irie, H., Wagner, T., Shaiganfar, R., Beirle, S., Apituley, A., Wilson, K., and Baltensperger, U.: Comparison of ambient aerosol extinction coefficients obtained from in-situ, MAX-DOAS and LIDAR measurements at Cabauw, Atmos. Chem. Phys., 11, 2603–2624, doi:10.5194/acp-11-2603-2011, 2011.

Journal of Quantitative Spectroscopy & Radiative Transfer 113 (2012) 1322–1329

Contents lists available at SciVerse ScienceDirect

Journal of Quantitative Spectroscopy & Radiative Transfer

journal homepage: www.elsevier.com/locate/jqsrt

Decrease of the carbon tetrachloride (CCl_4) loading above Jungfraujoch, based on high resolution infrared solar spectra recorded between 1999 and 2011

Curtis P. Rinsland [1], Emmanuel Mahieu [a,*], Philippe Demoulin [a], Rodolphe Zander [a], Christian Servais [a], Jean-Michel Hartmann [b]

[a] Institute of Astrophysics and Geophysics, University of Liège, B-4000, Liège, Belgium
[b] Laboratoire Interuniversitaire des Systèmes Atmosphériques (LISA), CNRS (UMR 7583), Université Paris Est Créteil, Université Paris Diderot, Institut Pierre-Simon Laplace, Université Paris Est Créteil, F-94010 Créteil Cedex, France

ARTICLE INFO

Available online 17 February 2012

Keywords:
Carbon tetrachloride
Atmospheric composition
FTIR spectroscopy
Jungfraujoch
NDACC

ABSTRACT

The long-term trend of the atmospheric carbon tetrachloride (CCl_4) burden has been retrieved from high spectral resolution infrared solar absorption spectra recorded between January 1999 and June 2011. The observations were made with a Fourier transform spectrometer at the northern mid-latitude, high altitude Jungfraujoch station in Switzerland (46.5°N latitude, 8.0°E longitude, 3580 m altitude). Total columns were derived from spectrometric analysis of the strong CCl_4 ν_3 band at 794 cm^{-1}, accounting for all interfering molecules (e.g., H_2O, CO_2, O_3, and a dozen weakly absorbing gases). A significant improvement in the fitting residuals and in the retrieved CCl_4 columns was obtained by taking into account line mixing in a strong interfering CO_2 Q branch. This procedure had never been implemented in remote sensing CCl_4 retrievals though its importance was noted in earlier studies. A fit to the CCl_4 daily mean total column time series returns a statistically-significant long-term trend of $(-1.49\pm0.08\times10^{13}$ mol/$cm^2)$/yr, $2-\sigma$. This corresponds to an annual decrease of (-1.31 ± 0.07) pptv for the mean free tropospheric volume mixing ratio. Furthermore, the total column data set reveals a weak seasonal cycle with a peak-to-peak amplitude of 4.5%, with minimum and maximum values occurring in mid-February and mid-September, respectively. This small seasonal modulation is attributed primarily to the residual influence of tropopause height changes throughout the year. The negative trend of the CCl_4 loading reflects the continued impact of the regulations implemented by the Montreal Protocol and its strengthening amendments and adjustments. Despite this statistically significant decrease, the CCl_4 molecule currently remains an important contributor to the atmospheric chlorine budget, and thus deserves further monitoring, to ensure continued compliance with these strengthenings, globally. Our present findings are briefly discussed with respect to recent relevant CCl_4 investigations at the ground and from space.
© 2012 Elsevier Ltd. All rights reserved.

1. Introduction

Measurement of the long-term trends of atmospheric species is a key responsibility of the Network for the Detection of Atmospheric Composition Change (NDACC, formerly NDSC; see http://www.ndacc.org). This Network is a coordinated international program that uses ground-based *in situ* and remote-sensing instruments as well as

* Corresponding author. Tel.: +32 4 366 97 86; fax: +32 4 366 97 47.
E-mail address: emmanuel.mahieu@ulg.ac.be (E. Mahieu).
[1] NASA-Langley Research Center, Hampton, VA, USA. Deceased on April 20, 2011.

0022-4073/$ - see front matter © 2012 Elsevier Ltd. All rights reserved.
doi:10.1016/j.jqsrt.2012.02.016

sondes to monitor composition changes in both the troposphere and the stratosphere, which are needed to quantify the impact of these changes upon living conditions and climate on Earth.

The carbon tetrachloride (CCl_4) molecule, emitted at the ground, has been and remains a key component of the stratospheric chlorine budget [1–6], still contributing over 10% to the total Cl loading, and to the stratospheric ozone depletion by a similar percentage. It is also a potent greenhouse gas with a global warming potential relative to CO_2 of 1400 on a 100-yr horizon [7]. Monitoring of its atmospheric budget evolution remains, therefore, of relevance to both the Kyoto and the Montreal Protocols.

In recent Scientific Assessments of Ozone Depletion (e.g., Table 1–4 in [8]; Box 1–2 in [9]), a mid-range CCl_4 total atmospheric lifetime of 26 (23–33) yr was reported, assuming that photolysis above the tropopause is the main sink, and that losses to oceans and to recently identified terrestrial biomes are also potential sinks, all remaining highly uncertain at this time. More recently, a stratospheric lifetime of 34 ± 5 yr was estimated from a CCl_4–CCl_3F tracer–tracer correlation [5], i.e., significantly larger than the above value for the global atmosphere. Based on polar ice and firn sample analyses, the CCl_4 emission history dates back to 1908, but experimental uncertainties in surface station measurements remain substantial (3–5%), resulting in spreading due to differences in the assumed productions, adjusted surface emissions, and in chemical model predictions [8, 10]. Firn-air results also indicate that nearly all of the CFCs (chlorofluorocarbons), halons, methyl chloroform and CCl_4 present in today's atmosphere are of anthropogenic origin, though the existence of small natural sources or some anthropogenic production and use in years predating the oldest firn air samples cannot be ruled out. Global *in situ* surface mixing ratios of carbon tetrachloride reached a maximum of about 105–106 pptv in late 1990 (1 pptv$=10^{-12}$ by volume) and have declined subsequently at a steady rate of about 1.0 pptv/yr ($\sim$1% yr^{-1}) as a result of reduced emissions (Fig. 1–6 in [8]). The annual global mean in 2004 was 92–96 pptv confirming that CCl_4 emission reductions have indeed begun, thus lowering its global radiative forcing [11]. A recent inverse analysis [6] of annual emissions from surface station measurements for a nine year period (1996–2004) and eight land regions again concluded that emissions of CCl_4 are continuing a slow global decline, consistent with earlier measurements and inventories with significant decrease in emissions over Europe and North America and growth in emissions from industrial regions in South Asia, India, and Southeast Asia. Limited knowledge of the CCl_4 emission budget, uncertainty in its lifetime, and surface station calibration differences make it difficult to reliably predict its future evolution.

The purpose of this study is to report on the long-term trend of the CCl_4 total columns derived from high spectral resolution solar absorption spectra recorded with a Fourier transform infrared spectrometer (FTIR) and encompassing the strong CCl_4 ν_3 and weaker $\nu_1+\nu_4$ combination bands in the vicinity of 12.7 μm. These observations were performed at the International Scientific Station of the Jungfraujoch (ISSJ) located in the Swiss Alps, at 46.5°N latitude, 8.0°E longitude, 3580 m altitude. The measurements cover the January 1999 to June 2011 time period. This ISSJ time series provides an updated assessment by remote sensing of the CCl_4 trend which is compared to those reported recently (see Table 1–2 in [8]). A significant improvement in the fit to the ISSJ observations was obtained by accounting for spectroscopic line mixing in a nearby interfering CO_2 Q branch, a procedure not implemented in previous remote sensing CCl_4 retrievals though its importance was noted in earlier papers. Our present findings will be discussed critically with respect to recent relevant CCl_4 investigations

2. Jungfraujoch measurements

Since the mid-1980s, solar spectra have been regularly recorded at the Jungfraujoch station under clear-sky conditions using very high-resolution (0.003 to 0.006 cm^{-1}) wide band-pass FTIR spectrometers. Altogether, the various optical filters and cooled detectors cover the 700 to 4500 cm^{-1} interval. This domain contains spectroscopic absorption features of over two dozen measurable gaseous constituents in ISSJ recordings, including source-, sink- and reservoir species (e.g., [3]). The number of days with available observations was around 50/yr until 1990; it increased to about 115 days per year thereafter, when the site became affiliated to the NDSC. Remote spectrometric observations and related analyses were originaly focusing on NDSC priority tasks in support to the initial Montreal Protocol of 1987, in particular the need to quantify composition changes in the stratospheric ozone layer caused by its catalytic destruction by inorganic Cl atoms. The latter resulted from the photolysis of increasingly produced and released anthropogenic organic chlorine-bearing source gases (primarily CFCs and then HCFCs) as first predicted by *Molina and Rowland* [12]. Subsequent amendments and adjustments to the Montreal Protocol and specific recommendations by the emerging Kyoto Protocol led the NDSC to progressively extend its list of targeted gases, namely halocarbons including CCl_4, as well as other trace gases (e.g., HBr, OCS, SO_2) that directly affect ozone, and greenhouse gases including CO_2, CH_4, N_2O which influence the global thermal environment. To reflect these extensions, the NDSC was renamed NDACC in 2006. The ISSJ Alpine station has the official NDACC task to monitor the state of the atmosphere at northern mid-latitudes.

3. Analysis

Spectroscopic parameters adopted here for the target gas CCl_4 are based on laboratory measurements by *Nemtchinov and Varanasi* [13]. Their spectra were recorded with an FTIR spectrometer at temperatures between 208 and 296 K and pressures ranging from 10 to 1013 hPa. The measured cross sections for the target gas and some interfering species (e.g., $CHClF_2$ (HCFC-22), CCl_2FCClF_2 (CFC-113), $ClONO_2$) were converted to "pseudolines" by G. C. Toon (Jet Propulsion Laboratory) with the rotational and vibrational partition functions and stimulated emissions included, solving for the intensity at 296 K and the ground state energy of each pseudoline [14, 15]. The intensities have an estimated error of 4% due to

potential uncertainties in that conversion. (G. C. Toon, private communication, 2008). In the present study, the pseudolines have been combined with line-by-line spectroscopic parameters for other interfering gases (e.g., H_2O, CO_2, O_3, C_2H_2, C_2H_6, HCN, NO, NO_2) compiled in the HITRAN 2004 database ([16], see also http://www.cfa.harvard.edu/hitran). The August 2006 updates were also adopted, in particular the improved air-broadened half-widths for the three most abundant isotopologues of water vapor [17].

Retrievals were performed with the SFIT2 version 3.81 algorithm. The approach is based on the optimal estimation method [18] modified on the basis of its semi-empirical implementation [19, 20]. Concentration profiles for two molecules can be derived. Realistic *a priori* vertical distributions of all other interfering gases can be either scaled or imposed. SFIT2 is widely used and includes the capability of modeling most strong solar line absorptions, namely CO (e.g., [21–24]). The covariance matrix is specified for each layer as a percentage of the *a priori* profile and a correlation length, which is interpreted as a gaussian decaying correlation between layers. In our retrievals, we assumed mid-day pressure and temperature profiles provided for ISSJ by the National Centers for Environmental Prediction (NCEP; see http://www.ncep.noaa.gov), combined with refractive ray-tracing calculations to derive the airmass distribution and mass-weighted effective pressures and temperatures for each layer [25, 26]. Since the solar OH quadruplets were not simulated by our solar line model, the eight narrow spectral intervals (typically 0.06 cm^{-1} wide) encompassing them were de-weighted. A Voigt line shape [27] has been assumed for all atmospheric lines, but the strong $^{12}C^{16}O_2$ Q branch at 791 cm^{-1} is poorly fitted with this approach due to line mixing [28–30]. The impact of line mixing in CO_2 Q branches has also been noted in other spectral regions (e.g., [31, 29, 32–34] and review in [35]) and in thermal emission spectra of Mars [33].

Fig. 1 reproduces molecule-by-molecule plots (offset vertically for clarity) of an experimental solar spectrum and of the primary simulated atmospheric molecular absorbers for the 785.0–807.0 cm^{-1} region adopted here to retrieve CCl_4. All the simulated spectra were calculated for a typical ISSJ observation at an apparent solar zenith angle of 80°. The strong CO_2 Q branch at 791 cm^{-1} appears prominently in the displayed spectral interval.

We selected an *a priori* mixing ratio profile for CCl_4 that decreases from 92 pptv in the bottom layer to 70 pptv at 17 km, 10 pptv at 23 km and 1.5 pptv at 25 km, based on predictions obtained with the version 4 of the WACCM model (Whole-Atmosphere Community Climate Model, e.g., [36]). This assumed *a priori* profile is a mean prediction for 1975–2020 at the location of the Jungfraujoch station. This model simulation includes the time period under investigation here; it is in agreement with surface data measurements showing a CCl_4 maximum in late 1990, followed by a gradual decrease of the mixing ratio with time. Vertical profiles were retrieved for CCl_4 and H_2O, in the 785.0–807.0 cm^{-1} spectral interval. Additionally, O_3 and CO_2 were fitted over the same wavenumber range by multiplicative scaling of a most realistic *a priori* profile for each molecule. Profile retrievals of CCl_4 were performed with strong constraints. A conservative signal-to-noise ratio of 150 was adopted for the inversion to avoid unrealistic oscillations in the retrieved profiles. A 10% per km diagonal covariance and a Gaussian half width for interlayer correlation of 10 km for extra diagonal elements were further adopted. Line mixing in the CO_2 Q branch at 791 cm^{-1} was treated with the software and data of Niro et al. [32] assuming the full relaxation operator model [37].

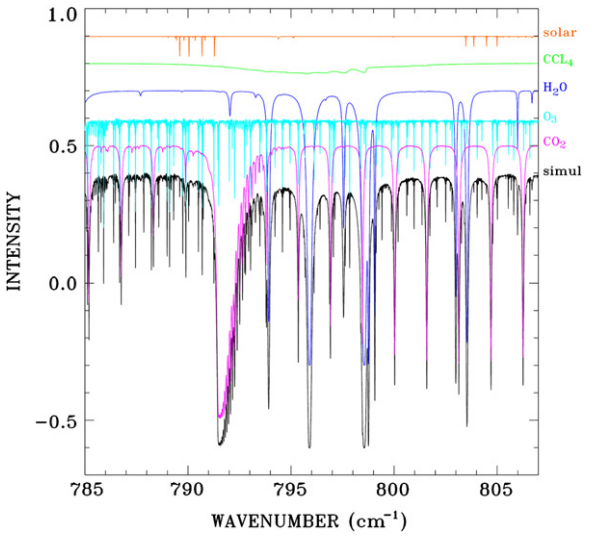

Fig. 1. Molecule-by-molecule plots for the four strongest atmospheric gases and solar lines simulated for the Jungfraujoch at an apparent zenith angle of 80° in the 785.0–807.0 cm^{-1} interval used to retrieve CCl_4. Each spectrum is normalized and offset vertically for clarity. Not shown here are weak second and third order interfering absorptions produced by a dozen other telluric species.

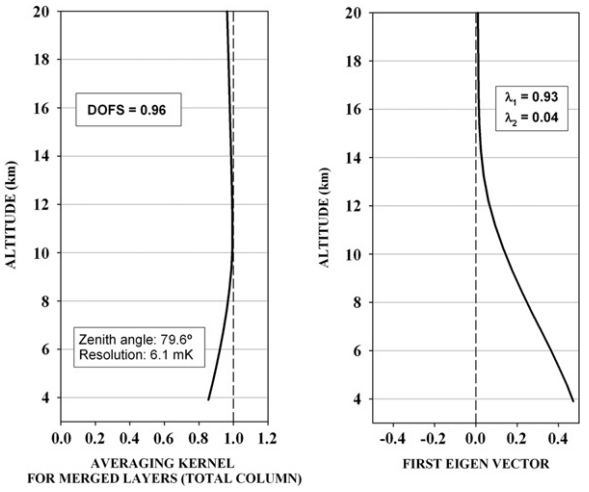

Fig. 2. Typical information content for the retrieval of CCl_4 from Jungfraujoch, in the troposphere and lower stratosphere. The left frame displays the total column averaging kernel vs. altitude for merged layers considered out to 100 km altitude. The right frame shows the first eigenvector which indicates that the retrieval is essentially sensitive to the troposphere. The corresponding eigenvalue of 0.93 confirms that only a small fraction of information comes from the *a priori* profiles in this altitude range.

The left frame of Fig. 2 shows a typical CCl_4 total column averaging kernel for merged layers, for the 3.58 to 20.0 km altitude region. The corresponding eigen vector is shown in the right frame. These curves and the reported values illustrate a limited vertical sensitivity for the target gas. The Degree of Freedom for Signal (DOFS) is indeed close to 1.0 for observations at solar zenith angles of $\sim 80^{\circ}$. Furthermore, sensitivity tests have shown that retrieved CCl_4 total columns were uncorrelated to the apparent solar zenith angle in the 75°–85° range. Hence, only spectra observed within that range were included in our analysis.

Fig. 3 presents spectral fits to a sample spectrum recorded at ISSJ on October 14, 2006, and measured minus calculated residuals with (frame A) and without (frame B) CO_2 line mixing included in the analysis. The root-mean-squares (RMS) residuals from the retrievals are reported for both cases with a reduction by over a factor two when accounting for CO_2 line-mixing. We have evaluated the impact of this spectroscopic effect on the retrieved total columns, using all available observations for 2006. This sensitivity study shows that CCl_4 total columns are on average $(15 \pm 2)\%$ lower $(1-\sigma)$ when line-mixing is included in the forward model. A similar magnitude was reported by Stiller et al. [38] who evaluated the impact of neglecting line-mixing in the retrieval of CCl_4 from infrared limb emission spectra, quoting typical errors of 10–15% around 7 km.

4. Error budget

Table 1 summarizes estimates of important sources of random and systematic errors affecting our retrieved CCl_4 columns, following approaches adopted in a recent study of ISSJ spectra [39]. Main random sources include uncertainties in the NCEP temperature profiles, in the limited signal-to-noise ratios and in the zero offset of the observed spectra. The most important systematic errors are associated with the uncertainties in the spectroscopic parameters of both the targeted CCl_4 and the main interfering gases. The accuracy of the retrieval algorithm, errors resulting from interfering

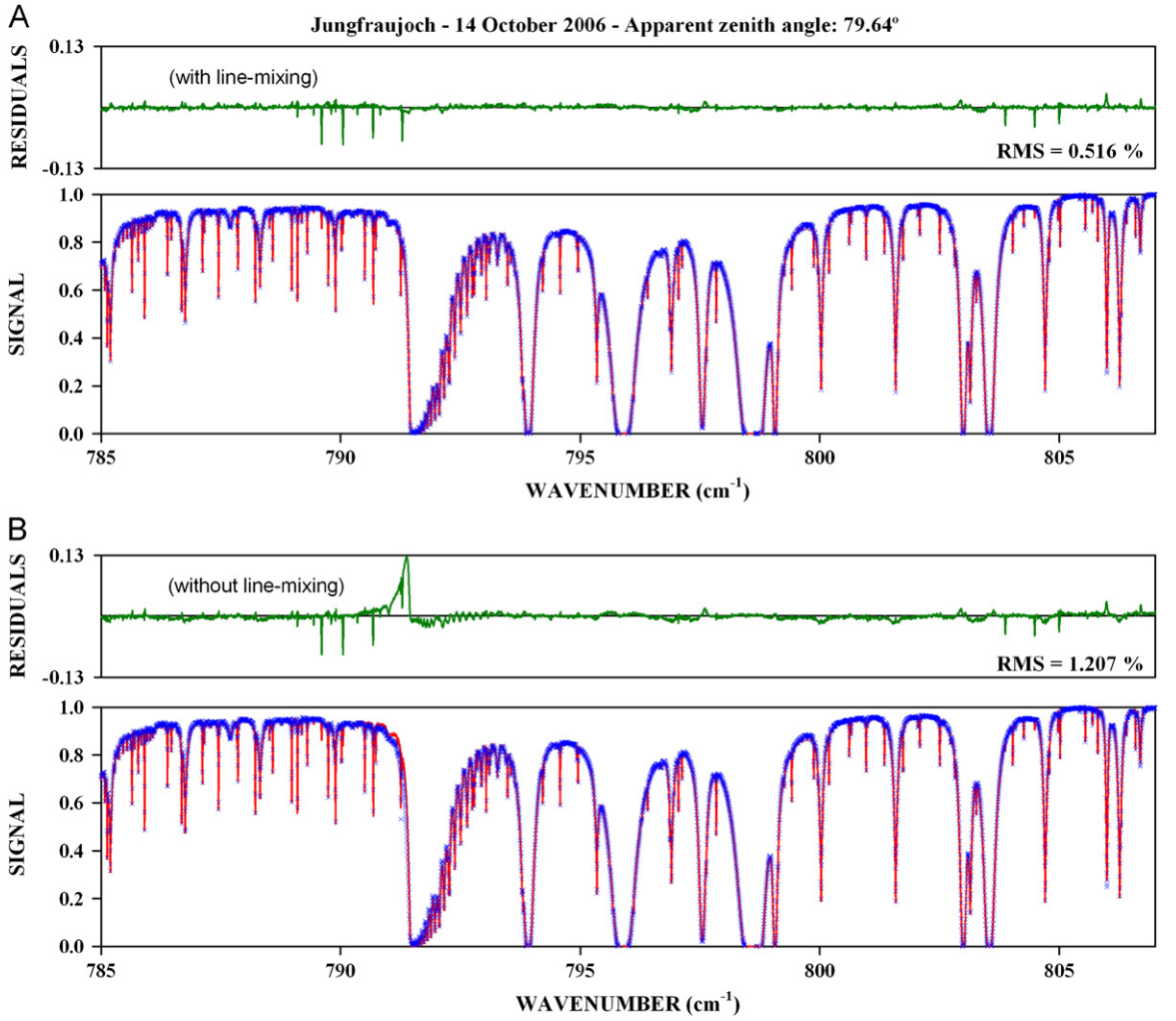

Fig. 3. Sample fits to a solar spectrum recorded on October 14, 2006 at the Jungfraujoch station. The observed and fitted spectra are reproduced in red and blue, respectively. Frame A displays in green the observed minus calculated residuals when accounting for the line mixing in the CO_2 Q branch. This corresponds to a significant improvement when compared to the residuals which were obtained when neglecting this spectroscopic effect (see frame B).

Table 1
Random and systematic sources of uncertainties on the retrieval of CCl_4 total columns above the Jungfraujoch.

Error source	Error type	Maximum relative uncertainty (%)
Finite signal-to-noise	R	4
Temperature profile	R	4
Retrieval algorithm	R	1
Local height variability among interfering gases	R	3
RSS total random		**<7**
Temperature profile	S	2
Retrieval algorithm	S	1
Spectroscopic parameters: CCl_4	S	8
$H_2O+CO_2+O_3$	S	5
Residues of solar OH quadruplets de-weighting	S	1
Instrumental line shape	S	1
CCl_4 *a priori* profile	S	4
Slope biases in profiles of interfering gases	S	3
RSS total systematic		**<11**

*S=systematic, R= random, RSS=square root of the sum of the squares.

atmospheric and solar lines and biases in modeling the ISSJ instrument line shape function, are of minor importance. Brief justifications regarding their estimated magnitudes are given hereafter.

4.1. Temperature profile uncertainty

NCEP quotes the temperature uncertainties as 1.5 K from the ground up to ~20 km, 2 K up to about 30 km, and from 5 to 9 K from ~35 km up to the stratopause. We have imposed such biases to our altitude–pressure–temperature profiles before retrieving CCl_4 total columns from a sample set of ISSJ spectra. For the $-\Delta T$ and the $+\Delta T$ changes, mean relative differences were found equal to +2% and −6%, respectively. Owing to the large asymmetry in these differences, we have realistically split them into −2% systematic and ±4% random. This latter value accounts for occasional imbalances between morning and late afternoon temperatures versus the adopted mid-day NCEP profiles.

4.2. Finite signal-to-noise ratio and zero offset

Individual inspection of all fitted spectra showed that their residuals are commensurate with their respective S/N ratios, and that their zero baseline offset rarely exceeded ±1%. Consequently, and as evaluated by Zander et al. [39], an upper combined random uncertainty of ±4% has been adopted here.

4.3. Spectroscopic parameters

An error of ±4% has been estimated by G. C. Toon (see Section 3) for the conversion into pseudolines of the CCl_4 absorption cross-sections derived by Nemtchinov and Varanasi [13]. In addition, the absorption cross-sections themselves are affected by instrumental uncertainties, which Allen et al. [5] estimated to be as large as 10%. Here, however, as we primarily deal with the strongest CCl_4 absorption feature of the ν_3 band investigated in the laboratory, we have adopted a realistic value of ±4%, which is commensurate with the evaluation of ±5% for the same peak cross-sections studied by Orlando et al. [40]. Therefore, a combined direct systematic bias of about ±8% may affect our CCl_4 total column retrievals. Based on spectroscopic uncertainty estimates documented in the HITRAN compilation, indirect impacts on the CCl_4 columns by the main interfering gases have been evaluated at 1% for O_3, 2% for CO_2, and 4% for H_2O, thus resulting in a combined systematic root square sum (RSS) uncertainty of less than ±5%.

4.4. Retrieval algorithm

The SFIT2 algorithm is widely used by NDACC investigators for partial and or total column retrievals. As in previous papers [23, 24, 41], we have estimated that total columns are retrieved within uncertainties of ±1%, both random and systematic, when dealing with high quality solar spectra, which is the case here.

4.5. Solar lines

Despite de-weighting narrow spectral intervals centered at the locations of the strongest solar OH multiplets, weak perturbations may persist, resulting in a systematic impact on the CCl_4 total column retrievals estimated to be less than ±1%. It should be noticed here that improved modeling parameters of solar OH lines occurring in the region 700 to 4430 cm^{-1} have been reported recently by Hase et al. [42] (based on solar occultation spectra recorded by the ACE-FTS instrument at tangent altitudes above 160 km) but these were not available when performing the overall fitting process for this work.

4.6. Uncertainty in the instrument line shape function

As shown by the sample fittings to the ISSJ spectra (Fig. 3), the instrument line shape is accurately reproduced by taking into account the ISSJ spectral resolution and apodization function, and no line shape asymmetries are observed in the fitting residuals. A systematic bias on the retrieved CCl_4 total columns has been estimated to be less than ±1%.

4.7. Uncertainty in the a priori profile of CCl_4

As noted previously, there remain significant uncertainties in both the *in situ* surface measurements and the vertical profiles from the ACE and MkIV spectra (see Fig. 4 to 6 in [5]). The impact of our chosen CCl_4 *a priori* profile has been evaluated by performing a run with a profile derived from MkIV balloon measurements. On average, the discrepancy amounts to about 4%. Despite the large scatter observed among the MkIV profiles, a systematic error of the same magnitude has been adopted here.

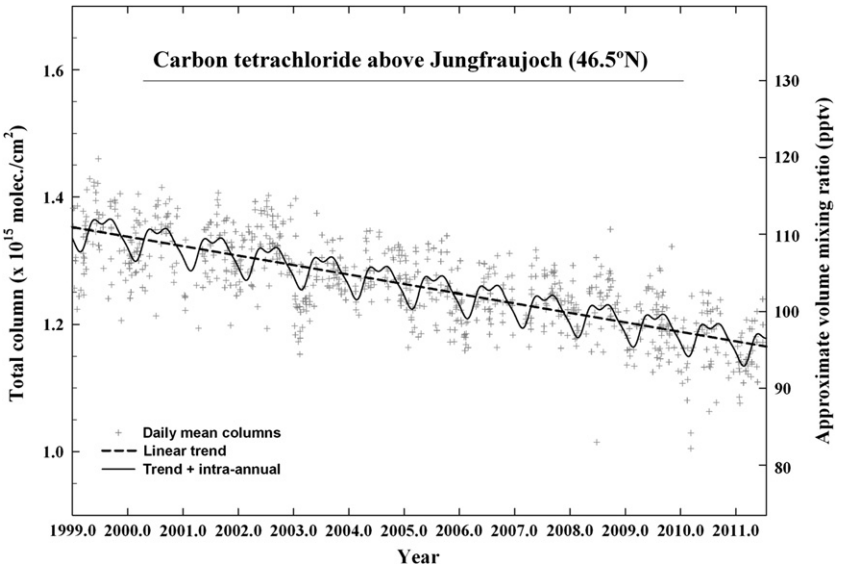

Fig. 4. Daily mean CCl_4 total columns above the Jungfraujoch station are shown as plus symbols. The dashed line shows the linear component of the function fitted to all available daily means. The solid curve reproduces the derived seasonal modulation.

4.8. Uncertainties in the a priori profiles of interfering species

As shown in Fig. 1, the weak broad CCl_4 absorption is overlapped by several strong interfering lines (e.g., H_2O, CO_2, O_3). Possible biases and local altitude dependent perturbations in the adopted *a priori* profiles for these gases introduce additional errors which have been estimated at maximum 3% systematic and 3% random.

4.9. Impact of subsidence

The WACCM *a priori* profile for CCl_4 has been shifted vertically by $+/-2$ layers ($\sim \pm 2$ km at the tropopause level). The impact on the retrieved total columns is negligible and can be omitted in the error budget.

5. Results and discussion

Crosses in Fig. 4 show all our retained daily averaged CCl_4 total columns above ISSJ for the January 1999 to June 2011 time period. This time series was fitted with the bootstrap resampling tool developed by *Gardiner* et al. [43] to determine the CCl_4 long-term linear trend, its uncertainty and the seasonal modulation. In the present case, a six-term Fourier series was adopted to model the intra-annual modulation. The resulting fit is reproduced by a solid curve in Fig. 4, while its linear component is shown as a dashed line. The latter returns a statistically-significant total column long-term trend of $(-1.49 \pm 0.08) \times 10^{13}$ mol/cm^2/yr, at the $2-\sigma$ confidence level. The Fourier coefficient vector as per equation 2 in [43] is equal to $\{-22.077, -13.576, -3.607, -7.771, +5.288, +0.147\}$ in units of 10^{12} mol/cm^2. Using the modeled 1999.0 column as reference, we compute a relative annual trend of (-1.10 ± 0.06)%/yr, still at the $2-\sigma$ confidence level. This column decrease corresponds to a mean tropospheric trend of about -1.3 pptv/yr. Furthermore, fit to the total column data set also reveals a seasonal cycle with a peak-to-peak amplitude of 4.5%, with minimum and maximum values found in mid-February and mid-August, respectively. Our CCl_4 trend for the full 1999-2011 time series is in agreement with the surface station measurements for 2000–2004 (see Table 1–2 in [8]), though as noted in Section 1, calibration differences exist among the surface *in situ* datasets. The weak but statistically-significant seasonal cycle derived from the ISSJ total column measurements is believed to result from residual effects of the seasonal changes in the tropopause height. However, the impact of the strong variation of water vapor throughout the year cannot be ruled out at this time.

A recent analysis of ACE solar occultation spectra recorded between February 2004 and August 2007 at latitudes between 70°S and 80°N reported higher CCl_4 mixing ratios of 100 to 130 pptv in the free troposphere above major industrial regions at 20°N–50°N latitude and near the equator. The zonal CCl_4 distribution from ACE further indicated a slight hemispheric asymmetry and decreasing mixing ratios with increasing altitude at all latitudes. Neglecting the line mixing in the nearby CO_2 Q branch at 791 cm^{-1} and the complexity of the spectrum at low altitudes limited the accuracy in fitting the measured spectra. An overestimation by up to 30% of the ACE mixing ratios was identified after comparison with *in situ* surface mixing ratios [5]. The differences demonstrated that ignoring the CO_2 Q branch line mixing was an important limitation in the accuracy of the ACE retrievals. This was confirmed by further ACE comparisons with calculations by three atmospheric models and balloon limb solar occultation measurements recorded with the Mark IV FTS [44].

A comparison of *in situ* with ISSJ total column results shows commensuration among the retrieved slopes (i.e., (-0.98 ± 0.07)%/yr versus (-1.10 ± 0.06)%/yr, respectively).

Efforts to understand the measurement differences are ongoing (B. Hall, National Oceanic and Atmospheric Administration, private communication, 2010).

6. Summary and conclusions

The trend of carbon tetrachloride (CCl_4) has been derived from infrared high resolution solar absorption spectra encompassing the January 1999 to June 2011 time period and recorded with a Fourier transform spectrometer at the northern mid-latitude Jungfraujoch station in Switzerland. Total columns were derived with the SFIT2 algorithm from a region of the strong CCl_4 ν_3 band at 794 cm^{-1} accounting for over a dozen interfering molecules with improvement in the residuals obtained by also taking into account, for the first time, line mixing in a nearby CO_2 Q branch at 791 cm^{-1}. Fits to the observations are close to the noise level of the measured spectra when line mixing is included in the forward model. A fit to the CCl_4 daily mean total column time series reveals a statistically-significant long-term trend of $(-1.49 \pm 0.08) \times 10^{13}$ mol/cm^2/yr at the $2-\sigma$ confidence level. Using 1999.0 as reference, we compute a relative trend of (-1.10 ± 0.06)%/yr. The measured total column data set also reveals a weak seasonal cycle with a 4.5% peak-to-peak amplitude with minimum and maximum in mid-February and mid-August, respectively. The seasonal modulation is tentatively attributed to tropopause height changes throughout the year. Our fit to the time series shows no significant interannual variations in the trend. This is in agreement with a recent inverse analysis, indicating small interannual variations in the trend based on *in situ* surface station measurements and chemical transport model predictions for the 1996–2004 time period.

A significant high bias of $\sim$10% is obtained when comparing Jungfraujoch CCl_4 column average mixing ratios with those reported at *in situ* surface stations. The cause of this bias remains poorly understood and further work is recommended to reduce the discrepancy among the monitoring techniques involved.

The present Jungfraujoch trend results assess the continued impact of the regulations implemented by the Montreal Protocol and its strengthening amendments for a molecule with high global warming potential, thus also of concern within the frame of the Kyoto Protocol. Although a statistically significant decrease in the total column is inferred, the CCl_4 molecule remains an important contributor to the stratospheric chlorine budget. The capability of deriving the total atmospheric burden of CCl_4 from the spectrometric analysis of high resolution infrared solar spectra recorded regularly at the ground is an important new NDACC challenge for long-term trend monitoring of all key components of the organic chlorine budget, worldwide.

Acknowledgments

Work at Langley was supported by NASA's Upper Atmospheric Chemistry and Modeling Program (ACMAP) and Upper Atmosphere Research Program (UARP). The University of Liège involvement was primarily supported by the Belgian Federal Science Policy Office, Brussels, through the SECPEA, A3C and AGACC-II projects. Emmanuel Mahieu is Research Associate with the F.R.S. – FNRS. We further acknowledge the contributions of the F.R.S. – FNRS and of the Fédération Wallonie-Bruxelles for funding the development and maintainance of the Jungfraujoch laboratory and for supporting travel costs to the station, respectively. We thank the International Foundation High Altitude Research Stations Jungfraujoch and Gornergrat (HFSJG, Bern) for supporting the facilities needed to perform the observations. We are grateful to the many Belgian colleagues who have performed the observations used here.

This paper was initiated and drafted by Curtis P. Rinsland during the last months of 2010, shortly before he passed away on April 20, 2011. We decided to finalize Curtis' present initiative in remembrance and recognition of the numerous research activities which we have had the chance and pleasure to share with him.

References

[1] Zander R, Gunson MR, Farmer CB, Rinsland CP, Irion FW, Mahieu E. The 1985 chlorine and fluorine inventories in the stratosphere based on ATMOS observations at 30°N latitude. J. Atmos. Chem. 1992;15:171–86.

[2] Zander R, Gunson MR, Abrams MC, Chang AY, Irion FW, Mahieu E, et al. The 1994 northern mid-latitude budget of stratospheric chlorine derived from ATMOS/ATLAS 3 observations. Geophys. Res. Lett. 1996;23:2357–60.

[3] Zander R, Mahieu E, Demoulin P, Duchatelet P, Roland G, Servais C, et al. Our changing atmosphere: evidence based on long-term infrared solar observations at the Jungfraujoch since 1950. Sci. Total Environ. 2008;391:184–95, doi:10.1016/j.scitotenv.2007.10.018.

[4] Nassar R, Bernath PF, Boone CD, Clerbaux C, Coheur PF, Dufour G, et al. The global inventory of stratospheric chlorine in 2004. J. Geophys. Res. 2006;111:D22312, doi:10.1029/2006JD007073.

[5] Allen ND, Bernath PF, Boone CD, Chipperfield MP, Fu D, Manney GL, et al. Global carbon tetrachloride distributions obtained from the atmospheric chemistry experiment. Atmos. Chem. Phys. 2009;9:7449–59.

[6] Xiao X, Prinn RG, Fraser PJ, Weiss RS, Simmonds PG, O'Doherty S, et al. Atmospheric three-dimensional inverse modeling of regional industrial emissions and global oceanic uptake of carbon tetrachloride. Atmos. Chem. Phys. 2010;10:10421–34.

[7] Solomon S, Qin D, Manning M, Alley RB, Berntsen T, Bindoff NL, et al. Technical Summary. In: Solomon S, Qin D, Manning M, Chen Z, Marquis M, Averyt KB, Tignor M, Miller HL, editors. Climate Change 2007: The Physical Science Basis. Contribution of Working Group I to the Fourth Assessment Report of the Intergovernmental Panel on Climate Change. Cambridge, United Kingdom and New York, N.Y. USA.: Cambridge University Press; 2007.

[8] World Meteorological Organisation (WMO): Scientific Assessment of Ozone Depletion: 2006, Geneva, Switzerland, Chapter 1: Long-lived compounds, 2007.

[9] World Meteorological Organisation (WMO): Scientific Assessment of Ozone Depletion: 2010, Geneva, Switzerland, Chapter 1: Ozone-Depleting Substances (ODS) and Related Chemicals, 2011.

[10] Martinerie P, Nourtier-Mazauric E, Barnola J-M, Sturges WT, Worton DR, Atlas E, et al. Long-lived halocarbon trends and budgets from atmospheric chemistry modeling constrained with measurements in polar firn. Atmos. Chem. Phys. 2009;9:3911–34.

[11] Forster P., Ramaswamy V., Artaxo P., Berntsen T., Betts R., Fahey D.W., et al. Changes in Atmospheric Constituents and in Radiative Forcing. In: S. Solomon et al., (Eds), Climate Change 2007: The Physical Science Basis. Contribution of Working Group I to the Fourth Assessment Report of the Intergovernmental Panel on Climate Change. Cambridge University Press, Cambridge, UK.

[12] Molina MJ, Rowland FS. Stratospheric sink for chlorofluoromethanes: chlorine atom-catalysed destruction of ozone. Nature 1974;249:810–2.

[13] Nemtchinov V, Varanasi P. Thermal infrared absorption cross-sections of CCl_4 needed for atmospheric remote sensing. JQSRT 2003;82:473–81.
[14] Norton RH, Rinsland CP. ATMOS data processing and science analysis methods. Appl. Opt. 1991;30:388–400.
[15] Brown LR, Gunson MR, Toth RA, Irion FW, Rinsland CP, Goldman A. The 1995 Atmospheric Trace Molecule Spectroscopy experiment (ATMOS) linelist. Appl. Opt. 1996;35:2828–48.
[16] Rothman LS, et al. The HITRAN 2004 molecular spectroscopic database. JQSRT 2005;96:139–204.
[17] Esposito F, Grieco G, Masiello G, Pavese G, Restieri R, Serio C, et al. Intercomparison of line-parameter spectroscopic databases using downwelling spectral radiance. Q. J. R. Meteorol. Soc. 2007;133(S3): 191–202.
[18] Rodgers CD. Characterization and error analysis of profiles retrieved from remote sounding measurements. J. Geophys. Res. 1990;95:5587–95.
[19] Parrish A, Connor BJ, Tsou JJ, McDermid IS, Chu WP. Ground-based microwave monitoring of stratospheric ozone. J. Geophys. Res. 1992;97:2541–6.
[20] Connor BJ, Parrish A, Tsou JJ, McCormick MP. Error analysis for the ground-based microwave measurements during STOIC. J. Geophys. Res. 1995;100:9283–92.
[21] Pougatchev NS, Rinsland CP. Spectroscopic study of the seasonal variation of carbon monoxide vertical distribution above Kitt Peak. J. Geophys. Res. 1995;100:1409–16.
[22] Rinsland CP, Mahieu E, Zander R, Demoulin P, Forrer J, Reimann S. Free tropospheric CO, C_2H_6 and HCN above Central Europe: recent measurements from the Jungfraujoch station including the detection of elevated columns during 1998. J. Geophys. Res. 2000;105: 24,235–49.
[23] Rinsland CP, Goldman A, Connor BJ, Stephen TM, Jones NB, Wood SW, et al. Correlation relationships of stratospheric molecular constituents from high spectral resolution, ground-based infrared solar absorption spectra. J. Geophys. Res. 2000;105:14,637–52.
[24] Rinsland CP, Goldman A, Stephen TM, Chiou LS, Mahieu E, Zander R. SF_6 ground-based infrared solar absorption measurements: long-term trend, pollution events, and a search for SF_5CF_3 absorption. JQSRT 2003;78(1):41–53.
[25] Gallery W.O., Kneizys F.X., Clough S.A. Air mass computer program for atmospheric transmittance/radiance calculation: FSCATM. AFGL-TR-83-0065, Environmental Research Papers No. 828 1983; Air Force Geophysics Lab., Hanscom Air Force Base, MA.
[26] Meier A, Goldman A, Manning PS, Stephen TM, Rinsland CP, Jones NB, et al. Improvements to air mass calculations from ground-based infrared measurements. JQSRT 2004;83:109–13.
[27] Drayson DR. Rapid calculation of the Voigt profile. JQSRT 1976;16: 611–4.
[28] Kochel J-M, Hartmann J-M, Camy-Peyret C, Rodrigues R, Payan S. Influence of line mixing on absorption by CO_2 Q branches in atmospheric balloon-borne spectra near 13 μm. J. Geophys. Res. 1997:12,891–9102 1997:12,891–9.
[29] Strow LL, Tobin DC, Hannon SE. A compilation of first-order line-mixing coefficients for CO_2 Q branches. JQSRT 1994;52:281–94.
[30] Funke B, Stiller GP, von Clarmann T, Echele G, Fischer H. CO_2 line mixing in MIPAS limb emission spectra and its influence on retrievals of atmospheric parameters. JQSRT 1998;59:215–30.
[31] Rinsland CP, Strow LL. Line mixing effects in solar occultation spectra of the lower stratosphere: measurements and comparisons with calculations for the 1932 cm^{-1} CO_2 Q branch. Appl. Opt. 1989;28:457–64.
[32] Niro F, Jucks KW, Hartmann J-M. Spectra calculations in central and wing regions of CO_2 IR bands. IV: software and database for the computation of atmospheric spectra. JQSRT 2005;95:469–81.
[33] Niro F, Boulet C, Hartmann J-M, Lellouch E. The effect of line-mixing in CO_2 near 15 μm on the emission of Mars atmosphere. JQSRT 2005;95:483–7.
[34] Hartmann J-M, Tran H, Toon GC. Influence of line mixing on the retrievals of atmospheric CO_2 from spectra in the 1.6 and 2.1 μm regions. Atmos. Chem. Phys. 2009;9:7303–12.
[35] Hartmann J-M, Boulet C, Robert D. Collisional Effects on molecular spectra. Laboratory experiments and models, consequences for applications. Amsterdam: Elsevier; 2008.
[36] Chang L, Palo S, Hagan M, Richter J, Garcia R, Riggin D, et al. Structure of the migrating diurnal tide in the Whole Atmosphere Community Climate Model (WACCM). Adv. Space Res. 2008;41(9): 1397–406, doi:10.1016/j.asr.2007.03.035.
[37] Rodrigues R, Jucks KW, Lacome N, Blanquet G, Walrand J, Traub WA, et al. Model, software, and database for computation of line-mixing effects in infrared Q branches of atmospheric CO_2 – I. Symmetric isotopomers. JQSRT 1999;61:153–84.
[38] Stiller GP, von Clarmann T, Funke B, Glatthor N, Hase F, Höpfner M, et al. Sensitivity of trace gas abundances retrievals from infrared limb emission spectra to simplifying approximations in radiative transfer modeling. JQSRT 2002;72:249–80.
[39] Zander R, Duchatelet P, Mahieu E, Demoulin P, Roland G, Servais C, et al. Formic acid above the Jungfrauoch during 1985–2007: observed variability, seasonality, but no long-term background evolution. Atmos. Chem. Phys. 2010;10:10047–65, doi: 10.5194/acp-10-10047-2010.
[40] Orlando JJ, Tyndall GS, Huang A, Calvert JG. Temperature dependence of the infrared absorption cross sections of carbon tetrachloride. Geophys. Res. Lett. 1992;19:1005–8.
[41] Rinsland CP, Mahieu E, Chiou LS, Herbin H. First ground-based infrared solar absorption measurements of free tropospheric methanol (CH_3OH): multidecade infrared time series from Kitt Peak (31.9°N 111.6°W): trend, seasonal cycle, and comparison with previous measurements. J. Geophys. Res. 2009;114:D04309, doi: 10.1029/2008JD011003.
[42] Hase F, Wallace L, McCloud SD, Harrison JJ, Bernath PF. The ACE-FTS atlas of the infrared solar spectrum. JQSRT 2010;111:521–8.
[43] Gardiner T, Forbes A, De Mazière M, Vigouroux C, Mahieu E, Demoulin P, et al. Trend analysis of greenhouse gases over Europe measured by a network of ground-based remote Fourier transform spectrometer instruments. Atmos. Chem. Phys. 2008;8 6719–2727.
[44] Toon GC, Blavier J-F, Sen B, Margitan JJ, Webster CR, May RD, et al. Comparison of MkIV balloon and ER-2 aircraft measurements of atmosphericrtrace gases. J. Geophys. Res. 1999;104:26779–90, doi: 10.1029/1999JD900379.

Atmos. Meas. Tech., 5, 161–180, 2012
www.atmos-meas-tech.net/5/161/2012/
doi:10.5194/amt-5-161-2012
© Author(s) 2012. CC Attribution 3.0 License.

Atmospheric Measurement Techniques

Information operator approach applied to the retrieval of the vertical distribution of atmospheric constituents from ground-based high-resolution FTIR measurements

C. Senten, M. De Mazière, G. Vanhaelewyn, and C. Vigouroux

Belgian Institute for Space Aeronomy (BIRA-IASB), Ringlaan 3, 1180 Brussels, Belgium

Correspondence to: C. Senten (cindy.senten@aeronomie.be)

Received: 5 April 2011 – Published in Atmos. Meas. Tech. Discuss.: 14 June 2011
Revised: 8 November 2011 – Accepted: 22 December 2011 – Published: 16 January 2012

Abstract. The analysis of high spectral resolution Fourier Transform infrared (FTIR) solar absorption spectra is an important issue in remote sensing. If this is done carefully, one can obtain information, not only about the total column abundances, but also about the vertical distribution of various constituents in the atmosphere. This work introduces the application of the information operator approach for extracting vertical profile information from ground-based FTIR measurements. The algorithm is implemented and tested within the well-known retrieval code SFIT2, adapting the optimal estimation method such as to take into account only the significant contributions to the solution. In particular, we demonstrate the feasibility of the method in an application to ground-based FTIR spectra taken in the framework of the Network for the Detection of Atmospheric Composition Change (NDACC) at Ile de La Réunion (21° S, 55° E). A thorough comparison is made between the original optimal estimation method, Tikhonov regularization and this alternative retrieval algorithm, regarding information content, retrieval robustness and corresponding full error budget evaluation for the target species ozone (O_3), nitrous oxide (N_2O), methane (CH_4), and carbon monoxide (CO). It is shown that the information operator approach performs well and in most cases yields both a better accuracy and stability than the optimal estimation method. Additionally, the information operator approach has the advantage of being less sensitive to the choice of a priori information than the optimal estimation method and Tikhonov regularization. On the other hand, in general the Tikhonov regularization results seem to be slightly better than the optimal estimation method and information operator approach results when it comes to error budgets and column stability.

1 Introduction

Since 2002 the Belgian Institute for Space Aeronomy (BIRA-IASB) has been responsible for measurements of high-resolution ground-based FTIR solar absorption spectra at the Observatoire de Physique de l'Atmosphère de La Réunion (OPAR). This station is located at 21° S, 55° E, in the Indian Ocean, East of Madagascar, at the edge between the southern tropics and subtropics and it is coordinated by the Laboratoire de l'Atmosphère et des Cyclones (LACy) of the Université de La Réunion. These FTIR observations contribute to the worldwide survey of the evolution of the atmospheric composition and structure, in the framework of NDACC (Kurylo and Solomon, 1990; Kurylo, 1991). It is therefore fundamental to extract as much information as possible about the vertical distribution of the target atmospheric constituents absorbing within the FTIR spectral ranges, and to make sure that the knowledge gained is reliable. The vertical profile information can be derived from the line shape of the absorption lines via the altitude dependence of the pressure broadening.

The analyses shown here focus on the atmospheric species ozone (O_3), nitrous oxide (N_2O), methane (CH_4) and carbon monoxide (CO). These gases have been selected for several reasons. First, they are mandatory species within the NDACC Infrared Working Group (IRWG), because of their important roles in tropospheric and stratospheric chemistry and their link to current environmental problems like climate change and stratospheric ozone depletion. Second, at Ile de La Réunion, CO is an important tracer of biomass burning. Additional arguments to study these trace gases are that they have different numbers of degrees of freedom for signal

(Sect. 2.2.2) and that they are very much wanted for satellite validation.

Within the NDACC IRWG it is common to use the optimal estimation method (OEM) (Rodgers, 2000) or Tikhonov regularization (TR) (Tikhonov, 1963) to solve the inverse problem. Nevertheless, in some cases one may encounter problems like vertical profile instability or physically unrealistic retrieval results. Looking for a more robust inversion method in order to eliminate these difficulties has led us to the information operator approach (IOA) (Doicu et al., 2007), which has been proved successful for the inversion of satellite data by Hoogen et al. (1999). The fact that the IOA is by definition based on the genuine information content of the measurements makes it presumable that the method improves the stability of the retrievals – avoiding spurious profile oscillations –, that it gives a more realistic idea of the actual information content that can be acquired, and that it generates smaller error budgets. As the IOA has never before been applied to spectra measured from the ground, it is very useful to test its feasibility for ground-based FTIR observations and to verify its possibilities with respect to the OEM and TR. In order to perform the retrievals of the above-mentioned trace gases with the IOA, we implemented this new algorithm into the retrieval code SFIT2 (v3.94), jointly developed at the NASA Langley Research Center, the National Center for Atmospheric Research (NCAR) and the National Institute of Water and Atmosphere Research (NIWA) (Rinsland et al., 1998; Hase et al., 2004).

The paper is organised as follows: Sect. 2 provides a theoretical description of the IOA retrieval method, while Sect. 3 shows the retrieval results and error budget evaluations for the target species obtained from the above mentioned FTIR spectra, when applying the OEM, IOA and TR. Section 4 discusses the influence of the a priori information on the OEM, IOA and TR results. Section 5 describes a theoretical study of the three methods based on synthetic spectra. Conclusions are given in Sect. 6.

2 General description of the information operator approach

The problem we are facing is the retrieval of the vertical distribution of target atmospheric species from ground-based high-resolution solar absorption spectra. The commonly used algorithm, SFIT2, is based on a semi-empirical implementation of the OEM of Rodgers (2000). Applying the IOA onto the OEM is an efficient way of automatically using only those components of the measurements that effectively contribute to the final information content, prior to knowing how much information you can get and where it is situated. How this can be achieved is explained in Sect. 2.2.

2.1 Forward model

The forward model in SFIT2 is a multi-layer multi-species line-by-line radiative transfer model and remains unchanged when applying the IOA. The instrument parameters in the forward model include a wavenumber scale multiplier and background curve parameters, as well as the actual optical path difference and field of view of the instrument. To account for deviations from the ideal instrument line shape (ILS) function due to small instrument misalignments or imperfections, empirical apodization and phase error functions are included in the forward calculations. These calculations are executed on a fine altitude grid to take into account the local atmospheric pressure and temperature variabilities.

2.2 Inverse model

The inverse problem consists of determining the best representation of the true state of the atmosphere from the observed absorption spectra, more specifically, the vertical distributions and total column amounts of the target molecules. In order to solve this ill-posed problem, some regularization within the ensemble of possible solutions is required. To enhance the performance of the standard SFIT2 retrieval code, results from information theory can be taken into account explicitly. We now present the theoretical background of this adapted optimal estimation scheme incorporating the IOA, as well as its implementation in the SFIT2 algorithm.

2.2.1 Adapted retrieval method

First note that the retrieval of vertical profiles from FTIR data is an underconstrained problem, because of the following reasons: (1) a profile is a continuous function of altitude, whereas an FTIR spectrometer provides measurements only at a discrete number of wavelengths; and (2) there are components in the actual profile which do not contribute to the measurements and, consequently, cannot be determined from them. In order to numerically solve the inverse problem, the profile is discretized to a finite number of height levels between which it is assumed to be a linear function of altitude. Additional information is needed to get a physically reasonable result. In particular, when using the OEM, a priori knowledge about the atmospheric trace gas distributions is used to adequately constrain the retrieved profile.

Since the vector of transmittances of the observed solar absorption spectrum within the ranges of the fitted microwindow(s) is a nonlinear function of the atmospheric state, the retrieval solution has to be found iteratively. In the iteration step $i+1$ the optimal estimation solution can be written as (Rodgers, 2000):

$$\boldsymbol{x}_{i+1} = \boldsymbol{x}_{\mathrm{a}} + (\mathbf{K}_i^{\mathrm{T}} \mathbf{S}_y^{-1} \mathbf{K}_i + \mathbf{S}_{\mathrm{a}}^{-1})^{-1} \mathbf{K}_i^{\mathrm{T}} \mathbf{S}_y^{-1} [\boldsymbol{y} - \boldsymbol{y}_i + \mathbf{K}_i (\boldsymbol{x}_i - \boldsymbol{x}_{\mathrm{a}})], \quad (1)$$

where $\boldsymbol{x}_{\mathrm{a}}$ is the a priori atmospheric state vector (of dimension N), $\mathbf{S}_{\mathrm{a}}$ is the a priori covariance matrix, $\boldsymbol{y}$ is the

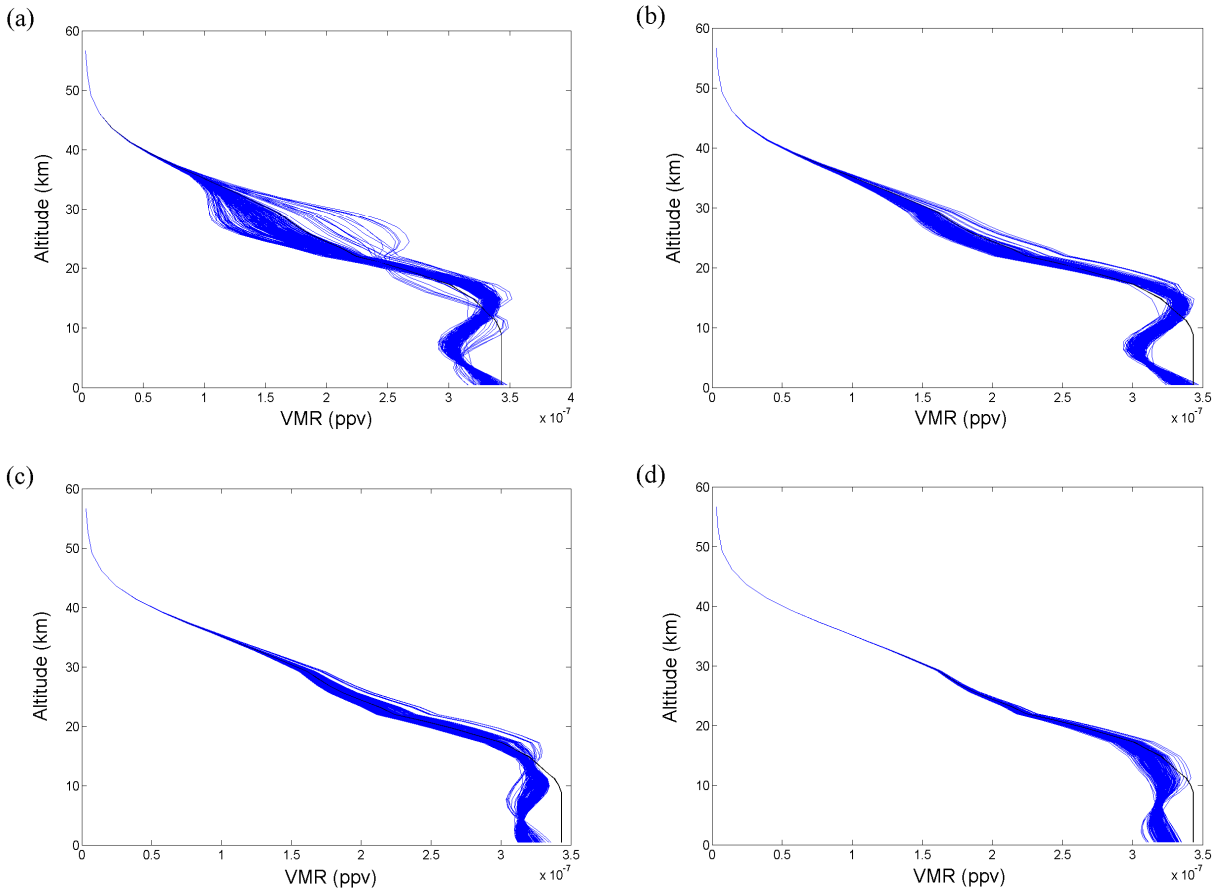

Fig. 1. N_2O profiles from all spectra taken at St.-Denis during the 2007 campaign, retrieved with the **(a)** OEM and with the IOA with threshold **(b)** 0.09, **(c)** 0.79 and **(d)** 0.99, respectively. The black line corresponds to the a priori profile used.

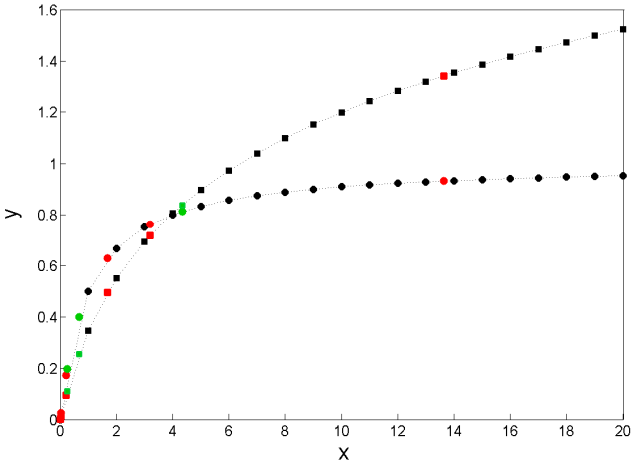

Fig. 2. Curves of $y = x / (1 + x)$ (black circles) and $y = 1/2 \ln (1 + x)$ (black squares) for x between 0 and 20 and for the eigenvalues of $\mathbf{P}_r$ that lay within this domain, for O_3 (red) and CO (green).

measurement vector (of dimension M), $\boldsymbol{y}_i$ is the same quantity calculated by the forward model using the result $\boldsymbol{x}_i$ from the previous iteration i, $\mathbf{S}_y$ is the measurement error covariance matrix, and $\mathbf{K}_i$ is the weighting function matrix, defined as $\delta \boldsymbol{y}/\delta \boldsymbol{x}$, after the i-th iteration. When convergence has occurred, the result of the last iteration is identified with the retrieval solution $\boldsymbol{x}_r$. The corresponding solution covariance matrix is then given by (Rodgers, 2000):

$$\mathbf{S}_r = (\mathbf{K}_r^T \mathbf{S}_y^{-1} \mathbf{K}_r + \mathbf{S}_a^{-1})^{-1}. \quad (2)$$

As mentioned in Sect. 2.1, $\boldsymbol{y}$ is not only influenced by the target species' absorption but also by several other parameters, such as the background curve and wavelength shift parameters, the empirical apodization and phase error polynomial function parameters, and the interfering species' absorptions. By including these additional fit parameters in the state vector $\boldsymbol{x}$, the target profile retrievals can be improved significantly. Note that the number of elements in $\boldsymbol{x}$ is much larger than the number of independent elements that can be retrieved from the measurement. Moreover, in practice, the number of independent retrieved parameters is even smaller due to inevitable measurement noise. Theoretically,

Table 1. Retrieval characteristics for each target species, for the 2007 FTIR campaign at Ile de La Réunion. The variances represent the diagonal elements of $\mathbf{S}_a$ and HWHM the applied inter-layer correlation length of a Gaussian probability distribution. The last three columns list the spectral micro-windows that are fitted simultaneously, the associated spectral resolution (depending on the optical filter and on the target gas), and the main interfering species, respectively.

Molec.	Variance [%]	HWHM [km]	Micro-window(s) [cm^{-1}]	Resol. [cm^{-1}]	Interf. species
O_3	10	4	1000.00–1005.00	0.0072	H_2O, CO_2, C_2H_4, O_3^{668}, O_3^{686}
N_2O	10	5	2481.30–2482.60 2526.40–2528.20 2537.85–2538.80 2540.10–2540.70	0.00513	CO_2, CH_4, O_3, H_2O, HDO
CH_4	variable*	5	2613.70–2615.40 2650.60–2651.30 2835.50–2835.80 2903.60–2904.03 2921.00–2921.60	0.00513	HDO, H_2O, CO_2, NO_2
CO	20	4	2057.70–2057.91 2069.55–2069.72 2140.40–2141.40 2157.40–2159.20 2165.37–2165.85 2168.84–2169.02	0.0036	O_3, OCS, CO_2, N_2O, H_2O, solar CO lines

* Ranging from 4 to 70 %, as a function of altitude.

Table 2. Evolution of 1/2 ln $(1+\lambda_{r,n})$ and $\lambda_{r,n}$ / $(1+\lambda_{r,n})$ for the largest 24 eigenvalues $\lambda_{r,n}$ of the Kozlov information matrix $\mathbf{P}_r$, for O_3, N_2O, CH_4 and CO.

	O_3		N_2O		CH_4		CO	
n	$1/2\ln(1+\lambda_{r,n})$	$\lambda_{r,n}/(1+\lambda_{r,n})$	$1/2\ln(1+\lambda_{r,n})$	$\lambda_{r,n}/(1+\lambda_{r,n})$	$1/2\ln(1+\lambda_{r,n})$	$\lambda_{r,n}/(1+\lambda_{r,n})$	$1/2\ln(1+\lambda_{r,n})$	$\lambda_{r,n}/(1+\lambda_{r,n})$
1	17.3168	1.0000	15.6414	1.0000	15.4139	1.0000	15.5225	1.0000
2	11.3409	1.0000	9.0650	1.0000	15.3273	1.0000	15.3972	1.0000
3	7.1326	1.0000	6.1980	1.0000	15.0916	1.0000	15.0273	1.0000
4	6.8262	1.0000	5.4902	1.0000	14.5332	1.0000	14.4747	1.0000
5	4.7069	0.9999	4.9038	0.9999	14.4930	1.0000	14.3777	1.0000
6	4.5662	0.9999	4.7459	0.9999	11.0533	1.0000	13.8888	1.0000
7	4.2232	0.9998	4.3099	0.9998	7.0866	1.0000	11.9066	1.0000
8	3.7078	0.9994	4.2361	0.9998	4.8829	1.0000	8.5702	1.0000
9	2.8993	0.9970	4.0495	0.9997	4.4885	0.9999	6.5113	1.0000
10	2.6263	0.9948	3.9281	0.9996	4.4172	0.9999	5.8351	1.0000
11	2.3000	0.9899	3.6862	0.9994	4.1455	0.9999	5.7922	1.0000
12	1.3416	0.9317	3.3634	0.9988	3.4401	0.9997	5.5019	1.0000
13	0.7166	0.7615	2.9367	0.9972	3.3155	0.9990	5.1528	1.0000
14	0.4941	0.6278	2.7310	0.9958	2.3465	0.9987	4.6797	0.9999
15	0.0942	0.1717	2.4667	0.9928	2.0997	0.9908	4.4398	0.9999
16	0.0133	0.0262	2.1979	0.9877	1.4615	0.9850	4.2783	0.9998
17	0.0031	0.0062	0.9955	0.8634	1.4586	0.9462	3.8915	0.9996
18	0.0023	0.0046	0.3338	0.4871	0.0342	0.1469	2.5302	0.9937
19	0.0003	0.0006	0.0869	0.1595	0.0342	0.1469	2.3931	0.9917
20	0.00007	0.0001	0.0840	0.1546	0.0060	0.0120	2.0579	0.9837
21	0.000006	0.00001	0.0124	0.0244	0.0060	0.0120	1.7362	0.9690
22	0.000003	0.000006	0.0012	0.0023	0.0002	0.0004	0.8377	0.8128
23	0.0000009	0.000002	0.0001	0.0003	0.0002	0.0004	0.2552	0.3998
24	0.00000006	0.0000001	0.0001	0.0003	0.00004	0.00007	0.1099	0.1973

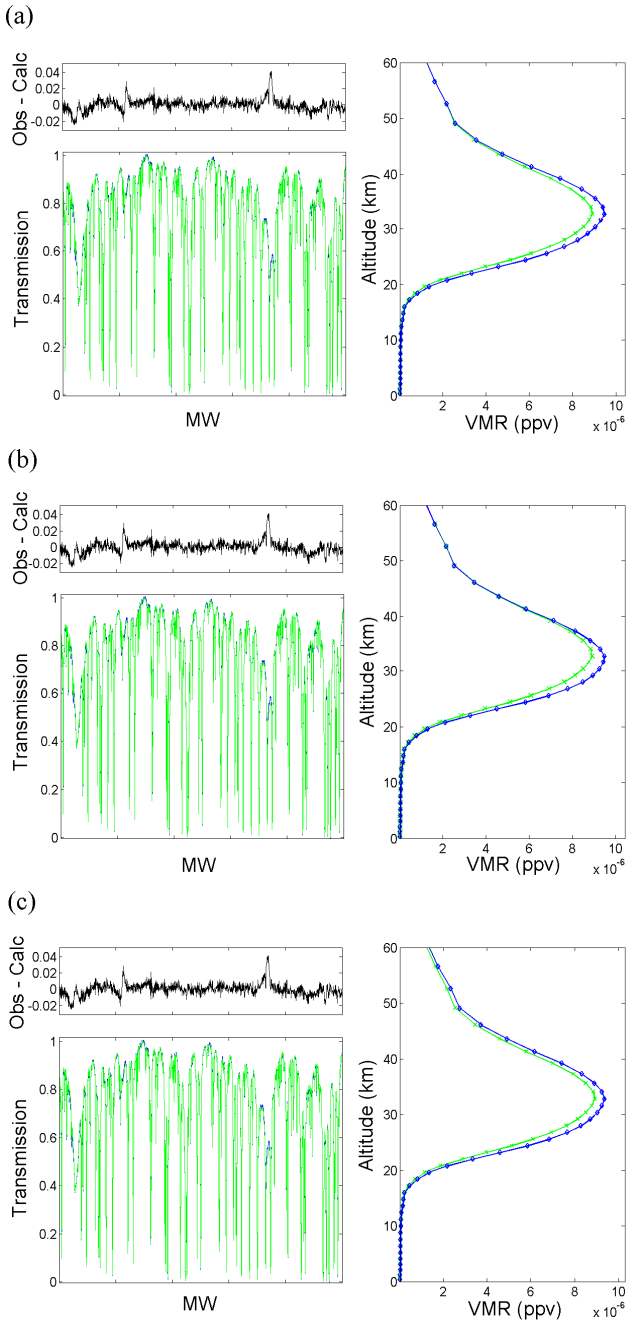

Fig. 3. Single micro-window (1000.00–1005.00 cm^{-1}) fit of O_3 plus interfering species from a single spectrum on 12 September 2007 at St.-Denis using the **(a)** OEM, **(b)** IOA and **(c)** TR. Measured (blue) and simulated (green) spectra are shown (left lower plot), together with the residuals (left upper plot), computed as measured minus simulated. The right plot shows the a priori (green crosses) and retrieved (blue diamonds) profile.

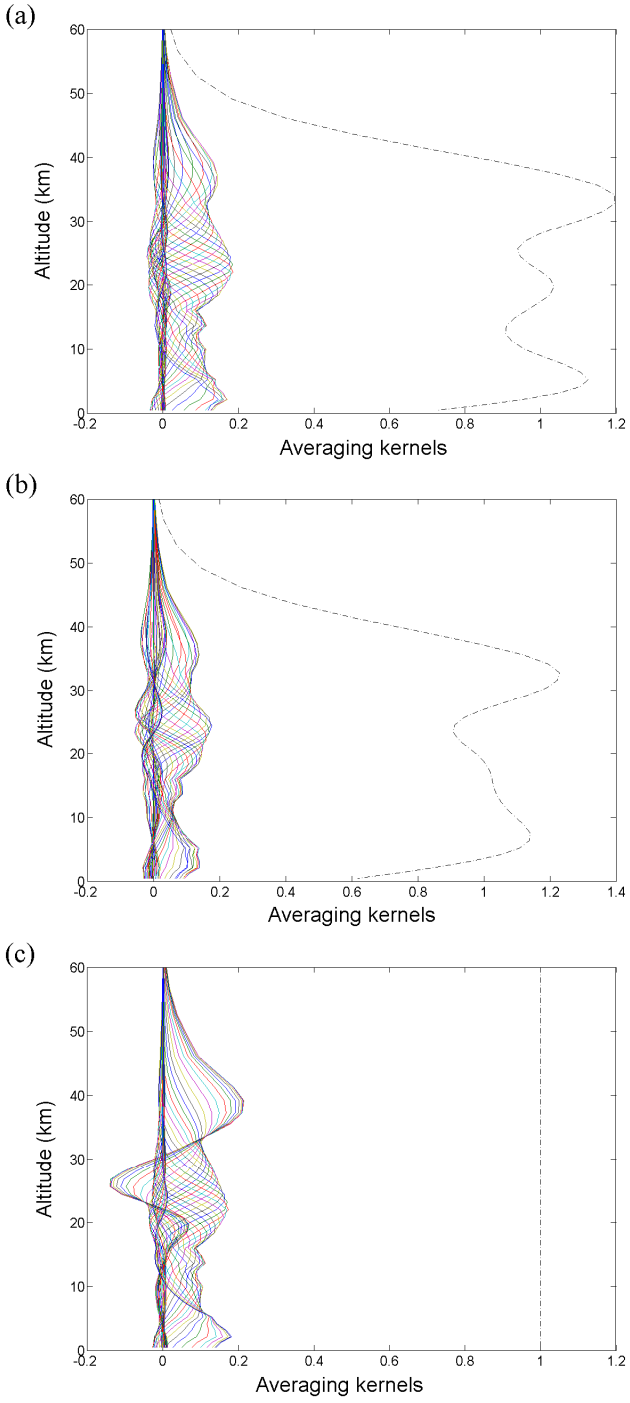

Fig. 4. Averaging kernels and sensitivity curve (black dashed) for the O_3 retrieval from a single spectrum on 12 September 2007 at St.-Denis using the **(a)** OEM, **(b)** IOA and **(c)** TR.

the information content of the measurement can be defined as the reduction in entropy of the a posteriori knowledge about the atmospheric state with respect to the a priori knowledge (Shannon and Weaver, 1949). Under the assumption that $\boldsymbol{x}_a$ and $\boldsymbol{x}_r$ are Gaussian distributed, the information content H of a measurement can be shown to be (Rodgers, 2000):

$$H = 1/2\ln[\det(\mathbf{S}_a)] - 1/2\ln[\det(\mathbf{S}_r)]. \quad (3)$$

Using the definition $\mathbf{P}_r = \mathbf{S}_a\mathbf{G}_r$, with $\mathbf{G}_r = \mathbf{K}_r^T\,\mathbf{S}_y^{-1}\,\mathbf{K}_r$, Eq. (3) can be rewritten as:

$$\begin{aligned} H &= 1/2\ln[\det(\mathbf{S}_a\mathbf{S}_r^{-1})] \\ &= 1/2\ln[\det(\mathbf{P}_r + \mathbf{I})] \\ &= 1/2\sum_{n=1}^{N}\ln(\lambda_{r,n}+1), \end{aligned} \quad (4)$$

where $\lambda_{r,n}$ $(n = 1,\ldots, N)$ are the eigenvalues of the $N \times N$ matrix $\mathbf{P}_r$, the so-called "Kozlov information matrix" (Kozlov, 1983). These eigenvalues thus represent the information content in the measurement, while the corresponding eigenvectors form a basis for the solution space. Hence, only the N_{opt} eigenvalues with a relevant contribution to the information content, i.e. $1/2\ln(\lambda_{r,n} + 1) \geq 1$ or $\lambda_{r,n}/(1 + \lambda_{r,n}) \approx 1$ $(n = 1,\ldots, N_{opt} \leq N)$, should be taken into account. The associated eigenvectors $\boldsymbol{\phi}_{r,n}$ $(n = 1,\ldots, N_{opt})$ span the effective state space accessible with the measurement. Therefore, the IOA retrieval results directly depend on the information content of the measurement by expanding – in each iteration – the difference between the a priori and the true state vector into a series of the significant eigenvectors of $\mathbf{P}_i$. This gives the following equation:

$$\boldsymbol{x}_{i+1} - \boldsymbol{x}_a = \sum_{n=1}^{N_{opt}} \beta_{i,n}\boldsymbol{\phi}_{i,n}. \quad (5)$$

Now, instead of the state vector $\boldsymbol{x}_{i+1}$ itself, the coefficients $\beta_{i,n}$ have to be determined. In Hoogen et al. (1999) some straightforward calculations lead to the derivation of the expansion coefficients $\beta_{i,n}$ $(n = 1,\ldots, N_{opt})$:

$$\begin{aligned} \beta_{i,n} = \lambda_{i,n}/[N_{i,n}(1+\lambda_{i,n})]\boldsymbol{\phi}_{i,n}^T\mathbf{K}_i^T\mathbf{S}_y^{-1}[\boldsymbol{y} - \boldsymbol{y}_i \\ + \mathbf{K}_i(\boldsymbol{x}_i - \boldsymbol{x}_a)], \end{aligned} \quad (6)$$

where $N_{i,n} = \boldsymbol{\phi}_{i,n}^T\mathbf{K}_i^T\mathbf{S}_y^{-1}\mathbf{K}_i\,\boldsymbol{\phi}_{i,n}$ $(n = 1,\ldots, N_{opt})$ are normalization factors defined as such.

In our implementation the calculation of the eigenvectors and eigenvalues of $\mathbf{P}_i$ is based on the common QR method (Golub and Van Loan, 1983), i.e. the matrix $\mathbf{P}_i$ is iteratively decomposed into the product of an orthogonal matrix $\mathbf{Q}$ and an upper triangular matrix $\mathbf{R}$, until the method converges and all eigenvalues and eigenvectors are determined. As the repeated QR factorizations can be quite expensive, the real non-symmetric matrix $\mathbf{P}_i$ is first reduced to the simpler upper Hessenberg form, i.e. having zero entries below the first subdiagonal, and then the similarity transformations are accumulated.

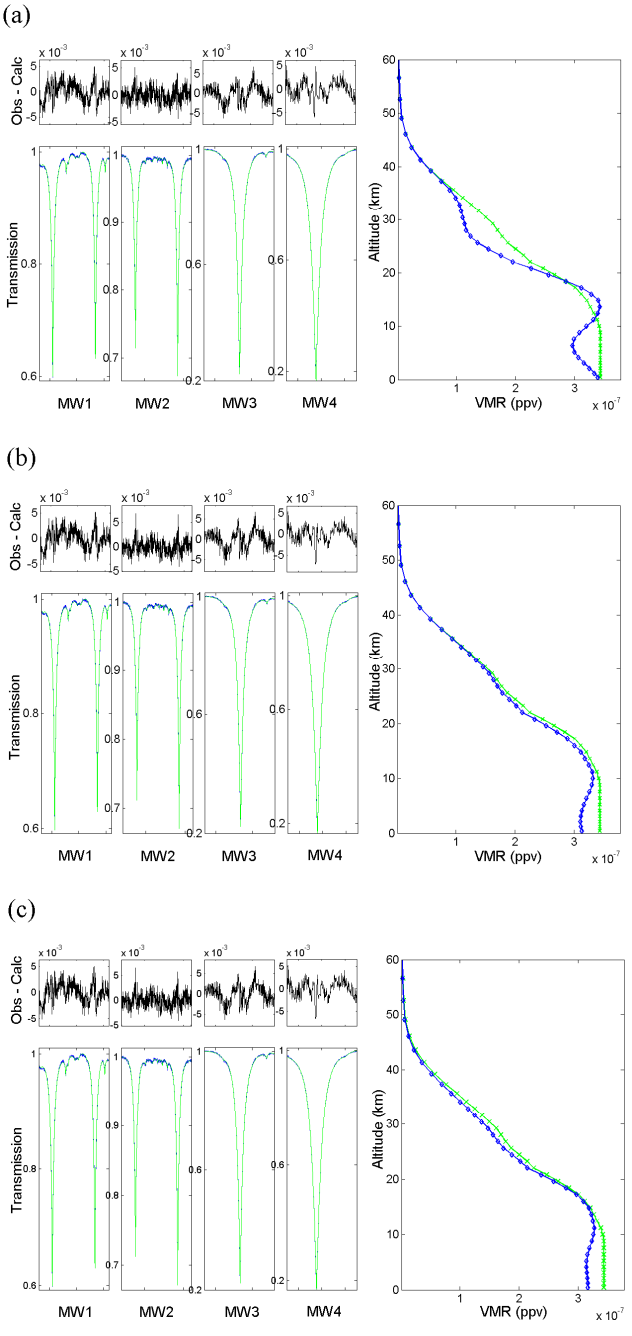

Fig. 5. Multiple micro-window (MW1: 2481.30–2482.60, MW2: 2526.40–2528.20, MW3: 2537.85–2538.80, and MW4: 2540.10–2540.70 cm^{-1}) fit of N_2O plus interfering species from a single spectrum on 8 October 2007 at St.-Denis using the **(a)** OEM, **(b)** IOA and **(c)** TR. Measured (blue) and simulated (green) spectra are shown (left lower plot), together with the residuals (left upper plot), computed as measured minus simulated. The right plot shows the a priori (green crosses) and retrieved (blue diamonds) profile.

Table 3. Date, OBP and SZA of the reference spectra for O_3, N_2O, CH_4 and CO measured at Ile de La Réunion in 2007, together with the RMS of the fit residual, DOFS and independent PC limits when using the OEM, IOA and TR.

Molec.	Date	OBP [cm^{-1}]	SZA	Meth.	RMS	DOFS	PC limits [km]
O_3	12 September	600–1400	51.83	OEM	1.01	4.68	0.05–7.0–19.0–26.2–100
				IOA	1.02	3.92	0.05–9.4–21.4–29.8–100
				TR	1.01	4.64	0.05–7.0–19.0–27.4–100
N_2O	8 October	2400–3310	42.03	OEM	0.18	3.35	0.05–4.6–13.0–100
				IOA	0.19	2.87	0.05–5.8–15.4–100
				TR	0.18	2.91	0.05–5.8–15.4–100
CH_4	2 October	2400–3310	46.43	OEM	0.29	2.32	0.05–8.2–100
				IOA	0.30	2.06	0.05–9.4–100
				TR	0.30	2.29	0.05–9.4–100
CO	29 July	1850–2750	42.19	OEM	0.39	3.04	0.05–2.6–9.4–100
				IOA	0.39	2.81	0.05–2.6–9.4–100
				TR	0.39	3.09	0.05–2.6–9.4–100

Table 4. Mean RMS of the fit residual, mean ITER, mean DOFS, total altitude range and common independent PC ranges, mean CA, and mean daily relative STD on the CA for the retrievals of O_3, N_2O, CH_4 and CO, from the 2007 campaign data at Ile de La Réunion, when using the OEM, IOA and TR.

Molec.	RMS OEM / IOA / TR	ITER OEM / IOA / TR	DOFS OEM / IOA / TR	Alt. range [km]	CA [10^{18} molec cm^{-2}] OEM / IOA / TR	STD [%] OEM / IOA / TR
O_3	0.86 / 0.87 / 0.86	7 / 7 / 7	4.6 / 3.9 / 4.6	0.05–100	7.90 / 7.90 / 7.90	0.32 / 0.35 / 0.31
				0.05–9.4	0.74 / 0.72 / 0.74	0.90 / 0.99 / 0.89
				9.4–21.4	1.33 / 1.32 / 1.34	0.98 / 1.38 / 0.99
				21.4–29.8	3.84 / 3.87 / 3.83	0.57 / 0.61 / 0.54
				29.8–100	1.99 / 1.98 / 1.99	0.88 / 1.02 / 0.74
N_2O	0.15 / 0.15 / 0.15	9 / 5 / 5	3.1 / 2.9 / 2.9	0.05–100	6.67 / 6.66 / 6.66	0.060 / 0.058 / 0.053
				0.05–5.8	3.48 / 3.43 / 3.44	0.29 / 0.16 / 0.16
				5.8–15.4	2.54 / 2.59 / 2.58	0.37 / 0.19 / 0.17
				15.4–100	0.64 / 0.64 / 0.64	0.53 / 0.24 / 0.29
CH_4	0.29 / 0.28 / 0.28	9 / 6 / 6	2.2 / 2.1 / 2.3	0.05–100	36.5 / 37.1 / 36.9	0.48 / 0.29 / 0.22
				0.05–9.4	25.1 / 25.8 / 25.5	0.41 / 0.72 / 0.30
				9.4–100	11.4 / 11.3 / 11.4	1.01 / 0.73 / 0.28
CO	0.44 / 0.45 / 0.44	7 / 7 / 7	3.1 / 2.8 / 3.0	0.05–100	1.67 / 1.67 / 1.66	0.73 / 0.75 / 0.73
				0.05–2.6	0.51 / 0.49 / 0.49	2.39 / 2.45 / 2.00
				2.6–9.4	0.72 / 0.75 / 0.76	2.42 / 2.13 / 1.47
				9.4–100	0.44 / 0.43 / 0.40	1.66 / 1.71 / 1.23

It is obvious that this "eigenvector approach" uses a priori information in the same statistical sense as the original optimal estimation method. Though, it has the advantage that only those components are considered about which the measurement actually provides information. In addition, since basically only a linear combination of the significant eigenvectors has to be calculated and since the QR method is very efficient and numerically stable, the IOA is expected to encounter fewer singularity problems than the OEM and TR.

2.2.2 Information content and sensitivity

The retrieved state vector $\boldsymbol{x}_r$ is related to the a priori and the true state vectors $\boldsymbol{x}_a$ and $\boldsymbol{x}$, respectively, by the equation (Rodgers, 2000):

$$\boldsymbol{x}_r = \mathbf{x}_a + \mathbf{A}\,(\mathbf{x} - \mathbf{x}_a), \tag{7}$$

where $\mathbf{A}$ is defined as $\delta\boldsymbol{x}_r/\delta\boldsymbol{x}$, or in the case of OEM:

$$\mathbf{A} = (\mathbf{K}_r^T \mathbf{S}_y^{-1} \mathbf{K}_r + \mathbf{S}_a^{-1})^{-1} \mathbf{K}_r^T \mathbf{S}_y^{-1} \mathbf{K}_r. \tag{8}$$

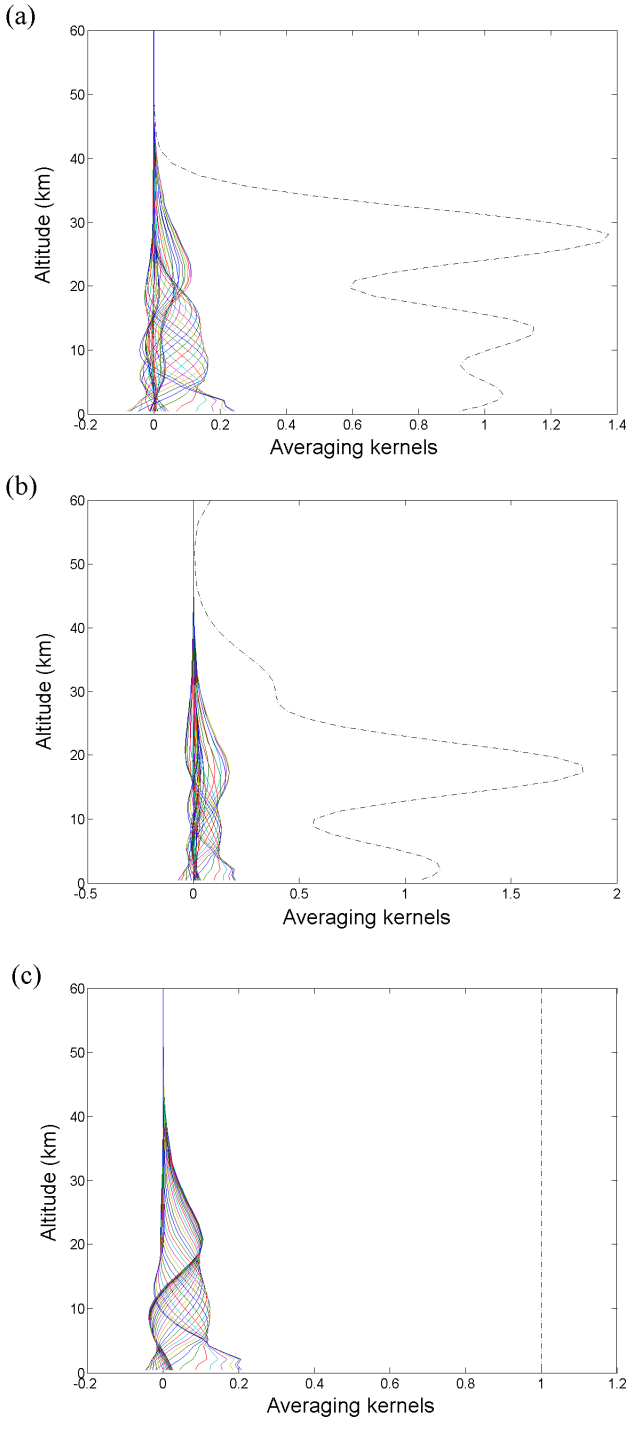

Fig. 6. Averaging kernels and sensitivity curve (black dashed) for the N_2O retrieval from a single spectrum on 8 October 2007 at St.-Denis using the **(a)** OEM, **(b)** IOA and **(c)** TR.

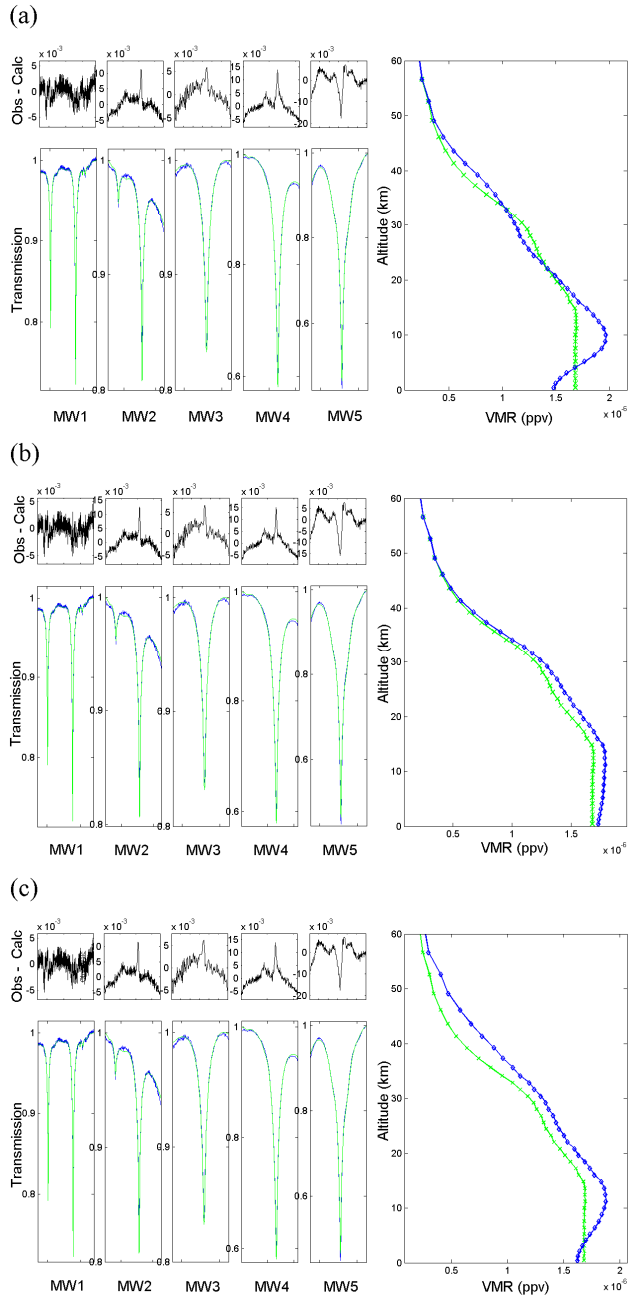

Fig. 7. Multiple micro-window (MW1: 2613.70–2615.40, MW2: 2650.60–2651.30, MW3: 2835.50–2835.80, MW4: 2903.60–2904.03, and MW5: 2921.00–2921.60 cm^{-1}) fit of CH_4 plus interfering species from a single spectrum on 2 October 2007 at St.-Denis using the **(a)** OEM, **(b)** IOA and **(c)** TR. Measured (blue) and simulated (green) spectra are shown (left lower plot), together with the residuals (left upper plot), computed as measured minus simulated. The right plot shows the a priori (green crosses) and retrieved (blue diamonds) profile.

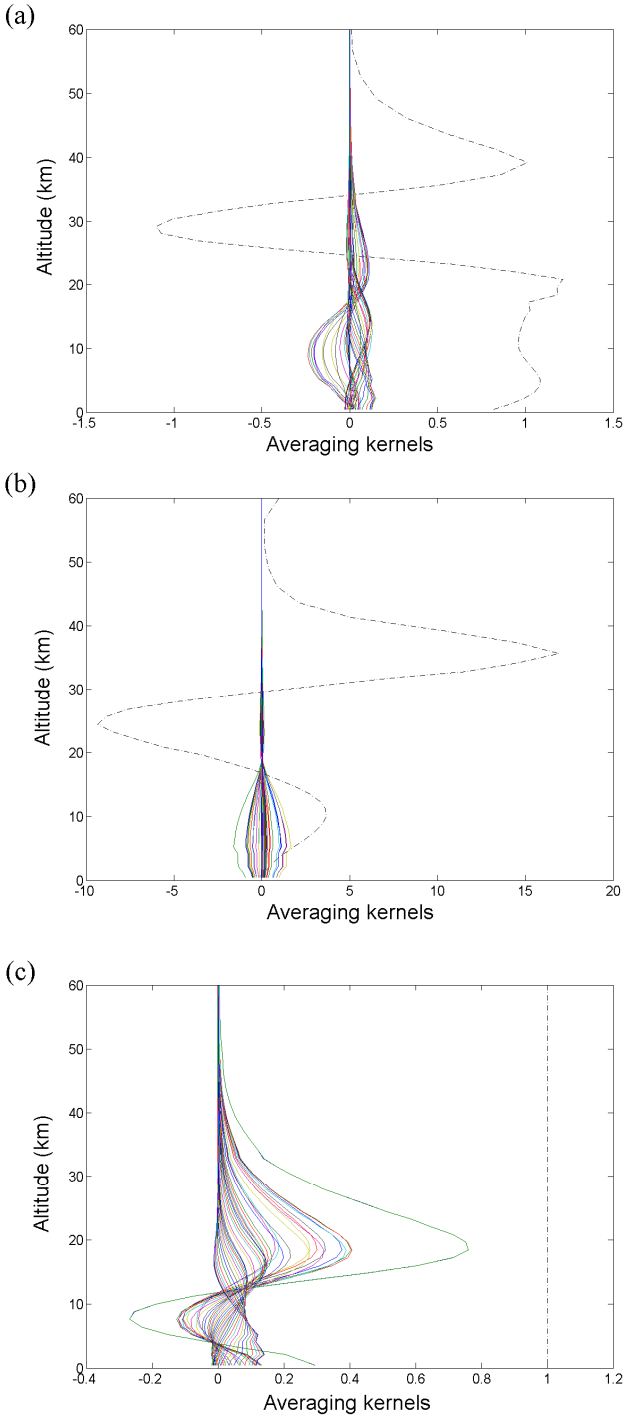

Fig. 8. Averaging kernels and sensitivity curve (black dashed) for the CH_4 retrieval from a single spectrum on 2 October 2007 at St.-Denis using the **(a)** OEM, **(b)** IOA and **(c)** TR.

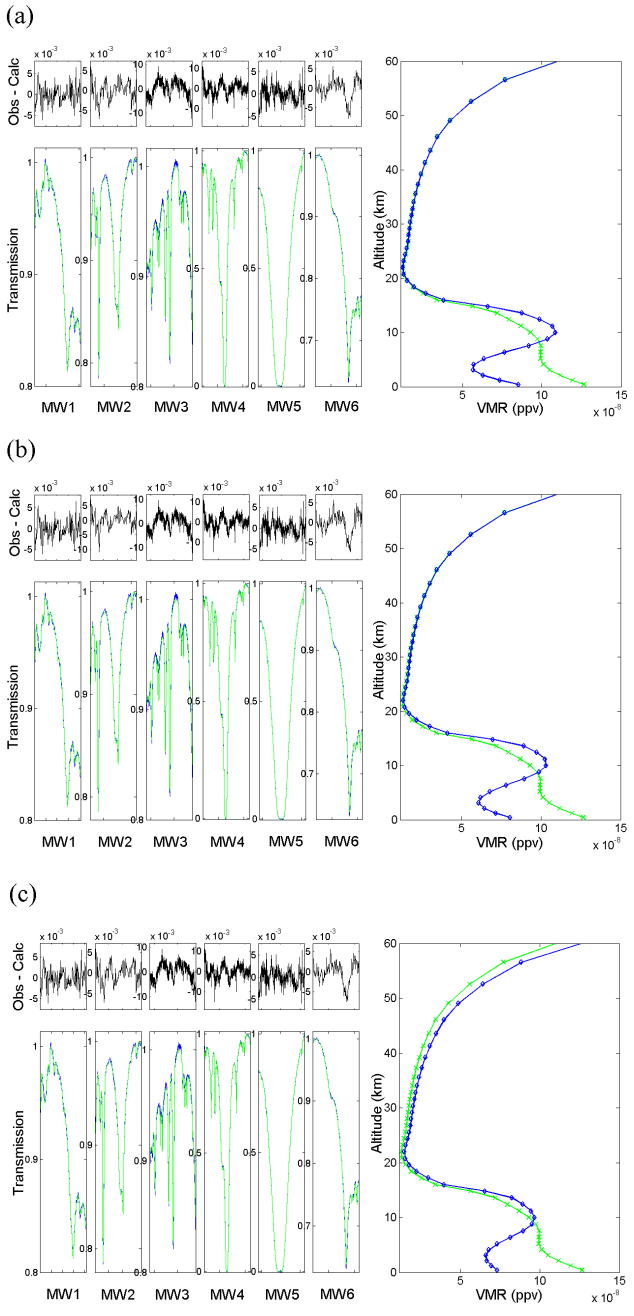

Fig. 9. Multiple micro-window (MW1: 2057.70–2057.91, MW2: 2069.55–2069.72, MW3: 2140.40–2141.40, MW4: 2157.40–2159.20, MW5: 2165.37–2165.85, and MW6: 2168.84–2169.02 cm^{-1}) fit of CO plus interfering species from a single spectrum on 29 July 2007 at St.-Denis using the **(a)** OEM, **(b)** IOA and **(c)** TR. Measured (blue) and simulated (green) spectra are shown (left lower plot), together with the residuals (left upper plot), computed as measured minus simulated. The right plot shows the a priori (green crosses) and retrieved (blue diamonds) profile.

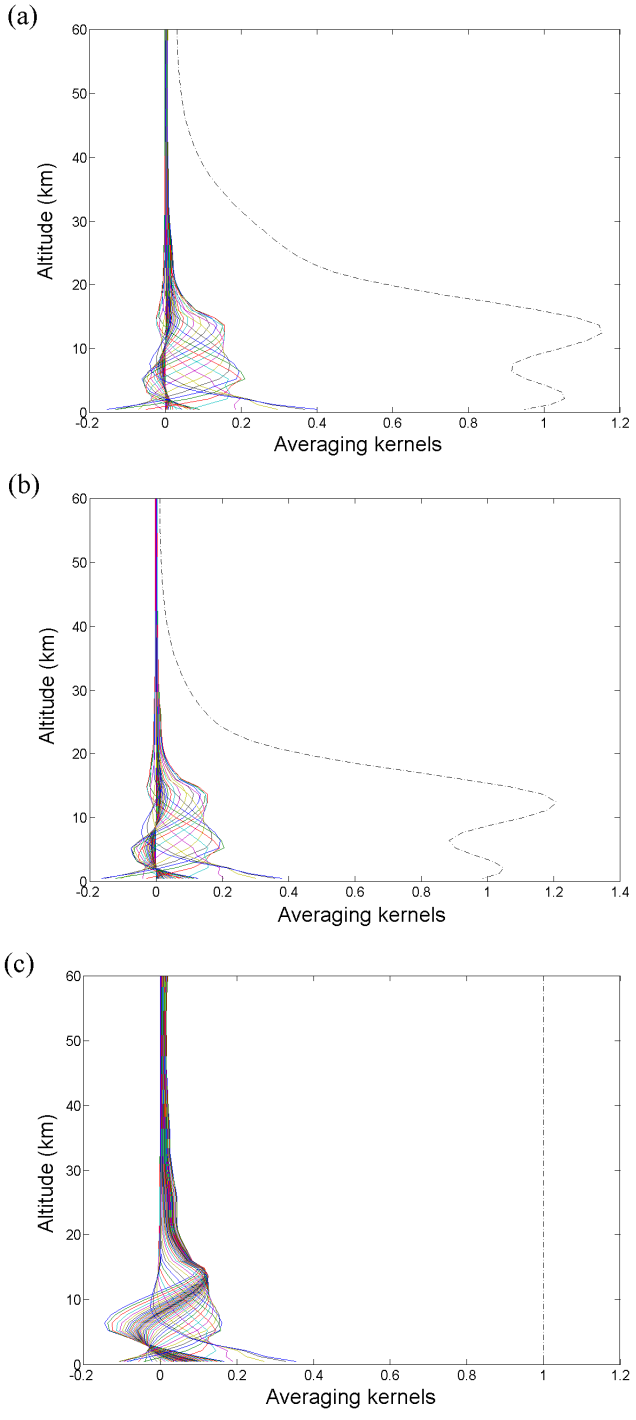

Fig. 10. Averaging kernels and sensitivity curve (black dashed) for the CO retrieval from a single spectrum on 29 July 2007 at St.-Denis using the **(a)** OEM, **(b)** IOA and **(c)** TR.

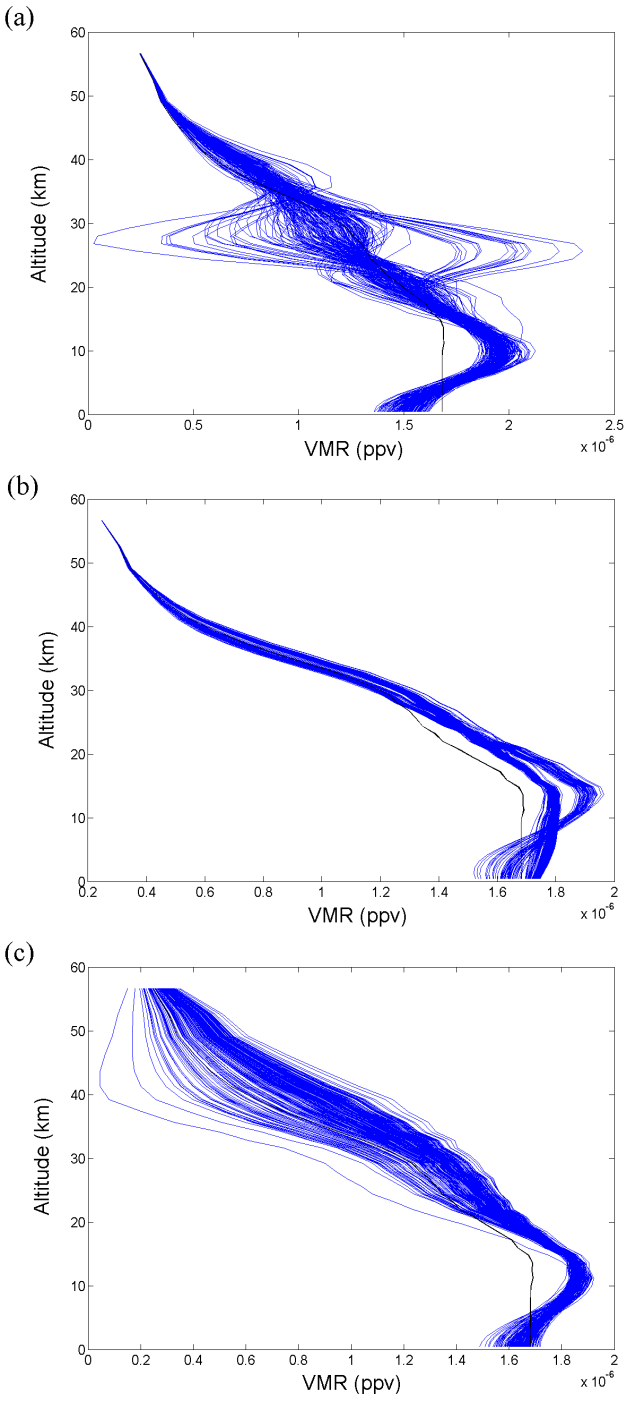

Fig. 11. CH_4 profiles from all spectra taken at St.-Denis during the 2007 campaign, retrieved with the **(a)** OEM, **(b)** IOA and **(c)** TR, respectively. The black line corresponds to the a priori profile used.

The rows of the matrix **A** are called the averaging kernels, and the trace of **A** equals the number of degrees of freedom for signal (DOFS). Note that essentially the DOFS comprises two shares, namely one corresponding to the fitted VMR values of the target profile and one corresponding to the other fitted parameters within the state vector. In what follows the term DOFS will refer to the target part only, unless stated otherwise.

For each of the retrieval layers the full width at half maximum of the averaging kernel provides an estimate of the vertical resolution of the profile retrieval at the corresponding altitude, while the area of the averaging kernel (i.e. the sum of its elements) represents the sensitivity of the retrieval at the corresponding altitude to the true state. The DOFS together with the averaging kernel shapes define the independent partial columns that best represent the retrieval results.

The matrix **A** in Eq. (8) can be written as a function of $\mathbf{P}_\mathrm{r}$, namely:

$$\mathbf{A} = (\mathbf{S}_\mathrm{a}\,\mathbf{K}_\mathrm{r}^\mathrm{T}\mathbf{S}_y^{-1}\mathbf{K}_\mathrm{r} + \mathbf{I})^{-1}\mathbf{S}_\mathrm{a}\,\mathbf{K}_\mathrm{r}^\mathrm{T}\mathbf{S}_y^{-1}\mathbf{K}_\mathrm{r} = (\mathbf{P}_\mathrm{r} + \mathbf{I})^{-1}\mathbf{P}_\mathrm{r}, \quad (9)$$

such that the trace of **A** equals $\sum_{n=1}^{N} \lambda_{\mathrm{r},n} / (1 + \lambda_{\mathrm{r},n})$ in the case of OEM.

When we derive **A** in the case of IOA, we get the following expression for each element i, j of **A** ($i = 1,\ldots, N$ and $j = 1,\ldots, N$):

$$(\mathbf{A})_{i,j} = \sum_{n=1}^{N_\mathrm{opt}} \lambda_{\mathrm{r},n}/[N_{r,n}(1+\lambda_{\mathrm{r},n})] \\ (\boldsymbol{\phi}_{\mathrm{r},n}^\mathrm{T}\mathbf{K}_\mathrm{r}^\mathrm{T}\mathbf{S}_y^{-1}\mathbf{K}_\mathrm{r})_{1,j}(\boldsymbol{\phi}_{\mathrm{r},n})_{i,1}. \quad (10)$$

The trace of **A**, or the total DOFS, now equals $\sum_{n=1}^{N_\mathrm{opt}} \lambda_{\mathrm{r},n} / (1 + \lambda_{\mathrm{r},n})$. Note that if we would use all eigenvalues of $\mathbf{P}_\mathrm{r}$ (i.e. $N_\mathrm{opt} = N$), instead of only the significant ones, this would correspond to the trace of **A** resulting from the OEM.

Analogous to **A**, in the case of IOA, the gain matrix $\mathbf{G}_\mathrm{r}$, defined as $\delta\boldsymbol{x}_\mathrm{r}/\delta\boldsymbol{y}$, becomes:

$$(\mathbf{G}_\mathrm{r})_{i,j} = \sum_{n=1}^{N_\mathrm{opt}} \lambda_{\mathrm{r},n}/[N_{\mathrm{r},n}(1+\lambda_{\mathrm{r},n})] \\ (\boldsymbol{\phi}_{\mathrm{r},n}^\mathrm{T}\mathbf{K}_\mathrm{r}^\mathrm{T}\mathbf{S}_y^{-1})_{1,j}(\boldsymbol{\phi}_{\mathrm{r},n})_{i,1}, \quad (11)$$

with $i = 1,\ldots, N$ and $j = 1,\ldots, M$.

Note that all definitions of the error components for the OEM are still valid for the IOA applied onto the OEM, as this alternative retrieval method is based on the same premises. In the numerical evaluations we have to use the adapted expressions for the averaging kernel and gain matrix (Eqs. 10 and 11).

2.2.3 Tikhonov regularization

Besides the OEM, Tikhonov regularization (TR) is another commonly used method for the retrieval of the vertical distribution of trace gases from FTIR absorption spectra. The TR solution is calculated iteratively by the following expression (Schimpf and Schreier, 1997):

$$\boldsymbol{x}_{i+1} = \boldsymbol{x}_\mathrm{a} + (\mathbf{K}_i^\mathrm{T}\mathbf{S}_y^{-1}\mathbf{K}_i + \alpha\mathbf{R}^\mathrm{T}\mathbf{R})^{-1}\mathbf{K}_i^\mathrm{T}\mathbf{S}_y^{-1}[\boldsymbol{y} - \boldsymbol{y}_i \\ + \mathbf{K}_i(\boldsymbol{x}_i - \boldsymbol{x}_\mathrm{a})], \quad (12)$$

where **R** and α are the regularization matrix and regularization parameter, respectively. Both are introduced to constrain the state vector or, in other words, to incorporate information about the solution magnitude and smoothness. Again, all error components are calculated in the same way as for the OEM retrievals.

For the retrievals obtained with TR, we have used the $\mathbf{L}_1$ regularization matrix, i.e. $\mathbf{R} = \mathbf{L}_1$. This $\mathbf{L}_1$ is by definition a $(N-1) \times N$ matrix composed by zeros except for the elements $\mathbf{L}_1$(i, i) = -1 and $\mathbf{L}_1(i, i+1) = 1$, for $i = 1,\ldots, N-1$. For this particular choice of **R** the averaging kernel matrix **A** becomes:

$$\mathbf{A} = (\mathbf{K}_\mathrm{r}^\mathrm{T}\mathbf{S}_y^{-1}\mathbf{K}_\mathrm{r} + \alpha\mathbf{L}_1^\mathrm{T}\mathbf{L}_1)^{-1}\mathbf{K}_\mathrm{r}^\mathrm{T}\mathbf{S}_y^{-1}\mathbf{K}_\mathrm{r}. \quad (13)$$

Consequently, the sum of all elements of each row of **A** equals 1, as can be seen from a simple matrix manipulation. This is valid for each choice of α. In other words, for the Tikhonov retrievals in this paper the sensitivity is always 1 at every altitude and is not a relevant parameter.

The parameter α we have used is the one that results in the best compromise between the DOFS and the total random error on the retrieved total column. Note that this total random error we have evaluated here by summing up the covariance matrices of the forward model parameter error, the smoothing error, the interfering species' errors and the measurement noise error, assuming that the other error components do not vary with α. This tuning method is based on the discussion in Steck (2002) showing that the DOFS as well as the total random error decreases with increasing α.

3 Application of the IOA to ground-based FTIR data

As discussed in the introduction, we have focused on the retrieval results of O_3, N_2O, CH_4 and CO. In addition to the total column abundances of these molecules, we have extracted information – whenever feasible – about their vertical distribution between the ground and 100 km altitude. In this section we give an overview of the measurement characteristics, the retrieval strategy used, and the OEM, IOA and TR retrieval results, including mutual comparisons.

3.1 Specifications of the FTIR measurements

Before continuous operations started in May 2009, three FTIR solar absorption measurement campaigns had been carried out at Ile de La Réunion, namely in 2002, 2004 and 2007. Within the scope of this paper we concentrate on

Table 5. Smoothing error, total random error without the smoothing error contribution, total random error, total systematic error and total error on the retrieved total and partial columns of O_3, N_2O, CH_4 and CO, at Ile de La Réunion in 2007, when using the OEM, IOA and TR.

Molec.	Alt. range [km]	Smoothing [%] OEM / IOA / TR	Total rand. without smoothing error [%] OEM / IOA / TR	Total rand. [%] OEM / IOA / TR	Total syst. [%] OEM / IOA / TR	Total [%] OEM / IOA / TR
O_3	0.05–100	0.44 / 0.54 / 0.51	0.80 / 0.62 / 0.81	0.91 / 0.83 / 0.96	2.54 / 1.71 / 2.84	2.70 / 1.90 / 3.00
	0.05–9.4	6.70 / 9.06 / 7.14	1.62 / 1.39 / 1.55	6.90 / 9.17 / 7.30	14.32 / 12.48 / 14.18	15.89 / 15.49 / 15.94
	9.4–21.4	9.05 / 10.71 / 10.31	3.35 / 2.26 / 2.91	9.65 / 10.94 / 10.71	27.20 / 13.76 / 23.77	28.86 / 17.58 / 26.07
	21.4–29.8	5.56 / 7.58 / 6.70	3.12 / 1.75 / 2.52	6.38 / 7.78 / 7.16	21.89 / 7.84 / 17.41	22.80 / 11.05 / 18.82
	29.8–100	5.03 / 6.57 / 6.34	2.48 / 2.03 / 2.02	5.61 / 6.88 / 6.65	13.83 / 7.75 / 9.75	14.93 / 10.36 / 11.81
N_2O	0.05–100	0.10 / 0.27 / 0.073	0.49 / 0.35 / 0.33	0.50 / 0.44 / 0.34	2.49 / 2.64 / 2.68	2.54 / 2.68 / 2.70
	0.05–5.8	0.55 / 1.36 / 0.40	1.05 / 0.64 / 0.64	1.18 / 1.50 / 0.75	5.41 / 4.77 / 4.68	5.53 / 5.00 / 4.74
	5.8–15.4	0.72 / 2.18 / 0.65	1.33 / 0.56 / 0.49	1.51 / 2.25 / 0.81	5.26 / 5.11 / 5.07	5.48 / 5.59 / 5.14
	15.4–100	1.39 / 4.84 / 1.47	2.85 / 1.51 / 1.07	3.17 / 5.07 / 1.82	12.61 / 5.56 / 4.05	13.00 / 7.53 / 4.44
CH_4	0.05–100	0.22 / 1.09 / 0.31	0.95 / 0.97 / 0.93	0.98 / 1.46 / 0.98	4.83 / 7.28 / 5.21	4.93 / 7.42 / 5.30
	0.05–9.4	0.41 / 2.29 / 0.64	1.08 / 0.94 / 0.97	1.16 / 2.48 / 1.16	7.54 / 7.48 / 7.72	7.63 / 7.88 / 7.81
	9.4–100	0.60 / 2.91 / 0.61	1.50 / 1.09 / 1.46	1.61 / 3.10 / 1.59	7.85 / 6.87 / 8.16	8.01 / 7.54 / 8.32
CO	0.05–100	0.15 / 0.15 / 0.37	1.29 / 1.22 / 1.15	1.30 / 1.23 / 1.21	3.52 / 2.88 / 2.93	3.75 / 3.13 / 3.17
	0.05–2.6	1.92 / 2.45 / 3.94	4.37 / 3.76 / 3.38	4.78 / 4.49 / 5.19	30.16 / 24.14 / 16.59	30.54 / 24.56 / 17.39
	2.6–9.4	2.22 / 2.67 / 4.16	2.20 / 2.15 / 1.24	3.13 / 3.43 / 4.34	35.92 / 27.31 / 15.90	36.05 / 27.53 / 16.48
	9.4–100	2.18 / 2.47 / 4.94	2.28 / 2.07 / 1.43	3.16 / 3.23 / 5.14	33.99 / 22.82 / 9.95	34.13 / 23.05 / 11.20

spectra taken during the third campaign, from May to October 2007. In particular, these spectra are recorded using a mobile Bruker 120M Fourier Transform spectrometer installed at the St.-Denis University campus (50 m a.s.l., 20°54′ S and 55°29′ E). The 2007 campaign was performed with the same experimental setup as the 2004 campaign, which is described in detail in Senten et al. (2008). Note that the FTIR experiment at Ile de La Réunion is qualified as an NDACC-compliant experiment, confirming that it satisfies all quality criteria imposed by the NDACC Infrared Working Group.

3.2 Retrieval results

3.2.1 Retrieval strategy and spectral fits

For all retrievals discussed in this paper the absorption line parameters were taken from the HITRAN 2008 spectral database (Rothman et al., 2009) in combination with available updates on the HITRAN website (http://www.hitran.com). The spectral micro-windows in which the absorption features of the target and interfering species are fitted, are selected such that they contain unsaturated well-isolated absorption features of the target species with a minimal number of interfering absorption lines, and such that the amount of information present in the spectra – represented by the DOFS – is maximized.

The a priori profile $\boldsymbol{x}_a$ used and its associated covariance matrix $\mathbf{S}_a$ should represent a good guess of the "true" state, in particular at those altitudes for which it is difficult to get information out of the measurements. Note that in order to compare the OEM and IOA retrievals, we use the same $\boldsymbol{x}_a$ and $\mathbf{S}_a$ for both methods, rather than imposing the same DOFS.

The diagonal elements of the measurement error covariance matrix are defined to be an estimate of the squared reciprocals of a representative signal-to-noise ratio (SNR). The off-diagonal elements are set to zero, which means that the measurement errors at different wavelengths are assumed to be uncorrelated.

For the N_2O and CH_4 retrievals the selected micro-windows (fitted simultaneously), the associated interfering molecules, the used a priori profiles and the corresponding a priori covariance matrices are adopted from Senten et al. (2008). The O_3 retrieval strategy is the one used by Vigouroux et al. (2008), and for CO we adopted the strategy from Duflot et al. (2010). An overview of these choices is provided in Table 1.

3.2.2 Choice of eigenvalues and eigenvectors to be used

Before discussing the IOA retrieval results, we clarify the criteria to determine the most appropriate number N_{opt} ($\leq N$) of terms to be used in the IOA sum, i.e. Eq. (5), yielding the best compromise between the information content and the stability of the retrieval results. In particular, a suitable threshold g has to be searched for, meeting the condition $\lambda_{r,n} / (1 + \lambda_{r,n}) \geq g$, with $g < 1$. As the eigenvectors corresponding to

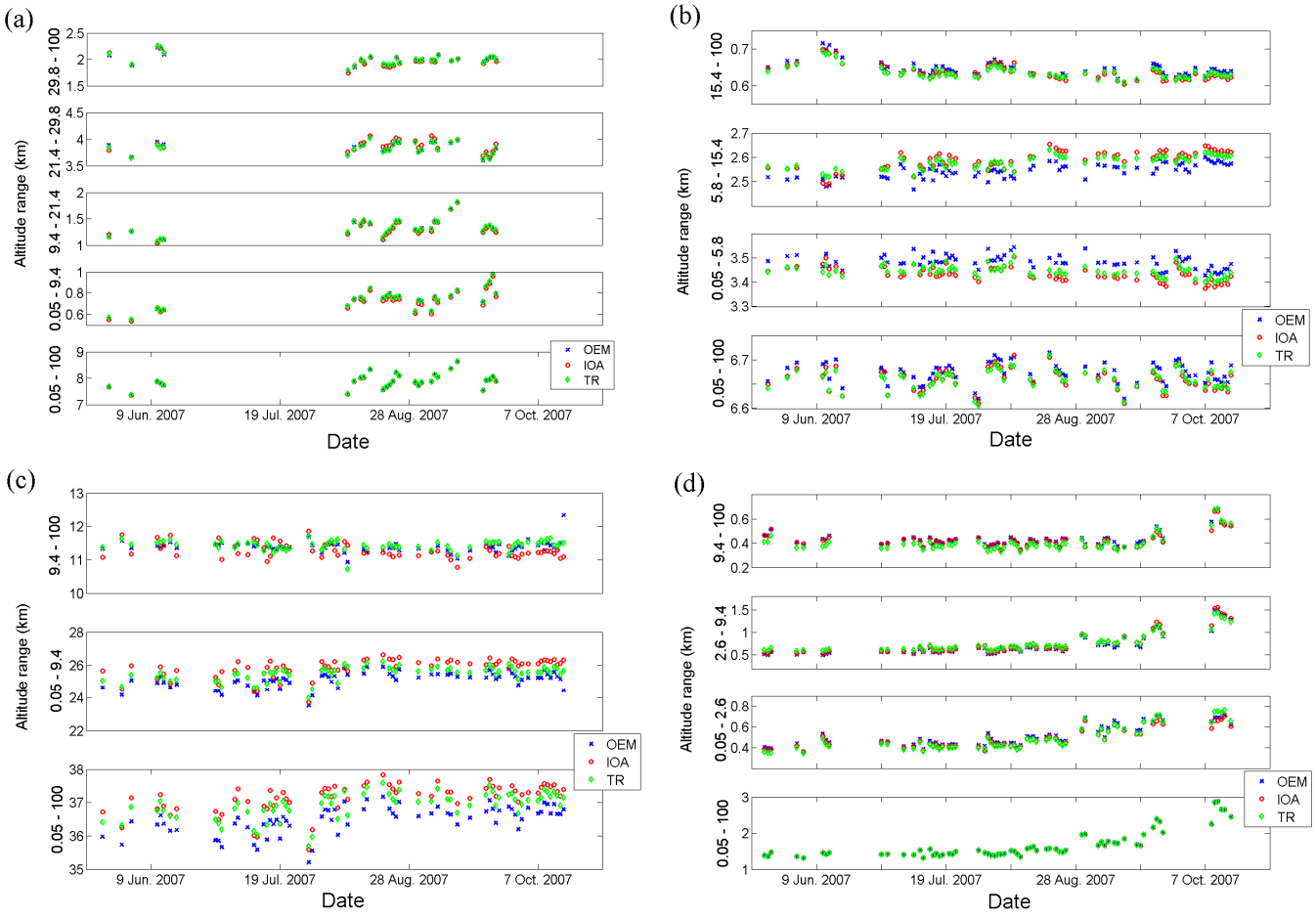

Fig. 12. Time series of the total and partial column amounts (in 10^{18} molec cm^{-2}) of **(a)** O_3, **(b)** N_2O, **(c)** CH_4 and **(d)** CO during the FTIR campaign at St.-Denis in 2007, retrieved with the OEM (blue crosses), IOA (red circles) and TR (green diamonds), respectively.

smaller eigenvalues have the property of being more oscillatory, it is easy to understand that the more eigenvectors we include in the linear combination defining the retrieval solution, the more this solution will oscillate. On the other hand, if we do not include enough eigenvectors, the solution will no longer be representative of the true state and the DOFS will be considerably smaller. Table 2 shows the evolution of 1/2 ln ($\lambda_{r,n}$ + 1) and $\lambda_{r,n}$ / (1 + $\lambda_{r,n}$) for the largest 24 eigenvalues $\lambda_{r,n}$ of $\mathbf{P}_r$ for an illustrative IOA retrieval of each target molecule. The systematic decrease of both quantities around 1 and 0.8, respectively, indicates that including the subsequent smaller eigenvalues and eigenvectors in the IOA calculations would not significantly contribute to the solution. On the contrary, they would only induce unrealistic oscillations in the retrieved vertical profiles.

By definition of the IOA, when decreasing g, the IOA solution approaches the OEM solution, up to the point of using all eigenvalues and eigenvectors in the IOA sum, i.e. $g = 0$, or equivalently, $N_{opt} = N$ in Eq. (5). The remaining difference – though very small – between the retrieval result from the OEM and IOA with $g = 0$ comes from the fact that the state space spanned by both methods is not exactly the same.

The impact of different threshold values between 0 and 1 on the retrieved profiles can be seen in Fig. 1, showing the N_2O profiles for the whole 2007 campaign obtained with the OEM and with the IOA for g equal to 0.09, 0.79 and 0.99. These three values of g correspond to including about 20, 17 and 15 terms in the IOA decomposition. These four approaches result in 3.1, 3.3, 2.9 and 1.6 DOFS on average, respectively. Consequently, the smoothing error increases. The root mean square (RMS) values of the spectral fit residual, calculated from the differences between the observed and simulated spectral points, equal 0.15, 0.15, 0.15 and 0.16 on average, respectively. This demonstrates the poor sensitivity of the spectral fit to the choice of g, or correspondingly, to the retained dimension of the state space. Obviously, the IOA profiles for $g = 0.99$ are less oscillatory than those for $g = 0.79$, which in turn are less oscillating than those for $g = 0.09$. These plots also confirm the statement that in the limit the IOA profiles move towards the OEM profiles. The

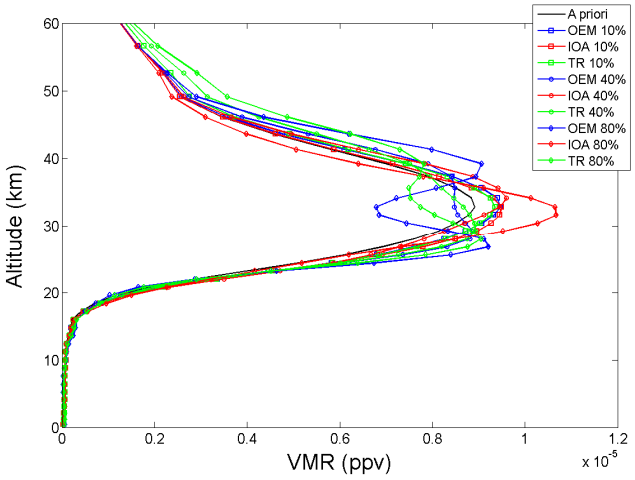

Fig. 13. O_3 profile on 12 June 2007 at St.-Denis obtained when using $\mathbf{S}_a$ with on its diagonal 10 % (squares), 40 % (circles) and 80 % (diamonds), retrieved with the OEM (blue), IOA (red) and TR (green), respectively. The black profile is the unchanged a priori profile.

same behavior was observed in the tests we performed for the other target molecules.

Figure 2 shows the curves of $y = 1/2\ln(x+1)$ and $y = x/(1+x)$ for x between 0 and 20 and for the eigenvalues of the Kozlov information matrix $\mathbf{P}_r$ that lay within this domain, for O_3 and CO. Clearly, the intersection point of these two curves is situated around 0.79. Note that the eigenvalues of $\mathbf{P}_r$ for N_2O and CH_4 yield similar graphs, but are left out here, just for clarity of the figure.

Based on the considerations above, we conclude that the best compromise is attained with the threshold $g = 0.79$. This lower limit for the contribution to the information content of the measurement is valid for each target species and is used in all subsequent IOA retrievals discussed in this paper.

3.2.3 Vertical profiles and column amounts

For the discussion of the characteristics of the IOA compared to the OEM and TR, we analyzed the vertical profile and column retrievals for the complete set of 2007 spectra. However, full error budget evaluations are made here only for one reference spectrum for each target molecule, because performing the error calculations for all spectra would have been too time-consuming. The choice of these typical reference spectra is based on their representativeness for the whole 2007 dataset, with respect to the solar zenith angle (SZA), the retrieved profile shape and the DOFS. Table 3 lists the date, the optical bandpass (OBP) and the SZA for the reference spectra analyzed for each species, together with the RMS of the spectral fit residual, the DOFS and the corresponding partial column (PC) ranges when applying the OEM, IOA and TR. For each molecule the RMS value and the integer nearest to the number of degrees of freedom for signal are the same for every method, whereas the partial column limits are slightly different. These limits correspond to the altitude ranges that comprise at least one degree of freedom for signal. In order to allow direct comparison of the OEM, IOA and TR partial columns, or in other words, to discuss the retrieval results in terms of partial columns with identical altitude boundaries, from now on, the altitude ranges are deduced from the averaging kernel matrices such that the sum of the diagonal elements of $\mathbf{A}$ is at least one for every method, thus possibly increasing some of the partial column widths. If the remaining diagonal elements add up to more than 0.6, the resulting altitude range is considered as an additional partial column.

Figures 3, 5, 7 and 9 illustrate the single or multiple microwindow fits of O_3, N_2O, CH_4, and CO, respectively, for the reference spectra listed in Table 3, together with the residuals, computed as measured minus simulated transmission. Figures 4, 6, 8 and 10 show the corresponding averaging kernels and sensitivity curves (black dashed), calculated at each altitude as the sum of the row elements of $\mathbf{A}$. As explained in Sect. 2.2.3, for the TR retrievals the sensitivity is 1 at every altitude and therefore a redundant quantity in the discussion. For O_3 the SNR and α are 150 and 1, respectively, for N_2O they are 150 and 5, for CH_4 they are 250 and 3, and for CO they are 150 and 5. As the reference spectra are carefully chosen, they represent the complete dataset well, and, in turn, their resulting vertical profiles have also been found to be representative. The retrieved vertical profiles will therefore not be shown individually.

For every target gas the spectral fits look very similar for each method. For O_3 and CO the retrieved profile is similar for each method. For N_2O and CH_4 the OEM retrieved profile slightly oscillates near the surface, whereas the IOA profile is more stable. The TR profile of CH_4 oscillates less than the OEM profile but more than the IOA profile. In order to confirm and to generalize this conclusion, Fig. 11 shows the CH_4 vertical volume mixing ratio (VMR) profiles obtained with the OEM, IOA and TR, from the whole set of FTIR spectra taken at St.-Denis in 2007. In the troposphere the TR profiles are slightly more stable than the OEM and IOA profiles, whereas at higher altitudes they are less stable than the IOA profiles, but still more stable than the OEM profiles. Note that the two groups that can be distinguished most clearly in the case of IOA correspond to spectra recorded at a SZA smaller and larger than 49°, respectively. The reason for this effect is not yet understood.

Table 4 summarizes the mean DOFS, the mean number of iterations in the fit (ITER), the mean RMS values of the spectral fit residual, the mean total and partial column amounts (CA) (in molecules cm^{-2}) and the mean daily relative standard deviation (STD) on the CA (in %) for each molecule when applying the OEM, IOA and TR. The mean daily relative standard deviations are considered to provide a good measure for the quality of the retrieval method, because they

Table 6. Impact of different choices of $\mathbf{S}_a$ on the O_3 total and partial columns retrieved with the OEM, IOA and TR, for the 2007 campaign data at Ile de La Réunion: mean daily relative STD and mean relative biases with respect to the retrieval with 10% $\mathbf{S}_a$.

Alt. range [km]	STD [%] 10% $\mathbf{S}_a$ OEM / IOA / TR	STD [%] 40% $\mathbf{S}_a$ OEM / IOA / TR	Bias [%] 40% $\mathbf{S}_a$ OEM / IOA / TR	STD [%] 80% $\mathbf{S}_a$ OEM / IOA / TR	Bias [%] 80% $\mathbf{S}_a$ OEM / IOA / TR
0.05–100	0.32 / 0.35 / 0.31	0.26 / 0.34 / 0.26	−0.037 / 0.035 / −0.073	0.25 / 0.28 / 0.25	−0.26 / 0.21 / −0.17
0.05–9.4	0.90 / 0.99 / 0.89	1.22 / 1.00 / 1.08	−0.30 / 0.060 / −0.27	1.68 / 1.14 / 1.30	−0.96 / 0.18 / −0.58
9.4–21.4	0.98 / 1.38 / 0.99	1.66 / 1.40 / 1.62	−0.16 / −0.035 / −0.20	2.21 / 1.60 / 1.92	−0.58 / 0.26 / −0.40
21.4–29.8	0.57 / 0.61 / 0.54	1.25 / 0.64 / 1.33	0.18 / 0.067 / 0.14	1.83 / 0.93 / 1.68	0.20 / 0.20 / 0.20
29.8–100	0.88 / 1.02 / 0.74	1.25 / 0.95 / 1.39	−0.36 / 0.010 / −0.40	2.41 / 0.78 / 2.15	−1.09 / 0.21 / −0.81

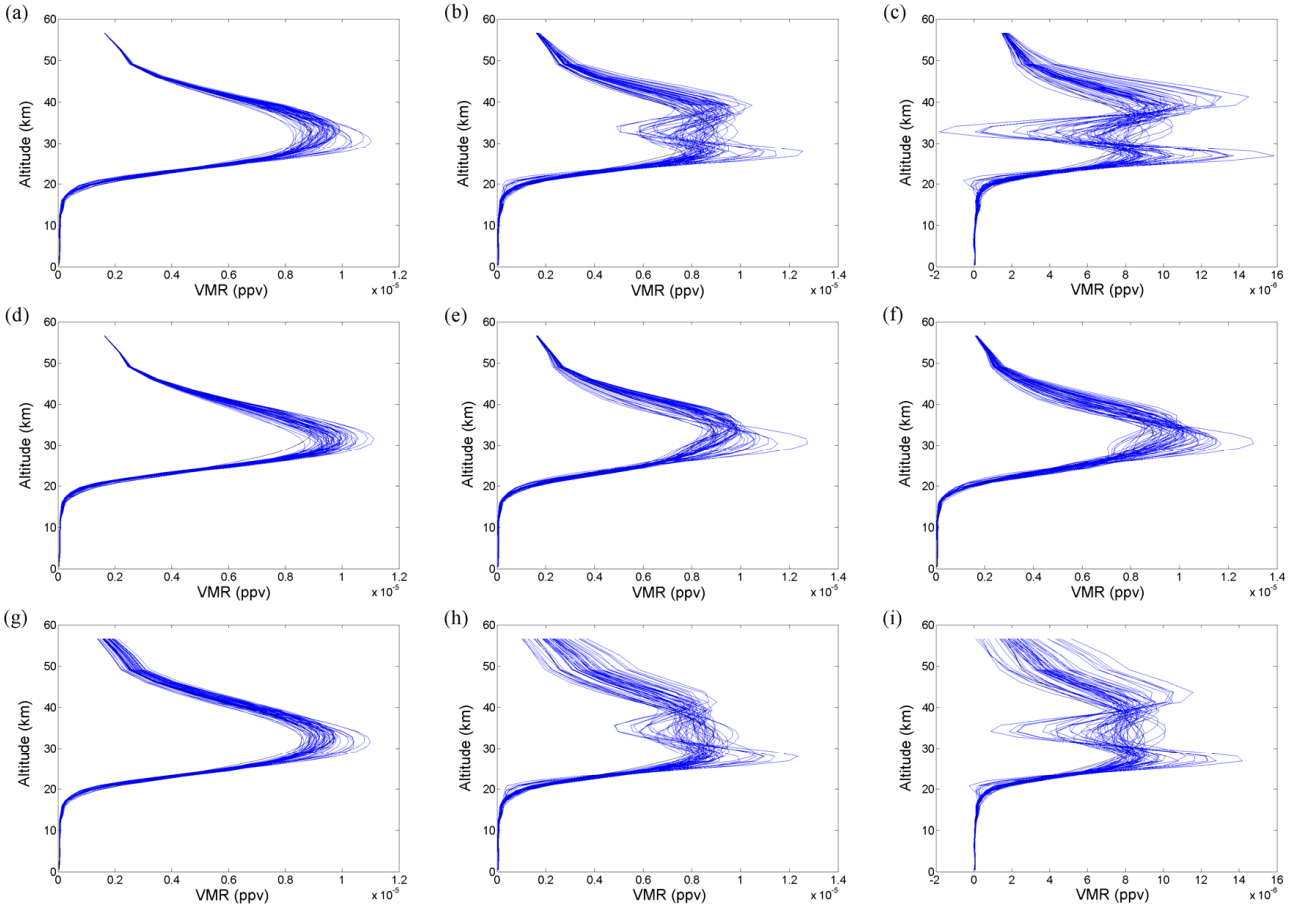

Fig. 14. O_3 profiles from all spectra taken at St.-Denis during the 2007 campaign, retrieved with the OEM **(a, b, c)**, IOA **(d, e, f)** and TR **(g, h, i)** with $\mathbf{S}_a$ diagonal elements 10 %, 40 % and 80 %, respectively. The black line corresponds to the used a priori profile.

reflect the stability of the retrieved column amounts. Ideally, the latter do not change much over the course of a day, as the diurnal variations of the retrieved target molecules are supposed to be small. For all retrievals performed, we observe that the quality of the spectral fits – characterized by the RMS –, as well as the mean vertical column amount (VCA) and partial column amounts (PCA), are similar for all three methods. For O_3 and CO the mean number of iterations before convergence is equal for each method, whereas for N_2O and CH_4 it is smaller for the IOA and TR. The information content – represented by the DOFS – is slightly smaller for the IOA. This is due to the fact that the IOA leaves out all components that do not contribute significantly to the information content. In general, this loss – between 0 and 0.5

Table 7. Impact of different choices of $\boldsymbol{x}_a$ on the O_3 total and partial columns retrieved with the OEM, IOA and TR, for the 2007 campaign data at Ile de La Réunion: mean daily relative STD and mean relative biases with respect to the retrieval with $\boldsymbol{x}_a$.

Alt. range [km]	STD [%] $\boldsymbol{x}_a$ OEM / IOA / TR	STD [%] $2\boldsymbol{x}_a$ OEM / IOA / TR	Bias [%] $2\boldsymbol{x}_a$ OEM / IOA / TR	STD [%] $1/2\boldsymbol{x}_a$ OEM / IOA / TR	Bias [%] $1/2\boldsymbol{x}_a$ OEM / IOA / TR
0.05–100	0.32 / 0.35 / 0.32	0.30 / 0.35 / 0.29	−0.23 / −0.47 / −0.0099	0.33 / 0.34 / 0.33	0.12 / 0.10 / −0.12
0.05–9.4	0.90 / 0.98 / 0.89	0.93 / 0.94 / 0.86	−0.34 / −0.53 / −0.044	1.08 / 0.92 / 1.01	0.12 / −0.049 / −0.14
9.4–21.4	1.15 / 1.35 / 1.12	1.42 / 1.46 / 1.30	−0.33 / −0.67 / −0.090	1.01 / 0.49 / 1.27	0.15 / 0.11 / 0.0061
21.4–29.8	0.67 / 0.60 / 0.61	0.90 / 0.65 / 0.87	−0.086 / −0.31 / 0.065	0.50 / 0.36 / 0.59	0.076 / 0.097 / −0.18
29.8–100	0.93 / 1.00 / 0.75	1.09 / 1.20 / 0.73	−0.49 / −0.67 / −0.11	0.78 / 0.72 / 0.84	0.19 / 0.12 / −0.075

Table 8. Mean relative differences with corresponding standard deviations (between brackets) between retrieved and "input" total and partial columns of O_3 from simulated spectra.

Alt. range [km]	Rel. diff. [%] OEM	Rel. diff. [%] IOA	Rel. diff. [%] TR
0.05–100	0.11 (0.087)	0.11 (0.092)	0.12 (0.064)
0.05–9.4	0.69 (0.56)	1.03 (0.86)	0.66 (0.51)
9.4–21.4	1.82 (0.62)	1.78 (0.60)	1.86 (0.50)
21.4–29.8	1.11 (0.57)	1.13 (0.47)	1.21 (0.37)
29.8–100	0.70 (0.60)	0.63 (0.51)	0.72 (0.37)

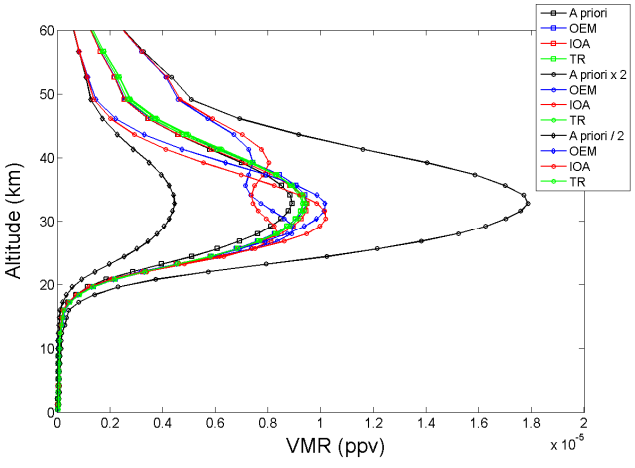

Fig. 15. O_3 profile on 12 June 2007 at St.-Denis obtained with the original $\boldsymbol{x}_a$ (squares), with $2\boldsymbol{x}_a$ (circles) and with $1/2\boldsymbol{x}_a$ (diamonds), retrieved with the OEM (blue), IOA (red) and TR (green), respectively. The black profiles are the respective a priori profiles.

– does not affect the number of partial columns that can be distinguished. For O_3, N_2O and CO the mean daily relative standard deviations on the VCA are alike for each method, whereas for CH_4 it is obviously smaller for the IOA and TR. For CO the mean daily relative standard deviations on the PCA are similar for each method. For O_3 they are largest for the IOA, for N_2O they are smaller for the IOA, and for CH_4 they are smallest for TR.

Figure 12 shows the time series of the total and partial column amounts (in molecules cm^{-2}) of O_3, N_2O, CH_4 and CO, respectively, during the FTIR campaign at St.-Denis in 2007, retrieved with the OEM, IOA and TR. For O_3 and CO each method gives about the same partial and total column values, i.e. without significant bias. For N_2O the partial and total columns are distributed in a slightly different way. The biases between the OEM and IOA total columns are about −0.2 % and the biases between the OEM and TR total columns are about −0.15 %. The biases between the OEM and IOA first and second partial columns are −0.8 and +0.8 %, respectively, whereas they are −0.5 and +0.5 % between the respective OEM and TR partial columns. For CH_4 there is a systematic bias of the order of +1.5 % between the OEM and IOA daily mean first partial and total columns, while the bias between the OEM and TR column amounts is about +1 %. So for the cases in which the IOA columns systematically deviate from the OEM columns, the same is observed for the TR columns, but with a smaller offset.

3.2.4 Error budget evaluations

For a detailed description of all error components quantifying the reliability of the retrieval results, we refer to Senten et al. (2008). In particular, the following error contributions are calculated: the smoothing error, the forward model parameter error, the measurement noise error, the errors due to the uncertainties in the temperature profile, in the solar zenith

angle, in the interfering species' profiles, and in the intensity and pressure broadening of the target spectral lines, as well as the errors due to the uncertainties in the instrument line shape, i.e. the modulation amplitude and phase. As said before, all error components for the IOA and TR retrievals are calculated in the same way as for the OEM retrievals, using the appropriate averaging kernels and gain matrices. For the calculation of the smoothing error, we use the same $\mathbf{S}_a$ matrices for each target species as in Senten et al. (2008). The covariance matrix used for the calculation of the error due to the temperature profile uncertainty is based on the differences between NCEP and ECMWF temperature profiles at St.-Denis. The covariance matrices used for the ILS uncertainty errors represent the degradation of the modulation efficiency and the evolution of the phase error. They are both calculated from the differences between the observed ILS functions – calculated with Linefit8 (Hase et al., 1999) – over a three months time period in 2007 at St.-Denis. The maximum uncertainty in the SZA was estimated at 0.2 degrees. The maximum uncertainties in the line intensity and pressure broadening of the spectral lines of the target molecule were derived from HITRAN 2008.

Table 5 gives an overview of the error budgets on the total and partial columns of O_3, N_2O, CH_4 and CO, when using the OEM, IOA and TR. More specifically, the smoothing error, the total random error without the smoothing component, the total random error, the total systematic error and the total error are shown. The individual contributions to the total random error are the forward model parameter error, the ILS errors, the temperature error, the measurement noise error, the SZA error, the interfering species errors, and the smoothing error, whereas the total systematic error includes the line intensity error and pressure broadening error. The complete table of all these individual contributions can be found in Appendix A.

Although at first sight each retrieval method behaves similarly regarding error budgets, we observe non-negligible differences.

For each species, except for N_2O, the smoothing error is smallest when applying the OEM, for the total as well as for the partial columns. The fact that the smoothing error is generally largest when using the IOA, is in agreement with the slightly smaller DOFS (see Table 3), or equivalently with the small loss of information with respect to the other two methods. For the O_3 and CH_4 total and partial columns the total random error without the smoothing component is smallest for the IOA, whereas for the N_2O and CO columns it is smallest for TR. The same is observed for the total systematic error, except for the N_2O and CO total columns for which the IOA seems to be better than TR. Note that the reduced random error for the IOA and TR columns – depending on the target gas – mainly comes from a decrease of the forward model parameter error, the measurement noise error and the temperature error (see Appendix A). As a result, for the O_3 total and partial columns and for the N_2O and CO total columns the total error is smallest for the IOA, while for the N_2O and CO partial columns it is smallest for TR. For CH_4 the total error is smallest for the OEM.

4 Influence of a priori information

One of the goals of implementing the IOA was to improve the robustness of the retrieval results. We therefore studied the impact of the choice of a priori information on the OEM, IOA and TR solutions. More specifically, we changed the diagonal elements of $\mathbf{S}_a$ and looked at the VMR profiles obtained, at the DOFS, at the daily relative standard deviations on the total and partial column amounts and at the mean relative biases with respect to the original column values. In each case, the off-diagonal elements of $\mathbf{S}_a$ are kept unchanged and are determined by a Gaussian correlation function with an inter-layer correlation length of 4 km.

Table 6 shows the mean daily relative standard deviations (in %) for the 2007 time series of the O_3 total and partial column amounts (CA), when using 10 %, 40 % and 80 % as priori uncertainties on the diagonal of $\mathbf{S}_a$, together with the mean relative biases (in %) with respect to the original retrieval using 10 % $\mathbf{S}_a$ (CA_{ref}). These biases are calculated as $100 * [\sum_{i=1}^{k}(CA - CA_{ref})/((CA + CA_{ref})/2)]/k$, with k the number of measured spectra. Obviously, the mean relative biases on the total and partial column values are smaller for the IOA retrievals than for the OEM and TR retrievals. Hence, the net effect of more stable column amounts in the case of IOA prevails, especially when allowing greater a priori uncertainties on the profiles. In agreement with this finding, the mean daily relative standard deviations on the IOA column amounts vary less with a change of $\mathbf{S}_a$ than those on the OEM and TR column amounts. For the above mentioned choices of $\mathbf{S}_a$ the mean DOFS for the OEM retrieval results are 4.6, 6.0 and 6.7, respectively, for the IOA results they are 3.9, 5.2 and 5.9, respectively, and for the TR retrievals they are 4.6, 6.0 and 6.5, respectively. Thus, for each method, the information content varies in the same way with respect to the applied a priori uncertainty, as expected.

As an illustration, Fig. 13 shows the OEM, IOA and TR O_3 profile at St.-Denis on 12 June 2007, obtained when using $\mathbf{S}_a$ with on its diagonal 10 %, 40 % and 80 %, respectively. Note that for the TR retrievals, changing $\mathbf{S}_a$ corresponds to changing α. In particular, in our test case of O_3 (SNR = 150), the mentioned diagonal values 10 %, 40 % and 80 % correspond to α equal to 1, 0.05 and 0.02, respectively. It is clear that when we apply a too large variability on the volume mixing ratios, i.e. 40 % or more in this example, the retrieved profile deviates strongly in the case of OEM and to a lesser extent in the case of TR, whereas it stays reasonably good for the IOA. This difference becomes larger as we increase the a priori uncertainty.

Figure 14 shows the OEM, IOA and TR O_3 profiles from all 2007 spectra at St.-Denis for 10 %, 40 % and 80 % $\mathbf{S}_a$, confirming the statements above. Thus, IOA retrievals are less sensitive to the choice of the a priori covariance matrix than OEM and TR retrievals. This can be understood by the fact that the IOA extracts the real information out of the measurements and is therefore less affected by unrealistic a priori choices.

Next, we looked at the same characteristics of the OEM, IOA and TR retrievals, but when changing $\boldsymbol{x}_a$ instead of $\mathbf{S}_a$. Table 7 shows the mean daily relative standard deviations (in %) on the 2007 time series of O_3 total and partial column amounts, when using $\boldsymbol{x}_a$, $2\boldsymbol{x}_a$ and $1/2\boldsymbol{x}_a$ as a priori profile, together with the mean relative biases (in %) with respect to the original retrieval using $\boldsymbol{x}_a$. The mean relative daily standard deviations appear to be most steady in the case of TR and, consistently, also the relative biases are smallest for the TR retrievals.

By means of example, Fig. 15 shows the OEM, IOA and TR O_3 profile on 12 June 2007, obtained with the original $\boldsymbol{x}_a$ and with $2\boldsymbol{x}_a$ and $1/2\boldsymbol{x}_a$, respectively. Clearly, the TR retrieval is less affected by the change of the a priori profile than the OEM and IOA retrieval. This is logical, as the TR vertical profile with $\mathbf{L}_1$ as regularization matrix is by definition mainly influenced by the shape of the a priori profile, rather than by its magnitude. Note that this second test tells us something about the importance of the choice of $\boldsymbol{x}_a$ for the three methods, but nothing about the robustness of the retrieved profile.

Finally, we have also tested the sensitivity of the OEM, IOA and TR retrieval results to the choice of the retrieval grid, varying from a fine 44 layer grid to a coarse 7 layer grid. We have found the effect on the retrieval results to be similar for each method. More specifically, we observed a decreasing accuracy for a decreasing number of layers.

5 Theoretical study

To quantify the additional benefit of the IOA a theoretical test has been done based on synthetic spectra. Hereto we created a large set of realistic vertical ozone profiles, and calculated the corresponding spectra using our forward model. Then we added Gaussian distributed random noise to these spectra, based on realistic SNR values, in agreement with the SNR values observed in our Réunion spectra. As such we generated a realistic ensemble of virtual measurements. We then performed OEM, IOA and TR retrievals of O_3 from these spectra with the same retrieval parameters as used before for the real observed spectra, and evaluated their respective reconstructions of the initial vertical profiles. More specifically, each retrieved total and partial column amount has been compared to the corresponding column value adopted in the forward model.

The results of these comparisons are shown in Table 8, as mean relative differences (in %), together with the standard deviations (between brackets). As for the total columns we see that the OEM and IOA slightly better reproduce the original values than TR (i.e. mean relative differences of 0.11, 0.11 and 0.12 %, respectively), although with larger standard deviations (i.e. 0.09, 0.09 and 0.06, respectively). For the second and fourth column, the IOA reproduces the input values best, whereas the first and third partial columns are better reconstructed by the TR and OEM, respectively. The standard deviations are smallest in the case of TR for each partial column. This test shows that the IOA is slightly better in reproducing the original input information, while TR produces more stable results.

6 Conclusions

In this paper we have shown the application of the information operator approach (IOA) to the retrieval of the vertical distribution of atmospheric constituents from ground-based high spectral resolution FTIR solar absorption measurements. All our tests have been performed on spectra taken at the southern hemisphere (sub)tropical site Ile de La Réunion in 2007. In addition, a theoretical study has been made, based on synthetic spectra. We have compared the IOA retrieval results for O_3, N_2O, CH_4 and CO with those obtained when using the optimal estimation method (OEM) and Tikhonov regularization (TR). Our findings prove that the IOA allows the derivation of more stable vertical profiles and total and partial column amounts than the OEM for the atmospheric species investigated, without significant loss of information. Moreover, the IOA is less sensitive to the choice of the a priori covariance matrix. Regarding the error budgets on the total and partial columns we can conclude that the IOA and TR generally perform better than the OEM.

Comparisons of the OEM and IOA retrieval results with those obtained with TR have shown that the stability of the TR column values is somewhat better than the OEM and IOA stability. The information content of the IOA retrievals is slightly smaller than the information content of the OEM and TR retrievals, a quantity being about the same for the last two methods. So, the IOA performs well, i.e. similar to TR, and has some advantages with respect to the OEM, especially regarding profile stability and error budget evaluations.

Based on this study, we can conclude that the IOA applied onto the OEM is a valuable alternative for the retrieval of vertical profile information of trace gases in the atmosphere from ground-based FTIR solar absorption measurements. It behaves better than the OEM from several points of view, but the significance of the improvements depends on the target species and on the chosen a priori information. The approach can easily be implemented in the existing retrieval codes that are used in the Infrared Working Group of NDACC.

Table A1. Summary of all individual error contributions (i.e. fit parameters, smoothing, measurement noise, temperature, intensity, pressure broadening, SZA, empirical apodization, empirical phase, and interfering species error) for each target species retrieved with the OEM, IOA and TR.

Molec.	Alt. range [km]	Fit. param. [%]	Smooth. [%]	Meas. noise [%]	Temp. [%]	Inten. [%]	Press. broad. [%]	SZA [%]	Emp. apod. [%]	Emp. phase [%]	Total interf. [%]
		OEM/ IOA/ TR	OEM/ IOA/ TR	OEM/ IOA/ TR	OEM/ IOA/ TR	OEM/ IOA/ TR	OEM/ IOA/ TR	OEM/ IOA/ TR	OEM/ IOA/ TR	OEM/ IOA/	OEM/ IOA/ TR
O_3	0.05–100	0.0070/ 0.0017/ 0.0077	0.44/ 0.54/ 0.51	0.19/ 0.14/ 0.20	0.60/ 0.46/ 0.60	2.53/ 1.70/ 2.83	0.22/ 0.19/ 0.22	0.44/ 0.39/ 0.44	0.00012/ 0.012/ 0.00014	0/ 0/ 0	0.23/ 0.10/ 0.26
	0.05–9.4	0.0046/ 0.0034/ 0.0058	6.70/ 9.06/ 7.14	1.25/ 1.13/ 1.19	0.23/ 0.21/ 0.22	14.14/ 12.34/ 14.00	2.27/ 1.89/ 2.23	0.44/ 0.56/ 0.44	0.00010/ 0.094/ 0.00011	0/ 0/ 0	0.91/ 0.53/ 0.86
	9.4–21.4	0.071/ 0.00036/ 0.064	9.05/ 10.71/ 10.31	1.89/ 1.40/ 1.64	2.43/ 1.37/ 2.19	27.08/ 13.69/ 23.66	2.62/ 1.36/ 2.26	0.44/ 0.32/ 0.44	0.0014/ 0.21/ 0.0012	0/ 0/ 0	1.23/ 1.06/ 0.90
	21.4–29.8	0.077/ 0.00023/ 0.064	5.56/ 7.58/ 6.70	1.47/ 0.87/ 1.18	2.20/ 1.25/ 1.86	21.81/ 7.81/ 17.34	1.85/ 0.73/ 1.50	0.43/ 0.49/ 0.43	0.0015/ 0.13/ 0.0013	0/ 0/ 0	1.60/ 0.70/ 1.14
	29.8–100	0.062/ 0.0088/ 0.041	5.03/ 6.57/ 6.34	1.37/ 1.09/ 1.10	1.89/ 1.29/ 1.63	13.78/ 7.71/ 9.72	1.16/ 0.76/ 0.84	0.46/ 0.18/ 0.44	0.0013/ 0.058/ 0.00087	0/ 0/ 0	0.69/ 1.10/ 0.093
N_2O	0.05–100	0.32/ 0.12/ 0.011	0.10/ 0.27/ 0.073	0.072/ 0.060/ 0.055	0.19/ 0.054/ 0.082	2.34/ 2.57/ 2.62	0.85/ 0.60/ 0.57	0.31/ 0.32/ 0.31	0.00053/ 0.00050/ 0.00023	0.0027/ 0.0072/ 0.0029	0.041/ 0.028/ 0.020
	0.05–5.8	0.73/ 0.19/ 0.040	0.55/ 1.36/ 0.39	0.28/ 0.25/ 0.20	0.59/ 0.39/ 0.50	4.22/ 3.52/ 3.55	3.38/ 3.22/ 3.05	0.31/ 0.35/ 0.32	0.00087/ 0.0017/ 0.00035	0.0055/ 0.029/ 0.0072	0.19/ 0.18/ 0.13
	5.8–15.4	1.19/ 0.30/ 0.11	0.72/ 2.18/ 0.65	0.34/ 0.32/ 0.22	0.28/ 0.14/ 0.23	2.15/ 2.52/ 2.58	4.80/ 4.45/ 4.37	0.32/ 0.24/ 0.31	0.0017/ 0.0038/ 0.0018	0.012/ 0.057/ 0.025	0.23/ 0.21/ 0.16
	15.4–100	2.76/ 0.70/ 0.34	1.39/ 4.84/ 1.47	0.55/ 0.58/ 0.35	0.15/ 1.09/ 0.89	9.31/ 3.23/ 2.29	8.51/ 4.53/ 3.34	0.26/ 0.46/ 0.31	0.0034/ 0.012/ 0.0080	0.012/ 0.16/ 0.098	0.29/ 0.17/ 0.075
CH_4	0.05–100	0.11/ 0.095/ 0.062	0.22/ 1.09/ 0.31	0.29/ 0.25/ 0.26	0.80/ 0.80/ 0.80	4.69/ 6.22/ 4.92	1.15/ 3.79/ 1.71	0.36/ 0.47/ 0.37	0.000074/ 0.000086/ 0.00025	0/ 0/ 0	0.21/ 0.12/ 0.13
	0.05–9.4	0.17/ 0.11/ 0.17	0.41/ 2.29/ 0.64	0.62/ 0.24/ 0.53	0.64/ 0.75/ 0.64	7.12/ 6.27/ 7.21	2.50/ 4.08/ 2.75	0.37/ 0.48/ 0.37	0.0013/ 0.00076/ 0.00072	0/ 0/ 0	0.46/ 0.11/ 0.29
	9.4–100	0.59/ 0.15/ 0.58	0.60/ 2.91/ 0.61	0.58/ 0.35/ 0.51	1.15/ 0.91/ 1.16	5.62/ 6.10/ 6.02	5.47/ 3.16/ 5.51	0.33/ 0.44/ 0.37	0.0031/ 0.0021/ 0.0024	0/ 0/ 0	0.34/ 0.18/ 0.27
CO	0.05–100	0.076/ 0.017/ 0.013	0.15/ 0.15/ 0.37	0.19/ 0.17/ 0.14	1.22/ 1.16/ 1.10	3.44/ 2.83/ 2.91	0.75/ 0.53/ 0.34	0.31/ 0.32/ 0.32	0.00069/ 0.00050/ 0.00025	0/ 0/ 0	0.23/ 0.14/ 0.10
	0.05–2.6	0.34/ 0.12/ 0.062	1.92/ 2.45/ 3.94	1.68/ 1.46/ 1.04	3.36/ 2.58/ 2.63	28.82/ 22.89/ 15.44	8.89/ 7.68/ 6.06	0.29/ 0.28/ 0.27	0.0026/ 0.0017/ 0.00032	0/ 0/ 0	2.19/ 2.30/ 1.83
	2.6–9.4	0.20/ 0.13/ 0.051	2.22/ 2.67/ 4.16	1.61/ 1.38/ 0.69	0.50/ 0.77/ 0.67	35.00/ 26.64/ 15.53	8.05/ 6.04/ 3.38	0.33/ 0.30/ 0.32	0.0012/ 0.0024/ 0.00057	0/ 0/ 0	1.36/ 1.42/ 0.71
	9.4–100	0.34/ 0.16/ 0.098	2.18/ 2.47/ 4.94	1.56/ 1.49/ 0.90	1.17/ 0.79/ 0.55	33.16/ 22.26/ 9.63	7.44/ 5.04/ 2.50	0.30/ 0.37/ 0.35	0.0030/ 0.0039/ 0.0016	0/ 0/ 0	1.11/ 1.13/ 0.89

Acknowledgements. Thanks for financial support are due to the Belgian Federal Science Policy (Ministerial Order MO/35/024, ESAC II and AGACC contracts) and to the PRODEX Office. We also acknowledge the support of the European Commission through the GEOmon (Global Earth Observation and Monitoring) Integrated Project (contract number FP6-2005-Global-4-036677) and through the HYMN (HYdrogen, Methane and Nitrous oxide: trend variability, budgets and interactions with the biosphere) project (contract number GOCE-037048) under the 6th Framework Programme.

Edited by: C. von Savigny

References

Doicu, A., Hilgers, S., von Bargen, A., Rozanov, A., Eichmann, K.-U., von Savigny, C., and Burrows, J. P.: Information operator approach and iterative regularization methods for atmospheric remote sensing, J. Quant. Spectrosc. Ra., 103, 340–350, doi:10.1016/j.jqsrt.2006.05.002, 2007.

Duflot, V., Dils, B., Baray, J. L., De Mazière, M., Attié, J. L., Vanhaelewyn, G., Senten, C., Vigouroux, C., Clain, G., and Delmas, R.: Analysis of the origin of the distribution of CO in the subtropical southern Indian Ocean in 2007, J. Geophys. Res., 115, D22106, doi:10.1029/2010JD013994, 2010.

Golub, G. H. and Van Loan, C. F.: Matrix computations, The Johns Hopkins University Press, USA, 1983.

Hase, F., Blumenstock, T., and Paton-Walsh, C.: Analysis of the instrumental line shape of high-resolution Fourier transform IR spectrometers with gas cell measurements and new retrieval software, Appl. Opt., 38, 3417–3422, doi:10.1364/AO.38.003417, 1999.

Hase, F., Hannigan, J. W., Coffey, M. T., Goldman, A., Höpfner, M., Jones, N. B., Rinsland, C. P., and Wood, S. W.: Intercomparison of retrieval codes used for the analysis of high-resolution ground-based FTIR measurements, J. Quant. Spectrosc. Ra., 87, 25–52, doi:10.1016/j.jqsrt.2003.12.008, 2004.

Hoogen, R., Rozanov, V. V., and Burrows, J. P.: Ozone profiles from GOME satellite data: description and first validation, J. Geophys. Res., 104, 8263–8280, doi:10.1029/1998JD100093, 1999.

Kozlov, V.: Design of Experiments Related to the Inverse Problem of Mathematical Physics, in: Mathematical Theory of Experiment Design, edited by: Ermakov, C. M., 216–246, Nauka, Moscow, 1983 (in Russian).

Kurylo, M. J. and Solomon, S.: Network for the Detection of Stratospheric Change, NASA Rep, Code EEU, 1990.

Kurylo, M. J.: Network for the detection of stratospheric change (NDSC), SPIE Proceedings 1991, Remote Sensing of Atmospheric Chemistry, 1491, 168–174, 1991.

Rinsland, C. P., Nicholas, B. J., Connor, B. J., Logan, J. A., Pougatchev, N. S., Goldman, A., Murcray, F. J., Stephen, T. M., Pine, A. S., Zander, R., Mahieu, E., and Demoulin, P.: Northern and southern hemisphere ground-based infrared spectroscopic measurements of tropospheric carbon monoxide and ethane, J. Geophys. Res., 103, 28197–28218, doi:10.1029/98JD02515, 1998.

Rodgers, C. D.: Inverse Methods for Atmospheric Sounding: Theory and Practice, Series on Atmospheric, Oceanic and Planetary Physics, Vol. 2, World Scientific, Singapore, 2000.

Rothman, L. S., Gordon, I. E., Barbe, A., Benner, D. C., Bernath, P. F., Birk, M., Boudon, V., Brown, L. R., Campargue, A., Champion, J.-P., Chance, K., Coudert, L. H., Danaj, V., Devi, V. M., Fally, S., Flaud, J.-M., Gamache, R. R., Goldmanm, A., Jacquemart, D., Kleiner, I., Lacome, N., Lafferty, W. J., Mandin, J.-Y., Massie, S. T., Mikhailenko, S. N., Miller, C. E., Moazzen-Ahmadi, N., Naumenko, O. V., Nikitin, A. V., Orphal, J., Perevalov, V. I., Perrin, A., Predoi-Cross, A., Rinsland, C. P., Rotger, M., Šimeková, M., Smith, M. A. H., Sung, K., Tashkun, S. A., Tennyson, J., Toth, R. A., Vandaele, A. C., and Vander Auwera, J.: The Hitran 2008 molecular spectroscopic database, J. Quant. Spectrosc. Ra., 110, 533–572, doi:10.1016/j.jqsrt.2009.02.013, 2009.

Schimpf, B. and Schreier, F.: Robust and efficient inversion of vertical sounding atmospheric high-resolution spectra by means of regularization, J. Geophys. Res., 102, 16037–16055, doi:10.1029/97JD00847, 1997.

Senten, C., De Mazière, M., Dils, B., Hermans, C., Kruglanski, M., Neefs, E., Scolas, F., Vandaele, A. C., Vanhaelewyn, G., Vigouroux, C., Carleer, M., Coheur, P. F., Fally, S., Barret, B., Baray, J. L., Delmas, R., Leveau, J., Metzger, J. M., Mahieu, E., Boone, C., Walker, K. A., Bernath, P. F., and Strong, K.: Technical Note: New ground-based FTIR measurements at Ile de La Réunion: observations, error analysis, and comparisons with independent data, Atmos. Chem. Phys., 8, 3483–3508, doi:10.5194/acp-8-3483-2008, 2008.

Shannon, C. E. and Weaver, W.: The Mathematical Theory of Communication, Univ. of Illinois Press, Urbana, 1949.

Steck, T.: Methods for determining regularization for atmospheric retrieval problems, Appl. Opt., 41, 1788–1797, doi:10.1364/AO.41.001788, 2002.

Tikhonov, A.: On the solution of incorrectly stated problems and a method of regularization, Dokl. Akad. Nauk SSSR, 151, 501–504, 1963.

Vigouroux, C., De Mazière, M., Demoulin, P., Servais, C., Hase, F., Blumenstock, T., Kramer, I., Schneider, M., Mellqvist, J., Strandberg, A., Velazco, V., Notholt, J., Sussmann, R., Stremme, W., Rockmann, A., Gardiner, T., Coleman, M., and Woods, P.: Evaluation of tropospheric and stratospheric ozone trends over Western Europe from ground-based FTIR network observations, Atmos. Chem. Phys., 8, 6865–6886, doi:10.5194/acp-8-6865-2008, 2008.